



The
University
Of
Sheffield.

Microwave Synthesis of Fluorescent Carbon Nanoparticles and their use in Bio-imaging Applications.

By:

Marwah Ahmed Alsharif

**A thesis submitted in partial fulfilment of the requirements for
the degree of
Doctor of Philosophy**

**The University of Sheffield
Department of Materials Science and Engineering**

2019

This PhD thesis is dedicated to

My dear loving parents Ahmed and Fatimah Alsharif

My Husband Abdullah and our daughter Noura

Without your generous support, encouragement and
love my dream would not have been possible.

Abstract

Carbon nanoparticles (CNPs) offer exciting potential in a number of practical areas, particularly in the biomedical and pharmaceutical sciences. Their small size (less than 100 nm), low cytotoxicity, high photo stability and strong fluorescence emission make them ideal candidates for the sensing of ions and biomolecules, for uptake in diseased cells, which can then be detected and monitored via the particle fluorescence, and for the efficient, targeted delivery and release of drugs to diseased areas for therapeutic treatments.

The aim of this thesis was to synthesise fluorescent carbon nanoparticles using a chemistry-based, bottom-up approach via microwave heating to synthesise them within 5 minutes at 200 °C and 220 °C respectively. Carbohydrates, especially glucose and sodium alginate, were used as the carbon source, which resulted in an inexpensive one-step production method. Additionally, the CNPs were stable in aqueous solution without the need for surface passivation. Fluorescent carbon nanoparticles characteristics have been investigated by using various techniques.

Transmission electron microscopy and Raman spectroscopy were used to analyse their structure and morphology. The results indicate that CNPs exhibit an amorphous structure with aromatic rings and carbon double bonds with average particle size calculated from glucose CNPs at 200 °C was estimated to be 133.4 ± 22.8 nm, but this increased to 174.15 ± 30.8 nm after heating to 220 °C. The particles from sodium alginate were highly agglomerated and formed linear carbon nanoparticle chains because of their high affinity. It proved difficult to isolate single carbon nanoparticles. The fluorescence properties of carbon nanoparticles were found to be dependent on the excitation energies and their dominant peaks were located at different positions. Commonly, the peak positions red shifted with reduced intensity as the excitation energy value increased.

Cell lines Fibroblast (HDF), as melanoma cancer cells (C8161), and mouse fibroblast NIH 3T3 were exploited for cytotoxicity evaluations. The obtained CNPs, which were found to be non-toxic and biocompatible, can be used as a unique material for bio-imaging applications. In addition, there has been successful uptake seen by different types of cells. Furthermore, these CNPs have readily entered the cytoplasm of selected cells and shown no significant cytotoxicity. The particles were localised at the cell membrane and the cytoplasm.

Acknowledgement

In the name of Allah, the Most Gracious and the Most Merciful. Thanks to ALLAH who is the source of all the knowledge in this world, for giving me the strength and guidance to complete this thesis. It is a pleasure to attribute credit to the many people who have contributed directly or indirectly to this work. First and foremost, I offer my sincerest gratitude to my supervisor, **Dr. Frederik Claeysens** for his guidance, positive support, knowledge, encouragement and assistance through all four years. Secondly, I must say a special thank you to **Dr Nicola Green** who helped me understand the biological aspects of my project. explaining to me everything related to cell culture and offering me the fullest support and advice in this area.

I would like to extend my sincerest thanks to all my colleagues. I have been blessed with a friendly and cheerful group who offered and shared many interesting discussions, ideas, thoughts and support, in particular Anastasia Brif, Sarina, Zena and Merie. Everyone at the Kroto Institute has helped me during my project and I am grateful for their enthusiasm, ideas, and constant support. I would like specially to thank **Dr Ian Ross** for TEM images and **Dr Deborah B Hammond** for XPS spectra. Also, **Dr Beverley J Inkson**.

I owe my deep sense of gratitude to my beloved Father, **Ahmed Alsharif**, and my mum, **Fatimah**, for their prayers, encouragement and affection, which helped me to complete my work successfully overcoming all the difficult situations. A special thanks also to my sisters, brothers and my mother-in law, for all of the sacrifices that they have made on my behalf. Your prayers for me were what sustained me thus far.

I owe thanks to a very special person, my husband **Abdullah**, for his continued and unfailing love, support and understanding during my pursuit of a PhD degree, which made the completion of this thesis possible. You were always around at the times when I thought that it would be impossible to continue, you helped me to keep things in perspective. I greatly value his contribution and deeply appreciate his belief in me. I appreciate my little girl, **Noura**, who is the pride and joy of my life. I love you more than anything and I appreciate all your patience and support during mommy's PhD studies. Words would never say how grateful I am to both of you. I consider myself the luckiest in the world to have such a lovely and caring family standing beside me with their love and unconditional support.

Lastly, I gratefully acknowledge the financial support for my research from Tabouk University in Saudi Arabia, who gave me a scholarship to pursue my PhD studies.

Presentations and Published abstracts

1.

- 1- **Alsharif, M.**, Frederik Claeysens., Nicola Green. (2015) “**Microwave Synthesis of Fluorescent Carbon Nanoparticles**” 17th annual meeting of the Biomaterials and Tissue Engineering Group. Poster Presentation, December, York.
- 2- **Alsharif, M.**, Frederik Claeysens., Nicola Green. (2016) “**Synthesis, characterisation and Bio-Imaging applications of highly fluorescent carbon nanoparticles**” 18th Biomaterials & Tissue Engineering Group (BiTEG) Meeting. Poster Presentation, Leeds, UK.
- 3- **Alsharif, M.**, Frederik Claeysens., Nicola Green. (2017) “**Microwave synthesis of fluorescent carbon nanoparticles for use in bio-imaging applications**” Tissue Engineering & Regenerative Medicine International Society TERMIS-EU 2017 Poster Presentation, Davos, Switzerland – June 26-30.

Table of contents

ABSTRACT	II
ACKNOWLEDGEMENT	III
PRESENTATIONS AND PUBLISHED ABSTRACTS	IV
LIST OF FIGURES	IX
LIST OF TABLES	XVI
LIST OF ABBREVIATIONS:	XVII
1. CHAPTER ONE: INTRODUCTION, AIMS AND OUTLINES	2
1.1. Introduction	2
1.2. Aims and objectives	4
1.3. Thesis outline	5
2. CHAPTER TWO: LITERATURE REVIEW	7
2.1. Introduction	7
2.2. Carbon Nanoparticles (CNPs)	10
2.2.1. Fullerene-based NPs	11
2.2.2. Carbon nanotubes (CNTs)	12
2.2.3. Carbon quantum dots (CQDs) or Carbon nanodots (CNDs)	13
2.3. Formation of CNPs (methods of synthesis)	16
2.3.1. 'Bottom up' synthesis of CQDs/CNDs	17
2.3.2. 'Top down' synthesis of CQDs/CNDs	20
2.4. Characterisation of CNPs	22
2.5. CNP Fluorescence	23
2.5.1. Up conversion	28
2.6. Mechanism of CNP Uptake in Cells	28
2.7. CNP Applications	31
2.7.1. In vitro bio-imaging	31
2.7.2. In vivo bio-labelling	33

2.8. Summary	36
3. CHAPTER THREE: MATERIALS AND METHODS	38
3.1. Introduction	38
3.2. Experimental	38
3.2.1. Discover SP – microwave synthesiser.	38
3.3. Materials	39
3.4. Synthesis of Carbon Nanoparticles (CNPs)	39
3.4.1. Purification of carbon nanoparticles	41
3.4.2. Freeze drying of carbon nanoparticles	41
3.5. Particle Characterisation	42
3.5.1. Introduction	42
3.5.2. Analytical methods	43
3.6. Biological Characterisation	53
3.6.1. Cell culture: Materials and Methods	53
3.6.2. Equipment and materials used for cell culture	54
3.6.3. Type of cell used	55
3.6.4. Cell culture and passaging	56
3.6.5. Cell counting	57
3.6.6. AlamarBlue assay	57
3.6.7. Preparation of alamarBlue™ medium	58
3.6.8. Cell Viability Assessment	58
3.6.9. Preparation of CNPs for toxicity assay	59
3.6.10. Quantum yield calculations	62
4. CHAPTER FOUR: SYNTHESIS AND CHARACTERISATION OF FLUORESCENT CARBON NANOPARTICLES - RESULTS	64
4.1. Introduction	64
4.2. Result and Discussion	67
4.2.1. Synthesis	67
4.2.2. Quantum Yield	68
4.2.3. Ultraviolet-Visible absorbance spectroscopy (λ ab)	69
4.2.4. Raman spectroscopy analysis.	70
4.2.5. Fluorescence Spectroscopy of CNPs	72
4.2.6. Fourier-transform infrared spectroscopy	74
4.2.7. X-ray photoelectron spectroscopy (XPS)	75
4.2.8. Transmission electron microscopy (TEM)	80
4.2.9. X-ray Powder Diffraction (XRD)	82
4.2.10. Dynamic light scattering (DLS)	82
4.2.11. Dynamic light scattering result for Alginate CNPs at 200°C and 200°C.	84
4.3. Summary	86

5. CHAPTER FIVE: TOXICITY ASSESSMENT OF CARBON NANOPARTICLES.-----	88
5.1. Introduction -----	88
5.2. Statistical analysis -----	90
5.3. Results and Discussion. -----	90
5.3.1. Toxicity study of Alginate CNPs in Human Dermal Fibroblast cells. -----	90
5.3.2. Toxicity study of glucose CNPs in Human Dermal Fibroblast cells. -----	92
5.3.3. Toxicity studies of alginate CNPs on melanoma C8161 cells -----	94
5.3.4. Toxicity studies of glucose CNPs on melanoma C8161 cells. -----	96
5.4. Wound healing study -----	98
5.4.1. Image capture and data analysis -----	98
5.4.2. Wound healing Scratch assay in Melanoma C8161 -----	98
5.4.3. Wound healing Scratch assay in fibroblast cells. -----	101
6. CHAPTER SIX: CELLULAR UPTAKE OF CARBON NANOPARTICLES AS DETERMINED BY EXPERIMENTAL CONDITIONS AND CELL TYPE -----	106
6.1. Introduction -----	106
6.2. Statistical analysis -----	107
6.3. Results and discussion -----	107
6.3.1. Cellular Uptake Studies of alginate CNPs at 200°C in HDF cells. -----	108
6.3.2. Cellular uptake studies of alginate CNPs at 200°C in C8161 cells -----	109
6.3.3. Cellular uptake studies of alginate CNPs at 200°C in NIH 3T3 cells -----	111
6.3.4. Cellular uptake studies of glucose CNPs at 200°C in HDF cells -----	112
-----	113
6.3.5. Cellular uptake studies of glucose CNPs at 200°C in C8161 cells -----	113
6.3.6. Cellular uptake studies of glucose CNPs at 200°C in NIH 3T3 cells -----	114
6.3.7. Comparison of fluorescence emissions of alginate CNPs at 200°C, after 1 hr incubation -----	116
6.3.8. Comparison of fluorescence emissions of glucose CNPs at 200°C, after 1 hr incubation -----	118
6.4. Localisation studies by fluorescence microscopy -----	119
6.5. Co-culture experiments. -----	125
6.6. Discussion -----	130
6.1 Summary -----	133
7. CHAPTER SEVEN: GENERAL DISCUSSION, CONCLUSION AND FUTURE WORK	134
7.1. Discussion -----	134
7.2. Conclusions -----	137

7.3.	Future Work -----	139
8.	APPENDIX -----	154
8.1.	Microwave synthesis of Carbon nanoparticles-----	154
8.2.	Carbon nanoparticles Under UV light-----	154
8.3.	Two photon imaging for glucose and alginate CNPs at different excitation wavelengths -----	155
8.4.	Ultraviolet-Visible absorbance spectroscopy (λ ab) -----	156
8.5.	Cellular uptake studies for alginate CNPs entering NIH-3T3 fibroblasts, human fibroblast and C8161 melanoma cells-----	157
8.6.	Co-culture of C8161 melanoma cancer cells and HDF cells incubated for 60 min with 150 μ g glucose and alginate at 200 and 220°C -----	158
8.7.	Transmission electron microscopy (TEM) for alginate Carbon nanoparticles-----	159
8.8.	Statistic analysis-----	160

List of Figures

Figure 2.1. An illustration of the huge range of current and future applications for nanoparticles in industry. The figure has been reprinted from ref [25] with permission from the copyright holder Interscience	9
Figure 2.2. Atomic structures of the different forms of carbon in nature: (a) graphite, (b) diamond, (c) Buckminsterfullerene (C ₆₀), (d) carbon nanotube or CNT, (e) carbon nanofibre and (f) graphene. Image reproduced with permission from [27].....	10
Figure 2.3. Reaction scheme/sequence used to co-dope CQDs/CNDs with N and S via respective amino acids and modify (extend) the fluorescence emission wavelength from the particles. Image reproduced from [31].	15
Figure 2.4. Electron microscope images of carbon nanodots synthesised hydrothermally using lignin as a carbon source. (a) low resolution showing distribution of NP sizes and (b) high resolution of a single dot. Image reproduced with permission from [48].	18
Figure 2.5. Schematic of the microwave-assisted generation of carbon nanodots ('C-Dots') starting from proteins present in egg shell membrane ('ESM'). Image reproduced with permission from [37].	18
Figure 2.6. Data obtained from the synthesis of fluorescent carbon nanodots by microwave-assisted pyrolysis of citric acid: (a) absorption ('Abs') and fluorescence ('PL') spectra of dots, (b) electron microscope image and size distribution (inset), (c) change in PL intensity with different excitation wavelengths and (d) change in PL intensity with different amine species for nanodot surface passivation. Images reproduced with permission from [40].	19
Figure 2.7. Schematic of the experimental set-up for the production of carbon nanodots via laser ablation of a carbon target under organic solvent. Image reproduced with permission from [53].	20
Figure 2.8. Schematic of the processes involved in the electrochemical synthesis of carbon nanodots using a glycine precursor. Image reproduced with permission from [55].	21
Figure 2.9. (a & b) HRTEM imaging of carbon nanodots formed by microwave irradiation of a mixture of PEI and GA precursors. (c & d) AFM imaging of the same NPs. Image reproduced with permission from [57].....	22
Figure 2.10. (a & b) FT-IR spectra of carbon nanodots shown in Fig. 9 (and the precursor PEI) and (c) XPS spectrum with main element edges labelled. Image reproduced with permission from [57].	23
Figure 2.11. A general electron energy level (Jablonski) diagram depicting the three stages involved in fluorescence within species such as organic molecules and NPs: (1) excitation from the ground state (S ₀) by adsorption of a photon of energy $h\nu_{EX}$ to a short-lived excited singlet state (S ₁ '), (2) decay of S ₁ ' to a relaxed singlet state and (3) fluorescence emission $h\nu_{EM}$ back to S ₀ . Image reproduced with permission from [59].....	24
Figure 2.12. Generalised fluorescence spectra (light intensity vs wavelength: EX = excitation, and EM = emission) showing how the intensity of the emission varies as the intensity of the excitation changes. Image reproduced with permission from [47].....	25
Figure 2.13. Optical spectra obtained from CNPs produced hydrothermally from citric acid. (left) absorption spectrum (black), overlaid with excitation and emission profiles as labelled (blue colour - see image top right of plot), and (right) variation of fluorescence emission intensity with excitation wavelength as indicated. Image reproduced with permission from [45].	26
Figure 2.14. Optical spectra of carbon NPs produced by ultrasonication of glucose – absorption in black, and fluorescence in other colours, resulting from excitation wavelengths indicated. (left panel)	

– CNPs produced in alkaline conditions and (right panel) those produced in acidic conditions. Image reproduced with permission from [62]...... 26

Figure 2.15. (left) absorption spectra and (right) fluorescence emission spectra of CNPs produced from microwave irradiation of a glucose solution with added ions as indicated in the panels. Image reproduced with permission from [63]...... 27

Figure 2.16. (Top) Physical form, observable colour of fluorescence emission and optical spectra (absorption - solid black line, excitation - dashed line and emission - coloured line) for CNPs obtained from the chemical treatment of different carbohydrate precursors. (Bottom) Summary of key data for the four types of fluorescent carbon NPs (FCN) synthesised. Images reproduced with permission from [26]...... 28

Figure 2.17. Schematic depiction of the uptake process for CNPs in cells and transfer through the cell membrane to the interior - see text for discussion. Image reproduced from [65]. 30

Figure 2.18. (top) cell viability-cytotoxic data from CNP seeding of cells and (bottom) fluorescence microscope images of HepG2 cells containing NPs at concentrations of (a) 0.5 mg/mL and (b) 1 mg/ml. Images reproduced from [68]. 31

Figure 2.19. (a and b) HeLa cell viability-cytotoxicity data for blue and yellow fluorescence emission carbon nanodots (microwave synthesised) and (c-e) fluorescence microscope images of CND uptake in HeLa cells. Images reproduced from [57]. 33

Figure 2.20. (top - A) optical images of zebrafish embryos and larvae post fertilisation and addition of CNDs (formed from skin; at 0.4 mg/mL) and (B-D) fluorescence microscope images with varying emission wavelengths from same samples. Image reproduced from [69]. 34

Figure 2.21. Fluorescence imaging of in vivo (mouse) uptake and time-dependent distribution of CNDs formed from aspartic acid, showing the enhanced ability of the particles to attach and penetrate to brain tumour (glioma) cells compared with normal tissue. Image reproduced from [64]. 35

Figure 3.1. (A) Discover SP microwave synthesiser (CEM). The reactor has one cavity with a pressure device. A monitor in front of the cavity shows the temperature and time and connects the instrument to a computer. (B) Schematic diagram illustrating the microwave heating process. During the heating process, the surrounding microwave reactor provides a uniform EM field which ensures the sample is heated evenly. A vent in the pressure device removes excess gas pressure; while keeping the reaction under sealed conditions. (C) Side view of the specific glass vessels with lip seals used in the synthesiser. Images reproduced from CEM Corporation website (2006) [71]. 38

Figure 3.2. Flow diagram showing the method sequence used for the microwave-assisted synthesis of carbon nanoparticles (CNPs). 40

Figure 3.3. Picture of the Christ EPSILON 1-4 LSC freeze dryer machine used in this study..... 42

Figure 3.4. Schematic highlighting the basic structure and optical components of a transmission electron microscope. 44

Figure 3.5. Picture and schematic view of Brookhaven Instruments Corporation ZetaPALS particle analyser. 46

Figure 3.6. Schematic of the components and light path for a typical single beam-diode array detector UV-Vis spectrometer for light absorption measurements..... 47

Figure 3.7. Schematic of the components and photon processes involved in a Raman spectrometer/Raman spectroscopy..... 48

Figure 3.8. The Raman spectrometer used for analysis of CNPs..... 48

Figure 3.9. FTIR spectrometer used for analysis of CNPs..... 50

Figure 3.10. Energy level (Jablonski) diagram showing the origin of fluorescence (light emission of energy = $h\nu_{Em}$) in a material (bulk or nanoparticle) irradiated (excited) by light photons of energy = $h\nu_{EX}$ 51

Figure 3.11. (A) The FluoroMax spectrofluorometer (HORIBA Scientific) used to study CNPs and (B) the instrument sample holder.....	51
Figure 3.12. Schematic of a confocal microscope used for imaging fluorescent emission from material samples.....	53
Figure 3.13. The blue dye resazurin is reduced to the fluorescent pink reduced form by viable, metabolically active cells only. The intensity of absorbance is proportional to the number of metabolically active cells.	58
Figure 3.143. Schematic representation the protocol used to assess the cell viability of Carbon nanoparticles.	59
Figure 4.1. Photographs of carbon nanoparticles (A) a transparent solution of glucose before the microwave reactions, (B) solution after microwave reaction, (C) dry powder of glucose carbon nanoparticles and (D) dry powder of alginate carbon nanoparticles.....	67
Figure 4.2. Typical UV–visible absorption spectra of CNPs. (A) absorption spectra of CNPs produced from glucose heated at 200°C, (B) absorption spectra of CNPs produced from glucose heated at (220°C), (C) absorption spectra of CNPs produced from alginate heated at (200°C). and (D) absorption spectra of CNPs produced from alginate heated at (220°C).	70
Figure 4.3. Raman spectra of (A) raw sodium alginate, (B) CNPs from sodium alginate heated at 200°C, (c) CNPs from sodium alginate heated at 220°C, (D) Raman spectra of raw Glucose, (E) CNPs from glucose heated at 200°C and (F) Carbon NPs from glucose heated at 220°C.....	71
Figure 4.4. Fluorescence emission spectra of synthesised CNPs from (A, B) alginate at 200°C and 220°C and (C, D) glucose at 200°C and 220°C, respectively. The samples existed at different wavelengths from 200 nm to 450 nm.....	73
Figure 4.5. FT-IR spectra of the synthesized (A, B) sodium alginate CNPs heated in the microwave at 200°C and 220°C respectively. (C, D) Glucose CNPs heated in the microwave at 200°C and 220°C, respectively.	75
Figure 4.6. (A) XPS survey scan from Alginate-based synthesis at 200°C, (b) High-resolution XPS spectrum of the C 1s scan from Alginate-based synthesis at 200°C, (C) High-resolution XPS spectrum of the O 1s scan, (D) High-resolution XPS spectrum of the N 1s scan	77
Figure 4.7. (A) XPS survey scan from Alginate-based synthesis at 220°C, (b) High-resolution XPS spectrum of the C 1s scan from Alginate-based synthesis at 220°C, (C) High-resolution XPS spectrum of the O 1s scan, (D) High-resolution XPS spectrum of the N 1s scan.	77
Figure 4.8. (A) XPS survey scan from Glucose-based synthesis at 200°C, (b) High-resolution XPS spectrum of the C 1s scan from Glucose-based synthesis at 200°C, (C) High-resolution XPS spectrum of the O 1s scan, (D) High-resolution XPS spectrum of the N 1s scan.	78
Figure 4.9. (A) XPS survey scan from Glucose-based synthesis at 220°C, (b) High-resolution XPS spectrum of C 1s scan from Glucose-based synthesis at 220 °C, (C) High-resolution XPS spectrum of O 1s scan, (D) High-resolution XPS spectrum of N 1s scan	79
Figure 4.10. TEM images of carbon nanoparticles from glucose at 200°C (A) shows high resolution images from different particles and (B) shows the histogram of different particle sizes.....	81
Figure 4.11. TEM images from glucose CNPs heated in the microwave at 220°C	81
Figure 4.12. (A) A scanning transmission electron microscope (STEM) images for alginate CNPs at 200°C. (B) Energy Dispersive X-Ray Spectroscopy (EDX) spectrum analysis for alginate CNPs.....	81
Figure 4.13. XRD patterns of synthesized CNPs (A) Glucose CNPs heated at 200°C (B) glucose CNPs heated at 220°C (C) alginate CNPs heated at 200°C.....	82
Figure 4.14. Dynamic light scattering (DLS) measurement of Glucose CNPs heated for 5 minutes at 200°C (a) correlation function and (b) the size distribution.	83
Figure 4.15. Dynamic light scattering (DLS) measurement of Glucose CNPs heated for 5.....	83

Figure 4.16. Dynamic light scattering (DLs) measurement of alginate CNPs heated for 5 minutes at 200°C (a) the correlation function and (b) the size distribution.....	84
Figure 4.17. Dynamic light scattering (DLs) measurement of alginate CNPs heated for 5 minutes at 220°C. (a) correlation function and (b) the size distribution.	85
Figure 5.1. Cytotoxicity studies of alginate CNPs Human Dermal Fibroblast cells. (A,D) absorbance value against the concentration of CNPs (B,E) relative cell viability against the concentration of CNP and (C,F) Relative Cell viability against time. (A,B and C) alginate CNPs at 200°C. (D,E and F) alginate CNPs at 220 °C.....	91
Figure 5.2. A) Wound healing assay in melanoma cancer cells forming a confluent monolayer. 100 mg/ml CNPs from glucose at 200°C was added to the cells and incubated for different durations; the images were taken at each time point (B) Quantification of total area analysis and (C) Statistical analysis expressed as percentage of wound closure.....	99
Figure 5.3. (A) Wound healing assay in melanoma cancer cells forming a confluent monolayer. 100 mg/ml CNPs from glucose at 220°C was added to the cells and incubated for different durations; the images were taken at each time points. (B) Quantification of total area analysis and (C) Statistical analysis expressed as percentage of wound closure.....	100
Figure 5.4. Wound healing assay in melanoma cancer cells forming a confluent monolayer. 100 mg/ml CNPs from alginate at 200°C was added to the cells and incubated for different durations; the images were taken at each time points, (B) Quantification of total area analysis and (C) Statistical analysis expressed as percentage of wound closure.....	100
Figure 5.5. A) Wound healing assay in melanoma cancer cells forming a confluent monolayer. 100 mg/ml CNPs from alginate at 220°C was added to the cells and incubated for different durations; the images were taken at each time points (B) Quantification of total area analysis and (C) Statistical analysis expressed as percentage of wound closure.....	101
Figure 5.6. Wound healing assay in HDF cells forming a confluent monolayer. Important to notice that the cells were not treated with the CNPs. Scale bar 100µm.	102
Figure 5.7. (A) Wound healing assay in melanoma cells forming a confluent monolayer. 100 mg/ml CNPs from alginate at 200°C added to the cells and incubated for different durations; the images were taken at each time interval; (B) Quantification analysis shows the reduction distance after scratch;(C) Statistical analysis, Scale bare 100µm	102
Figure 5.8. (A) Wound healing assay in melanoma cells forming a confluent monolayer. 100 mg/ml CNPs from alginate at 220°C added to the cells and incubated for different durations; the images were taken at each time interval; (B) Quantification analysis shows the reduction distance after scratch; (C) Statistical analysis. Scale bar 100µm.....	103
Figure 5.9. A) Wound healing assay in melanoma cells forming a confluent monolayer. A 200-µl sterile tip made the wound across an HDF monolayer. 100 mg/ml CNPs from glucose at 220°C added to the cells and incubated for different durations; the images were taken at each time interval; (B) Quantification analysis shows the reduction distance after scratch; (C) Statistical analysis.	103
Figure 6.1. (A) Cellular Uptake of CNPs derived from alginate at 200°C onto HDF cells at different concentrations and incubation times (B) Integrated intensity of green fluorescent channel of the micrograph vs. the concentration at times points from 5min to 60 min (C) Time points and concentration-dependent uptake of Alginate CNPs in HDF cells. Scale bare 25µm.....	109
Figure 6.2. (A) Cellular Uptake of CNPs derived from alginate at 200°C onto Melanoma (C8161) cells, at different concentrations and incubation times. (B) Integrated intensity of green fluorescent channel of the micrograph against the concentration at times points from 5min to 60 min. (C) Time points and concentration-dependent uptake of Alginate CNPs in C8161 cells.....	110
Figure 6.3. A) Cellular Uptake of CNPs derived from alginate at 200° C cells into NIH 3T3 cells at different concentrations and incubation times. (B) Integrated intensity of green fluorescent channel of	

the micrograph vs the concentration at times points from 5min to 60 min. (C) Time points and concentration-dependent uptake of Alginate CNPs in NIH 3T3cells.	111
Figure 6.4. Cellular uptake of CNPs derived from glucose at 200°C onto HDF cells, at different concentrations and incubation times. (B) Integrated intensity of green fluorescent channel of the micrograph vs the concentration at times points from 5min to 60 min. (C) Time points and concentration-dependent uptake of Glucose CNPs in HDF cells.	113
Figure 6.5. Cellular uptake of CNPs derived from glucose 200°C onto Melanoma (C8161) cells at different concentrations and incubation times. (B) Integrated intensity of green fluorescent channel of the micrograph vs the concentration at times points from 5min to 60 min. (C) Time points and concentration-dependent uptake of Glucose CNPs in C8161 cells.....	114
Figure 6.6. Cellular uptake of CNPs derived from glucose at 200°C into NIH3T3 cells at different concentrations and incubation times. (B) Integrated intensity of green fluorescent channel of the micrograph vs the concentration at times points from 5 to 60 min. (C) Time points and concentration-dependent uptake of glucose CNPs in NIH 3T3 cells.....	115
Figure 6.7. Time-course confocal microscopy images of cellular uptake of Alginate CNPs by HDF, NIH 3T3 and C8161 cells in DMEM supplemented with 1% (v/v) at different times. Green colour represents cell membrane. Nuclei stained with DAPI ($\lambda_{ex}=488$ nm $\lambda_{em}=780$ nm) Scale bars = 25 μ m.	116
Figure 6.8. Fluorescence data from Confocal microscopy of cellular uptake of alginate 200°C CNPs by HDF, NIH 3T3 and C8161 cells in DMEM supplemented with 1% (v/v) FCS at different times points. Two ANOVA Comparing the means of each column with the mean of every other column'. Significance was denoted by a * symbol (* p < 0.05, ** p < 0.01, *** p < 0.001).	117
Figure 6.9. Time-course confocal microscopy images of cellular uptake of glucose CNPs by HDF, NIH3T3 and C8161 cells in DMEM supplemented with 1% (v/v) FCS at different times. Green colour represents cell membrane. Nuclei stained with $\lambda_{ex}=488$ nm DAPI $\lambda_{em}=780$ nm. Scale bars = 25 μ m.	118
Figure 6.10. Confocal microscopy data of cellular uptake of glucose CNPs by HDF, NIH3T3 and C861 cells in DMEM supplemented with 1% (v/v) FCS at one hour of incubation. Two ANOVA Comparing the means of each column with the mean of every other column'. Significance was denoted by a * symbol (* p < 0.05, ** p < 0.01, *** p < 0.001).	118
Figure 6.11. Localisation of photo luminescent alginate CNPs in Human dermal fibroblast. (A) Confocal microscopy images of HDF incubated with (30 μ g/ml) alginate CNPs at 200°C and 220°C Green channel (488nm). (B) Cells were labelled with mitochondrial deep red tracker 25nM. mitochondrial deep red tracker channel 633 nm. (C) Merged images of both channels. (D) Scatter plot of red and green pixel intensities of the image shown in C. Scale bar 25 μ m.....	119
Figure 6.12. Localisation of photo luminescent CNPs in human dermal fibroblast. (A) Confocal microscopy images of HDF incubated with (30 μ g/ml) glucose CNPs from heated at 200°C and 220°C Green channel (488) nm. (B) Cells were labelled with mitochondrial deep red tracker 25nM. mitochondrial deep red tracker channel 633 nm. (C) Merged images of both channels. (D) Scatterplot of red and green pixel intensities of the image shown in C. Scale bar 25 μ m.....	120
Figure 6.13. Localisation of photoluminescent CNPs C8161 melanoma cancer cells. (A) Confocal microscopy images of HDF incubated with (30 μ g/ml) alginate CNPs from heated at 200°C and 220 °C. Green channel (488) nm. (B) Cells were labelled with mitochondrial deep red tracker 25nM. Mitochondrial deep red tracker channel 633 nm. (C) Merged images of both channels. (D) Scatterplot of red and green pixel intensities of the image shown in C. Scale bar 25 μ m.	121
Figure 6.14. Localisation of photoluminescent CNPs in C8161. (A) Confocal microscopy images of HDF incubated with (30 μ g/ml) glucose CNPs heated at 200 and 220°C Green channel (488) nm. (B) Cells were labelled with mitochondrial deep red tracker 25nM. Mitochondrial deep red tracker	

channel 633 nm. (C) Merged images of both channels. (D) Scatterplot of red and green pixel intensities of the image shown in C. Scale bar 25µm	122
Figure 6.15. Localisation of photoluminescent CNPs in human dermal (A) Confocal microscopy images of HDF incubated with (150 µg/ml) alginate CNPs from heated at 200 and 220°C. Green channel (488) nm. (B) Cells were labelled with mitochondrial deep red tracker 50 nM. Mitochondrial deep red tracker channel 633 nm. (C) Merged images of both channels. (D) Scatterplot of red and green pixel intensities of the image shown in C. Scale bar 25µm	123
Figure 6.16. Localisation of photoluminescent CNPs in Human dermal fibroblast. (A) Confocal microscopy images of HDF incubated with (150 µg/ml) glucose CNPs heated at 200 and 220°C. Green channel (488) nm. (B) Cells were labelled with mitochondrial deep red tracker 50 nM. Mitochondrial deep red tracker channel 633 nm. (C) Merged images of both channels. (D) Scatterplot of red and green pixel intensities of the image shown in C. Scale bar 25µm	123
Figure 6.17. Localisation of photoluminescent CNPs in c8161. (A) Confocal microscopy images of HDF incubated with (150 µg/ml) alginate CNPs heated at 200 and 220°C. (B) Cells were labelled with mitochondrial deep red tracker 50 nM. Green channel (488) nm. (B) Mitochondrial deep red tracker channel 633 nm. (C) Merged images of both channels. (D) Scatterplot of red and green pixel intensities of the image shown in C. Scale bar 25µm	124
Figure 6.18. Localisation of photoluminescent CNPs in c8161. (A) Confocal microscopy images of HDF incubated with (150 µg/ml) glucose CNPs heated at 200 and 220°C. (B) Cells were labelled with mitochondrial deep red tracker 50 nM. Green channel (488) nm. (B) Mitochondrial deep red tracker channel 633 nm. (C) Merged images of both channels. (D) Scatterplot of red and green pixel intensities of the image shown in C. Scale bare 25µm	125
Figure 6.19. Optical images of C8161 and HDF co-cultures of ratios 1:1 during (A) 24h and (B) 48h of culture. Original magnification 10×	126
Figure 6.20. A) Co-culture of C8161 melanoma cancer cell and HDF cells incubated between 5-60 min with 150 µg alginate samples at 200°C green: (CNPs) red: deep cell tracker red, magnification: 40× scale bar 25 µm. (B) Quantitative analysis by using T-Test shows the significant differences between two cells. (C) Time course analysis for cellular uptake of alginate CNPs (200°C). Scale bar 25µm	126
Figure 6.21. (A) Co-culture of C8161 melanoma cancer cells and HDF cells incubated for 5-60 min with 150 µg alginate sample at 220°C green: (CNPs) red: deep cell tracker red, magnification: 40× scale bar 25µm. (B) Quantitative analysis by using T-Test shows the significant differences between two cells. (C)Time course analysis for cellular uptake of alginate CNPs. (220°C).....	127
Figure 6.22. (A) Co-culture of C8161 melanoma cancer cells and HDF cells incubated for 5-60 min with 150 µg glucose 200°Cgreen: (CNPs) red: deep cell tracker red, magnification: 40X scale bar 25µm. (B) Quantitative analysis by using T-Test shows the significant differences between two cells. (C)Time course analysis for cellular uptake of glucose CNPs (200°C).....	128
Figure 6.23. (A) Co-culture of C8161 melanoma cancer cells and HDF cells incubated for 5-60 min with 150 µg glucose 220°C green: (CNPs) red: deep cell tracker red, magnification:40X scale bar 25µm. (B) Quantitative analysis by using T-Test shows the significant differences between two cells. (C)Time course analysis for cellular uptake of glucose CNPs (220°C).....	129
Figure 8.1. A glucose solution before the microwave reaction (B) reaction of glucose at 1 minute and (c) Carbonisation images of glucose inside the microwave at 5 minutes	154
Figure 8.2. Confocal microscopy images for alginate carbon nanoparticles and glucose CNPs at different excitation wavelength (A) 760 nm , (B) 780 nm ,(C) 800 nm ,(D) 820 nm , (E) 840 nm , (F) 860 nm , (G) 880 nm, (H) 900 nm , (I) 920 nm, (J) 940 nm (K) 960 nm and (L) 980 nm. . A drop liquid of nanoparticles was placed into cover glass and images under two photon excitation.	155

Figure 8.3. UV-Vis spectra for CNPs from (A) glucose at 200 °C (B) glucose 220 °C , (C) alginate 200 °C and (D) alginate 220 °C 156

List of Tables

Table 3.1. Chemical reagent and suppliers used in this project	39
Table 3.2. Chemicals and equipment used in cell culture	54
Table 3.3. Quantum yield calculation results	68
Table 4.1. The CNP peaks in Raman spectrometer.....	72
Table 4.2. Summary of the results derived from fluorescence spectra in Figure 4.4.....	74

List of Abbreviations:

µg	microgram
µl	Microliter
µm	Micrometre
Ab	Absorption
C-dots	Carbon nanodots
CNPs	Carbon nanoparticles
DAPI	4',6-diamidino-2-phenylindole
DLS	Dynamic light scattering
FTIR	Fourier transform infrared spectroscopy
HDF	Human dermal fibroblast
HRTEM	High-resolution transmission electron microscopy
IR	Infrared
ml	Millilitre
mm	Millimetre
MTT	3-(4,5-Dimethylthiazol-2-yl)-2,5-diphenyltetrazolium bromide
Mw	microwave
MWCNT	Multi-walled carbon nanotubes
NIH 3T3	mouse embryo fibroblast cell line
NIR	Near infrared
nm	Nanometre
NP	nanoparticles
PBS	Phosphate buffered saline
PEG	Poly ethylene glycol
PL	photoluminescence
QD	quantum dots
SEM	scanning electron microscopy
UV	Ultraviolet
UV/Vis	Ultraviolet
XPS	X-ray photoelectron spectroscopy
XRD	X-ray diffraction

λ	Wavelength
λ_{em}	Emission wavelength
λ_{ex}	Excitation wavelength
Φ	Quantum yield

Chapter one: Introduction, aims and outlines

1. Chapter One: Introduction, Aims and Outlines

1.1. Introduction

Since Richard Feynman came up with the idea of manipulating matter at the atomic level, nanomaterials have become an innovative field of research combining the fundamentals of all natural sciences [1]. These first investigations grew into nanoscience, where numerous applications for emerging technologies that are based on nanoparticles have been identified in areas ranging from the biomedical sciences to sporting equipment. A key characteristic of nanoparticles is their significant surface-to-volume ratio, which is compatible with the use of therapeutic agents in medical applications. Additionally, the targeting features that are associated with nanoparticles enable their accumulation in inflamed tissues or tumours. As a result, the therapeutic possibilities that have been unlocked by the mobilisation of nanoparticles in clinical settings are greater than most commentators had ever anticipated. In addition, the valuable optical properties of nanoparticles have created a use for them in optical imaging (OI), and they can also be utilised as triggers for photochemical reactions in biological environments. Therefore, researchers world-wide have sought to gain insight into the various ways in which biocompatible photoluminescent (PL) nanoparticles, with each characterised by controlled dimensional and morphological features, can be fabricated effectively. Noteworthy developments include semiconductor nanocrystals. These are also referred to as quantum dots (QDs), and the *in vivo* and *in vitro* applications of these nanoparticles have been facilitated in the form of OI contrast agents, many of which display promising detection limits and resolutions. A semiconductor nanoparticle is a semiconductor nanocrystal (or QD), with its key features being a diameter of 1–10 nm and its composition drawn from elements of groups II-VI (e.g. ZnO) or III-V (e.g. GaN) in the periodic table. As a quasi-zero-dimensional nanomaterial, the three dimensions of QDs are each no more than 10 nm, with the implication being that internal electron mobility is limited inside the nanoscale dimensions in every direction. Regarding standard fluorescent dyes, QDs are characterised by an array of distinctive optical characteristics, including effective fluorescence stability, broad excitation and emission spectra. These properties are important to note because QDs can be employed in numerous applications. Nevertheless, standard QDs are typically fabricated using semiconducting materials (particularly cadmium and selenium) in either organic-phase or water-phase systems, a critical fact that has given rise to worries about potential toxicity and cost effectiveness. Carbon quantum dots (C-dots), which are nano-structured materials, are characterised by excellent water solubility, biocompatibility

and optical properties. They are paired with chemical inertness, straightforward functionalisation, photo bleaching resistance and negligible cytotoxicity. Due to these characteristics, researchers have increasingly been focusing on these materials over the last 10 years [2]. Especially noteworthy is that it is possible to synthesise C-dots that are characterised by elevated levels of fluorescence in a cost-effective way by applying numerous one-step approaches on an expansive scale. Hence, the evidence indicates that C-dots can be utilised as novel fluorescent materials and as a substitute for standard QDs in a variety of applications. A multitude of advantages are associated with this shift, including the avoidance of excessive heavy metal utilisation, which is expected to surmount difficulties that may arise from toxicity and environmental sustainability.

Fluorescent nanomaterials that contain carbon are categorised into a unique group of nanoparticles, with one of the most distinctive features being the wide variety of shapes included in the class. These shapes include short carbon nanotubes (CNTs) [3], nanodiamonds, [4] graphene QDs [5] and fluorescent C-dots, among others. In the years following the publication of the initial paper addressing C-dot photoluminescence (PL)[6], in which C-dots were also referred to as carbogenic dots, researchers began focusing on the ways in which fluorescent C-dots can be prepared. A range of benefits have been linked to C-dot utilisation when compared to QDs, including straightforward synthesis and negligible cytotoxicity. Based on their properties, fluorescent C-dots constitute one of the most consequential fluorescent labels for applications as far reaching as cellular imaging, bioimaging, energy conversion, energy storage, drug delivery, probes and optoelectronics [6]. Generally speaking, C-dots can be classified per a pair of approaches. Given that the variability of reaction parameters in the context of synthesis can alter C-dots' characteristics, research initiatives have focused on the correlation between certain properties and key variables, such as synthetic techniques and initial materials, in the fabrication of C-dots. The evidence indicates that various C-dot surface groups (e.g. amino, carboxyl and hydroxyl groups) are consequential in informing additional modifications that are related to the improvement of optical properties, biocompatibility and targeting capabilities, thereby promoting the degree to which they are sensitive and selective. The enhancement of properties such as these has augmented the number of areas in which C-dots can be viably applied.

Aside from normal or down-converted PL, the literature indicates that C-dots are associated with superior up-converted PL, thereby holding considerable promise for the development of

high-performance complex photodynamic therapy [6-8]. Additionally, the evidence indicates that C-dots are associated with PL emission in the near-infrared (NIR) spectral region in the context of NIR light excitation—a finding that may give rise to seminal advances in a variety of fields, such as bioimaging, photoacoustic imaging, anticancer therapies and drug delivery [7]. Additionally, due to the excellent levels of photostability and fluorescence exhibited by C-dots, the possibility of utilising these nano-structures as probes is also worth considering. The anticipation surrounding the eventual application of C-dots in these varied areas is clearly indicated by the significant increase in the publication of C-dot-related papers, including both review studies and research projects that have evaluated potential applications [2, 6, 9]. In view of the numerous properties and possible applications of carbon-containing nanomaterials, the purpose of the present work is to synthesise carbon nanoparticles by using microwave techniques, follow by studying the properties, characterisation and bio imaging applications of C-dots. We anticipate that the information presented here will provide a useful theoretical background for researchers who are intending to conduct in-depth investigations of C-dots in the future.

1.2. Aims and objectives

The aim of this thesis was to synthesise fluorescent carbon nanoparticles using a microwave synthesiser. Carbohydrates, especially glucose and sodium alginate, were used as the carbon source. The structural characteristics and optical properties of these carbon nanoparticles were investigated through diverse spectroscopic and analytical techniques. Another aim of this research was to study and understand the mechanisms of cellular uptake and their potential use for bio-labelling and bio-imaging. Further aims were to determine the biocompatibility of the synthesised carbon nanoparticles in cancer cells like melanoma C8161, mouse fibroblast cell line NIH 3T3 and normal cells such as human dermal fibroblast. The objectives of the thesis are listed in detail below:

- 1- To synthesise carbon nanoparticles from sodium alginate and glucose at two different temperatures, 200°C and 220°C, for 5 minutes, comparing the properties between them.
- 2- To assess the structural characteristics of C-dots using transmission electron microscopy, X-ray photoelectron spectroscopy, X-ray powder diffraction, Raman, and Fourier-transform infrared spectroscopy.

- 3- To determine the optical properties of these nanoparticles by using ultraviolet-visible spectroscopy and fluorescence spectroscopy.
- 4- Using resazurin (AlamarBlue) and scratch assay to study the cell viability and toxicity of the synthesised particles.
- 5- Studying the mechanism of cellular uptake by incorporating these particles into melanoma, fibroblast and NIH 3T3.
- 6- Evaluating the cellular uptake mechanism via co-culture experiments and conduct quantitative visualisation and evaluation of different cells and different types of particles on cellular uptake by using confocal microscopy.

1.3. Thesis outline

Chapter 1: Provides an introduction summarising the aims and objective of the study, and outlining the chapters contained in this thesis.

Chapter 2: Gives a detailed literature review of carbon nanoparticles, their synthesis, properties, characterisation and their application in vivo and vitro.

Chapter 3: Describes the materials and methods used in this thesis.

Chapter 4: Sets out and discusses the results of the synthesis and characterisation of carbon nanoparticles

Chapter 5: Sets out and discusses the results of the cytotoxicity studies for cell and tissue culture (in vitro) studies on Melanoma C8161 cell lines and fibroblast.

Chapter 6: Undertakes a study of the cellular uptake of carbon nanoparticles depending on cell type and experimental conditions.

Chapter 7: General discussion

Chapter 8: Conclusion and future work

Chapter Two: Literature Review

2. Chapter Two: Literature Review

2.1. Introduction

Nanoparticles (NPs) are those particles characterized by a size dimension typically in the range below 100 nanometres (nm), where a nanometre is 1 billionth (10^{-9}) of a metre. Broadly they can be classed into two main forms; (i) environmental NPs (aerosols) which are formed via different chemical and physical processes (natural or human-influenced) that occur in the environment (e.g. combustion of biomaterials, volcanic eruptions or vehicle exhaust emissions) and (ii) engineered NPs - those synthesised in laboratory or industrial settings with the specific tailoring of size and properties for a target application [10]. This thesis is focused on the laboratory synthesis of carbon nanoparticles and their resulting optical properties, and so all further discussion concerns matters relating to engineered NPs.

Research into nanoparticle design, synthesis and properties is a rapidly growing area of nanotechnology - the branch of science/engineering which relates to the deliberate manipulation of matter at the nanoscale (atoms - molecules - molecular clusters - NPs as defined above). NPs with a large number of sizes and shapes have been developed and put into regular use for a diverse range of practical applications. NPs can be made in a number of different morphologies such as spherical, tubular or irregular, with all exhibiting quite different or enhanced chemical and physical properties compared with bulk materials of equivalent composition [11].

Many of the unique properties of NPs (compared with those of equivalent bulk materials) result from the large ratio (R) of surface area A (proportional to r^2 , where r is the particle radius) to volume V (proportional to r^3), such that $R \propto 1/r$. As the particle size decreases, this ratio therefore increases with many surface-related processes becoming important for a target application. Other important features, including increased material strength, as well as unique optical and electronic/magnetic properties are also displayed by NPs, increasing their attractiveness across a range of industrial uses.

In terms of chemical composition, metal NPs such as those of gold and silver have found many applications (for example as 'optical markers' in medical diagnosis and cancer treatment therapy), metal oxides including those of titanium and zinc, TiO_2 and ZnO respectively, are incorporated into solar cells and anti UV sun creams and paints, while non-metals, such as silica (SiO_2) and quantum dots composed of semiconducting materials such as

zinc sulphide (ZnS) and cadmium selenide (CdSe), are used in nanoelectronic devices and medical applications.

A number of forms of carbon-based NPs (CNPs) have also now been synthesised for specific purposes. These include

- **Fullerenes** (C_{60}), spherical cage-like structures that have a high electron affinity [12].
- **Carbon nanotubes** (CNTs) and nanofibres - extended tubular structures with very high length to diameter ratio [13, 14].
- **Carbon quantum dots** (CQDs) or **nano dots** (CNDs) - spherical particles less than 10 nm in size which emit light via photoluminescence/fluorescence [15].
- **Graphene nanofolds** [16].
- **Carbon nanofoams** [17].
- **Organic (carbon-based) polymeric structures** [18].

The next section of this thesis (2.2) will focus specifically on the main structural characteristics and properties of the fullerene, CNT and CQD/CND forms of CNP, while more background on the experimental methods used to measure and characterise CNP physical properties and their fluorescent properties (spontaneous light emission subsequent to absorption) are provided in sections 2.4 and 2.5 respectively.

A number of different techniques have been utilised for the synthesis of NPs of varying composition, shape and size (thereby controlling the resulting particle properties). These include chemical methods (vapour phase or sol-gel/hydrolysis reactions), physical methods, such as laser pyrolysis, evaporation-condensation, plasma-based and microwave-assisted, and mechanical methods (e.g. densification) [19]. Section 2.3 outlines some of the most commonly adopted methods for the production of CNPs, with a specific focus on the microwave techniques reported in the scientific literature, as this is the primary concern of this study [20]. These techniques are subdivided according to the approach taken; either 'top down' approaches, where larger structures are first formed and then broken down to smaller NP dimensions as desired (2.3.1) or 'bottom up' approaches (2.3.2), where the final particle size is developed from smaller to larger dimensions.

Many key industries now incorporate NPs into their products, including those manufacturing materials (i.e. ceramics) and chemicals, in the agriculture, automotive and aeronautical industries (for structural components and anti-corrosion surface films/paints), electronic

communications and health/medicine (see Figure 2.1). For example in the health and biomedical industries, NPs are finding ever more applications as either biomarkers for medical diagnosis, since some forms exhibit optical features such as fluorescence and increased optical contrast, which allow for the identification and monitoring of infected areas, or as 'carriers' of drugs within the NP structure for the targeted and organ/tissue-specific delivery of pharmaceutical therapies for diseases such as cancers or central nervous system degenerative conditions (Parkinson's disease or Alzheimer's disease for example) [21, 22].

Since this thesis focuses on the use of CNPs in medical contexts, section 2.6 takes a closer look at the mechanisms by which CNPs are transported within the body to the target area/organ, how they are then taken up by specific cells and how they interact with cell components [23]– obvious and critical considerations for the subsequent imaging of specific areas in the body in medical monitoring and diagnosis, or in the targeted delivery and release of pharmaceuticals for combating disease or other conditions [24].

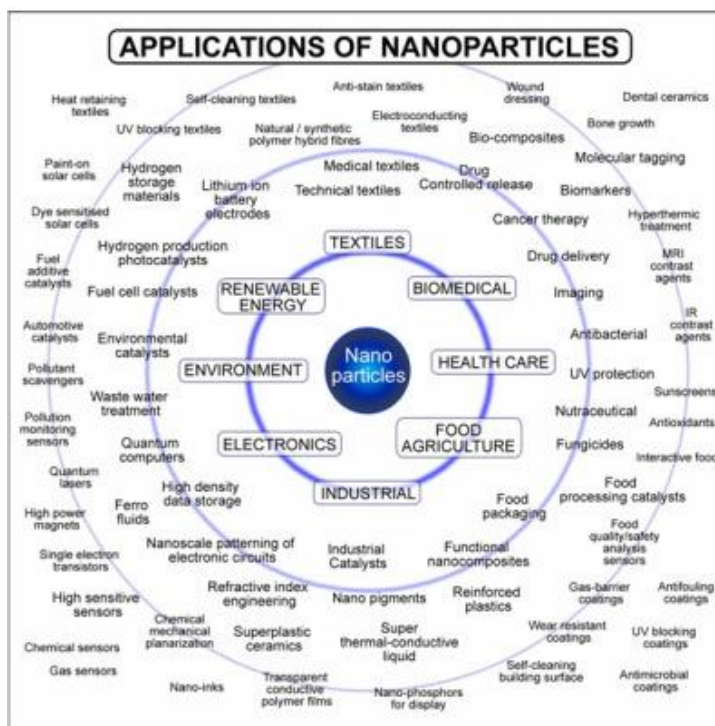


Figure 2.1. An illustration of the huge range of current and future applications for nanoparticles in industry. The figure has been reprinted from ref [25] with permission from the copyright holder Interscience .

Section 2.7 of this thesis takes a more detailed look at the different medical applications of CNPs, with recent key research efforts and insights highlighted in the areas of *in vitro* (cell culture) bio-imaging (2.7.1) and *in vivo* (within the test animal or human system) bio-labelling (2.7.2) [26]. Some discussion is also devoted to the important health & safety issues

related to the use of such NPs in biomedical/drug applications. It is of course essential that in performing the desired role within the body, CNPs do not simultaneously present any potential biological dangers or cause physiological damage by their presence or action.

Finally, section 2.8 provides a summary and the main conclusions of this initial review part of the thesis prior to the rest of the report, which details the experimental side of the study.

2.2. Carbon Nanoparticles (CNPs)

The term carbon nanoparticle can refer to any particle composed either purely of the element carbon (C), or any carbon-based (organic) compound/material. Carbon itself has long been known to exist in the three common structural forms (allotropes) of graphite, diamond and amorphous. Graphite and diamond are both crystalline in structure; in graphite, the carbon atoms are bonded to form a planar, layered structure, whilst in diamond, carbon atoms form a rigid lattice based upon a face-centred cubic structure (see Figure 2.2).

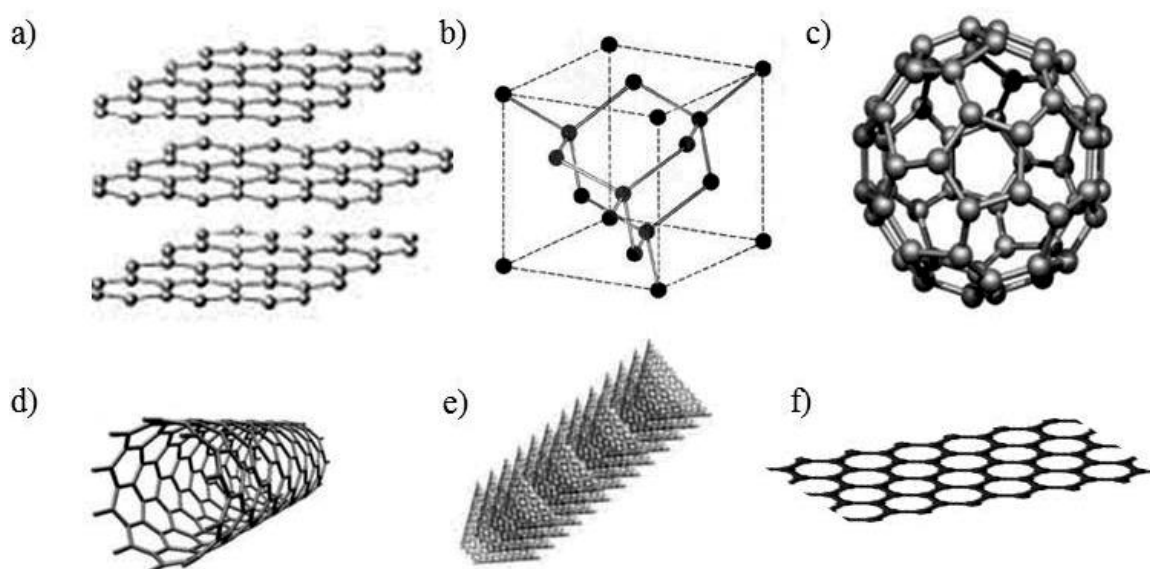


Figure 2.2. Atomic structures of the different forms of carbon in nature: (a) graphite, (b) diamond, (c) Buckminsterfullerene (C₆₀), (d) carbon nanotube or CNT, (e) carbon nanofibre and (f) graphene. Image reproduced with permission from [27].

These respective atomic arrangements are the reason for the obvious differences in the physical properties of the two forms - graphite being soft and diamond hard in nature, for example. In contrast, amorphous carbon displays no ordered arrangement of carbon atoms which again, results in properties in between graphite and diamond. For example, amorphous carbon can be made as a very hard material (similar to diamond), which resulted in the use of this material as a hard coating on drill bits, hard drive platens and shaving blades. Unlike diamond, amorphous carbon is typically non-transparent and black.

In terms of carbon nanoparticles, however, many of the recent advances made involve more recently discovered forms of carbon, including the fullerene structures (e.g. C₆₀ - 'Buckminsterfullerene'), carbon nanotubes (CNTs), carbon quantum/nano dots (CQDs/CNDs) and nanofibres, carbon nanofoams and graphene-based NPs. The rest of this section focuses on the fullerene, CNT and CQD/CND particles since these are the most developed in terms of their applications, in particular with regard to current and future biomedical imaging methods and drug delivery uses [28].

2.2.1. Fullerene-based NPs

First discovered in the 1980s, fullerenes are a class of pure carbon compounds which all possess both sp² and sp³ bonded carbon atoms and form closed structures that can have spherical, elliptical or tubular geometries [29, 30]. The most common forms are C₆₀ and C₇₀, although other fullerene molecules exist with both fewer and greater numbers of carbon atoms. C₆₀ (named as Buckminsterfullerene) has a spherical, ball-like closed structure with icosahedral symmetry (see Figure 2c) consisting of both hexagonal (C₆) and pentagonal (C₅) structural units - consequently NPs of C₆₀ are often referred to as 'Bucky balls'. The diameter of C₆₀ is ~ 0.7 nm, with the interior space providing the potential for encapsulation of other molecules (e.g. drugs), thereby making C₆₀ (and other fullerene structures of different geometries and internal sizes) attractive for research in a number of areas, including the medical and pharmaceutical sciences.

C₆₀ is a highly stable molecule that, as a result of being electron deficient, has a high affinity for and reactivity with other, electron rich species, and so can form a number of functionalised compounds. It is insoluble in water (as with most forms of carbon) but readily soluble in common organic solvents including benzene (C₆H₆), toluene (C₆H₅CH₃) and chloroform (CHCl₃). Fluorescence from C₆₀ NPs in pyridine solvent (C₅H₅N) under sonication was reported by Zhang et al. [31], who observed a particle size-dependent emission red-shift from 424 to 468 nm resulting from the strong interaction of C₆₀ molecules within individual NP structures. Further, aggregation of the NPs led to a broader fluorescence emission band at longer wavelengths (550-570 nm).

Jeong et al. [32] showed that 'colour-tuning' (controlled variation of the emission wavelength) of the fluorescence emission is possible for water soluble C₆₀ NPs via oxidation with hydroxide and conjugation with an attachment of the organic molecule TEG (tetra-ethylene glycol). This ability was attributed to a change in the electronic transition arising from a distortion of the fullerene structure as a result of the chemical modification.

One of the outstanding properties of C₆₀ NPs, which give them such great potential in disease therapies, is their ability to induce cellular autophagy (the process by which cell components including proteins and organelles are degraded and recycled). Wei et al. [33] showed that water soluble Nd-derived C₆₀ NPs exhibited were even more effective than conventional C₆₀ NPs initiating autophagy and the corresponding sensitisation of cancer cells for subsequent interaction with drug molecules.

Shi et al. [34] recently reported on a novel and precise drug delivery system based on C₆₀ NPs for photodynamic-chemotherapy. Molecules of the drug, Doxorubicin, or DOX, were attached to aggregated C₆₀ NPs via covalent bonding to a linker species (attached directly at the NP surface), all of which was then contained within a hydrophilic shell of a functionalised amine-based species. This shell protected and stabilised the drug delivery system during transport to the affected tissue/organ. *In vitro* and *in vivo* studies with this C₆₀ NP-based system displayed a high antitumor efficacy and a low toxicity to other (non-cancerous) areas, as desired.

2.2.2. Carbon nanotubes (CNTs)

These are forms of layered carbon (rolled up graphene) with a tubular geometry and with radial dimensions typically of around 1 nm but much greater lateral dimensions (100s of nm to microns (10⁻⁶ m)). CNTs with a great multiplicity of structures can be produced with careful synthesis, with differences in methods leading to structures with different lengths, thicknesses and numbers of layers. Single walled (SW) CNTs possess a single surface with an inner space, while multi-walled (MW) CNTs have a composite structure (consisting of two or more rolled sheets) that exhibits a number of surfaces and spaces between component elements. These inner spaces within the CNT structures are ideally suited as containment volumes for applications such as hydrogen storage and energy storage devices, in addition to a range of potential and already realised novel biomedical uses [35].

The strong bonding between carbon atoms within the nanotube structures makes CNTs very strong (high tensile strength) yet light (due to the small dimensions) and flexible (high elastic modulus), while they are also very highly electrically and thermally conductive along the length of the tube structure. Electrically, they can exhibit either a metallic or semiconducting nature depending on the precise geometry of the rolled graphene sheets of which they are comprised. Both in terms of electrical current and heat, CNTs conduction far exceeds (by 2-3 orders of magnitude) that displayed by metals such as copper.

SWCNTs and MWCNTs in aqueous solution exhibit strong fluorescence emission properties. Although the fluorescence efficiency of NTs is inherently low, this can be significantly improved through careful covalent functionalisation – for example, Lee et al. [35] reported on a reversible brightening effect (increase in fluorescence emission efficiency) for DNA-wrapped SWCNTs upon the addition/removal of a number of chemical reducing agents. The poor emission characteristics of the CNTs was consequently attributed to structural defects in the nanotubes. In the case of MWCNTs, meanwhile, it has been shown that their fluorescence efficiency can be greatly enhanced through selective functional group (amine and amide) covalent attachment, with control of efficiency possible by variation in the chain length of the attached species [36].

The high strength and flexibility of the CNT structure has led to a number of applications in medicine and other areas. For example, both SWCNT and MWCNT structures have been used for medical implants, in tissue engineering and in the detection, diagnosis and treatment of cancers [37]. In the latter application, for example Liu et al. [38] used functionalised CNTs for the encapsulation and transport of metal oxide (ferrite) particles for use in medical imaging and magnetically-controlled drug delivery. The magnetic iron-based NPs were formed directly within CNTs, which were then amine-functionalised to make them water soluble. These structures were highly dispersed within a diseased target area with magnetic manipulation of NP orientation and interaction uptake between cancer cells and the CNT-based NP structures with no toxicity effects.

A number of clinical studies have also highlighted the potential of CNTs as drug delivery devices in cancer therapies. For example, Chen et al. [39] developed a system for the targeting of leukaemia cells by CNTs functionalised with both the drug molecule (Taxoid) and a fluorescent marker molecule to enable monitoring of transport and uptake to the target area. The system was shown to deliver the drug efficiently and to result in high potency towards the specific cancer cells and low toxicity towards other non-cancerous cells/areas.

2.2.3. Carbon quantum dots (CQDs) or Carbon nanodots (CNDs)

Following on from the discoveries and now routine synthesis and application of the previously discussed forms of CNPs (fullerenes and CNTs), the most recent addition to this group of nanomaterials is the carbon quantum or nano dot [40]. The literature variably refers to either of these names and so from this point on, the abbreviation CQD/CND will be used. While many CQDs/CNDs are composed of graphitic carbon, other forms have been

synthesised using graphene, a recently discovered carbon allotrope whose structure is composed of a two-dimensional lattice of hexagonal carbon-bonded units (with each carbon at the vertex of the unit). These are correspondingly known as graphene quantum/nano dots GQDs/GNDs.

CQDs/CNDs are surface passivated (to prevent chemical oxidation), often chemically functionalised, tiny spherical particles (10 nm or less in size) that are the carbon-equivalent of the metal-based (e.g. cadmium, Cd or zinc, Zn) quantum dots (QDs) whose novel optical properties have long been the subject of research. While CQDs/CNDs share many of the same features and properties of the metal-based QDs such as size, wavelength-dependent emission of fluorescent light (typically at blue, green and yellow wavelengths, approx. 450-590 nm) and the ability to attach to biomolecules (bioconjugation), they have the distinct advantages of low toxicity in the body, and are able to be formed relatively easily and cheaply on a large scale by a variety of techniques that all start from a common and cheaply sourced precursor. This combination of factors makes them an exciting tool in a number of applications, especially in medical bioimaging, disease monitoring/diagnosis and drug delivery/treatment applications.

Mao et al. (2010) published work looking at the fluorescence properties of 1.5 nm CQDs/CNDs formed from lampblack, a cheap commercial form of carbon derived from the combustion product soot [41]. The NPs formed remained highly soluble in water over months (essential for delivery to and within the body), were stable against photobleaching (chemical degradation by adsorption of light, resulting in loss of the ability to fluoresce) and were easily passivated and functionalised for enhanced properties of increased light emission efficiency and longer emission lifetimes.

As well as the pure carbon-based QDs, another recent strategy has been to dope CQDs/CNDs with other elements (e.g. nitrogen N, and sulphur S) in order to modify the fluorescence properties of the NPs. For example, Zeng et al. [42] used both N and S to co-dope hydrothermally synthesised CQDs/CNDs (see Figure 2.3) in order to extend fluorescent emission to longer (red light) wavelengths (> 600 nm) from that of the particle, and thereby extend the potential range of applications for such NPs.

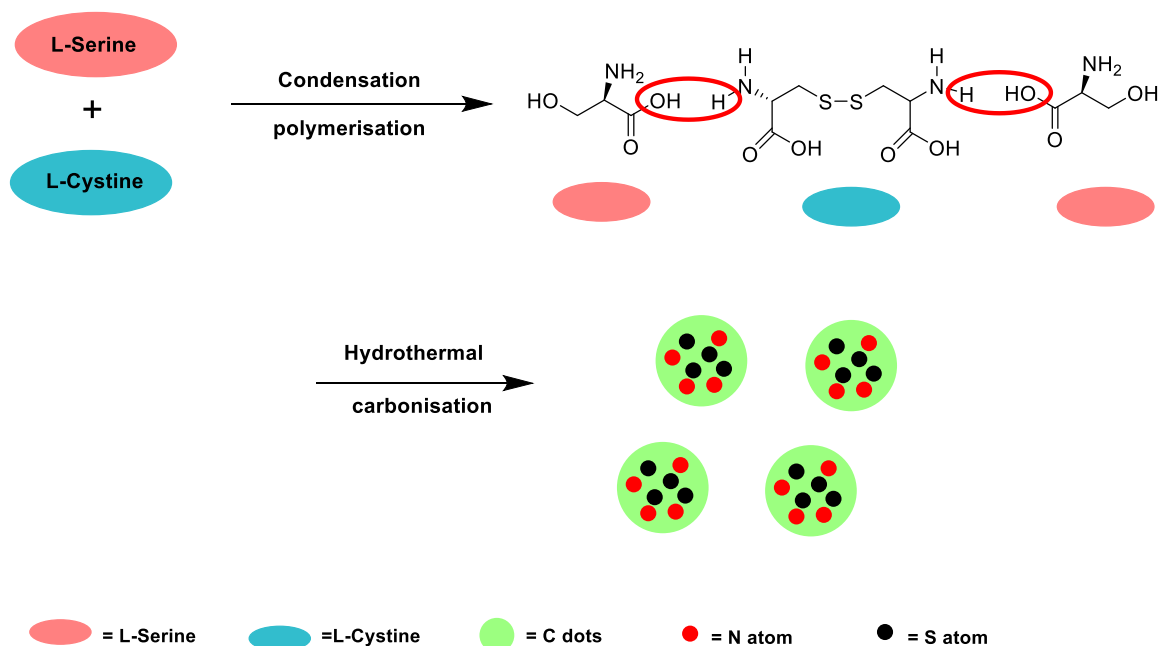


Figure 2.3. Reaction scheme/sequence used to co-dope CQDs/CNDs with N and S via respective amino acids and modify (extend) the fluorescence emission wavelength from the particles. Image reproduced from [31].

The authors reported an orange emission (> 590 nm) at room temperature (showing the doping had indeed extended the wavelength range of fluorescence) and then showed that these NPs could be used to image mice macrophage cells.

Similarly, in the case of GQDs/GNDs, tuneable fluorescent light emission is possible by doping of the bare particles. Qu et al. [43] showed that by doping GQDs/GNDs with N and simply varying the nature of the solvent (water to organic to solvent free) in which the NPs are formed, it is possible to tune the light emission through from blue to yellow wavelengths. Again, this ability to modify the fluorescent properties of these forms of CNPs in a controlled manner is of great importance for future application in the area of medical bioimaging.

In terms of drug delivery potential, CQDs/CNDs offer many exciting possibilities for a route towards routine methods of effectively and efficiently targeting affected areas within the body with corresponding low toxicity towards surrounding non-affected areas. Ding et al. [44] reported on DNA-conjugated CQDs/CNDs and functionalised variations which showed potential use as fluorescent drug delivery vehicles. Very recently, Feng et al. [45] described a 'charge convertible' polymer-functionalised CQD/CND system for the transport and release of cisplatin (platinum-based drugs) to cancer cells. The ability to change the charge nature of the system in slightly acidic conditions (often caused by cell disease) allowed for the quick and efficient release of the drug once at the target cells. It was shown *in vivo* that this system

afforded high efficacy towards tumour inhibition, as well as low toxicity to surrounding normal cells.

The following sections of this review chapter now focus on other aspects of CNPs, with particular reference to CQDs/CNDs, since this was the form of CNP that was studied in the experimental part of the study.

2.3. Formation of CNPs (methods of synthesis)

A large and diverse range of methods have been developed for the small- and large-scale generation of CNPs, with each individual method having advantages and disadvantages compared with the others. All start with some form of bulk-phase carbon as the precursor material from which the NPs are then synthesised. Often, fine-tuning of reaction conditions (e.g. temperature, precursor, reaction/process time) can be used to tailor the final dimensions and properties of the generated CNPs. The different methods are generally separated as being either *top down* in nature (e.g. laser ablation/arc discharge), where NPs are formed by the breakdown-removal of a larger carbon structure (e.g. a graphite block/electrode) or *bottom up* (e.g. thermal or microwave-assisted) where particles are grown from smaller units (molecular clusters derived from organic precursors such as glycine or sucrose) to the desired size [46].

In the case of fullerene NPs, the original method of production was via the electric arc discharge between graphite electrodes in an inert (helium) atmosphere at low pressure. Carbon is evaporated and condenses out in the form of soot with small levels of the desired NPs (C₆₀). Alternatively, laser evaporation of a suitable target material can also be used for small-scale production of fullerenes. For larger scale production, high temperature/low pressure flame combustion of organic materials such as ethene and benzene is used.

CNTs are synthesised by three main evaporation-condensation based methods; low temperature (< 800 °C) catalytic chemical vapour deposition (CCVD), and high temperature (> 1000 °C) electric arc discharge and laser ablation. CCVD involves the decomposition of an organic vapour (methane or ethene, for example) in the presence of a metal catalyst, which promotes the growth of CNTs at catalyst surface sites. Focused laser ablation of a heated graphite block (1200°C/argon atmosphere) with a metal catalyst efficiently produces SWCNTs, with their diameter varying with the laser power used (higher power leading to smaller diameters). Electric discharge between graphite electrodes in a sealed chamber (1700°C/high pressure He-H₂ atmosphere) leads to the evaporation and condensation of soot at the cathode and on the chamber wall surfaces. In all cases, MWCNTs are the main product

in the absence of a suitable metal catalyst, whilst SWCNT formation is promoted by catalytic growth at metal surfaces (e.g. those of Co, Ni, Fe, Pt and Ag) [13].

2.3.1. 'Bottom up' synthesis of CQDs/CNDs

2.3.1.1. Thermal synthesis

Guo et al. [47] described a simple and cost-effective thermal route to the formation of fluorescent CQDs/CNDs using hair (containing the structural protein keratin) as a source of carbon for particle generation. The human hair (sourced from barber shop waste) was heated continually for 24 hours at 200°C in an oven, resulting in the production of a solid black deposit (via the process of carbonisation). After being dissolved in water and then centrifuged, this produced a very high yield (95%) of CQDs/CNDs with a modal size of 4-5 nm. Upon irradiation with UV light (365 nm), the NPs exhibited bright blue fluorescence, with the peak emission (observable colour) shifting to longer visible wavelengths as the excitation wavelength was increased. The particles were reported to be photostable (maintaining fluorescence emission) for over an hour and showed good potential for the sensing of Hg²⁺ ions (an environmental pollutant species with high cellular toxicity) [47].

2.3.1.2. Hydrothermal-aqueous synthesis

Chen et al. [48] synthesised CQDs/CNDs through the hydrothermal (solution heating) treatment of lignin (a key structural organic polymer present in plants and algae) in the presence of hydrogen peroxide (H₂O₂) – see Figure 2.4. Separate mixtures of lignin dispersed in water with added H₂O₂ were heated in an autoclave at 180°C for periods of 10 minutes through to an hour in order to study differences in the NPs obtained. The solutions obtained were then filtered to remove any remaining lignin and dialysed to remove excess peroxide.

Maximum product yield was reported as 12% for those NPs obtained after hydrothermal treatment for 10 minutes, with the yield decreasing for longer periods of treatment. The CQDs/CNDs obtained in this way showed strong blue fluorescence with good stability. They also exhibited the key properties of low cytotoxicity and high biocompatibility and appeared to have promising potential for bioimaging applications.

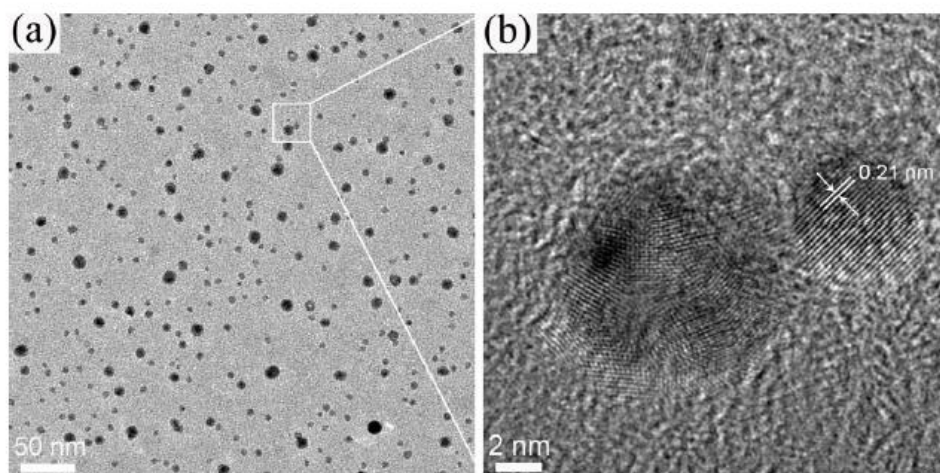


Figure 2.4. Electron microscope images of carbon nanodots synthesised hydrothermally using lignin as a carbon source. (a) low resolution showing distribution of NP sizes and (b) high resolution of a single dot. Image reproduced with permission from [48].

2.3.1.3. Microwave-assisted synthesis

Microwave-based methods involve the placing of a solid carbon precursor or a reaction solution containing the precursor in a microwave oven and subsequent exposure to microwaves for a set period of time. Wang et al. [49] used this method for the production of CQDs/CNDs using the proteins present in egg shell membrane as a source of carbon (Figure 2.5).

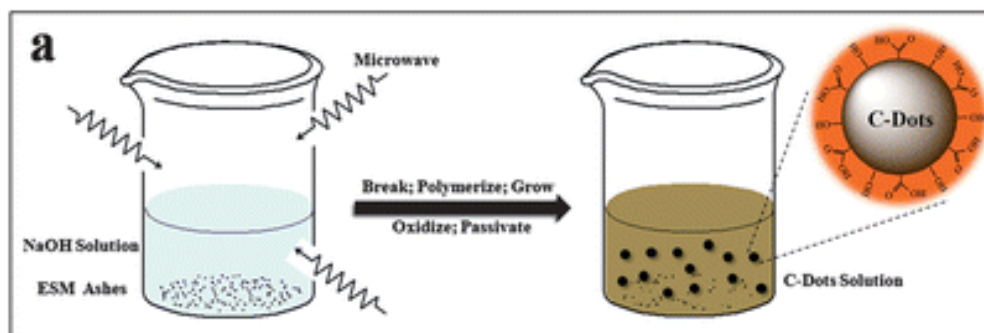


Figure 2.5. Schematic of the microwave-assisted generation of carbon nanodots ('C-Dots') starting from proteins present in egg shell membrane ('ESM'). Image reproduced with permission from [37].

The NPs showed the desired optical property of strong fluorescence emission (peaking at 450 nm) with a quantum yield of 14%, and so could be developed for applications such as bioimaging and the sensing/monitoring of specific ionic pollutants (mercury and iron, for example). The authors concluded that this was a viable, cheap and fast method for CQD/CND synthesis with a recyclable waste product carbon source (egg shell).

He et al. [50] reported on their study in which N-doped CQDs/CNDs were rapidly generated (over the course of less than 10 minutes) from the solid-phase microwave irradiation of the amino acid L-glutamic acid. The NPs produced in this way were ~ 1.6 nm in size and showed strong and stable blue fluorescence with a high quantum yield ($\sim 41\%$), which varied with both pH and excitation wavelength. These NPs exhibited potential for cellular bioimaging as a result of their strong and tuneable fluorescence and low cytotoxicity. In a further example of the microwave-based synthesis method, Zhang et al. [51] produced N-doped CQDs/CNDs by the aqueous-phase microwave irradiation of diammonium hydrogen citrate, with the dots showing high fluorescence quantum yield (27%), high biocompatibility and low cytotoxicity. It was therefore concluded that these dots showed good promise in cellular imaging applications.

Finally, Zhai et al. [52] used a microwave-assisted pyrolysis technique involving a citric acid precursor and a surface passivating agent, EDA (1,2-ethylenediamine) – Figure 2.6. The CQDs/CNDs produced by this method were 2-3 nm in size and showed high fluorescence quantum yield (30%). In addition, they were shown to be efficiently taken up in specific cells and to have low cytotoxicity, therefore again showing the potential of CQDs/CNDs for bioimaging applications.

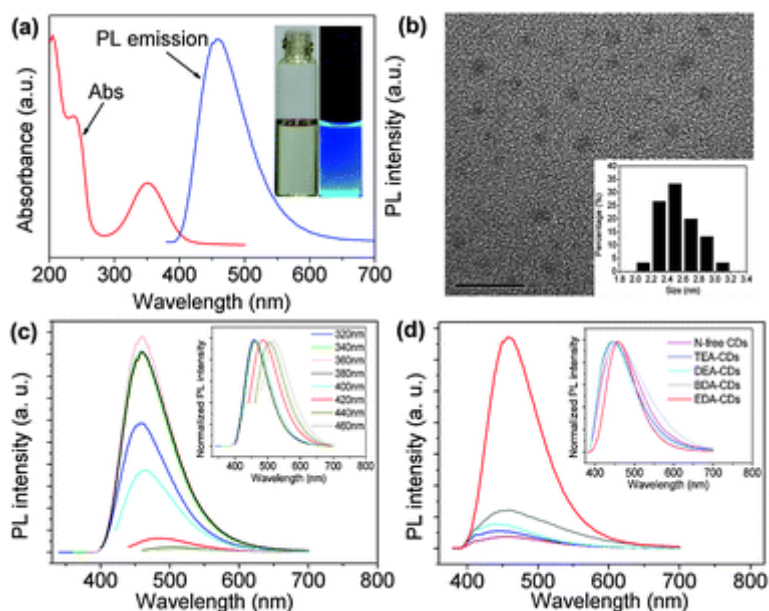


Figure 2.6. Data obtained from the synthesis of fluorescent carbon nanodots by microwave-assisted pyrolysis of citric acid: (a) absorption ('Abs') and fluorescence ('PL') spectra of dots, (b) electron microscope image and size distribution (inset), (c) change in PL intensity with different excitation wavelengths and (d) change in PL intensity with different amine species for nanodot surface passivation. Images reproduced with permission from [40].

2.3.2. 'Top down' synthesis of CQDs/CNDs

2.3.2.1. Laser ablation

Reyes et al. [53] described the focused laser ablation of a solid carbon target in a beaker of acetone (see Figure 2.7) for the generation of CQDs/CNDs. A pulsed Nd:YAG laser (with pulse durations on nanosecond timescale) was used for irradiation at infrared (IR), visible and ultraviolet (UV) wavelengths of 1064, 532 and 355 nm, respectively. This produced spherical-like NPs between 5 nm and 20 nm in size in numbers controlled by the ablation process (e.g. laser power/pulse, duration/repetition, rate/wavelength) – with higher numbers of smaller NPs resulting from UV ablation while lower numbers of larger (agglomerated) NPs resulting from IR ablation. The particles produced at all wavelengths showed fluorescence emission, but this was most intense from ablation at 355 nm. The peak emission wavelength from the CQDs/CNDs was shown to be tuneable according to both ablation and excitation wavelength and ablation time.

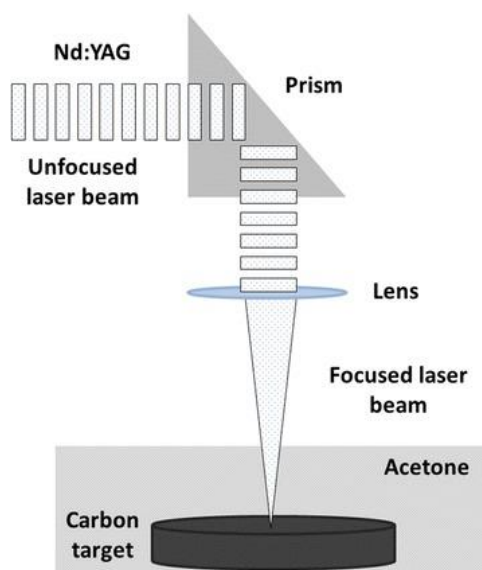


Figure 2.7. Schematic of the experimental set-up for the production of carbon nanodots via laser ablation of a carbon target under organic solvent. Image reproduced with permission from [53].

Nguyen et al. [54] described their formation of CQDs/CNDs by the laser ablation (using a Ti Sapphire laser pulsed at a femtosecond timescale) of graphite powder dispersed in polyethylene glycol (PEG), which led to the generation of graphitic NPs with a size of 1-3 nm. In turn, it was shown that these nanodots were both strongly fluorescent and highly selective and sensitive in the detection of a range of biologically relevant ion species.

2.3.2.2. Electrochemical synthesis

As implied by the name, these synthesis methods involve the use of electricity to initiate a reaction between chemical precursors in solution, leading to the production of CQDs/CNDs. An example is that of Wang et al. [55], who used the amino acid glycine in an alkaline solution as a precursor to form NPs via electro-oxidation/polymerisation, carbonisation and surface passivation (see Figure 2.8).

The NPs they formed showed strong and stable fluorescence emission at 440 nm (from excitation at 365 nm), which in the presence of haemoglobin (blood cell protein) exhibited concentration-dependent emission (decreasing with increasing haemoglobin), and therefore these CQDs/CNDs have the potential to be used as a biological sensor.

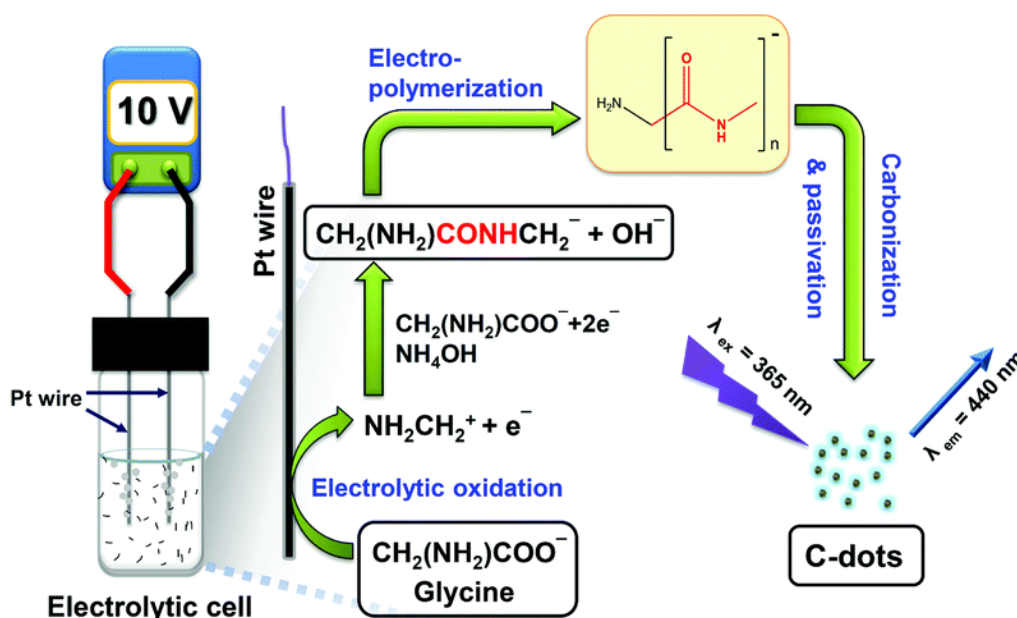


Figure 2.8. Schematic of the processes involved in the electrochemical synthesis of carbon nanodots using a glycine precursor. Image reproduced with permission from [55].

Another example is the study of Niu et al. [56], who reported on the formation of CQDs/CNDs (with an average size of 3 nm) by electro-carbonisation of nitrile compounds in an ionic liquid (to charge the NPs for easy separation and collection) using carbon-free electrodes. The NPs showed strong and broad fluorescence emission and were successfully used for cell imaging and ion (Fe^{3+}) detection.

2.4. Characterisation of CNPs

A number of state-of-the-art analytical techniques are typically used to study the physical and optical properties of synthesised carbon-based NPs. Usually, the first step is the imaging of the particles using transmission electron microscopy (TEM), in order to estimate a size distribution and an average or modal size from a sample of particles viewed at low-medium instrument resolution, while high resolution (HR)-TEM is used to image individual NPs. Single particle imaging/analysis is important for determining particle morphology and surface structure-integrity. Other methods for measuring particle size include atomic force microscopy (AFM) and dynamic light scattering (DLS), which involves measuring the intensity of scattered laser light from a solution containing the NPs. TEM/AFM gives size information on dry particles while DLS gives a hydrodynamic size of hydrated particles.

Liu et al. [57] used a microwave-assisted method for the rapid and easy synthesis of CQDs/CNDs using polyethyleneimine (PEI) and glutaraldehyde (GA). By varying the relative concentrations of these two species, a range of NPs were formed with tuneable fluorescence emission. Figure 2.9 shows a composite of images obtained from both TEM and AFM imaging of the particles formed by this method.

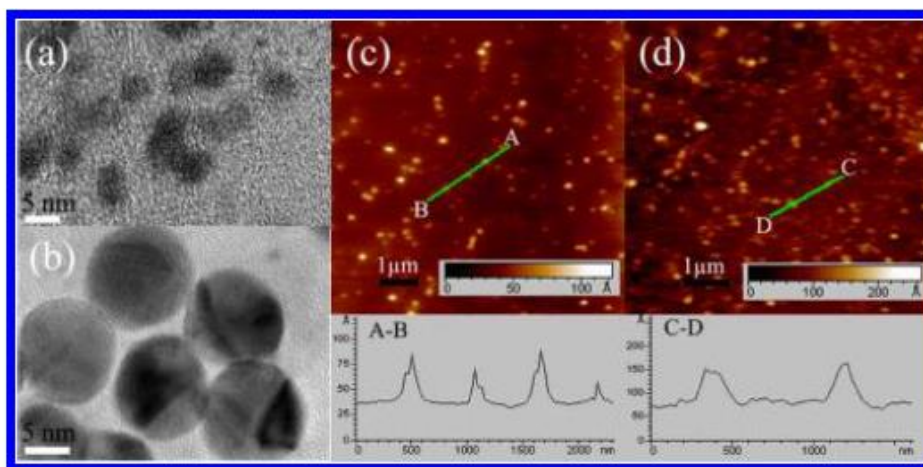


Figure 2.9. (a & b) HRTEM imaging of carbon nanodots formed by microwave irradiation of a mixture of PEI and GA precursors. (c & d) AFM imaging of the same NPs. Image reproduced with permission from [57].

HRTEM showed that the particles were crystalline in nature with a narrow size distribution of 2-7 nm (average = 5 nm). The sizes measured using DLS were larger at 10-15 nm due to the presence of a hydration shell in the solution. AFM, however, confirmed the TEM sizes.

In this same study, other characterisation techniques used included:

- (1) X-ray photoelectron spectroscopy (XPS) for the verification of the chemical composition of NPs from the determination of characteristic x-ray absorption edges present in XPS spectra (Figure 10c);
- (2) Fourier-transform (FT)-IR spectroscopy for identifying the presence of surface functional groups from their characteristic IR absorption peaks in FTIR spectra (Figure 2.10 a & b),
- (3) UV-visible absorption spectroscopy to measure the light absorption spectrum of the NPs
- (4) Fluorescence spectroscopy to measure the fluorescence emission properties (e.g. peak wavelength position and dependence on excitation wavelength, and fluorescence efficiency or quantum yield QY (%)) of the particles and how they vary with changes in the synthesis conditions, e.g. changes in the precursor concentration ratio and surface group functionalisation. More detail on the nature of fluorescence, how it arises in CNPs and how it is measured is given in the next section (1.5).

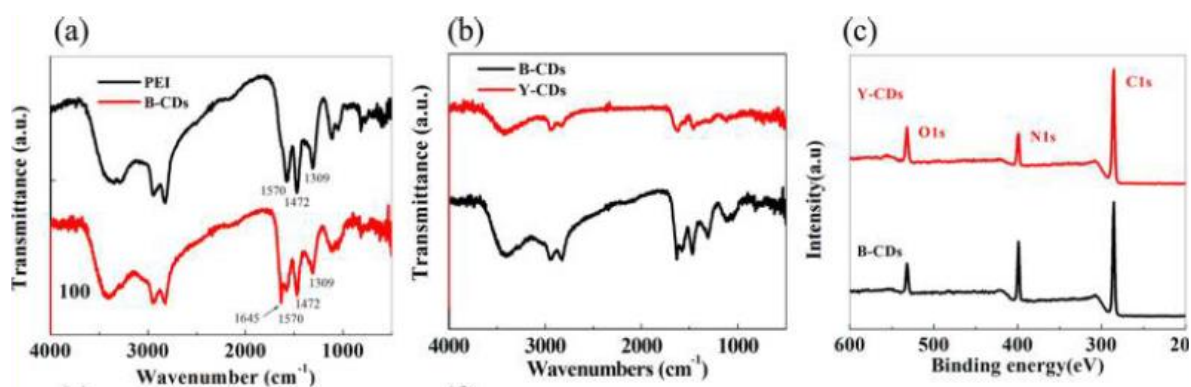


Figure 2.10. (a & b) FT-IR spectra of carbon nanodots shown in Fig. 9 (and the precursor PEI) and (c) XPS spectrum with main element edges labelled. Image reproduced with permission from [57].

Fluorescence emission measurements are also typically used to monitor the susceptibility, selectivity and efficiency of the binding of the NPs with biologically-relevant ions (e.g. Fe^{3+}) in order to evaluate their potential as biosensing tools. Fluorescence emission measurements are also used to assess the uptake of NPs in specific cell types for bioimaging applications, and thus their possible role in the targeted, non-toxic delivery of specific drugs for the treatment of diseases and neurological conditions.

2.5. CNP Fluorescence

Fluorescence (often also referred to as photoluminescence or PL) is an optical property of certain organic molecules and NPs whereby, upon absorption/excitation of light incident on them with usually short wavelength UV light (<350 nm), electrons then undergo specific

electronic transitions which result in the emission of light ($E_{EM} = hv_{EM}$ or hc/λ_{EM}) at longer wavelengths (usually in the visible range, $\sim 400\text{-}600\text{ nm}$; $E_{EM} < E_{EX}$ or $\lambda_{EM} > \lambda_{EX}$) – see Figure 2.11 [58]. This fluorescence emission gives a colourless solution containing the species a distinct observable colour that can be tuned (i.e. the peak emission moves to different wavelengths) by varying certain NP synthesis conditions that determine particle size and surface chemistry. Once the excitation light is removed, the system returns immediately to the ground electronic state (lowest energy, most stable), and the solution of NPs becomes colourless once more.

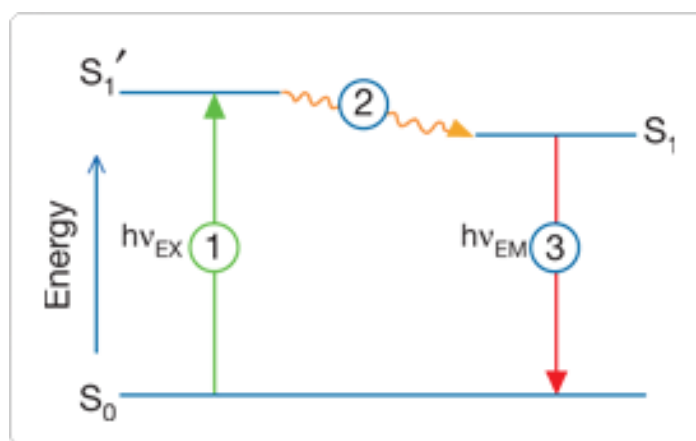


Figure 2.11. A general electron energy level (Jablonski) diagram depicting the three stages involved in fluorescence within species such as organic molecules and NPs: (1) excitation from the ground state (S_0) by adsorption of a photon of energy hv_{EX} to a short-lived excited singlet state (S_1'), (2) decay of S_1' to a relaxed singlet state and (3) fluorescence emission hv_{EM} back to S_0 . Image reproduced with permission from [59].

Such properties obviously make fluorescent QDs/CNDs extremely attractive as medical/environmental sensor species where they interact and bind with the target ions or molecules which are being detected and monitored, and as biomedical marker species for the imaging of cells within the body for the identification and tracking of diseased areas [60].

NP fluorescence is experimentally measured using a spectrofluorometer, i.e. a spectrometer in which a sample of the NP solution is placed and irradiated by an excitation light source. The resultant fluorescence emission is then collected and displayed as a fluorescence spectrum for further analysis (see Figure 2.12). In all such experiments, it is crucial to avoid photobleaching of a species – that is overexposure (caused by excitation light at too high an intensity), resulting in the destruction of the fluorescent nature and loss of emission. With these instruments, the average properties of bulk samples are obtained from typically μl - ml sample volumes. Other types of fluorescence-based instrumentation are also used for resolving fluorescence variation with spatial direction (fluorescence microscope/scanner)

while biological studies often use a cytometer to measure the fluorescence emission within cells in a flowing stream.

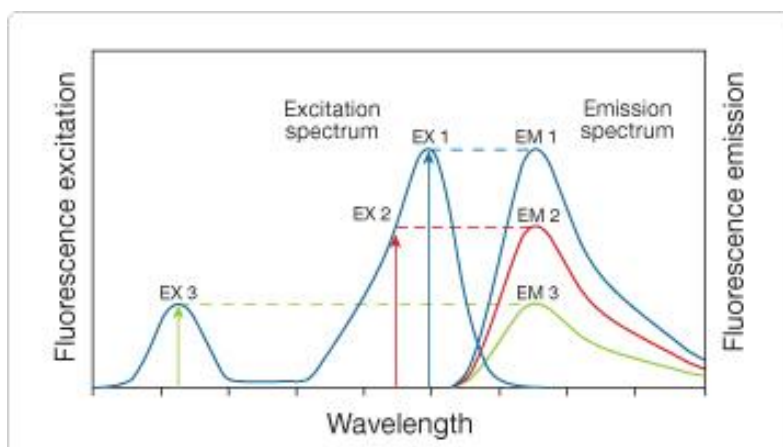


Figure 2.12. Generalised fluorescence spectra (light intensity vs wavelength: EX = excitation, and EM = emission) showing how the intensity of the emission varies as the intensity of the excitation changes. Image reproduced with permission from [47].

Examples of spectra for synthesised CQDs/CNDs are discussed in more detail shortly. Important properties of fluorescent NPs that are routinely measured and reported in studies are (i) the peak emission wavelength (and how it varies with varying excitation wavelength), (ii) the quantum yield (QY), which is an indication of the efficiency of the fluorescence process under a given set of conditions, and (iii) the fluorescence lifetime or inherent stability of the emission from the NP. These are all key factors in deciding the suitability and potential for a particular CQD/CND system for any future biosensor/biomarker application [26].

In the study reported by Li et al. (2017), CQDs/CNDs (~ 3-6 nm size) were synthesised by the hydrothermal treatment of citric acid with PEI. Both UV-Vis absorption and fluorescence properties of the NPs were subsequently studied (see Figure 2.13), with absorption peaks at 252 nm and 358 nm [61] Using an excitation wavelength of 360 nm, strong fluorescence was observed at 459 nm, with the intensity decreasing at longer excitation wavelengths (up to 410 nm) but remaining centred at 459 nm. Fluorescence QY was determined relative to the reference fluorophore quinine sulphate with a known QY = 0.54 or 54% (i.e. for every 100 photons incident, 54 photons are emitted via fluorescence). QY for the CQDs/CNDs was reported at 48%, significantly higher than that reported in the work published on other NP systems. The fluorescence emission was observed to be highly stable but pH dependent and was used to test the ability of the NPs to detect morin, a plant-derived organic molecule used for detection of aluminium and tin ions in solution.

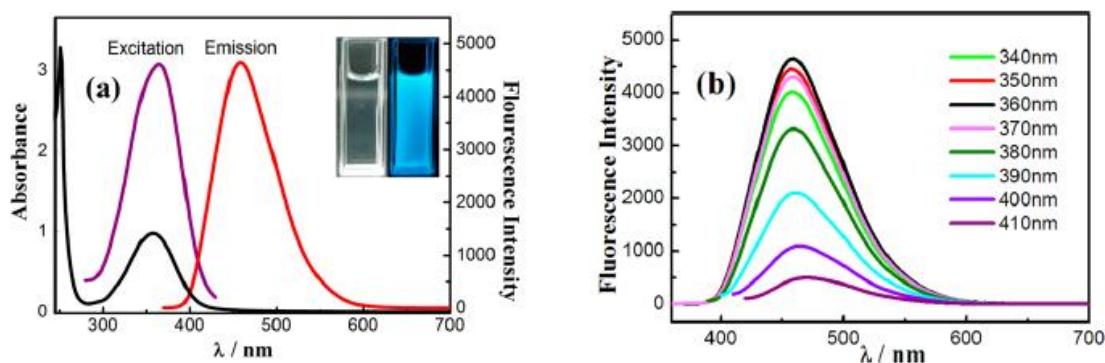


Figure 2.13. Optical spectra obtained from CNPs produced hydrothermally from citric acid. (left) absorption spectrum (black), overlaid with excitation and emission profiles as labelled (blue colour - see image top right of plot), and (right) variation of fluorescence emission intensity with excitation wavelength as indicated. Image reproduced with permission from [45].

Li et al. [62] synthesised water soluble CQDs/CNDs (< 5 nm size) using ultrasonic treatment of glucose in the presence of both acidic and alkaline solutions. The authors used UV-Vis absorption spectroscopy along with fluorescence spectrophotometry and microscopy to optically characterise these NPs, and found that they emitted strong fluorescence across a broad wavelength range from the visible to near-IR (~ 460-620 nm) – Figure 2.14. Despite good photostability, however, the QY value determined for these CQDs/CNDs was relatively low at just 7% (relative to the reference, Rhodamine B in ethanol).

Wang et al. [63] studied the optical properties of CQDs/CNDs (2-3 nm size) synthesised by microwave treatment (domestic 750 W oven, exposure for 10-15 minutes) of different carbohydrates such as glycerol, glucose and sucrose in the presence of a small concentration of inorganic ions (e.g. phosphate).

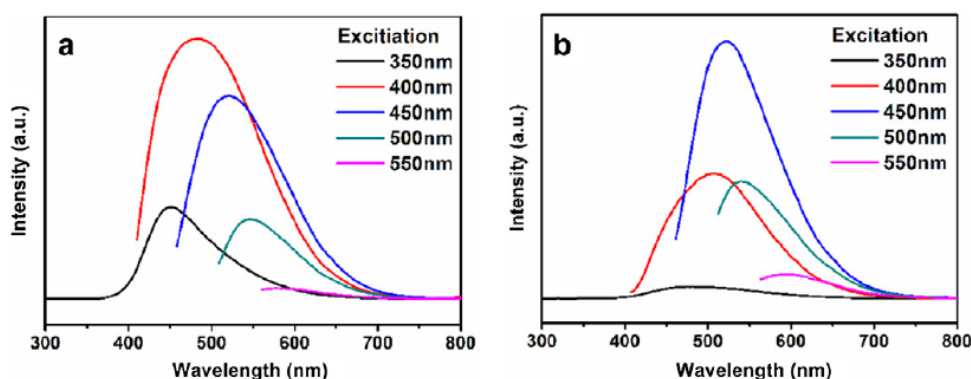


Figure 2.14. Optical spectra of carbon NPs produced by ultrasonication of glucose – absorption in black, and fluorescence in other colours, resulting from excitation wavelengths indicated. (left panel) – CNPs produced in alkaline conditions and (right panel) those produced in acidic conditions. Image reproduced with permission from [62].

It was found that the fluorescence emission was broad (~ 430-525 nm, see Figure 2.15) and varied in intensity with the excitation wavelength. The NPs exhibited good stability (i.e. no loss of emission intensity due to photobleaching effects) and QY values of ~ 3-6%, depending on the inorganic ions used in the reaction and the length of the microwave exposure time.

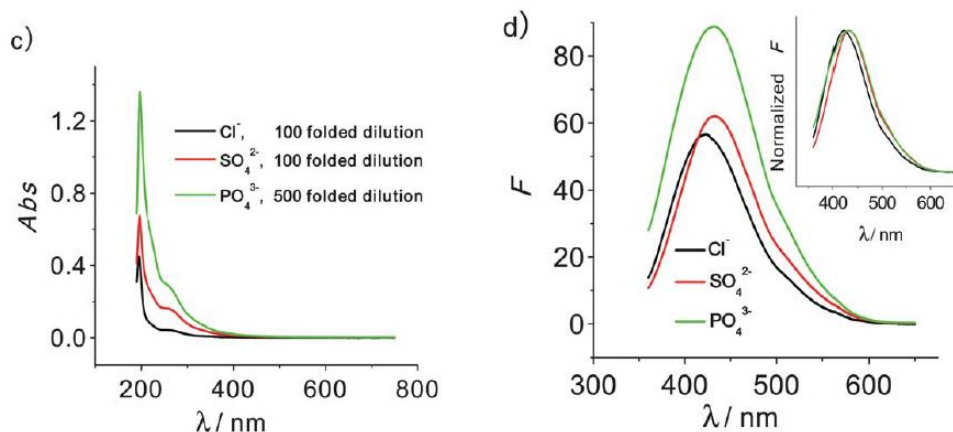


Figure 2.15. (left) absorption spectra and (right) fluorescence emission spectra of CNPs produced from microwave irradiation of a glucose solution with added ions as indicated in the panels. Image reproduced with permission from [63].

A final example of the type of fluorescence data obtained from experimental synthesis and characterisation of CQDs/CNDs is that from [26], who chemically generated a range of CNPs from carbohydrates (including dextrose, ascorbic acid and cellulose) in the presence of dehydrating agents in various solvents over a range of temperatures (80-300 °C). Figure 16 shows images for two of these fluorescent carbon nanoparticle forms, labelled FCN blue and FCN green after the peak position of fluorescence emission from them. FCN yellow and FCN red particles were also synthesised, and their optical properties measured. The table in Fig. 16 lists the measured fluorescent properties of all the CNPs formed, including emission peak wavelength, extinction coefficient (measure of absolute intensity) and the QY values.

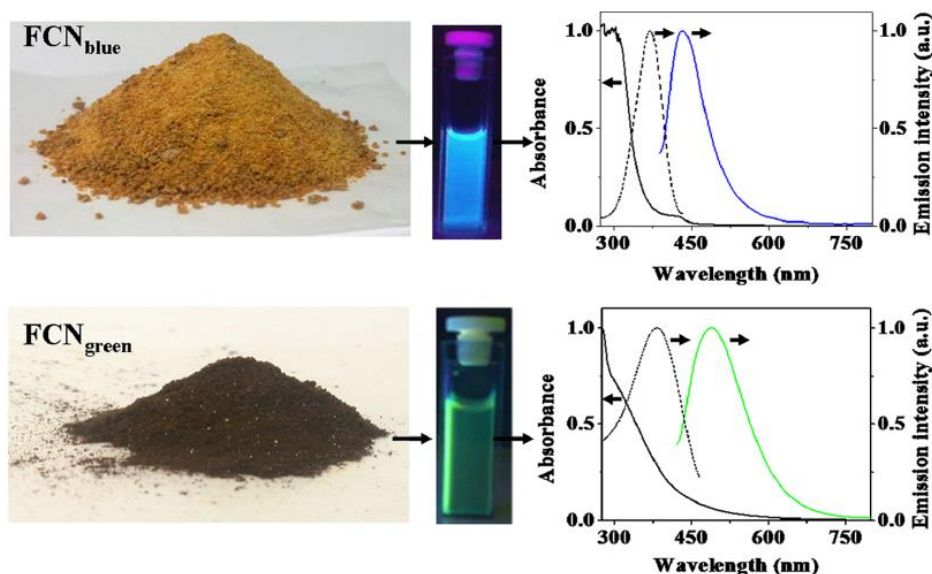


Table 1 | Property of different fluorescent carbon nanoparticles (FCN)

FCN	Molecular weight/ Particle Size	Elemental composition (C:H:N:O)	Emission _{max} (excitation)	Molar extinction coefficient at excitation	Fluorescence quantum yield
FCN _{blue}	400–2200 Da	65:6:8:21	440 nm (370 nm)	2×10^3	6–30%
FCN _{green}	2500–14000 Da, 2–4 nm	75:10:5:10	500 nm (400 nm)	5×10^4	14%
FCN _{yellow}	1–4 nm	50:15:2:33	560 nm (425 nm)	4×10^3	12%
FCN _{red}	~4–10 nm	70:5:1:24	600 nm (385 nm)	7×10^5	7%

Figure 2.16. (Top) Physical form, observable colour of fluorescence emission and optical spectra (absorption - solid black line, excitation - dashed line and emission - coloured line) for CNPs obtained from the chemical treatment of different carbohydrate precursors. (Bottom) Summary of key data for the four types of fluorescent carbon NPs (FCN) synthesised. Images reproduced with permission from [26].

2.5.1. Up conversion

Another useful optical property of CQDs/CNDs that can be used to extend the range of bioimaging applications is up conversion, whereby upon simultaneous multi-photon absorption, the particles are able to fluoresce at shorter wavelengths than that of the incident light [64]. Typically, NIR excitation wavelengths are used for stimulating up conversion in CNPs, with subsequent fluorescence emission occurring at visible wavelengths. This property is especially useful for bioimaging applications where scenarios such as high spatial resolution, low background interference or low photon-induced toxicity is required, since the multi-photon absorption process is a highly localised and non-linear one.

2.6. Mechanism of CNP Uptake in Cells

In order for any form of nanoparticle (< 100 nm), including CNPs, to be practical options for either bioimaging or drug delivery applications, they must, of course, be able to be taken up by the specific cell type/s being targeted. For this to happen, the nanoparticles must first be

stable enough to be transported through the bloodstream, without loss of function and without presenting any adverse effects in surrounding tissues or organs (cytotoxicity). Secondly, once they have arrived at the target area, the NPs have to be able to interact with the cell and cross the cell membrane in order to enter the cells [65].

The membrane is the key barrier surrounding and enclosing the cell interior (organelles and cytoplasm) which protects the interior and facilitates the selective transport of key ions and biomolecules both into and out of the cell. Cell membranes are typically composed of a bilayer of phospholipid molecules containing both hydrophilic and hydrophobic 'head' and 'tail' units respectively, with some degree of cholesterol within which provides and maintains membrane flexibility whilst imparting sufficient rigidity.

Typically, NPs larger than around 30 nm are unable to cross a cell membrane [65]. Consequently, carbon NPs such as QDs/NDs are, in theory, ideal, since they can be routinely synthesised in the 1-10 nm range, as discussed previously. The two main mechanisms thought to be responsible for CQD/CND uptake in cells are *endocytosis* and *diffusion*. Endocytosis is the process by which molecules or NPs outside a cell become enveloped and enclosed by the cell, and is a well-described mechanism by which cells regularly 'self-clean' the body by removing dead cell debris or foreign matter (see Figure 2.17).

Endocytosis is further sub-classified with respect to the type of cell involved in NP uptake; *phagocytosis*, which describes the removal of cell debris from within cells, including macrophages, monocytes and neutrophils, and *pinocytosis*, where soluble species (ions and small molecules such as lipoproteins and transferrin) are taken up in non-phagocytic cells. On the far left of Fig. 17, the uptake of a large NP by phagocytosis is depicted, where the cell completely envelops the particle. To the right of this, another mechanism is depicted where smaller NPs are internalised by the cell via pinocytosis, where specific ligands bind to cell surface receptors [66]. Finally, the inset of Fig. 17 depicts the process of NP diffusion, where specific channel-transporter proteins within the cell membrane bind to the NP surface and facilitate the transport of the particles across the membrane to the cell interior.

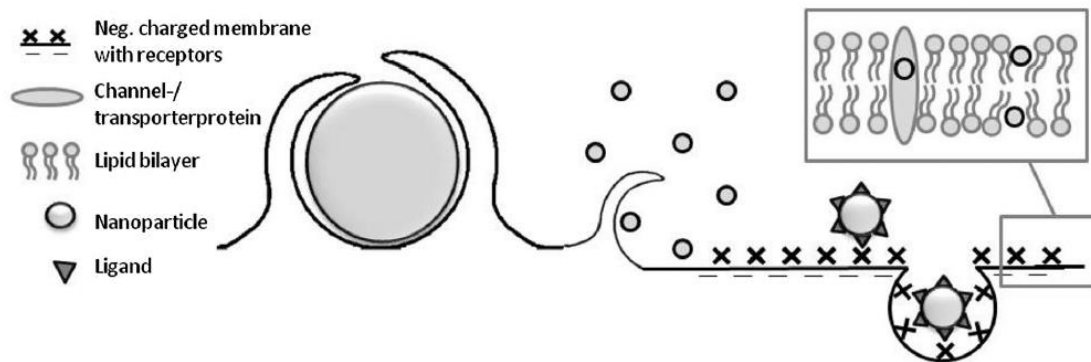


Figure 2.17. Schematic depiction of the uptake process for CNPs in cells and transfer through the cell membrane to the interior - see text for discussion. Image reproduced from [65].

The efficiency of the uptake of NPs by cells is dependent upon a number of key NP properties, both physical and chemical. These include factors such as particle size and shape, surface charge, surface functionalisation (the nature of the functional groups attached at the particle surface) and the extent to which the NP is hydrophilic. As mentioned at the start of this section, spherical NPs below around 30 nm in size are readily taken up by most cells, whilst the uptake efficiency for larger spherical particles or irregularly shaped particles is generally reduced [67].

In terms of surface charge, generally, charged NPs are taken up by most cells more readily than those either with no charge or those that are zwitterionic in nature (i.e. consisting of both positive and negative components). This is thought to be a consequence of the negatively charged nature of the membrane itself, which naturally facilitates binding with positively charged NPs and the formation of a hydration layer, in both phagocytic and non-phagocytic cells. In addition, it has been observed that the uptake of charged particles increases as the initial surface charge increases.

The nature of surface functional groups is also key, with groups such as hydroxyl (OH), carboxylic (COOH) and amine (NH₂) all promoting more efficient cellular uptake of NPs. Both negative and positive surface charges can be enhanced by careful selection and synthesis of functional groups (carboxylic for negative charges and amine for positive charges). The hydroxyl group does not impart a particle surface charge but has been found to promote uptake by absorption in non-phagocytic cells. Numerous other uncharged NP surface ligands (for example proteins and carbohydrates) can also be attached via synthesis for subsequent enhanced cellular uptake.

Finally, further surface functionalisation can be tailored to vary the overall hydrophilic nature of NPs towards cell membrane components via changes to the flexibility/rigidity of the membrane upon particle attachment.

2.7. CNP Applications

Throughout this review, the properties and potential applications of CNPs have been outlined and numerous references to published work given with respect to the three main areas in which they are finding increasing use; (1) biosensing of key ionic species and molecules, (2) bioimaging of specific cell types for detection and monitoring of disease and (3) drug delivery in the therapeutic treatment of diseased cells. This final section will now provide a more detailed look at the second of these areas, since this is the primary focus for extension of the findings from the experimental part of this study, with recent examples discussed for both *in vitro* and *in vivo* studies.

2.7.1. In vitro bio-imaging

Before testing for the bioimaging potential of a particular NP type, it is crucial to establish that it poses no significant risk in terms of cytotoxicity. In the first example of *in vitro* testing of synthesised CQDs/CNDs, Park et al. [68] studied the cytotoxicity and uptake of fluorescent CNPs of 2-4 nm size, formed by the ultrasonic treatment of food waste in ethanol, for a range of animal cell types (see Figure 2.18).

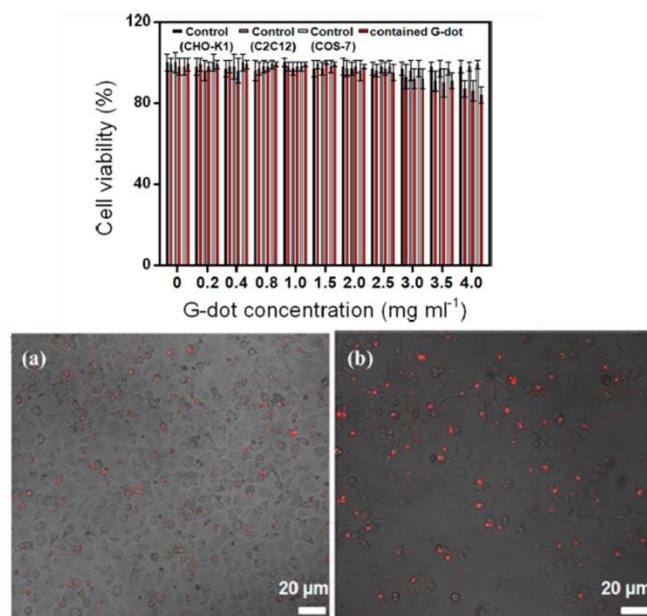


Figure 2.18. (top) cell viability-cytotoxic data from CNP seeding of cells and (bottom) fluorescence microscope images of HepG2 cells containing NPs at concentrations of (a) 0.5 mg/mL and (b) 1 mg/ml. Images reproduced from [68].

For cytotoxicity testing, Chinese Hamster ovary (CHO-K1), mouse muscle (C2C12) and African green monkey kidney (COS-7) cells were seeded with the synthesised CNPs at concentrations of up to 4 mg per ml, and monitored using optical density measurements. Figure 2.18 (top) shows the toxicity results as a plot of cell viability (%) versus CNP concentration (after 24 hours of exposure) for the three cell types, compared with control samples. Up to approx. 2 mg per ml of NPs, no cytotoxic effects were observed on any of the cells, while cell viability began to decrease at higher levels.

Uptake and bioimaging of the NPs in HepG2 (human liver cancer cells) were observed using a confocal fluorescence microscope and Argon ion (Ar^+) and helium-neon (HeNe) lasers for excitation of fluorescence (observed to occur in the 400-470 nm region (decreasing intensity) for excitation at between 330 and 405 nm).

Figure 2.18 (bottom) shows images from cell uptake at two NP concentrations (after 30 minutes) as given in the caption. Strong red fluorescence is evident, resulting from uptake by the cells, while none is present from the surrounding cytoplasm or control cells. Consequently, these CNPs were concluded to show strong potential for future routine bioimaging applications.

Another example study is that of Liu et al. [57], who used CQDs/CNDs (2-7 nm size) synthesised from the microwave treatment of PEI (poly-ethylenimine) in the presence of a glutaraldehyde cross-linker for NP surface functionalisation. Two types of CNPs were synthesised based on their resulting fluorescence properties; blue carbon nanodots (B-CDs) and tuneable carbon nanodots (T-CDs). B-CDs exhibited the highest fluorescence intensity, at 464 nm (excitation at 347 nm) while T-CD emission could be varied to yellow wavelengths (up to 556 nm).

Cytotoxicity assays were performed on HeLa (human cervical cancer) cells seeded with the CNDs at varying concentrations (10-400 $\mu\text{g/ml}$), with cell viability determined by optical density measurements after a 24-hour period (Figure 2.19).

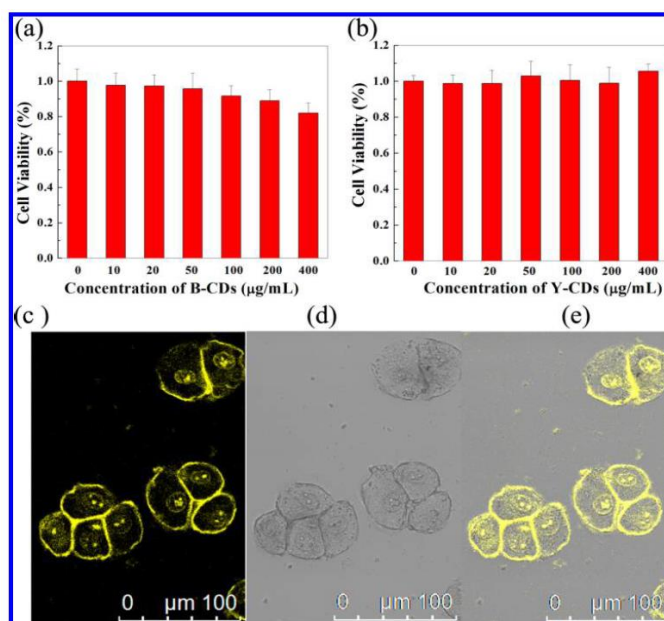


Figure 2.19. (a and b) HeLa cell viability-cytotoxicity data for blue and yellow fluorescence emission carbon nanodots (microwave synthesised) and (c-e) fluorescence microscope images of CND uptake in HeLa cells. Images reproduced from [57].

Both blue and yellow types of CNDs showed low cytotoxicity up to a particle concentration of 200 µg/ml, with higher cell viability (greater biocompatibility) at all NP levels for the T-CDs (Fig. 2.19 a&b).

HeLa cells were then studied for NP uptake-bioimaging potential, again by seeding with different concentrations of the synthesised B- and T-CDs. After 2 hours, cells were imaged using confocal fluorescence microscopy (Fig. 2.19c-e), with the yellow light emitting T-CDs showing efficient passage through the cell membranes and uptake within the cell nucleus and therefore possessing good potential for bioimaging (and biosensing and drug delivery) applications.

2.7.2. In vivo bio-labelling

The process of bio-labelling refers to the specific chemical binding of a fluorescent species (label/tag/probe) to a target biomolecule (protein/amino acid/antibody) or cell in order to detect and monitor that molecule. For many years, this function was performed by well-known organic molecular fluorophores such as fluorescein, but upon the discovery of the optical properties of CNDs, and advances in their synthesis and functionalisation, these NPs are increasingly of interest as *in vivo* bio-labels.

Zhang et al. [69] described *in vivo* studies with synthesised CNDs in zebrafish embryos. CNDs of 3-6 nm size were generated using both thermally- and microwave-assisted

carbonisation starting with citric acid, human hair and pig skin as sources of carbon. Zebrafish were chosen as a model organism for evaluating associated factors (e.g. absorption, distribution, metabolism and excretion) determining the CND bioprobe potential. They represent a good model for a number of reasons, including their low cost, ease of handling and relatively simple life cycle, but also due to their short period of embryonic development and the fact that the embryos are transparent and therefore amenable to optical *in vivo* imaging. At early development stages, the fish cells are especially susceptible to uptake of species and so offer a good subject for testing of toxicity, and the transport and biocompatibility of CNDs. The primary reason for their selection, however, was that the zebrafish genes share many similarities with those of humans, therefore allowing for experimental *in vivo* findings to be extrapolated to some reasonable extent to human physiology.

Zebrafish embryos (at different periods of time in hours post fertilisation, or hpf) and larvae were injected with varying concentrations of synthesised CNDs that showed strong fluorescence throughout the visible range and at high QY. They were then imaged using a confocal fluorescence microscope (see Figure 2.20). The figure shows optical images of CND-treated embryos (A: 6-48 hpf) and larvae (3-15 days post fertilisation), while the images in B-D labelled rows show in turn blue, green and red fluorescence emission from CNDs at each corresponding developmental stage of the two zebrafish forms.

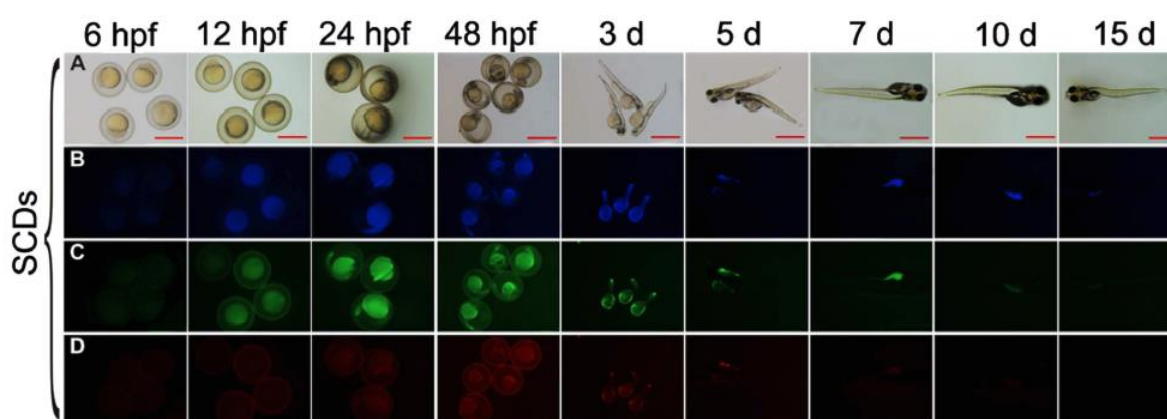


Figure 2.20. (top - A) optical images of zebrafish embryos and larvae post fertilisation and addition of CNDs (formed from skin; at 0.4 mg/mL) and (B-D) fluorescence microscope images with varying emission wavelengths from same samples. Image reproduced from [69].

It was concluded that the fluorescence intensity was both time and CND dose-dependent and that intensity decay with time was slow enough (therefore the CNDs photostable enough) to

make the hair and skin-derived NPs a viable bioprobe for *in vivo* studies in other organism systems.

Huang et al. [70] used mice for *in vivo* studies of the potential of synthesised NIR fluorescent CNDs as bio-labels and found that they showed the desired NP properties (photostability/low cytotoxicity), were efficiently distributed but also that the cellular excretion and tumour uptake of the NPs depended upon the nature of/position at which they are injected, with the highest clearance rate resulting from intravenous injection (compared with intramuscular and subcutaneous injection).

Zheng et al. [64] also used mice for *in vivo* studies with synthesised CNDs (made using carbohydrate and amino acid precursors) for targeting brain cancer tumours. The CNDs exhibited strong, tuneable, fluorescence emission after injection into mouse subjects, with good biodistribution and biocompatibility. Fluorescence intensity was observed to be significantly stronger from the tumour sites (compared with non-tumour locations) for CNDs made using aspartic acid, indicating the ability of these NPs to penetrate effectively into the targeted area. NPs formed from other amino acid and sugar precursors were not able to discriminate between normal and cancerous tissue, showing much weaker intensity. The images shown in Figure 2.21 track the transport of the NPs through the mouse over the course of 90 mins with the targeted tumour site showing highest emission intensity.

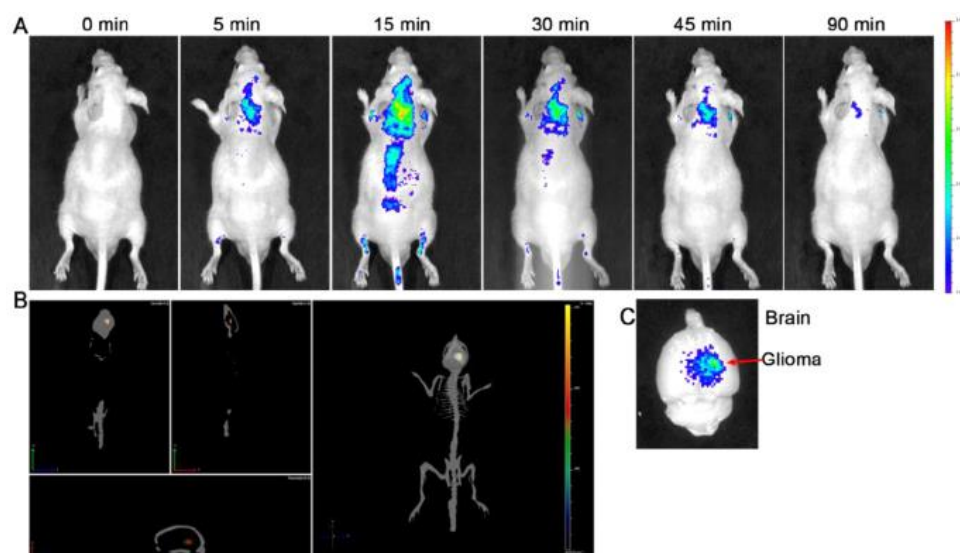


Figure 2.21. Fluorescence imaging of *in vivo* (mouse) uptake and time-dependent distribution of CNDs formed from aspartic acid, showing the enhanced ability of the particles to attach and penetrate to brain tumour (glioma) cells compared with normal tissue. Image reproduced from [64].

2.8. Summary

This review chapter has discussed a number of key topics concerning carbon nanoparticles, with a focus on carbon nano (or quantum) dots, small (< 10 nm size) particles. These can be synthesised relatively cheaply and quickly by green (environmentally-friendly) methods, starting from simple, easily sourced carbon-based materials, such as food waste, hair and egg shell membrane (amongst many other examples that have been outlined).

Many of the synthesis methods, both top down and bottom up in nature, have been devised for both small- and large-scale production of carbon nanodots (CNDs). This review has outlined many of these, with a particular focus on the microwave-assisted approach that was adopted in the experimental part of the work described in this thesis. By careful choice of reaction conditions, and inclusion of other reagents for the attachment of functional groups at the particle surfaces, it is possible selectively to tailor a particle's dimensions and properties as required for a target application.

Accurate characterisation of synthesised CNDs is vital, and, to this end, a number of techniques are typically used, including electron (and atomic force) microscopy for imaging of particles and determination of their size and shape, some form of elemental characterisation technique (e.g. x-ray photoelectron spectroscopy), and a number of spectroscopic methods (UV-Vis/FTIR/fluorescence) to determine the optical properties.

CNDs invariably display strong light absorption and fluorescence emission properties, making them excellent candidates for a number of practical applications, including ion/molecule biosensing, cell uptake and bioimaging and drug delivery vehicles. Fluorescence emission can often be tuned over a range of wavelengths through the visible to NIR wavelengths, with CNDs exhibiting good photostability and high fluorescence quantum yield.

For applications involving cell imaging or drug delivery, it is essential that the CNDs are not cytotoxic in nature towards cells other than those targeted, and that they can readily interact with the target cells, cross the cell membrane and be taken up in the cell interior for imaging purposes or for release of a drug molecule.

A number of recently published studies (from 2013 onwards) have been highlighted in the review in order to (i) reflect on each of the key aspects of CND synthesis, characterisation and optical properties and (ii) indicate the surge in the research done in recent years on these nanoparticle forms as techniques improve and the range of potential applications increase.

Chapter Three: Materials and Methods

3. Chapter Three: Materials and Methods

3.1. Introduction

This chapter describes the materials and methods used to synthesise and characterise the carbon nanoparticles. The chapter first explains the process through which the carbon nanoparticles were synthesised and stored, before outlining the various characterisation techniques used to determine the physical and chemical properties of the particles. Finally, it sets out the biological characterisation that was undertaken to assess cellular viability.

3.2. Experimental

3.2.1. Discover SP – microwave synthesiser.

Microwave technology is being widely used for chemical synthesis, both in academic research and industry. The microwave instrument used in this project was the Discover SP (CEM) which is a single mode microwave system (Fig. 3.1). The main advantages of using this microwave synthesiser to produce carbon nanoparticles are that the reaction power, pressure and time can be accurately controlled. The maximum power is 300W, with a magnetron frequency of 2.45 GHz. Also, the system is able to operate both in pressurised reaction vials and at atmospheric pressure. An optical IR thermometry sensor is situated under the reaction vessel to detect and control the temperature. This system can work at temperatures up to 300°C. Synergy™ software controls and monitors the reaction temperature, time, power and pressure during the synthesis process.

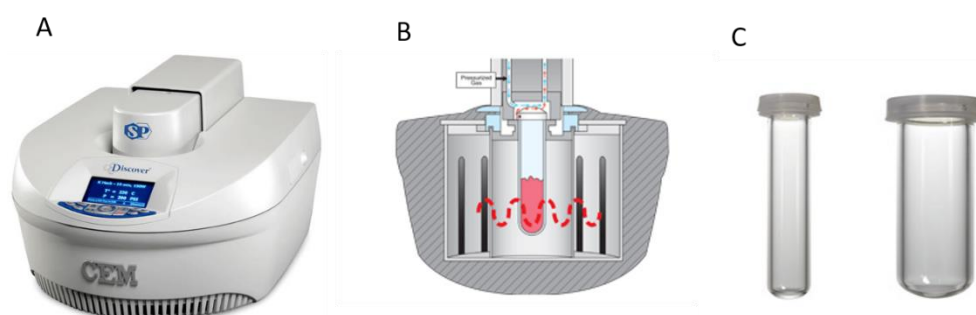


Figure 3.1. (A) Discover SP microwave synthesiser (CEM). The reactor has one cavity with a pressure device. A monitor in front of the cavity shows the temperature and time and connects the instrument to a computer. (B) Schematic diagram illustrating the microwave heating process. During the heating process, the surrounding microwave reactor provides a uniform EM field which ensures the sample is heated evenly. A vent in the pressure device removes excess gas pressure; while keeping the reaction under sealed conditions. (C) Side view of the specific glass vessels with lip seals used in the synthesiser. Images reproduced from CEM Corporation website (2006) [71].

3.3. Materials

Alginate sodium salt [W201502-1kg] was purchased from Sigma-Aldrich, glycerol [G5516-1L] was purchased from Sigma Aldrich and the D-(+) glucose (Mw =180.16 g/mol) was purchased from Sigma-Aldrich. All materials were used as received from either Sigma-Aldrich or Fisher Scientific. All the aqueous solutions were prepared using distilled water. The main chemicals used in the study are listed below with the full details of grade, molecular weight and supplier.

Table 3.1. Chemical reagent and suppliers used in this project

Reagent	Supplier	
Sodium alginate	Sigma Aldrich	W201502-1kg
D-(+)-Glucose	Sigma Aldrich	50-99-8-1kg
Glycerol	Sigma Aldrich	G5516-1L
Quinn sulphate	Sigma Aldrich	207671-44-1
Ethanol	Fisher Scientific	64-17-5
Sulphuric acid	Sigma Aldrich	07208-2.5L

3.4. Synthesis of Carbon Nanoparticles (CNPs)

Glucose and Na-alginate were used as carbon sources to produce carbon nanoparticles (see Fig. 3.2 for molecular structures). They are a highly favourable for use as biomaterials due to their highly stable, non-toxic, safe, hydrophilic and biodegradable nature. For example, Glucose being one of the cheapest and most abundant carbohydrates has been extensively studied. [72-74]. Also, sodium alginate was previously chosen as a molecular precursor for synthesis because it was a food additive approved by the Food and Drug Administration (FDA) and is certified safe for human consumption[75]. The alginate has also been used in biomedical applications, including drug delivery, which has shown good biocompatibility. This would minimize possible toxicity issues for CNPs products and could be adopted for biomedical applications in the future with a higher level of confidence. A limited amount of

studies have been reported where sodium Alginate was used as carbon source [76, 77]. To the best of our knowledge until date, there is no report yet on the production of CNPs from alginate nanoparticles that were pre-formed via Discover SP – microwave synthesiser

5 g of each material was added to 10 ml of glycerol and 40 ml of distilled water to form clear aqueous solutions. These solutions were then transferred to 35 ml vials, placed in the microwave synthesiser and irradiated under set temperature/pressure conditions. Within the first two minutes of heating, the colour of the solutions was seen to change to brown/dark brown due to formation of carbon nanoparticles (CNPs). The obtained mixture was ultra-centrifuged in order to separate the larger sized carbon particles from the CNPs. The larger sized carbon particles settled at the bottom of centrifuge tube and the CNPs contained within the supernatant solution were removed carefully for dialysis. The dialysis process was performed using a cellulose acetate membrane. After dialysis, the CNPs were freeze dried and finally stored in glass vials at a low temperature prior to physical/chemical characterisation and the final bio-application study.

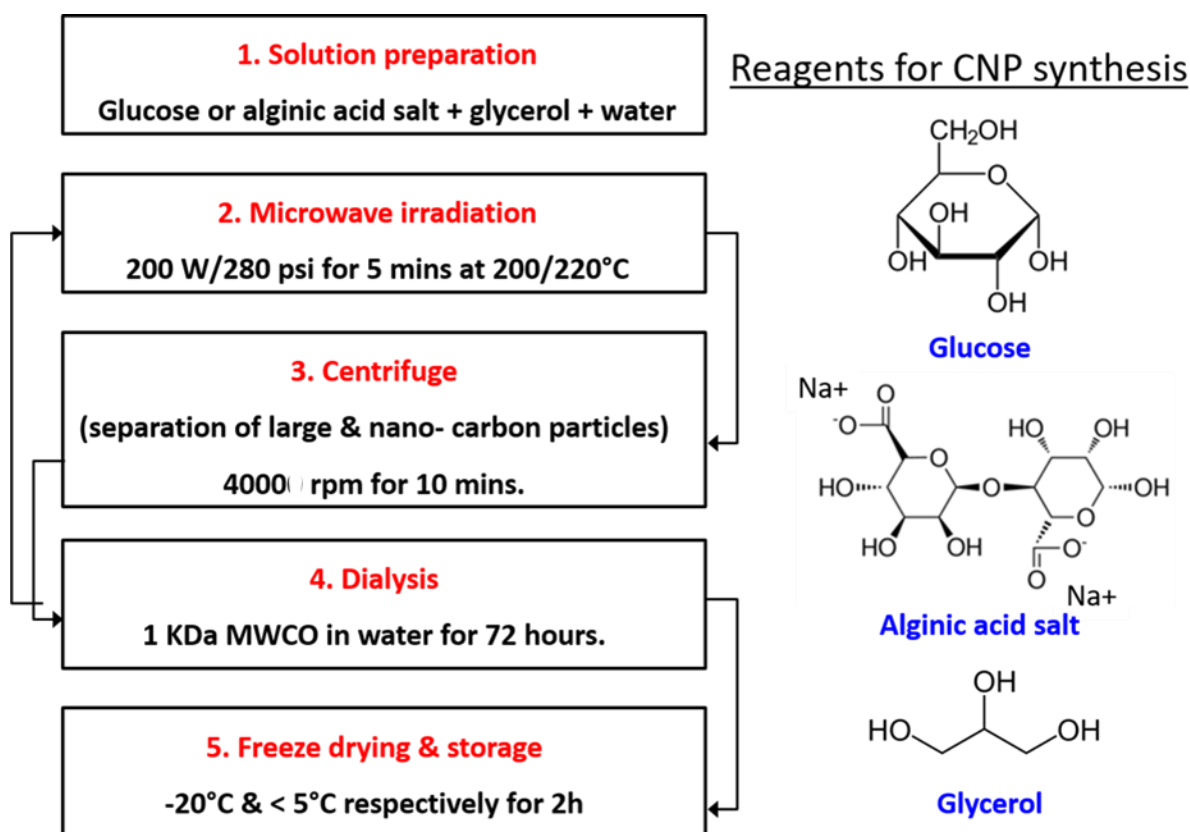


Figure 3.2. Flow diagram showing the method sequence used for the microwave-assisted synthesis of carbon nanoparticles (CNPs).

3.4.1. Purification of carbon nanoparticles

After the carbon nanoparticles were synthesised, the suspension needed to be purified in order to remove impurities and any reagent left over from the synthesis. Two steps were used for these purifications. Firstly, centrifugation was important to remove the aggregation and large particles from the suspensions. All the samples were centrifuged at 4000 rpm for 10 min at which point a pellet was removed and the supernatant observed and re-suspended with distilled water. The supernatant was then centrifuged again, and this step was repeated three times. Secondly, 10 m rolls of dialysis membranes with a molecular weight cut-off of 1 kDa MWCO and flat-width of 45 mm were obtained from Spectrum Labs. Before use the membrane was rinsed with deionised water. Dialysed carbon nanoparticles were obtained by adding 15 ml of CNPs suspension into a dialysis membrane. The samples were moved to a beaker with 2 litres of deionised water under mild stirring, allowing solvent/water exchange to take place. In the first two hours the water colour changed from clear to yellow due to the colour of the CNPs. This indicated that the water needed to be replaced every two hours. Nanoparticle dialysis was allowed to take place overnight, resulting in a total exchange time of ≈ 24 h. [78, 79].

3.4.2. Freeze drying of carbon nanoparticles

Storing CNPs as suspensions presents a risk of microbial contamination [80]. Also, the high aggregation rate of CNPs may result in a change in their properties during storage. The CNP suspensions were therefore transferred to dry powder by freeze drying. This is very widely used for drying nanoparticles and is used to ensure the long-term stability of CNPs so that they retain their original properties [80]. The main principle of this process to remove the water from the samples during the freezing process by sublimation and desorption under vacuum. In this study a Christ EPSILON 1-4 LSC freeze dryer (see **Figure 3.3**) was used. In general, the freeze-drying process can be divided to three steps: firstly, pre-freezing the samples at (-20°C) (solidifications), then primary drying which provokes sublimation of the ice and secondary drying which removes the remaining unfrozen water through desorption. After drying the powder, the CNPs were obtained and stored in an airtight container at <5°C until further use [80].



Figure 3.3. Picture of the Christ EPSILON 1-4 LSC freeze dryer machine used in this study

3.5. Particle Characterisation

3.5.1. Introduction

The main analysis or characterisation of a substance can be defined as the identification and study of its structural and elemental properties of the substance that are important with respect to use within particular preparations or the reproduction of particular substances [81].

Characterising nanomaterials is vital for understanding their properties. It is essential to consider that the properties like size distribution, average particle diameter and charge have an effect on the physical stability of nanoparticles distribution [82]. The physiochemical characteristics of biomaterials contribute significantly to cellular interaction and play a key role in the *in vivo* functioning of a material [81]. Of special importance is the surface of the biomaterial. This may be only a few atomic layers wide but forms the interface connecting the biomaterial and its surroundings, thereby participating in both the *in vitro* and *in vivo* biological and chemical reactions. The physical characteristics of the biomaterial are dependent upon the inherent internal molecular configuration or micro-architectural geometry, including factors such as the density and surface area, as well as the morphology or size of molecules and pores, general porosity, percentage porosity and pore orientation. Using advanced microscopy techniques such as atomic force microscopy (AFM), scanning electron microscopy (SEM) and transmission electron microscopy (TEM) help to determine the size, morphology and surface charge of the particles.

This project used different characterisation techniques to evaluate the material properties of particle produced. The physical properties were analysed using characterisation methods including transmission electron microscopy (TEM), dynamic light scattering (DLS) and fluorescence spectroscopy. The chemical properties, meanwhile, were evaluated using Fourier transform infrared (FTIR) spectroscopy, ultraviolet-visible (UV-Vis) spectroscopy, Raman spectroscopy and X-ray photoelectron spectroscopy (XPS).

The biological analysis and biocompatibility of the CNPs was studied using resazurin (blue dye) assays along with other methods described in section 4.6.

3.5.2. Analytical methods

3.5.2.1. Transmission electron microscope (TEM)

TEM has shown itself to be an extremely useful analytical technique in material sciences. Passing a high energy electron beam through a very thin sample produces interactions between the electrons and the sample atoms that can be employed to identify characteristics including crystal structure, atomic dislocations and grain boundaries within the sample material. Chemical analysis can also be conducted using TEM and the technique is useful for examining the growth of layers, layer structure and defects in semiconductors. High resolution TEM scanning can also be implemented to examine the quality, shape, size and density of quantum wells, wires and dots [83].

TEM operates along the same fundamental principles as light microscopy, except employing electrons in place of visible light (see Fig. 3.4 for microscope configuration). As the wavelength of electrons is much shorter than that of visible light, the optimal resolution achievable for TEM images is many orders of magnitude greater than that achieved with light microscopy. TEM is therefore invaluable for elucidating the finest aspects of internal morphology, even down to the atomic level [83].

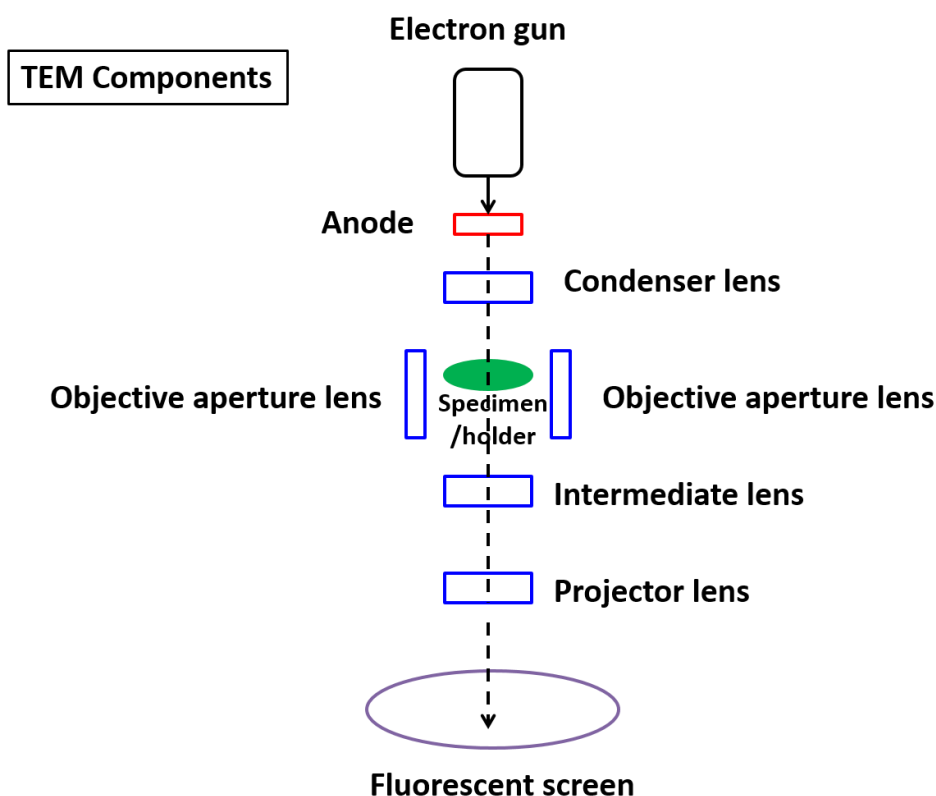


Figure 3.4. Schematic highlighting the basic structure and optical components of a transmission electron microscope.

In the study described in this dissertation, EEE JEOL 2010F TEM was used to obtain very high-resolution images. All the images were acquired using Digital Micrograph 1.8 software (Gatan, CA, USA). 10 μl solutions of CNPs were pipetted onto a 300-mesh copper grid. The sample was allowed to air-dry for one hour and any remaining liquid was dried manually using filter paper. Finally, the carbon film was attached to the grids for sample TEM imaging. The grids were examined using EEE JEOL 2010F EM at voltage 200 keV.

3.5.2.2. Dynamic light scattering (DLS)

Dynamic light scattering (or photon correlation spectroscopy) is a common technique for the evaluation of particle size. A monochromatic light source, such as a laser, is directed onto a suspension containing spherical particles in Brownian motion (see Fig. 3.5). A Doppler shift results when the light makes contact with a moving particle, altering the wavelength of the incident light. The extent of the wavelength change can be correlated with the size of the particle. This enables computer analysis of sphere size distribution, particle motion in the

suspension, and determination of the diffusion coefficient of the particle by means of the autocorrelation function [84].

This technique offers several benefits: firstly, it is a rapid technique and almost entirely automatised so, for routine investigations, significant expertise is not essential; secondly, it is not an expensive technique. Industrial particle sizing equipment tends to function at only a single angle (90°) and employs only red light (675 nm). Generally, there is little dependence on concentration. While it is possible to use more sophisticated experimental equipment (e.g. projector, short-wavelength light source, etc.) and these can dramatically improve the accuracy and flexibility of the method, they also involve more complexity and incur greater costs.

Whilst this technique is theoretically capable of differentiating whether a protein is a monomer or dimer, it is however of much lower accuracy for differentiating small oligomers than classical light scattering or sedimentation velocity. The strength of dynamic scattering is the ability to evaluate samples consisting of a broad range of chemical moieties of greatly varying molecular masses (such as a native protein and various sizes of aggregates), and also to identify minute quantities of the higher mass species ($< 0.01\%$ typically). Furthermore, this methodology offers the capability of obtaining absolute measurements of a variety of parameters, (e.g. molecular weight, radius of gyration, translational diffusion constant, etc.). [84, 85]

In this study, a ZetaPALS analyser instrument (Brookhaven Instruments Corporation - **Figure 3.5**) was used to study the size of the CNPs. This instrument was operated at 4 mW laser power with incident wavelength of 632.8 nm. The CNPs were diluted in water and filtered with a Millipore filter of 0.2-micron pore size. The backscattered light was collected at a 90° angle.

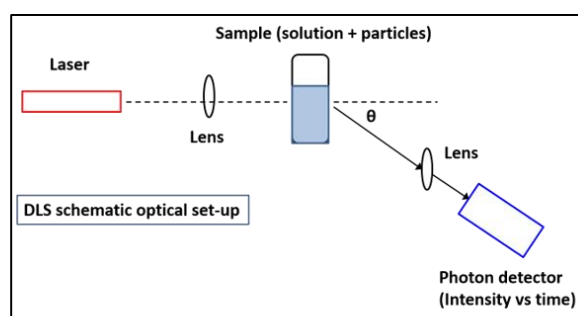


Figure 3.5. Picture and schematic view of Brookhaven Instruments Corporation ZetaPALS particle analyser.

3.5.2.3. Ultraviolet-visible absorption spectroscopy

Ultraviolet-visible (UV-Vis) spectroscopy is a form of absorption spectroscopy that used to analyse the chemical structure of substance by using a visible light and ultraviolet. It is a type of spectroscopy used to measures the molecular absorption of light in the wavelength range of approximately 200-800 nm (see Fig. 3.6). UV spectroscopy makes use of the Beer-Lambert law (which expresses a linear correlation between absorbance and concentration of an absorbing species). More specifically; the drop in intensity of radiation from a beam of monochromatic light passing through an absorbing solution, is directly proportional to the concentration of that absorbing solution and also the strength of the incident radiation. The energy of the radiation absorbed is therefore equal to the energy difference between the electron ground state and higher energy states $\Delta E = h\Delta\nu = hc/\Delta\lambda$ where, h is Planck's constant, c is the velocity of light and ΔE is the energy absorbed in an electronic transition in a molecule from a low-energy state (ground state) to a high energy (excited) state [86].

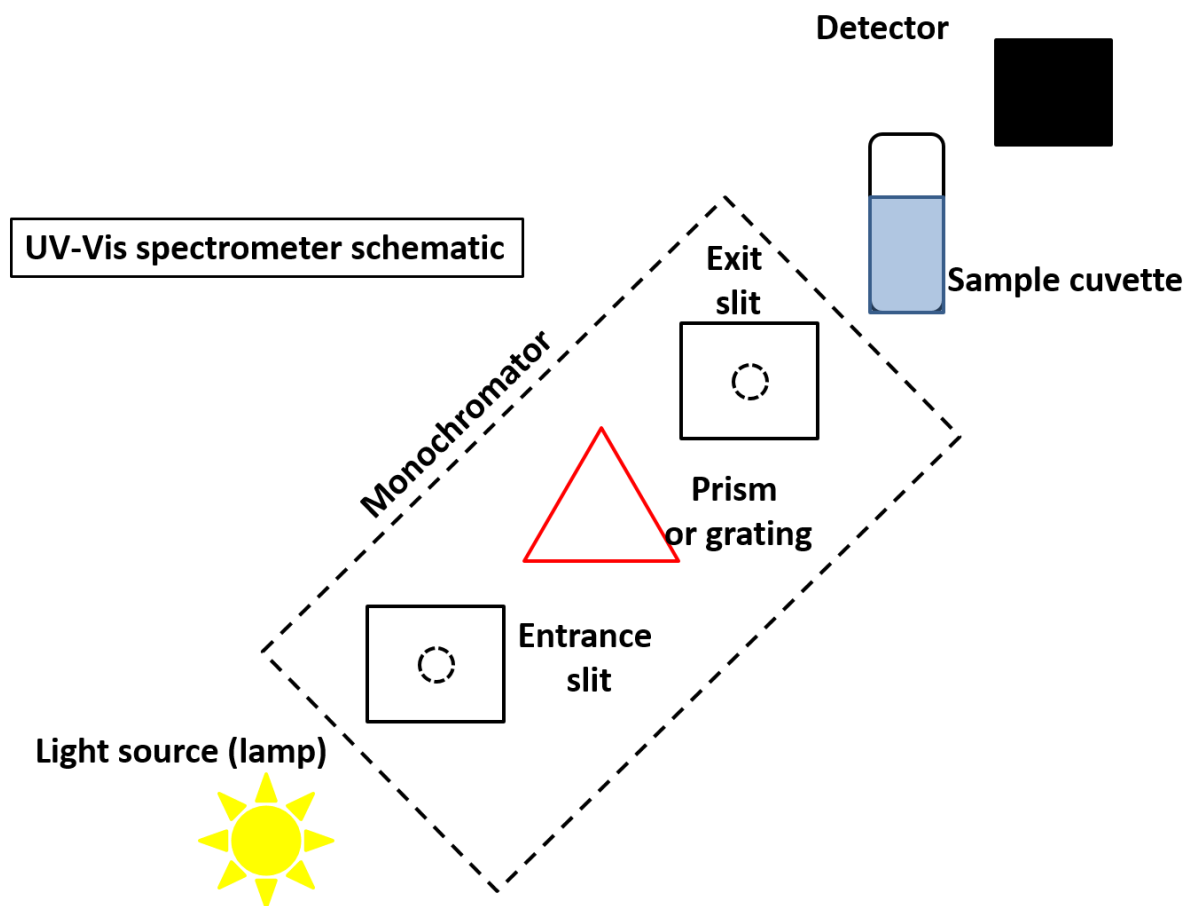


Figure 3.6. Schematic of the components and light path for a typical single beam-diode array detector UV-Vis spectrometer for light absorption measurements

In this study the UV-VIS analysis of CNPs is described, whereby small quantities of diluted sample (1:10) were transferred to quartz UV cuvettes with a 1 cm path length. Distilled water was used as a reference and all spectra were recorded from 200 to 800 nm and analysed by a CARY 50 probe UV-Vis spectrometer.

3.5.2.4. Raman spectroscopy

Raman spectroscopy is similar to infrared (IR) spectroscopy, since both are based on vibrational spectroscopy (see Fig. 3.7). The difference between the two techniques is that Raman bands result from variations in the polarisation of the target molecule caused by the incident light, whereas for IR, bands result from a variation in the dipole moment of the molecule in the presence of incident light. Raman spectroscopy is considered to be a conventional and useful technique for chemical analysis and characterisation, appropriate for a variety of chemical moieties. Samples may be analysed in various phases: solids (particles, pellets, powders, films, fibres), liquids (gels, pastes) and gases[87, 88].

Raman spectrometer schematic

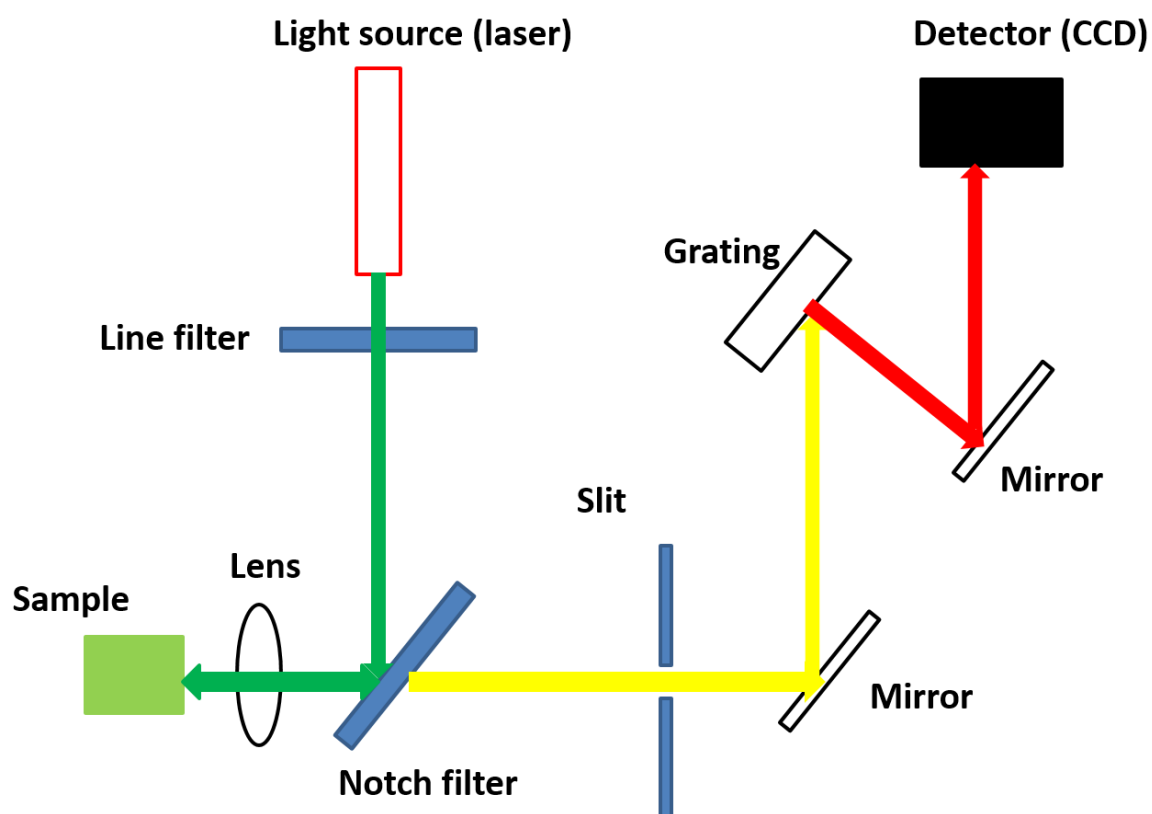


Figure 3.7. Schematic of the components and photon processes involved in a Raman spectrometer/Raman spectroscopy.

In the current study a Raman DXRi instrument (Thermo Scientific, USA) was used (Fig. 3.8). The sample was first dried on glass, subsequent to which two accrual readings were obtained at 532 nm at an exposure time of 1 second for each measurement. The scanning laser was set at 10% intensity and 1 W power. The microscope was equipped with a 10× objective lens. The acquired spectral data was processed and analysed by OMNIC XRi™, OMNIC Atlas™ and TQ Analyst™ software suit (Thermo Scientific, USA).



Figure 3.8. The Raman spectrometer used for analysis of CNPs.

3.5.2.5. X-ray photoelectron spectroscopy (XPS)

X-ray photoelectron spectroscopy (XPS) is also called electron spectroscopy for chemical analysis (ESCA). This is the most common technique for surface analysis since it can be used for a wide variety of substances whilst offering invaluable empirical and qualitative details on the surface of the substance under examination. Spatial distribution details are produced by scanning the micro-focused x-ray beam over the surface of the sample. Depth distribution details are produced by amalgamating XPS measurements with ion milling (sputtering) to identify thin film morphologies. [89]

The analytical procedure involved placing the sample in an ultrahigh vacuum environment where it is exposed to low-energy, monochromatic X-rays. X-ray bombardment effects the expulsion of core-level electrons from atoms within the sample. The energy of these expelled electrons is a function of their binding energy, being characteristic of the source element from whence they were derived.

In this study, the sample was prepared for analysis by depositing it onto indium foil. The analyses were carried out using a Kratos Ultra instrument with a monochromatic aluminium source, with one analysis point per sample. A survey scan was collected between 1200 to 0 eV binding energy, at a 160 eV pass energy with 1 eV intervals. High-resolution O 1s and C 1s spectra were then collected over an appropriate energy range at a 20 eV pass energy with 0.1 eV intervals. Charge neutralisation was used. The analysis area was 700 μm by 300 μm .

The data collected was calibrated in intensity using a transmission function characteristic of the instrument (determined using software from NPL) so as to make the values instrument independent. The data could then be quantified using theoretical Scofield relative sensitivity factors. The XPS data was calibrated to force the C 1s peak to be at 285.0 eV.

3.5.2.6. **X-Ray Diffraction (XRD)**

The composition of atoms in any structure can clearly be seen after the application of X-Ray diffraction, hence the latter is perfect to use for the analysis of atomic-level matter. If the space between the sheets of mineral material is equal, X-Rays are equally dispersed at an angle. An arrangement of diffraction will be prevalent as a result of the X-Rays reacting with the crystalline material. In substances without a clearly defined shape or form, the space between atoms is not equal and they may appear to be disarrayed. This will be transferred into the diffraction pattern of the X-Rays, based on the dispersal of the interatomic spacing. In such materials without shape or form, a histogram displaying the interatomic spacing will be produced, as opposed to a lattice-style edifice from materials composed of crystals. Such information is covered by the so-called 'Bragg's law', which focuses on the link between the angle of incidence, the spacing between atoms, and the incident light wavelength. This ultimately shows the relation of the atom spacing and the subsequent derived pattern [90]. In this study X-ray diffraction (XRD) patterns were obtained with a Bruker 2d at an accelerating potential of 30 kV and tube current of 10 mA and 2Theta 20-69.

3.5.2.7. **FTIR spectroscopy**

Fourier transform infrared (FTIR) spectroscopy is the most popular IR technique. It involves subjecting the sample to IR radiation, some of which will be absorbed by the sample, whilst the rest will pass through and be transmitted. The spectrum produced by the transmitted radiation depicts the molecular absorption and transmission uniquely associated with the sample. In the same way as a fingerprint, no two different molecular structures can give rise to identical infrared spectra. This observation means that IR is invaluable for different forms

of analysis [86]. In this study, FTIR spectroscopy was carried out using a Thermo Scientific instrument (Fig. 3.9).



Figure 3.9. FTIR spectrometer used for analysis of CNPs

3.5.2.8. **Fluorescence spectroscopy**

Fluorescence occurs when a compound is excited (irradiated) by light of one wavelength and as a consequence emits light of another, typically longer, wavelength (see Fig. 3.10). A fluorometer is the term used for a spectrometer designed to record such a process, and closely resembles a spectrophotometer, comprising a light source and a filter, or monochromator, to select a defined range of excitation wavelengths, that are then directed towards the sample. The light produced by the sample is subsequently passed through another monochromator, which determines the emission wavelength of interest, in addition to removing most of the excitation light, before measurement at the detector. [91]

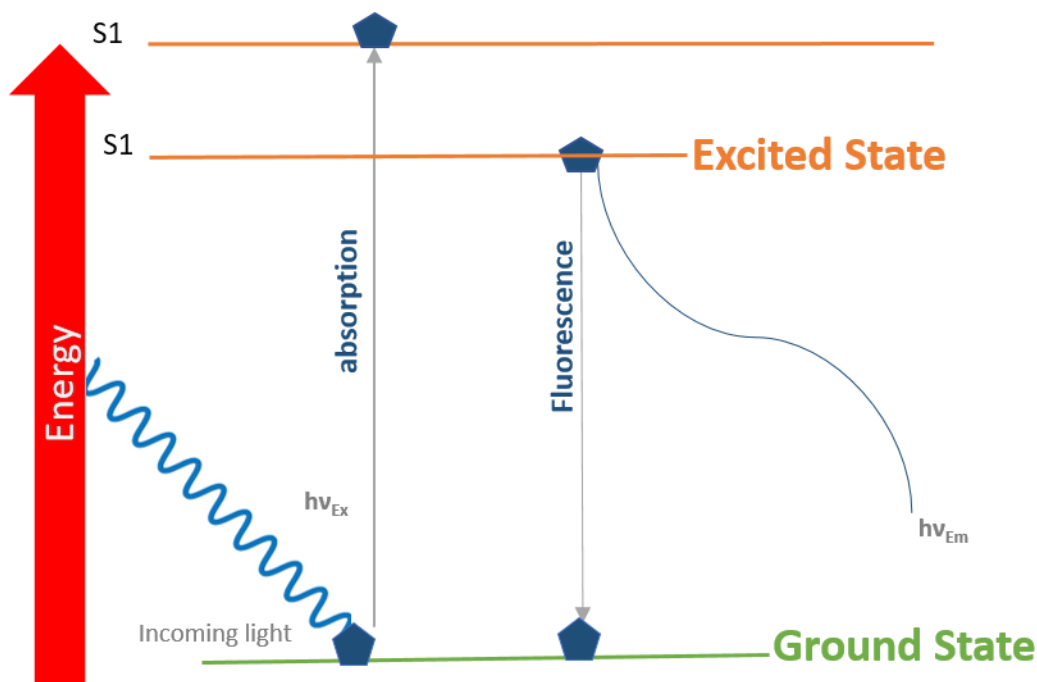


Figure 3.10. Energy level (Jablonski) diagram showing the origin of fluorescence (light emission of energy = $h\nu_{Em}$) in a material (bulk or nanoparticle) irradiated (excited) by light photons of energy = $h\nu_{Ex}$.

To measure the fluorescence spectra of CNPs, samples (in solution) were placed in a 1 cm path length quartz cuvette. These CNP solutions were analysed using a Fluoromax-4 fluorescence spectrometer (Horiba) - see Fig. 3.11. All the samples were excited over a different range of wavelengths from 275 nm to 600 nm.

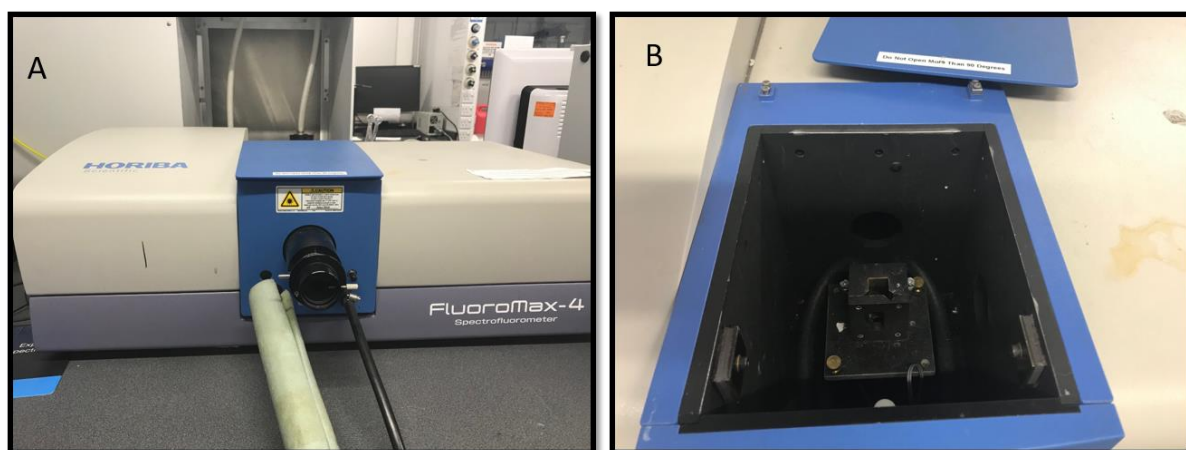


Figure 3.11. (A) The FluoroMax spectrofluorometer (HORIBA Scientific) used to study CNPs and (B) the instrument sample holder.

3.5.2.9. Confocal fluorescence microscope

Laser scanning confocal microscopy has therefore become an invaluable tool for researchers examining cell structure and function, mainly due to its ability to offer sample visualisation deep within living and fixed cells, tissues and other samples. This technique offers the ability to collect precisely defined optical sections and use these to derive 3-D renderings. The basic structure of a confocal microscope is shown below in Fig. 3.12. Confocal microscopy provides several distinct benefits when compared with conventional light and electron microscopy. Firstly, the optical sectioning required by confocal microscopy eliminates the requirement for the physical sectioning needed with conventional light and electron microscopic techniques. As optical sectioning is relatively non-invasive, living tissue samples, rather than just fixed samples, can be examined with greater accuracy. Since optical sections have a relatively shallow depth (0.5–1.5 μm) this permits data to be collected from a clearly-defined plane, rather than from across the entire thickness of the sample. This means that, rather than gathering out-of-focus light whilst the focal plane is above or below the sample, the image is black. This circumvention of out-of-focus light leads to an improvement in contrast, clarity and detection sensitivity. An additional benefit of confocal microscopy is the ability to take optical sections across different planes, i.e. the xy plane (at right angles to the optical axis of the microscope) and the xz and yz planes (parallel to the optical axis of the microscope). Additionally, confocal microscopy provides optical sections in a digital format. This dramatically enhances image processing and facilitates the production of digital prints of the image, whilst removing the time-consuming requirement for darkrooms and chemicals [92].

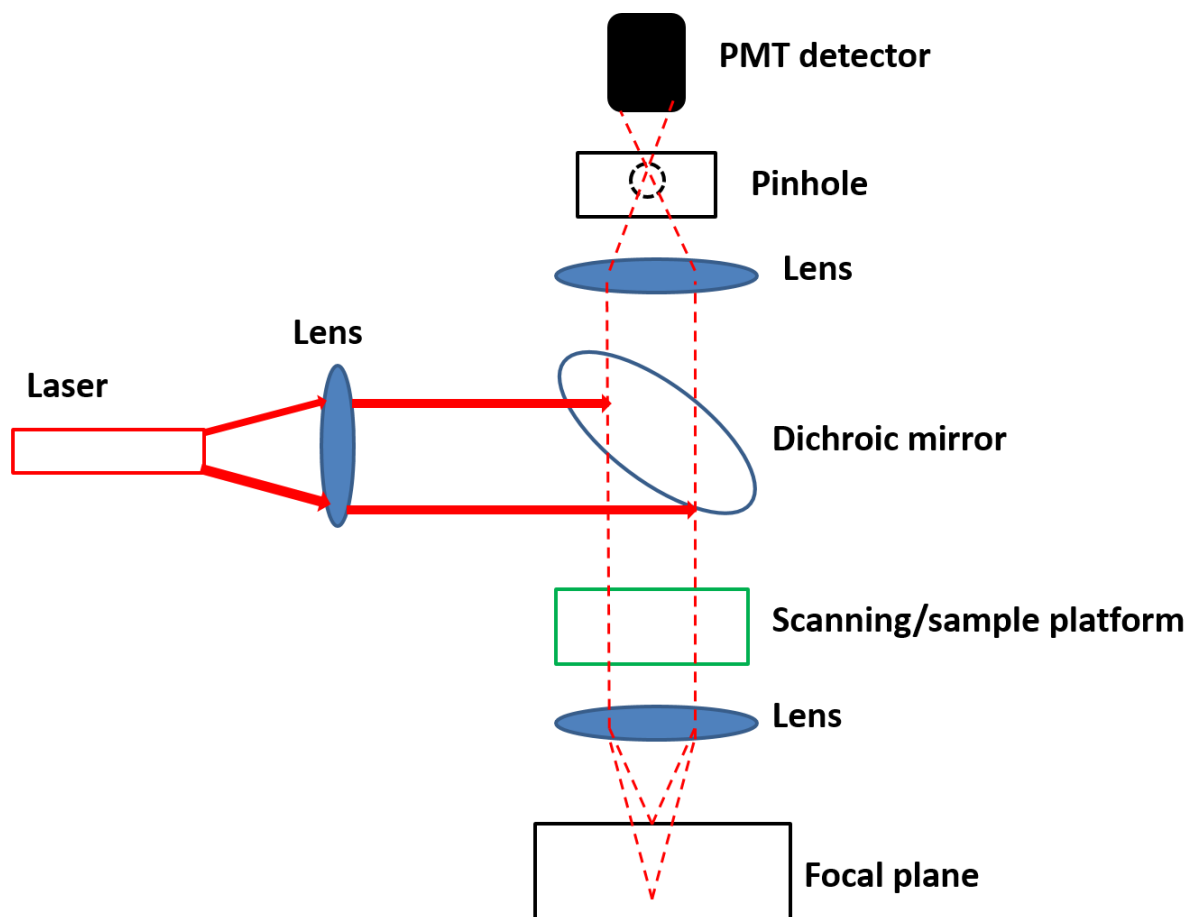


Figure 3.12. Schematic of a confocal microscope used for imaging fluorescent emission from material samples.

3.6. Biological Characterisation

3.6.1. Cell culture: Materials and Methods

The main equipment required for cell culture studies are a standard class II laminar flow hood (Walker Safety Cabinets, UK), water bath (operational temperature of 37°C), centrifuge, humidified incubator maintained at 37 °C with 5% CO₂, a cell counter for counting and seeding sample cells, an inverted microscope and a refrigerator and freezer (-20°C and -80°C respectively).

A sterile cell culture vessel (T75 flasks), Petri dishes and multi-well plates were employed for the cell cultures. All pipettes and tips were pre-sterilised with alcohol.

3.6.1.1. Cell culture medium

A suitable medium was prepared for all the cell culture experiments. Firstly, from a 500 ml flask of high glucose DMEM (Biosera, Boussens, France) 61.25 ml of media was removed. Then the remaining DMEM was supplemented with 40 ml foetal calf serum (FCS), 5 ml L-Glutamine (100×), 5 ml penicillin streptomycin (10,000 µg / ml, 10,000 µg / ml) and 1.25 ml amphotericin (Fungizone™). This provided 500 ml of DMEM. This medium was then stored at 4°C and replaced at least every six weeks.

3.6.2. Equipment and materials used for cell culture

Table 3.2. Chemicals and equipment used in cell culture

Chemical	Grade	Supplier
Phosphate Buffered Saline (PBS)		Oxoid Ltd, (Dulbecco A, Basingstoke, Hampshire.UK
Dimethyl sulphoxide (DMSO) C₂H₆OS	78.13 g/mol	(Fisher Scientific, UK) Lot 1214398
Reassuring sodium salt	251.17 Mw	(Lot No MKBN4870V, Sigma Aldrich®
EDTA-trypsin		Sigma Aldrich®, USA)
Mitochondrial deep red tracker	543.50 Mw	Invitrogen™ by thermos fisher scientific
Cell Tracker Far red DDAO-SE	505.35 Mw	Invitrogen Molecular probes
Equipment		
Water bath		
Laminar flow hood		
Refrigerator, freezer (-20°C) and deep freezer (-80°C)		
Centrifuge machine		
plate reader		
Inverted phase contrast microscopes		
2, 20, 200 and 1000 µl pipettes and pipette tips		
75 cm²/25 cm² culture flasks		
centrifuge tubes		
0.22 µm and 0.44 µm sterile filters		
Plate reader		
Petri dishes		
24 well plate, 6 well plate and 96 well plate		

3.6.3. Type of cell used

3.6.3.1. Human dermal fibroblast (HDF)

Fibroblasts are the most abundant type of cell in connective tissues where they form the structural framework by secreting components of the extracellular matrix (ECM). Human dermal fibroblasts, obtained from abdominoplasty or breast reduction operations according to local ethically approved guidelines (Northern General Hospital Trust (NHS), Sheffield, U.K.) Research Tissue Bank license number 12179. It is a widely used cell type we chose to study these effects on human dermal fibroblast cells from primary cultures because the skin is the principal boundary against presentation to natural variables containing nanoparticles. In addition, to gain a fundamental understanding of the process involved, we felt that it was critical to concentrate at first on the impacts of nanoparticles on individual living cells, instead of on whole organs, where different elements can confound the understanding [93]. HDF cells have also been used previously in the study of onion carbon nanodots for live cell imaging and accelerated skin wound healing [94]. Moreover, previous study shows there was no toxic effect of using nanoparticles on human dermal fibroblast [95].

Cell were cultured in a humidified 37°C, 5% CO₂/95% air(vol/vol) environment in Dulbecco's Modified Eagle's Medium (DMEM; Sigma–Aldrich) supplemented with 10% (vol/vol) FCS, 100 units/ml penicillin, 100g/ml streptomycin, and 0.625g/ml amphotericin B. Cells were passaged routinely by using 0.02% (wt/vol) EDTA and used for experimentation between passages 3 and 9 at 60% confluence.

3.6.3.2. NIH3T3 fibroblast:

The 3T3 cells come from a cell line created in 1962 by George Todaro and Howard Green at the New York School of Medicine, Cell line 3T3 became the standard cell line for fibroblast. Todaro and Greene initially got 3T3 cells from the tissues of the Swiss white mouse embryos. The name of this line refers to the protocol by which the cell line was established. That is, the primary cells were cultured using the '3-day transfer, inoculum 3×10⁵ cells' method, which is shortened to 3T3. Within this method, primary cells were continuously cultured by transferred (T) every three days (3) at a stringent density of 3×10⁵ cells per 20 cm² culture surface [96].

In this study, NIH-3T3 mouse cells were used to study mammalian cellular events and cellular responses that occur when cells interact with carbon nanomaterials. NIH-3T3 cells

were selected because their adhesion properties (integrin expression, focal adhesion group and proliferation) were well studied [97]. It has also been used frequently in studies of cellular functions such as cell shape change, adhesion, movement, and proliferation and to demonstrate the key roles of cytoskeletal components in cell adhesion, division, and growth [98].

3.6.3.3. **Melanoma cancer cells**

Skin cancer is melanocytic cell carcinoma that exists as individual cells in the basal layer of the epidermis. It is a very aggressive skin cancer with a malignant tumor potential and is responsible for the majority of skin-related deaths. The 5-year survival of diffuse skin cancer is approximately 10% [99]. Recent advances in cancer nanotechnology treatment was encouraged. Nano drugs can be killed tumor cells can serve as chemotherapy carriers directly and gene therapy. In addition, nanomaterials can be can target tumour cells passively or actively to improve treatment specificity, while reducing side effects. Many different types of nanoparticles have been studied previously in order to find treatment of skin cancer [100]. Melanoma C8161 was used as cancer cell line to study the effect of carbon nanoparticles when incubated with C8161 and their cellular uptake behaviour.

The C8161 human melanoma line was kindly donated by F. Meyskens (University of California, Irvine, CA)[101]. It is from an abdominal wall metastasis from a woman with recurrent malignant melanoma.

3.6.4. **Cell culture and passaging**

All equipment in the cell culture studies were initially sterilised inside the biological safety cabinet or laminar flow hood to offer aseptic conditions and to avoid any contaminations. All cells were cultured with T75 flasks to allow passage of the cells and observation of the cell morphology and density by means of inverted microscopy. When the cells reached 70% confluence they were split in a ratio according to the cell line specifications, and the media was changed every 3-4 days. Using the microscope, cells were observed and assessed when confluent passage could be performed. For this, cell media were removed from the T75 flask and washed three times with PBS (Phosphate-buffered saline), 1.5 ml of EDTA-trypsin (Sigma Aldrich®, USA) (Ethylene diamine tetra acetic acid/Trypsin 0.05%/0.02% EDTA w/v stored in -20°C) was then added to the flask, which was incubated for 5-10 minutes to detach cells and further incubated at 37°C for 5 to 15 minutes. When the cells had detached,

10 ml of fresh medium was added to halt the trypsin-EDTA reaction. The suspension was transferred to a centrifuge tube and centrifuged at 1000 rpm for 5 minutes. After centrifuging, a cell pellet was obtained in a universal tube. The supernatant of this suspension was removed and the cell pellet was re-suspended in 10-13 ml of fresh media. Then, haemocytometers were used to count the cells. The corresponding volume of medium containing cells was added to a new T75 flask containing 15 ml of cell DMEM to freeze the cells for use in further experiments. Cold freezing media (usually 10% dimethyl sulphoxide, DMSO) - 90% FCS (Foetal calf serum, Sigma Aldrich®, UK) was used for this purpose. The cold media was added to cell pellets and quickly re-suspended by adding 1 ml freezing media per vial for freezing overnight at -80°C.

3.6.5. Cell counting

A Neubauer haemocytometer (Weber Scientific International, UK) was used to count the cells. Four 1 mm² squares [1×10⁴ ml volume] were counted and an average was calculated to acquire the total cell number using equation 3.1 below:

$$\frac{\text{mean number of } \frac{\text{cells}}{1\text{mm}^2} \text{ dilution factor}}{\text{volume counted, } 1 \times 10^4 \text{ ml}} = \text{cell/ml} \quad \text{Eq. 3.1}$$

3.6.6. AlamarBlue assay

AlamarBlue is a resazurin-based colorimetric dye used to detect metabolic activity and thereby evaluate cell viability. It is a non-toxic substance suitable for use with the MTT cell viability assay (3-(4,5-dimethylthiazol-2-yl)-2,5-diphenyl-tetrazolium bromide [102] (Fig. 3.13). A colour change from dark blue to light pink indicates the onset of cell metabolism and the resulting fluorescence is read on a plate reader or using a fluorescence spectrophotometer. Alternatively, the absorbance of alamarBlue® reagent can be measured on a spectrophotometer. Finally, results were analysed by plotting fluorescence intensity (or absorbance).

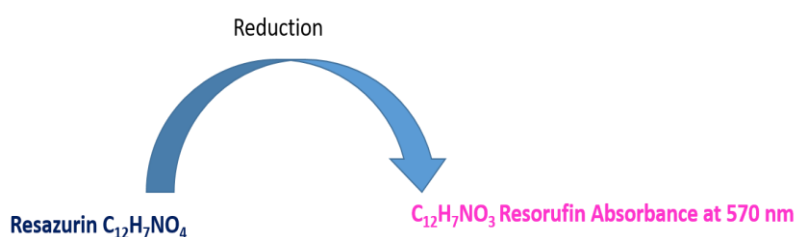


Figure 3.13. The blue dye resazurin is reduced to the fluorescent pink reduced form by viable, metabolically active cells only. The intensity of absorbance is proportional to the number of metabolically active cells.

3.6.7. Preparation of alamarBlue™ medium

Resazurin sodium salt (Lot No MKBN4870V, Sigma Aldrich®, USA, Mw = 251.17 g/mol) was dissolved in distilled water to prepare the alamarBlue reagent. The solution was covered with silicon foil and stored at 4°C. 10% of alamarBlue was added to the final sample volume, with incubation varying from 1-4 hours at 37°C.

3.6.8. Cell Viability Assessment

3.6.8.1. Preparation of synthesised QDs preparation in a DMEM medium

The carbon nanoparticles produced from glucose and alginate were mixed with glycerol and heated in the microwave for 5 min. then, 40 ml of DI water were added and centrifuged at 4000 rpm. Finally, CNPs were dried in a freeze dryer at -20°C. The obtained powder was used for cell experiments. In order to use the CNPs in the cells a dry powder of each sample was weighted. Then, the powder was suspended in PBS buffer and adjusted to contain 500 mg/mL as a stock for experimental use. Samples were stored at 4°C until further experiments.

3.6.8.2. Seeding of cells in the culture plates for toxicity evaluation

All the cell types were cultured and grown in DMEM under a humidified atmosphere of (5% CO₂ at 37°C). The DMEM was supplemented with 10% v/v FCS, 1% w/v glutamine, 1% w/v penicillin. When cells reach 75 % confluence, they were treated with trypsin and centrifuged at 1500 rpm for 5 min at room temperature. A cell count was performed for the three types of cells using a haemocytometer, and (1×10^4) cells were plated into each well of a 96-well culture plate (Corning USA) 200 µL/well (replicates of 3). All cell cultures were used for toxicity assessment after 24 h growth

3.6.8.3. Cytotoxicity assays

AlamarBlue was used to investigate the viability of the cells treated with the appropriate CNPs. After 24 h incubation, the growth medium was carefully removed and the cells were washed thoroughly with PBS three times. Then, 200 µL of different concentration of CNPs were added in replicates of three wells in a 96-well plate. The selected concentrations were as follows; 0, 10, 20 50, 100, 150 200, 250 and 300 µg/mL. Cells were incubated with the CNPs for one hour, at which point the wells were washed three times with PBS buffer fresh medium was added, and they were then incubated for 24 hours. After the incubation period,

20 µl of alamarBlue solution (10×) was added to the medium in each well and incubated for another 4 h. The live and metabolically active cells will convert resazurin to the fluorescent/absorbing molecule, resorufin, indicating the number of viable cells. The amount of absorbance is proportional to the number of living cells and corresponds to the cell metabolic activity. The absorbance was read using a 96 well-plate reader (Bio-Tek Instruments, UK) The absorbance at 570 nm was monitored using 600 nm as a reference wavelength. Cell viability data was obtained as the percentage of treated cells to untreated cells, using equation 3.2:

$$\text{Cell viability (\%)} = \text{Abs (treated)}/\text{Abs (control)} \times 100 \quad \text{Eq. 3.2}$$

3.6.9. Preparation of CNPs for toxicity assay

Each dry powder CNPs (glucose and alginate) heated in a CEM microwave at 200 and 220°C were weighted and suspended in PBS, and subsequently were filter-sterilized with a Whatman filter (consisting of a anodised aluminium membrane of 0.2 µm pore size). All cells lines were cultured in a 96-well plate and incubated for 24 h. After 24h each concentrations of CNPs were added to each cell and incubated for 1h. Finally, the CNPs were removed and fresh medium (DMEM) were added and were allowed to grow for 24, 48, and 72h. Figure 3.13.

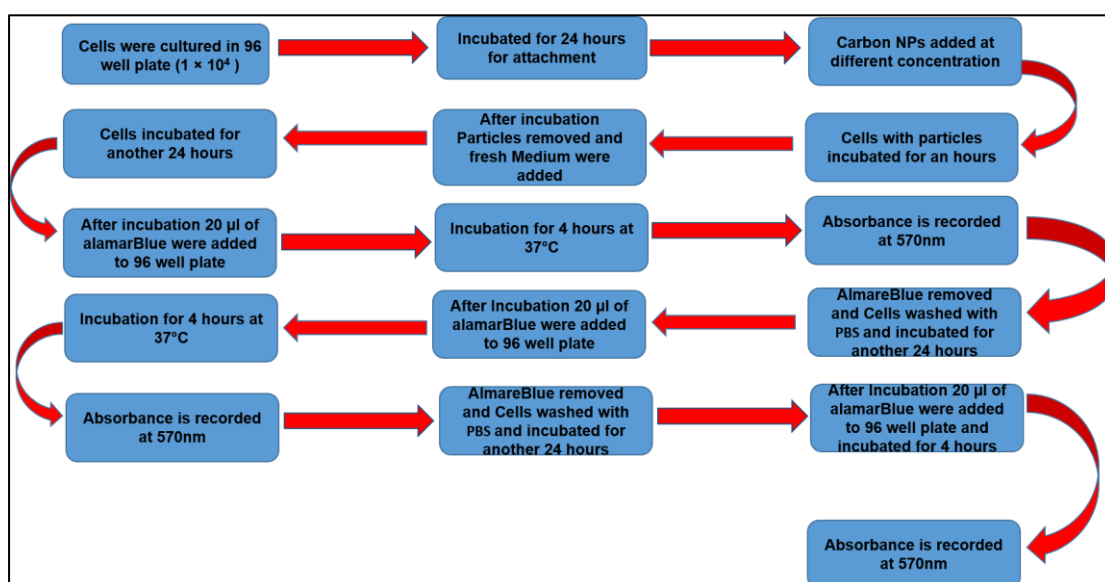


Figure 3.13. Schematic representation the protocol used to assess the cell viability of Carbon nanoparticles.

3.6.9.1. Nanoparticles uptake

Evaluation of the cellular uptake of carbon nanoparticles was determined by LSM confocal microscopy techniques. Human dermal fibroblast (HDF), Melanoma cancer cells (C8161)

and NIH 3T3 were seeded in 6-well plates with a density of 1×10^4 per well. After incubation for 48 h, the cells were treated with different concentrations (10, 20, 50, 100, 150 and 200 $\mu\text{g}/\text{mL}$ CNPs). Each CNPs concentrations were incubated for 5, 10, 20, 30 and 60 min. After each time point, cells were washed three times in PBS to remove the medium and the free CNPs. Then, 500 μl of formalin (3.7% v/v in PBS) was applied and incubated for 20 min, after which the cells were washed twice more with PBS. Nuclei were labelled with DAPI (dilution of 1: 10000 in water) for 15 minutes at room temperature. Finally, the cells were imaged by confocal fluorescence microscopy

3.6.9.2. **Confocal Imaging**

An upright confocal/multiphoton laser scanning microscopy system was used to visualise the cells uptake of CNPs (Zeiss LSM510 META, Carl Zeiss, Jena, Germany). Images were taken at 512×512 and 625×625 pixels with $40\times$ objective (Achromplan $40\times/0.75$ N.A., Carl Zeiss Ltd, UK).

3.6.9.3. **DAPI (4',6-diamidino-2-phenylindole) nucleus staining.**

DAPI is a staining fluorescence used to observe every cell within a sample and works as a control to differentiate between cells stained with carbon nanoparticles. Nuclei were labelled with DAPI (1: 10000 in water) for 45 minutes at room temperature and samples were observed under LSM confocal microscopy. DAPI was excited using a 760 nm laser (16% transmission) and emission detected between 435 and 485 nm.

3.6.9.4. **Cell tracker Deep Red**

The cell tracker deep red is a fluorescent dye has been intended to go through cell membranes into a cell, where they are converted into non-labelled cell interaction products. It is stable, nontoxic at the working concentration, brightly fluorescent, well held in cells and can display fluorescence for 72 hours. The fluorescent dye is held in living cells through several generations. The dye is moved to daughter cells but neighbouring cells. The dye can be used for multiplexing with green and fluorescent dyes and protein. The fluorescent dye excitation/emission spectra (630/650 nm maxima). Cell tracker red should store in freezer Store in a freezer (-5 to -30°C) and protect from light [103].

3.6.9.5. **Preparing a working Deep Red solution**

Before opening the colour vial, the item was left to warm to room temperature. The lyophilised item was broken down in high quality DMSO to a final concentration of 10 mM. For Cell Tracker™ Dark Red dye, 20 μL of DMSO was added per vial to make a 1 mM

(1000×) solution. The final solution was diluted to a concentration of 0.5 - 25 μM in serum-free medium. The CellTracker™ working solution was finally heated to 37°C.

3.6.9.6. **Deep tracker staining protocol**

Human dermal fibroblast (HDF) and Melanoma cancer cells (C8161) were cultured separately in T75 flasks at density of 10×10^3 cells/well. After reach confluence, the cells were removed and trypsin added. After that, cells were centrifuged and aspirated. The supernatant cells were suspended in pre-warmed Cell Tracker (serum free).

3.6.9.7. **Mitochondrial tracker Deep Red**

MitoTracker®Red CMXRos (Invitrogen, M22426) was added into the culture media at final concentrations of 50 nM. The cells were incubated under normal culture conditions for 30 min and then visualised by LSM confocal microscopy [104].

3.6.9.8. **Human fibroblast (HDF) and Melanoma (c8161) localisation studies**

Co-localization experiments were performed using carbon nanoparticles and Mito Tracker Deep Red. Human dermal fibroblast and melanoma cancer cells C8161 cells were grown at a density of 5×10^3 cells/well into six well plates in complete medium for 24 h at 37°C. Thereafter, the cells were incubated with 150 μg of CNPs for different time (5 min, 10 min, 20 min, 30 min and 1 h). Then, the cells were incubated 50 nM of MitoTracker®Red CMXRos (Invitrogen, M22426) for 30 min at 37°C. The cells were washed regularly three times with DMEM culture media and PBS (three times). The CNPs from glucose and sodium alginate were excited at 488 nm and the emission was collected in the FITC Channel (500 to 550 nm) and the Lyso or Mito Tracker Deep Red or Hoechst was excited at 644 nm and emission was collected in the Alexa Fluor 647 Channel (> 650 nm).

3.6.9.9. **Scratch assay**

Scratch assays were used according to the protocol described in [105], to examine the effect of CNP synthesis from glucose and alginate on the healing rate of fibroblast and melanoma cancer cells. For the in vitro scratch assay, melanoma C8161 and fibroblasts were seeded in 6 well plates at a density of 1×10^4 cells per well in the culture medium. The cells were allowed to grow until a monolayer formed. To create the scratch, a sterile 200 ml pipette tip was used on each wall plate and then washed twice with PBS to remove the cell debris from the denuded path. Further, complete medium (positive control, untreated group) and 150 μg

CNPs, (treated group) was added to each plate, then incubated for 2 hours incubation time. Then cells were imaged using an optical microscope at 0, 2, 3, 4, 5, 19 and 24 hours.

3.6.9.10. Co-cultures of HDF and C8161

Human dermal fibroblast and melanoma cancer (C8161) cells were grown in 75 cm² cell T-flasks with DMEM medium supplemented with 10% v/v FCS, 1% w/v glutamine, 1% w/v penicillin. All cells were incubated at 37°C, in a humidified atmosphere with 5% CO₂. Upon attaining confluence, both cell types were harvested using 1.5 ml trypsin to obtain two single cell suspensions. Cells were counted using a haemocytometer. Subsequently, co-cultures were seeded at 1:1 C8161 to HDF ratios, onto 6-well plates, with a total number of 2×10⁴ cells per well. Control cultures of HDF and C8161 cells were seeded using the same total number of cells per well in separate wells. CellTracker Red was used to label both cells so as to differentiate the cells in which CNPs were present. To determine the CNP-cellular uptake in co-culture, 100 µg/mL of CNPs were added and incubated for varying durations times (5, 10, 20, 30 and 60 min). After each incubation period, the cells were washed with PBS three times to remove carbon dots. Then 500 µl of formalin (3.7 % v/v in PBS) was applied and incubated for 20 min after which the cells were washed twice more with PBS. Finally, co-cultures were maintained in DMEM complete medium throughout all experiments. The evolution of co-cultures in terms of cellular uptake was analysed using LSM confocal microscopy.

3.6.10. Quantum yield calculations

The quantum yield (Φ) of CNPs was calculated using quinine sulphate as reference. Quinine sulphate (from the literature [106], $\Phi = 0.54$) was dissolved in 0.1 M H₂SO₄ (refractive index (η) of 1.33) while the nanoparticles were added to water ($\eta = 1.33$). Their fluorescence spectra were recorded at the same excitation of 340 nm. Then, by comparing the integrated photoluminescence intensities (excited at 340 nm) and the absorbance values (at 340 nm) of the sample with the references, the quantum yield was calculated using equation 3.3;

$$\Phi_Y = \Phi \times \frac{I_R}{I_S} \times \frac{A_R}{A} \quad \text{Eq. 3.3}$$

Where Φ is the quantum yield, I_R represents the integrated photoluminescence intensity of the quinine sulphate. I_S integrated photoluminescence intensity of the CNPs samples. A_R and A represents the absorbance at the excitation wavelength of 340 nm of the quinine sulfate and CNPs respectively.

*Chapter Four: Synthesis and Characterisation of Fluorescent
Carbon Nanoparticles*

4. Chapter Four: Synthesis and Characterisation of Fluorescent Carbon Nanoparticles - Results

4.1. Introduction

As nanotechnology continues to grow and mature, the need for new/or improved functional nanomaterials for a wide variety of applications remains at the forefront of worldwide research. As these materials and become more complex however, investigations into their characteristics and properties become more relevant. A particular focus of research effort in the last two decades has been the synthesis and purification of highly luminescent metal-containing nanoparticles due to their superior physiochemical properties. Specifically, their size-dependent optoelectrical properties have led to their use in various fields such as bio-imaging, sensing, solar cells and light-emitting diodes. The use of toxic metals such as cadmium, lead and tellurium have raised concerns about in vivo toxicity and harmful impacts on the environment, however. Lately, there has been a lot of interest in carbon nanoparticles because of their non-blinking fluorescent properties, biocompatibility and low toxicity. Moreover, the synthesis of carbon nanoparticles does not involve any toxic heavy metals. In addition, carbon nanoparticles have carboxylic acid functionalities at their surfaces which enhances their water solubility and their suitability for chemical functionalisation with a variety of inorganic, organic, polymeric or biological moieties.

The synthesis of carbon nanoparticles was initially a serendipitous event during the electrophoretic purification of single-walled carbon nanotubes synthesised from arc-discharge soot [91]. The synthesis of fluorescent carbon nanoparticles using a bottom-up approach initially involved one-step dehydration of the carbohydrate using sulfuric acid. After oxidising the raw product with nitric acid for 12 hours, carbon nanoparticles rich with carboxylate groups were successfully synthesised. Importantly, the reaction does not involve any additional surface passivation steps [92]. The bottom-up approach has also been demonstrated to yield carbon nanoparticles through the heating of glycerol with a phosphate solution using a domestic microwave. The resulting nanoparticles exhibited excitation-dependent emission properties [93].

Recent investigations on the synthesis and processing of carbon nanoparticles have diverted towards the use of a hydrothermal approach, however. This method involves the crystallisation of starting materials in an autoclave at high temperatures and pressures for several hours. For example, treating glucose with mono-potassium phosphate at 200°C in an autoclave produces carbon nanoparticles [94]. In a similar fashion, nitrogen-doped carbon

nanoparticles have been prepared through heating grass and water at 180°C in an autoclave [95]. To obtain smaller nanoparticles, raw solution was centrifuged at 12000 rpm to remove unreacted starting materials and larger nano- and micro-particles. Due to their smaller sizes, the resulting nanoparticles exhibited superior fluorescence properties with high quantum yields.

Microplasma has also been exploited to speed up the rate of reactions and thus shorten the time needed to process carbon nanoparticles. For example, thermal activation involving electron and radical injection is often employed to accelerate the chemical reactions. Good quality carbon nanoparticles with reduced dimensions of 2.4 nm were produced in a shorter time by heating fructose and sodium hydroxide [96]. A supported approach has also been used to achieve complete control over the size, and size distributions, of synthesised carbon nanoparticles. In one such example, Bourlinos and co-workers have used NaY zeolite as a catalyst to provide large surface for producing tightly controlled carbon nanoparticles [97]. In this method, after ion exchanging zeolite with 2,4-diaminophenol dihydrochloride, the reaction mixture was thermally oxidised at 300°C to produce quasi-spherical carbon nanomaterials with dimensions of 4 - 6 nm.

To increase the suitability of carbon nanoparticles for various bio-applications, multicoloured nanoparticles have been synthesised from an aqueous solution involving surfactant-modified silica spheres and phenol/formaldehyde resins used as carbon precursors [98]. During the reaction, silica spheres were used as carriers and provided anchors for the polymerisation of resins (phenol/formaldehyde). Interestingly, the resulting nanoparticles were not fluorescent, and fluorescence could only be achieved after passivating surfaces with polyethylene glycol 1500 g/mol. The carbon nanoparticles produced demonstrated a broad peak, and quantum yields as high as 14.7 % were reported by the group. Indeed, much of the work reported on the synthesis of carbon nanoparticles involves passivation of surfaces to promote fluorescence. This is often done through the refluxing of raw materials with nitric acid for a period of time since this serves to introduce oxygen rich carboxyl groups on the surface [92]. This enhances fluorescence and provides opportunities for further surface modification. Poly(ethylene glycol) is often the preferred choice of surfactant because of its biocompatibility and enhanced water solubility [99]. A single-step surface functionalisation method is possible during thermal decomposition of precursors. For example, various (organic) functionalities can be added by choosing different ammonium citrate salts [97]. The citrate part acts as a carbon source while the ammonium component provides the anchor for

the covalent attachment of surface modifiers. Through the judicious choice of organic molecules, the solubility of the carbon nanoparticles can be altered to suit a given application. Since carbon nanoparticles are made up of the element carbon, however, it is important to consider carbon-rich sources as the starting materials. This chapter will focus on the straightforward single-step pyrolytic synthesis of fluorescent carbon nanoparticles from two different types of polysaccharides, namely glucose and sodium alginate, because these have a large number of reactive groups and display varied structural and chemical properties. They are also highly favourable for use as biomaterials due to their highly stable, non-toxic, safe, hydrophilic and biodegradable nature. For example, sodium alginate is carbon rich and is composed of hydrophilic groups like carboxyl and hydroxyl moieties, and therefore is a good candidate for the carbon nanoparticle synthesis. The preparation of nanoparticles will be performed in a microwave, which is not only fast but also more flexible and reliable. This will be followed by detailed structural and optical investigations using a variety of characterisation techniques. For example, UV/Vis and photoluminescence spectroscopies will be used to probe the absorption and emission properties of resulting materials and to determine their potential as an optical probe for the target application. Surface-sensitive X-ray photoelectron spectroscopy will be used to study the surface chemistry and determine the types and the amounts of elements present at the nanoparticle surfaces. Raman and infrared spectroscopies will also be performed to complement the surface studies. The particle morphologies and sizes will be examined using transmission electron microscopy in conjunction with dynamic light scattering, and X-ray powder diffraction studies will be utilised to determine the crystallinity of deposited structures.

This chapter describes the synthesis of highly fluorescent carbon nanoparticles using low-cost and widely available carbohydrates, glucose and sodium alginate. These are both approved food additives and can be used for biomedical applications due to minimum toxicity issues. Furthermore, their low melting points means that the reaction can be carried out easily at a low temperature. They have large number of reactive groups, varying chemical composition, a wide range of molecular weights and are diverse in structural and chemical properties. The use of a microwave for heating has the advantage of allowing for direct heating and control over the growth conditions, enabling reproducible batch-to-batch synthesis of carbon nanoparticles. It is worth mentioning that the type of microwave has important implications for the quality of the materials being generated. A typical domestic microwave reduces the chance of reproducible synthesis because the heating is non-uniform and because of how the

radiation reaches the sample. The cavity walls reflect much of the radiation entering the reaction vessel in a domestic microwave. In the monomode system used for the synthesis here, however, the heat is directed towards the sample at a fixed distance by means of a standing wave. During the synthesis, all the parameters such as irradiation time, power, reaction time were fixed except for the growth temperature.

4.2. Result and Discussion

4.2.1. Synthesis

One-step synthesis of highly fluorescent carbon nanoparticles was successfully performed in a CEM microwave. The bottom-up approach involves strong heating to facilitate the “burning” or carbonisation process during the formation of the nanoparticles. As illustrated in Figure 4.1, the reaction involved heating the glucose and sodium alginate precursors in the presence of glycerol at 200 and 220°C, respectively, for 5 minutes. During the reaction, the colour of the mixture changed from transparent to brown and thence to dark brown with prolonged heating indicating the formation of carbonised material. A change in colour was taken as the benchmark for judging whether the reaction had taken place or not. The prepared carbon nanoparticles were highly soluble in water. The dry powder of carbon nanoparticles were highly hygroscopic and long term storage in ambient atmosphere resulted in CQD powder that stuck to the inner walls of the vials.

The mechanism for synthesis of carbon nanoparticles from glucose and sodium alginate involves carbonization of its constituents. The dehydration and decomposition of glucose, gives rise to different soluble products such as furfural compounds (for ex: 5-hydroxymethyl furfural, furfural, 5-methyl furfural etc) and several organic acids such as acetic, lactic, propionic, levulinic acid, dihydroxyacetone and formic acid [72].

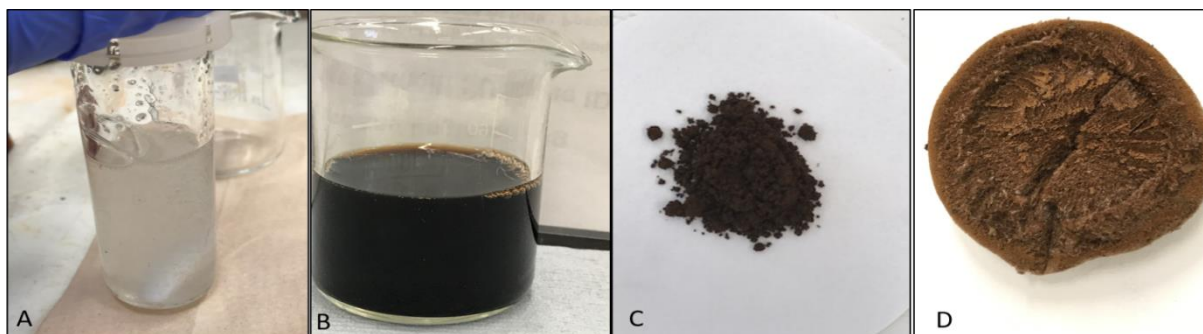


Figure 4.1. Photographs of carbon nanoparticles (A) a transparent solution of glucose before the microwave reactions, (B) solution after microwave reaction, (C) dry powder of glucose carbon nanoparticles and (D) dry powder of alginate carbon nanoparticles.

4.2.2. Quantum Yield

The Quantum yield of the carbon nanoparticles was calculated in order to assess the carbon nanoparticles as tracking agents. The quantum yield (Φ) of a fluorophore is an important factor and can be defined as the ratio between the number of photons emitted and the number of photons absorbed. The theoretical highest quantum yield of 1.0 (100%), where every photon absorbed is consequently emitted, is extremely difficult to achieved. Nonetheless, there are some molecule fluorophores reach close to this such as fluorescein in ethanol has a quantum yield of 0.91 ± 0.05 (in 1 M NaOH) [107]. In addition, the quantum yield of carbon nanoparticles is highly depend on the synthesis method used the nature of the precursor and the passivation method employed. Researcher reported that, the quantum yield is generally low when the fabrication method used produces dots with carboxyl-functionalised surfaces but is improved with the addition of organic molecules [108-110].

Initially, quantum yield (Φ) of the carbon nanoparticles from glucose and sodium alginate were calculated using quinine sulfate as reference (detailed in section 3.6.10). The quantum yield for glucose at 200 °C and 220 °C were 0.0112 and 0.0113 respectively as see in table 3.3. While in alginate calculated 0.0302 and 0.0306 respectively. The quantum yield increased when the temperature increased.

Table 4.1. Quantum yield calculation results

Sample	Integrated emission intensity (I)	Abs. at 340 nm (A)	Refractive index of solvent (η)	Quantum Yield (Φ)
Quinine sulphate	40893.5	0.03835	1.33	0.54 (known)
Alginate CNPs- 200°C	149490	0.187154	1.33	0.0302
Alginate CNPs- 220°C	142010	0.194347	1.33	0.0306
Glucose CNPs - 200°C	386450	0.19599	1.33	0.0112
Glucose CNPs - 220°C	319470	0.233709	1.33	0.0113

4.2.3. Ultraviolet-Visible absorbance spectroscopy (λ ab)

Produced carbon nanoparticles were easily dispersed in water and exhibited good transparency without any ultra-sonication. This allows recording UV-Vis spectrum for the samples at wavelengths between 200 – 800 nm. The spectra clearly indicate that the nanoparticles exhibit a strong blue absorption in the UV region and a weaker absorption in the visible region, although their absorption frequencies were different depending on the choice of carbon source, i.e. glucose or sodium alginate.

For the glucose-based nanoparticles (Figure 4.2 A and B), the major absorption peak found at 283 nm was typical of an aromatic π -system as it relates to the $n\rightarrow\pi^*$ and $\pi\rightarrow\pi^*$ transitions of the C=O band and conjugated C=C band, respectively, within the structure of carbon nanoparticles. This further indicates that a complete conversion of glucose to carbon nanoparticles had taken place. A similar observation has been previously noted for other polycyclic aromatic hydrocarbons [100, 101]. When the growth temperature was increased from 200 to 220°C (from 4.2A to B), a marginal but important increase in the absorption intensity was evident. Replacing glucose with sodium alginate, however, led to a reduced absorption intensity peak, which is also red shifted. The difference in the absorption intensity could be an indication of similar structural properties with slight variation in the number of functional groups (Figure 4.2C). At 220°C, the alginate nanoparticles did not show any absorption in the UV-Vis range, possibly because of the lack of a conjugated system within the alginate structure (Figure 4.2D). The weak absorption peak found at 200 nm for alginate was related to the $n\rightarrow\pi^*$ transition of the C=O band and is in line with previous studies [94]. It can be deduced from these absorbance spectra that there were structural differences in the produced nanoparticles.

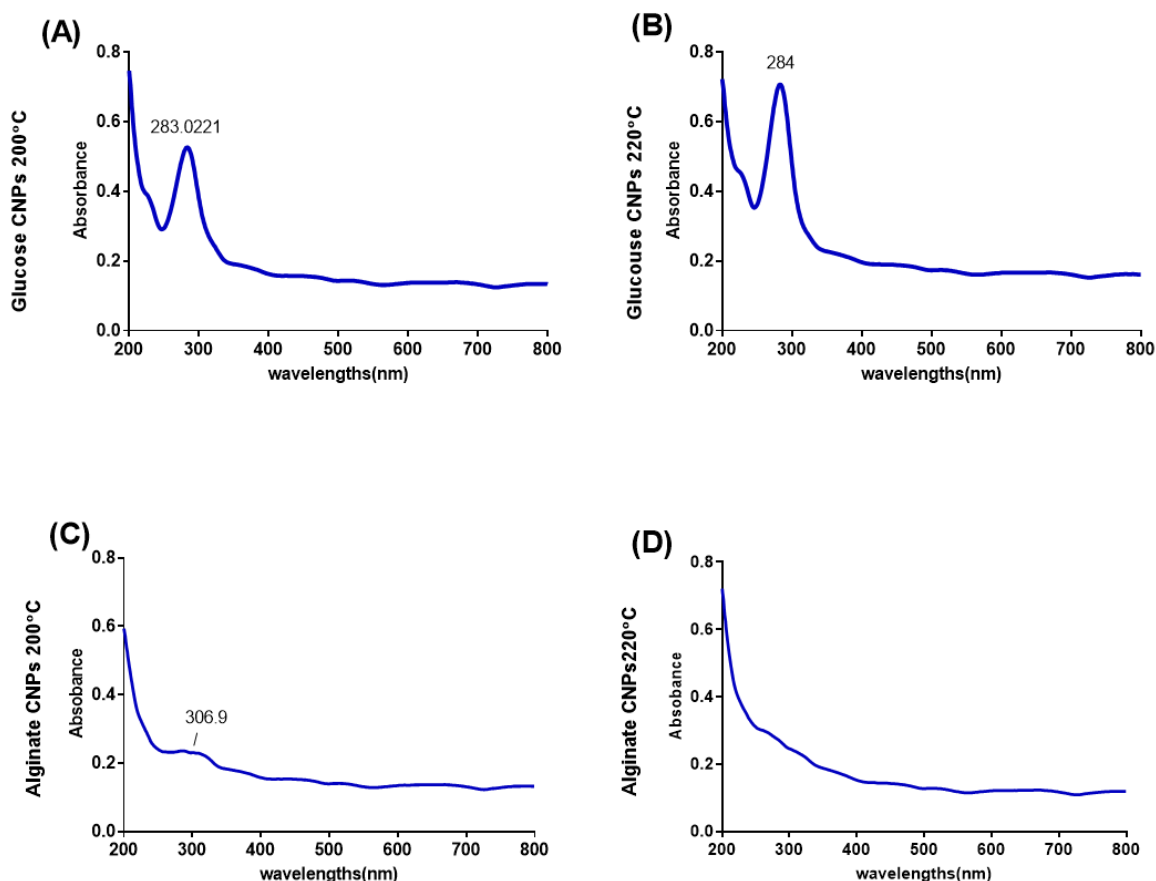


Figure 4.2. Typical UV–visible absorption spectra of CNPs. (A) absorption spectra of CNPs produced from glucose heated at 200°C, (B) absorption spectra of CNPs produced from glucose heated at (220°C), (C) absorption spectra of CNPs produced from alginate heated at (200°C). and (D) absorption spectra of CNPs produced from alginate heated at (220°C).

4.2.4. Raman spectroscopy analysis.

To determine the structure and bonding types of the prepared nanoparticles, Raman studies were carried out at room temperature using a spectrometer equipped with a 532 nm laser. The resulting spectra were dominated by high intensity D- and G-bands. For alginate-based nanoparticles, D-bands were located at 1370 cm^{-1} for both set of samples. This D-band corresponds to vibrations of disordered carbon atoms with dangling bonds and is located at the edge of graphene sheets within the structure [10, 11]. The D-band further includes the disordered aromatic structure in the sp^2 carbon structure. The D-band peak position for the glucose samples changed from 1350 cm^{-1} (at 200°C) to 1320 cm^{-1} (at 220°C), which was possibly affected by the strong fluorescence from the resulting carbon nanoparticles. The G-band originates from the vibration of sp^2 -bonded carbon atoms arranged in a 2D hexagonal lattice of a graphite cluster or graphene sheet. The G-band peak positions for sodium alginate

and glucose-containing nanoparticles altered from 1560 to 1550 cm^{-1} and 1580 to 1570 cm^{-1} , respectively. These different G-band values correspond to different sizes of nanoparticles and/or the existence of different oxygen species at the surface. For glucose samples, there was an additional broad peak at 2750 cm^{-1} and this was a characteristic of the 2D band in graphitic forms of carbon. Apart from these D- and G-bands for the glucose-based samples, the spectral region of 820–980 cm^{-1} which is often referred to as an anomeric region, was used to distinguish between α -glucose and β -glucose. This anomeric region corresponds to various vibrations such as $\nu(\text{C-O})$, $\delta(\text{C-C-H})$, $\nu(\text{C-C})$ and $\delta(\text{C-C-O})$ modes. Although these peaks were quite dominant in the pure glucose spectrum, after the heating, they were encased together, and no prominent peak is observed. The small peaks found at 600 cm^{-1} imply that carbon nanoparticles have carbon linear chains. The decomposition products of glucose during microwaving are 5-(hydroxymethyl) furfural and 3-deoxyglucosone [72][102]. 5-(hydroxymethyl) furfural consequently polymerise into a carbon network which gives rise to the carbon nanoparticle formation. In this work, however, no evidence was found of these two molecules within the collected nanoparticles, possibly due to overlapping of peaks at low wavelengths. Additionally, these water-soluble particles are preferentially eliminated during the washing step.

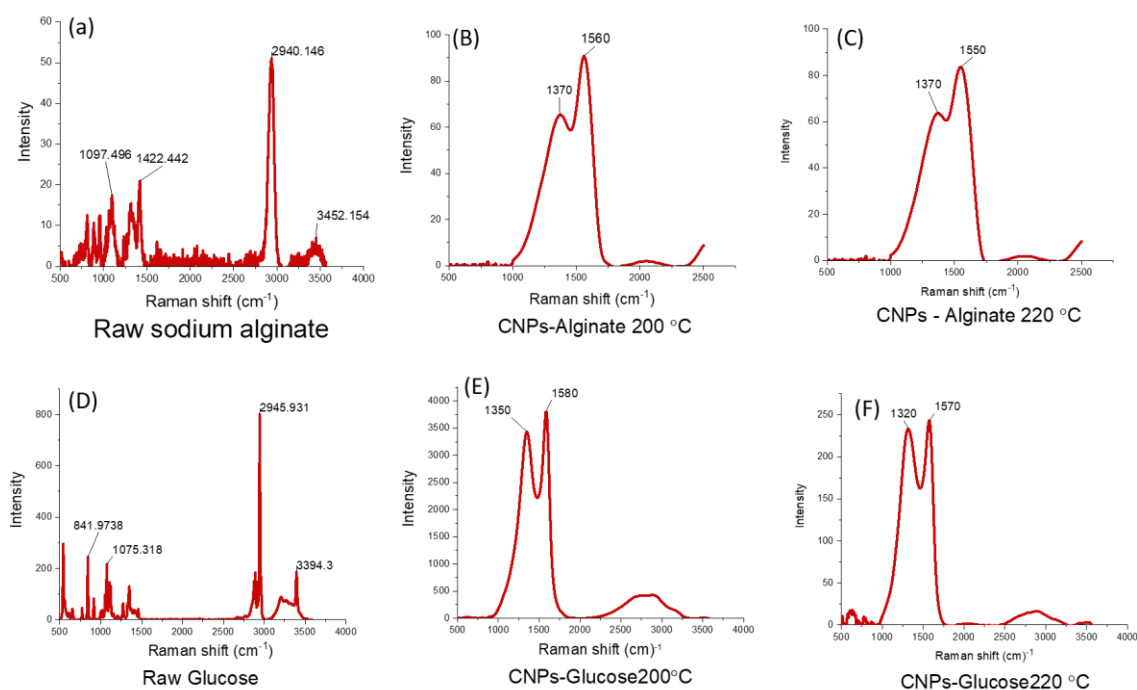


Figure 4.3. Raman spectra of (A) raw sodium alginate, (B) CNPs from sodium alginate heated at 200°C, (c) CNPs from sodium alginate heated at 220°C, (D) Raman spectra of raw Glucose, (E) CNPs from glucose heated at 200°C and (F) Carbon NPs from glucose heated at 220°C.

Table 4.2. The CNP peaks in Raman spectrometer

Carbon Nanoparticles	D band (cm⁻¹)	G band (cm⁻¹)
CNPs-Glucose -200°C	1350	1580
CNPs-Glucose-220°C	1320	1570
CNPs-sodium Alginate -200°C	1370	1560
CNPs sodium Alginate- 220°C	1370	1550

4.2.5. Fluorescence Spectroscopy of CNPs

Considering the size of these nanoparticles (< 200 nm, discussed below), it is unlikely that their fluorescence would be dominated by quantum confinement effects. Such quantum confinement effects are generally observed when the size of the particle is too small to be comparable to the wavelength of the electron [103]. If the size of the quantum dots is larger than this then confinement would not occur, and this leads to a transition from continuous to discrete energy levels. The origin of fluorescence in the nanoparticles is most likely to be a result of emissive traps on the surfaces, due to the large particle sizes. In the trap states, the charge carriers can be trapped anywhere within the system, i.e. either in the bulk or on the surface, and do not take part in the transportation of charges. The presence of surface energy traps is a result of surface defects during passivation steps. The effects of surface defects on the fluorescence of carbon nanoparticles of similar sizes has been recently studied and it was concluded that fluorescence emitted at 520 nm was a result of surface defects caused by the oxygen rich terminals [103]. Meanwhile, emissions below 450 nm were caused by the quantum size effects because of small particle sizes.

It is clear from the spectra in Figure 4.4 that the emission wavelengths rely on the excitation wavelength, so excitation-dependent fluorescence emissions for the nanoparticles were noticed after the samples were excited with increments of 10 nm in the wavelengths and using water as a solvent. For the glucose samples, increasing excitation energies from 300 to 440 nm led to a red shift of the fluorescence peaks coupled with a significant decrease in intensity. For example, at 200°C, there was an intense fluorescence peak at 497 nm in the case of the glucose sample once that sample was excited at 400 nm. The most intense peak

for the glucose sample prepared at 220°C, however, was found out to be at 444 nm after exciting at 370 nm. A similar observation was also noted by Tang et al., who described the synthesis of graphene nanoparticles from glucose. These authors reported excitation-dependent emission between excitation energies of 300 – 380 nm for nanoparticle surfaces enriched with carboxyl groups. However, the emission wavelength was independent of particle size instead, depend on the surface passivation [104]. For alginate-containing samples, maximum fluorescence was found to be at 510 nm (at 200°C) and 491 nm (at 20°C) after exciting at 410 and 390 nm, respectively. These excitation-dependent emissions of carbon nanoparticles clearly point towards the multiple surface states of different functional groups.

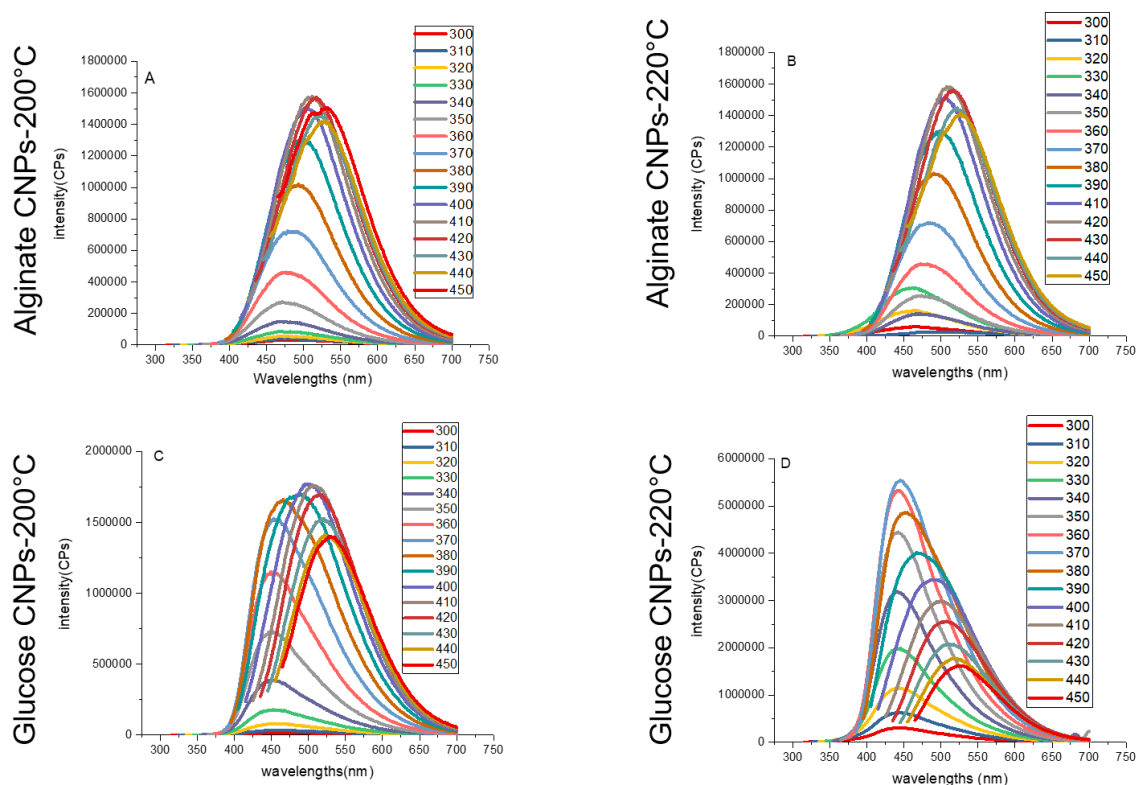


Figure 4.4. Fluorescence emission spectra of synthesised CNPs from (A, B) alginate at 200°C and 220°C and (C, D) glucose at 200°C and 220°C, respectively. The samples existed at different wavelengths from 200 nm to 450 nm.

The maximum emission intensity (counts per second), excitation and emission wavelength at theses maxima were deduced from the data shown in Figure 4.4 and presented in Table 4.2.

Table 4.3. Summary of the results derived from fluorescence spectra in Figure 4.4

	Glucose CNPs at 200°C	Glucose CNPs at 220°C	Alginate CNPs at 200°C	Alginate CNPs at 220°C
Maximum Emission Intensity (CPS)	1772100	5541300	1573850	15846000
Emission Wavelength of Maximum Intensity (nm)	500	445	509	510
Excitation Wavelength of Maximum Intensity (nm)	400	370	410	420

4.2.6. Fourier-transform infrared spectroscopy

The Fourier-transform infrared (FT-IR) spectra shown in Figure 4.5 were used to identify the functional groups present on the surfaces of nanoparticles. Clearly, there are similarities but also significant differences in FT-IR for the CNPs produced by two different base materials. The sharp bands located around 2900 and 1600 cm^{-1} supported the aromatic C=C stretching of nanoparticles. The presence of peaks at $\sim 3300 \text{ cm}^{-1}$ (O-H vibrational stretch), $\sim 1700 \text{ cm}^{-1}$ (C=O vibrational stretch) and $\sim 1040 \text{ cm}^{-1}$ (C-OH vibrational stretch) implied the presence of a large number of hydroxyl and carboxylate groups on the surfaces. The strong peak at $\sim 3300 \text{ cm}^{-1}$ was due to the loss of water or hydroxyl groups after the carbonisation.

For Alginate based CNPs specifically, the prominent peak at around 1400-1600 cm^{-1} which originate due to asymmetric carboxylate O-C-O stretching. This corresponded to the presence of aldehyde or ketone groups in the final collected carbon nanoparticles. It further suggested that oxidation had occurred on the surface during the pyrolytic carbonisation process. A minor peak at $\sim 2360 \text{ cm}^{-1}$ due to the acetal groups indicates that the long polysaccharide chains were broken during the reaction and gave rise to CH_3 and CH_2 groups. This is confirmed by a stretching at 2900 cm^{-1} which indicated the existence of CH_3 groups. The presence of OH and CHO groups on the surfaces improved the stability and hydrophilic behaviour of nanoparticles and could be selectively modified with different functional groups for any given application.

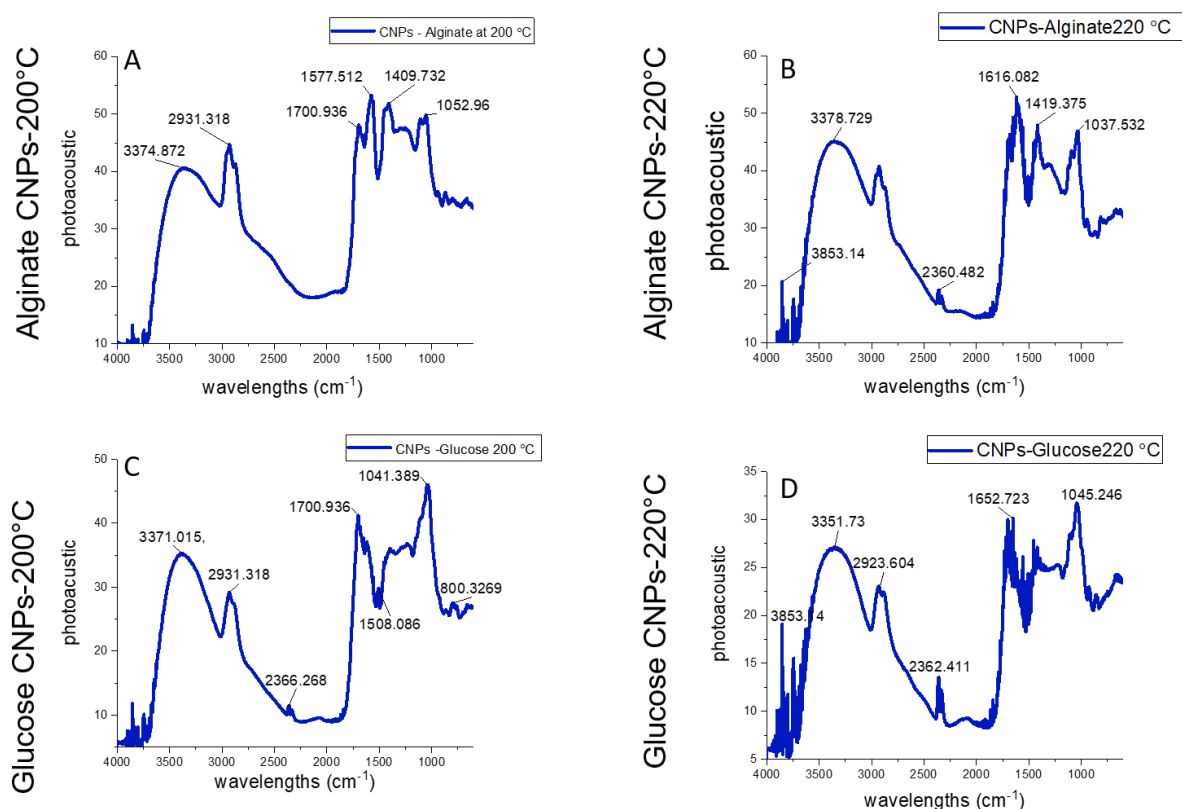


Figure 4.5. FT-IR spectra of the synthesized (A, B) sodium alginate CNPs heated in the microwave at 200°C and 220°C respectively. (C, D) Glucose CNPs heated in the microwave at 200°C and 220°C, respectively.

4.2.7. X-ray photoelectron spectroscopy (XPS)

As the samples were in the powder form they were mounted by compacting them onto indium foil and was then used for all analyses. The analyses were carried out using a Kratos Supra instrument with a monochromated aluminium source, and two analysis points per sample, each of area 700 μm by 300 μm . Survey scans were collected between 1200 to 0 eV binding energy, at 160 eV pass energy, 1 eV intervals, and 300 seconds/sweep. High-resolution O 1s, N 1s, C 1s, P 2p, S 2p and Si 2p XPS spectra were also collected at 20 eV pass energy and 0.1 eV intervals for each analysis point over an appropriate energy range, with one 300 second sweep for O 1s, C 1s and Si 2p and two 300 second sweeps for N 1s, S 2p and P 2p. (A longer collection time was used for these elements due to their smaller relative sensitivity factors). Collected data were calibrated for intensity using a transmission function characteristic of the instrument (determined using software from NPL) to make the values instrument independent. The data were then quantified using theoretical Schofield relative sensitivity factors. All high resolution spectra have been calibrated during analysis to force the C-C/C-H C 1s peak to be 285.0 eV.

4.2.7.1. XPS of CNPs derived from Alginate-based synthesis at 200°C and 220°C

X-ray photoelectron spectroscopy (XPS) was successfully used to conduct compositional analysis and to investigate the content of surface features of fluorescent carbon nanoparticles. Survey scans of carbon nanoparticles prepared from alginate at 200°C and 220°C are given in Figures 4.6A and 4.7A, respectively. It is apparent that the samples predominantly consisted of carbon (binding energy C 1s = 281 eV) and oxygen (binding energy O 1s = 528 eV).

No nitrogen peak was presented for any of the samples, although the high resolution scans were collected to confirm its concentration was lower than the limit of detection, approximately 0.1 at%. For the phosphorus, sulphur and silicon - these were not all detected for every sample, so a curve-fit has only been provided where a peak was seen. From the curve fitting, chemical composition of each sample was computed.

For the sample prepared at 200°C, the percentages of carbon and oxygen found were 74.43% and 22.27%, respectively. When the temperature was increased to 220°C, the amount of carbon (74.72%) and oxygen (22.71%) were marginally increased. Other elements such as sodium (Na 1s), calcium (Ca 2p), chlorine (Cl 2p), phosphorus (P 2p) and silicon (Si 2p) were also present as traces. In Figures (4.6B and 4.7B), high-resolution spectra of C 1s can be fitted to five peaks. For O 1s, there are four chemical bonds (Figure 4.6C and 4.7C). Broad O 1s peaks at 530.4 and 532.5 eV coupled with C 1s peaks at 285.08, 286.78 and 288.18 eV point towards the carboxylate groups. Other O 1s with binding energies of 533.08 eV, 531.78eV and 536.38 eV were a result of carbonyl and hydroxyl groups at the nanoparticle surfaces. No N 1s peak was found in the high-resolution spectra, which implies the absence of any nitrogen containing groups.

Alginate CNPs-200°C

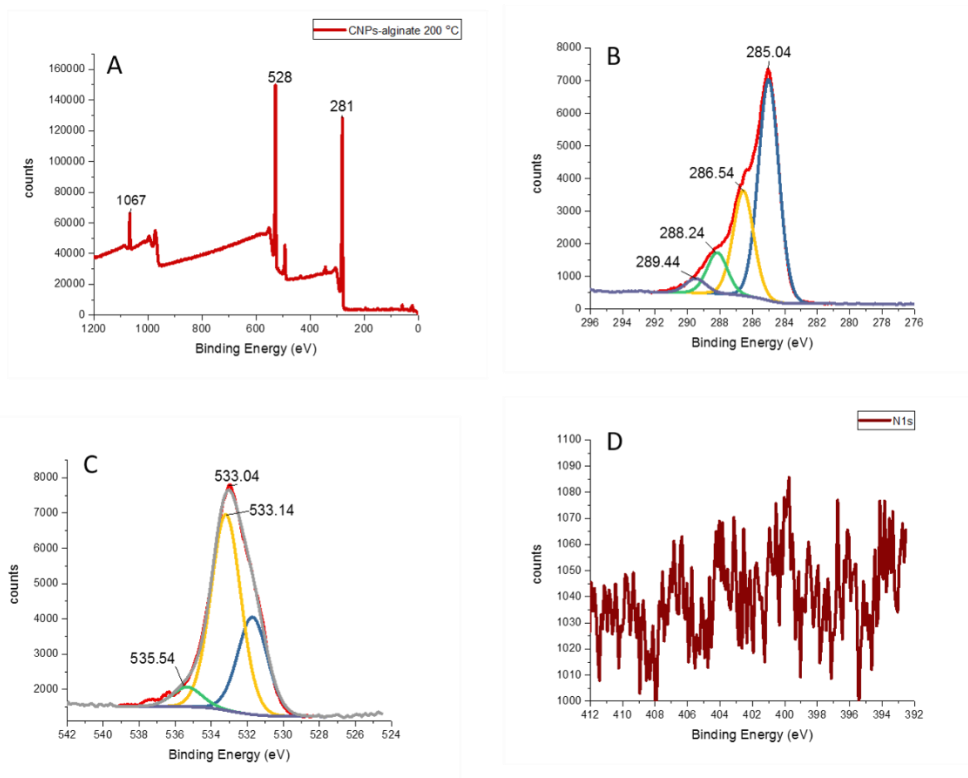


Figure 4.6. (A) XPS survey scan from Alginate-based synthesis at 200°C, (b) High-resolution XPS spectrum of the C 1s scan from Alginate-based synthesis at 200°C, (C) High-resolution XPS spectrum of the O 1s scan, (D) High-resolution XPS spectrum of the N 1s scan

Alginate CNPs-220°C

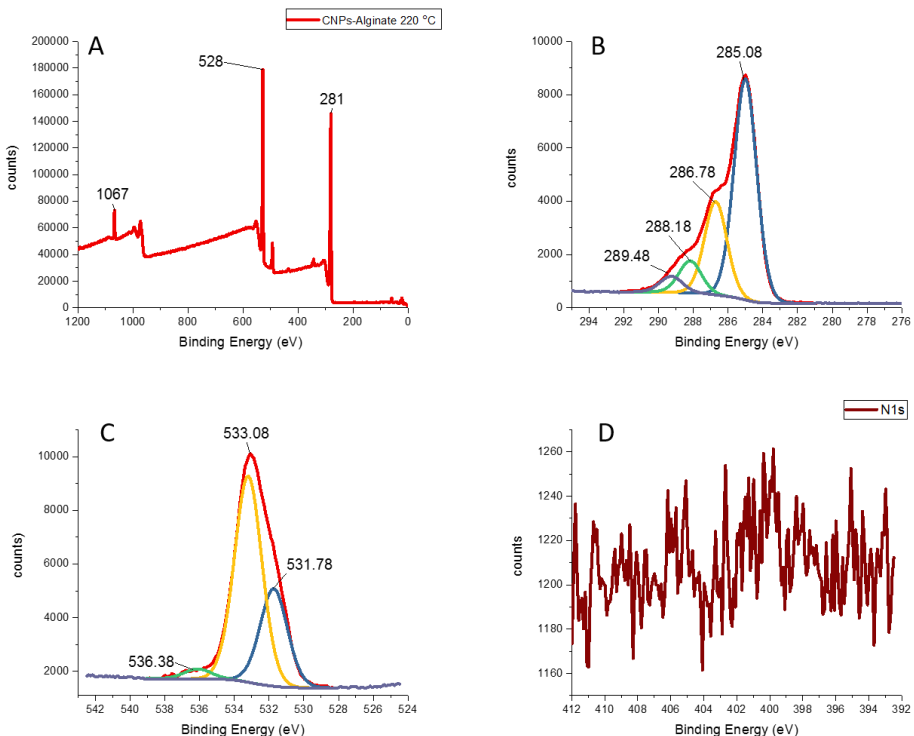


Figure 4.7. (A) XPS survey scan from Alginate-based synthesis at 220°C, (b) High-resolution XPS spectrum of the C 1s scan from Alginate-based synthesis at 220°C, (C) High-resolution XPS spectrum of the O 1s scan, (D) High-resolution XPS spectrum of the N 1s scan.

4.2.7.2. XPS of CNPs derived from Glucose-based synthesis at 200°C and 220°C

Figures 4.8 and 4.9 are the XPS scans of glucose-based carbon nanoparticles synthesised at different temperatures. The spectra are again dominated by expected peaks for the carbon at ~281 eV and oxygen at ~529 eV. The percentage of carbon in the samples was similar to that calculated for the alginate samples. The absence of Ca 2p and P 2p impurities in both sets of data resulted in purer samples than the alginate ones. In the high-resolution spectra of the C 1s peaks, there were five chemical bonds: C=C at 284.1 eV, C-C and C-H at 285.5 eV, C-OH/C-O-C at 285.7 eV, C=O at 288 eV and -COOH at 289.3 eV. Unlike the high-resolution spectra of O 1s for the alginate samples, only two different chemical environments were observed for glucose samples, i.e. C=O at 533.04 eV and C-OH/C-O-C at 534.54 eV. The atomic percentage of oxygen species in glucose was higher (approaching 25%) than in the alginate samples, which improved dispersity of material in water.

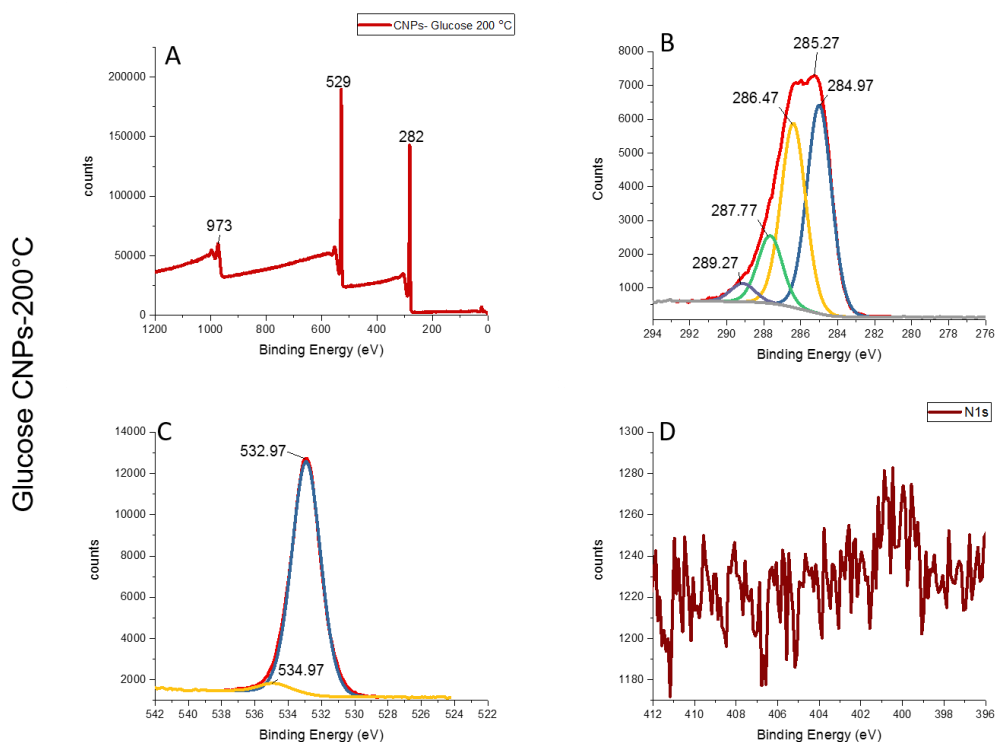


Figure 4.8. (A) XPS survey scan from Glucose-based synthesis at 200°C, (b) High-resolution XPS spectrum of the C 1s scan from Glucose-based synthesis at 200°C, (C) High-resolution XPS spectrum of the O 1s scan, (D) High-resolution XPS spectrum of the N 1s scan.

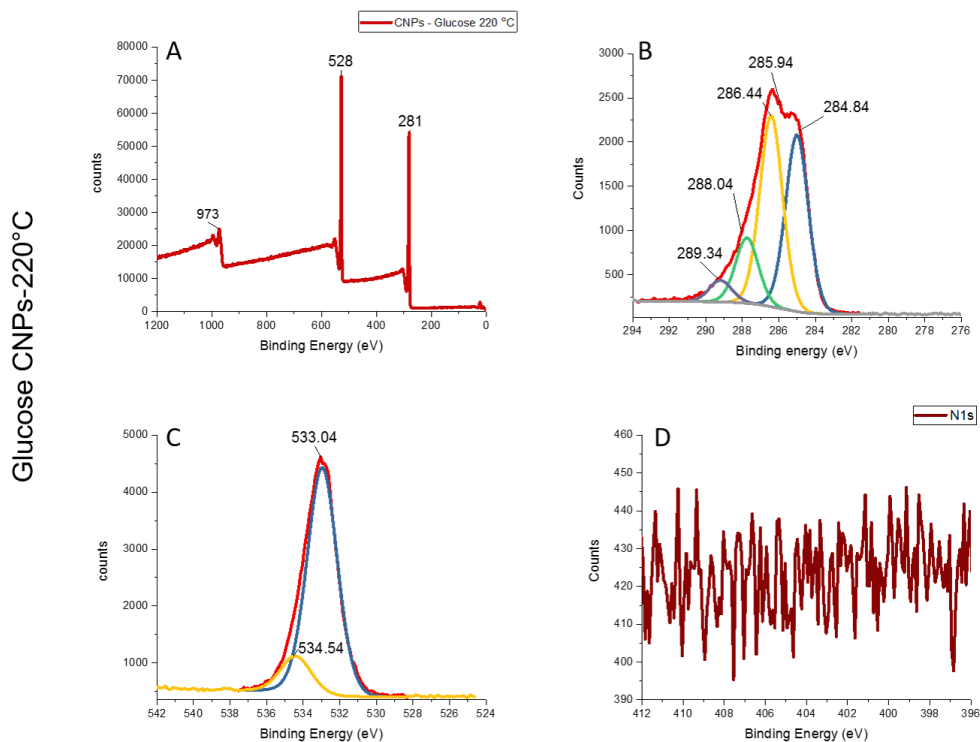


Figure 4.9. (A) XPS survey scan from Glucose-based synthesis at 220°C, (b) High-resolution XPS spectrum of C 1s scan from Glucose-based synthesis at 220 °C, (C) High-resolution XPS spectrum of O 1s scan, (D) High-resolution XPS spectrum of N 1s scan

Summary of overall XPS results are presented in Table 4.3. When considering only carbon and oxygen, the results indicate that the ratio between carbon to oxygen is approximately 4.4 for Alginate based CNPs and approximately 4 for Glucose CNPs. When the heating temperature increased by 20°C, the oxygen concentration is slightly increased which is expected. According to deconvoluted C 1s and O 1s peaks, there are four different chemical environments on Alginate CNPs while only two different chemical environments on Glucose CNPs. It is evident that carbonyl and hydroxyl groups are present for Alginate based CNPs while carbonyl and ether/hydroxyl groups are present for glucose based CNPs. These results along with the results of FT-IR spectra, it can be said that the carboxylic acids and ketone/aldehyde groups are present on Alginate CNPs while carboxylic acids are present on Glucose CNPs.

Table 4.3. Summary of elemental analysis of all the samples produced during this work.

Elements	CNPs -ALG			CNPs -Glucose		
	Binding energy	200°C (At %)	220°C (At %)	Binding energy	200°C (At %)	220°C (At %)
Na 1s	1067	1.65	1.40	1068	0.07	-

O1s	528	22.27	22.71	529	24.61	24.92
Ca2p	343	0.64	0.64	-	-	-
C1s	281	74.43	74.72	281	75.09	74.75
Cl2p	195	0.27	0.19	194	0.03	-
P2p	129	0.21	0	-	-	-
Si2p	99	0.53	0.27	98	0.20	0.33

4.2.8. Transmission electron microscopy (TEM)

The shape and size of carbon nanoparticles from glucose were studied by transmission electron microscopy (TEM) (Figures 4.10 and 4.11). For TEM analysis, samples dispersed in a solvent were deposited on a copper-coated grid before drying in air. The resulting nanoparticles were highly homogenous with a slightly oval shape caused by the interaction between neighbouring particles. The particles were highly agglomerated and formed linear carbon nanoparticle chains because of the high surface tension of the solvent. It proved difficult to isolate single carbon nanoparticles. For the samples at 200°C and, to a lesser degree, at 220°C, different contrasted small spherical particles were also found, which were likely to be due to unreacted or unsuccessful removal of the starting precursor after the dialysis. The average particle size calculated at 200°C was estimated to be 133.4 ± 22.8 nm, but this increased to 174.15 ± 30.8 nm after heating to 220°C. The absence of any lattice planes in the high-resolution images confirmed the amorphous structure of the nanoparticles (Figure 4.12A).

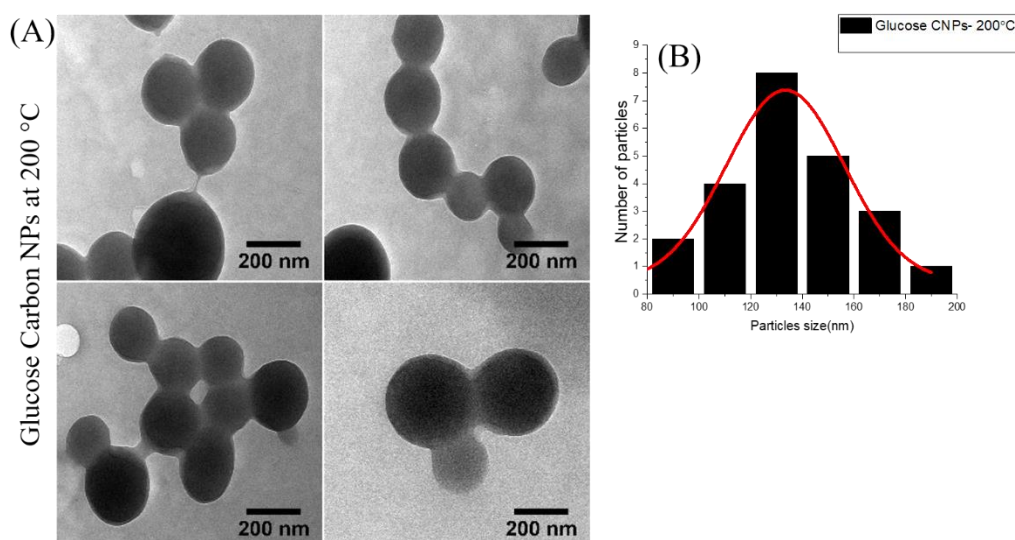


Figure 4.10. TEM images of carbon nanoparticles from glucose at 200°C (A) shows high resolution images from different particles and (B) shows the histogram of different particle sizes

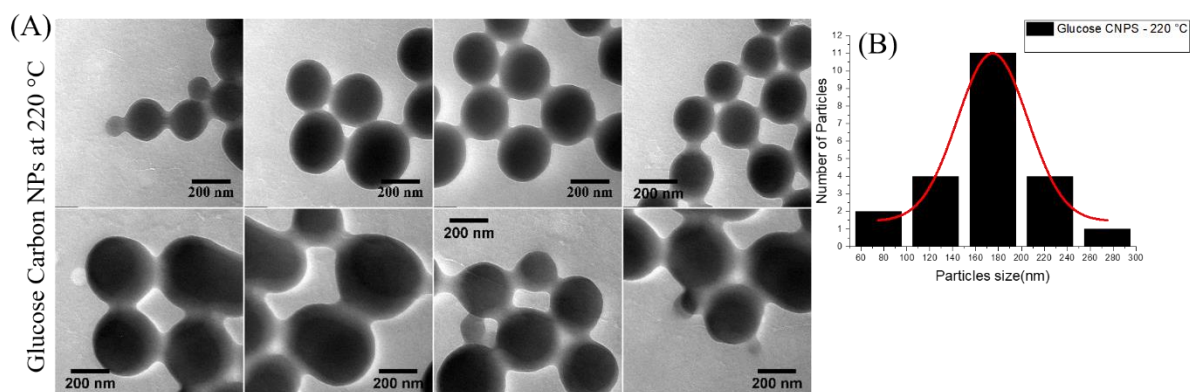


Figure 4.11. TEM images from glucose CNPs heated in the microwave at 220°C

In the bulk energy dispersive X-ray analysis, chemical analysis of materials was performed. Since EDX cannot detect light elements such as hydrogen, carbon and oxygen are the dominant peaks in the spectrum (Figure 4.12B). The result showed that the carbon nanoparticles were hydrocarbon products. Various impurities such as sodium, potassium or calcium were also detected, which was in-line with the above XPS results. A strong copper signal originates from the copper TEM grid. Suitable images could not be obtained for the sodium alginate samples, possibly due to the presence of excess carbon at the surface which resulted in the sample being charged under the working conditions.

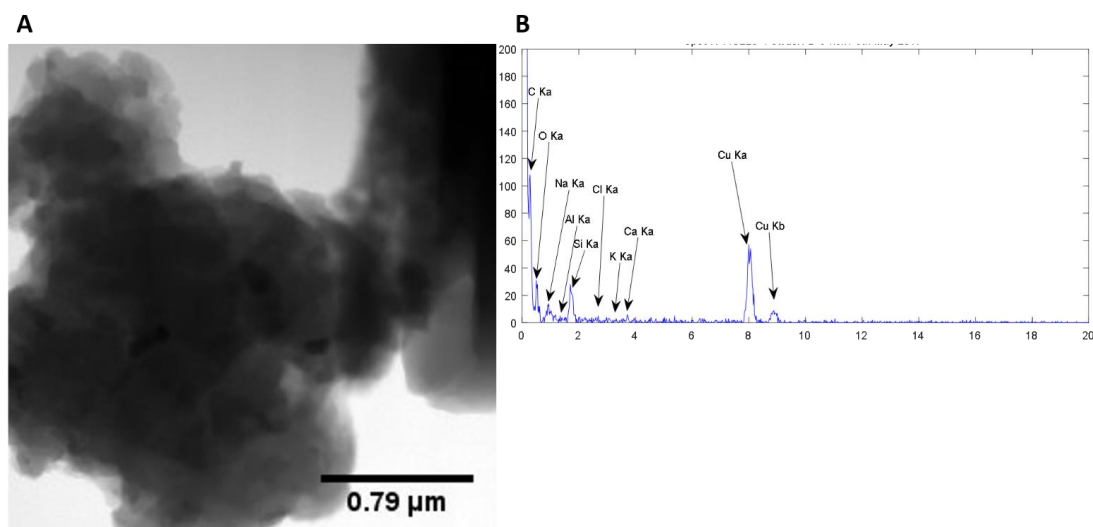


Figure 4.12. (A) A scanning transmission electron microscope (STEM) images for alginate CNPs at 200°C. (B) Energy Dispersive X-Ray Spectroscopy (EDX) spectrum analysis for alginate CNPs.

4.2.9. X-ray Powder Diffraction (XRD)

X-ray powder diffraction measurements of the resulting carbon nanoparticles were carried out in order to determine their crystallinity of the materials. Figure 4.13 shows the XRD pattern obtained. It is clear that there are no distinguishable diffraction patterns which confirms the amorphous nature of the deposited materials. This is further consolidated by the lack of lattice signals in the high-resolution TEM images, as seen above (Figure 4.12A).

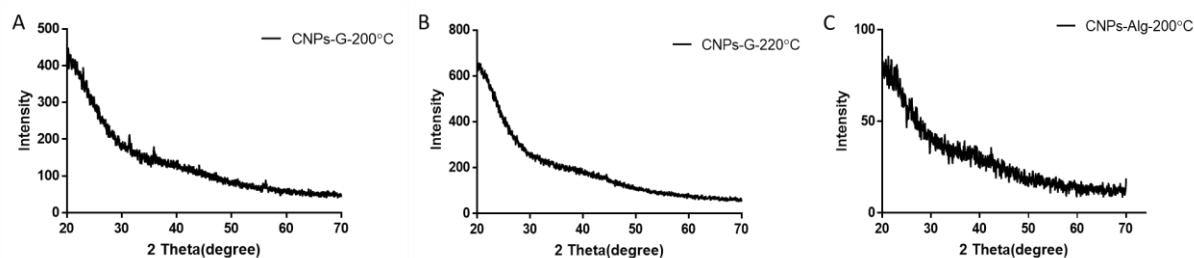


Figure 4.13. XRD patterns of synthesized CNPs (A) Glucose CNPs heated at 200°C (B) glucose CNPs heated at 220°C (C) alginate CNPs heated at 200°C.

4.2.10. Dynamic light scattering (DLS)

DLS measurements were found to give many diameters larger than expected for carbon dots and must be used in combination with others imaging techniques to measure the true, rather than hydrodynamic, diameter of the nanoparticles. The particle sizes and size distributions of the samples were estimated using dynamic light scattering (DLS) measurements. A typical result of dynamic light scattering measurements is shown in Figure 4.14. The correlation function shown in Figure 4.14A gives important information;

- (1) the quality of data – if the intercept (backward extrapolation of correlation function to Y axis) is larger than 0.1, the quality of the data is good.
- (2) The rate of correlation decay gives the idea of the particle size and number of particle distributions within a system.

Extended time to starting the decay clearly indicates the particle sizes are large. Two decay rates are visible in the graph, one is correlated with small particle distribution at around 50 nm, but the more significant distributions seem to have overlapped decay rates.

4.2.10.1. Dynamic light scattering result for glucose CNPs at 200°C and 220°C

Glucose CNPs treated at 200°C, resulted in two different well-defined narrow size distributions, each one presenting 50% of the number of total particles. On the other hand, at higher temperature, a single but very wide particle size distribution was resulted.

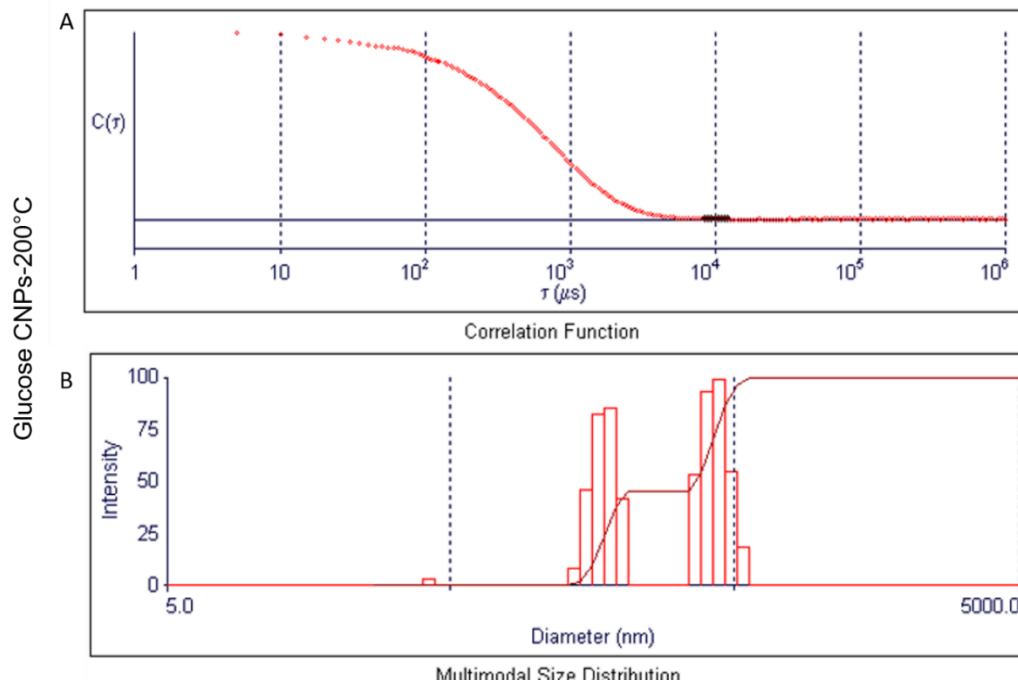


Figure 4.14. Dynamic light scattering (DLS) measurement of Glucose CNPs heated for 5 minutes at 200°C (a) correlation function and (b) the size distribution.

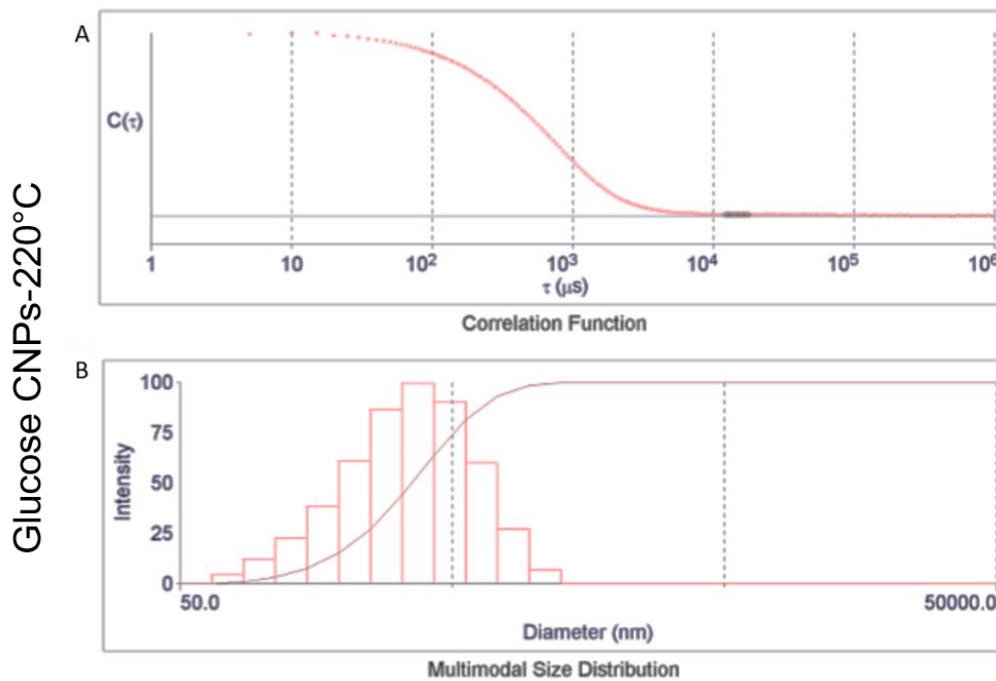


Figure 4.15. Dynamic light scattering (DLS) measurement of Glucose CNPs heated for 5 minutes at 220°C (A) correlation function and (B) the size distribution

4.2.11. Dynamic light scattering result for Alginate CNPs at 200°C and 200°C.

Alginate CNPs also produced a multimodal particle size distribution at 200°C and increasing the treatment temperature to 220°C, one particle size distribution with majority of the particles and alongside with small number of particles (<10%) separating as another distribution. In addition, it has been suggested that alginate could be present on the surface of nanoparticles and this interaction could agglomerate the nanoparticles to produce larger nanoparticle agglomerates. [111]

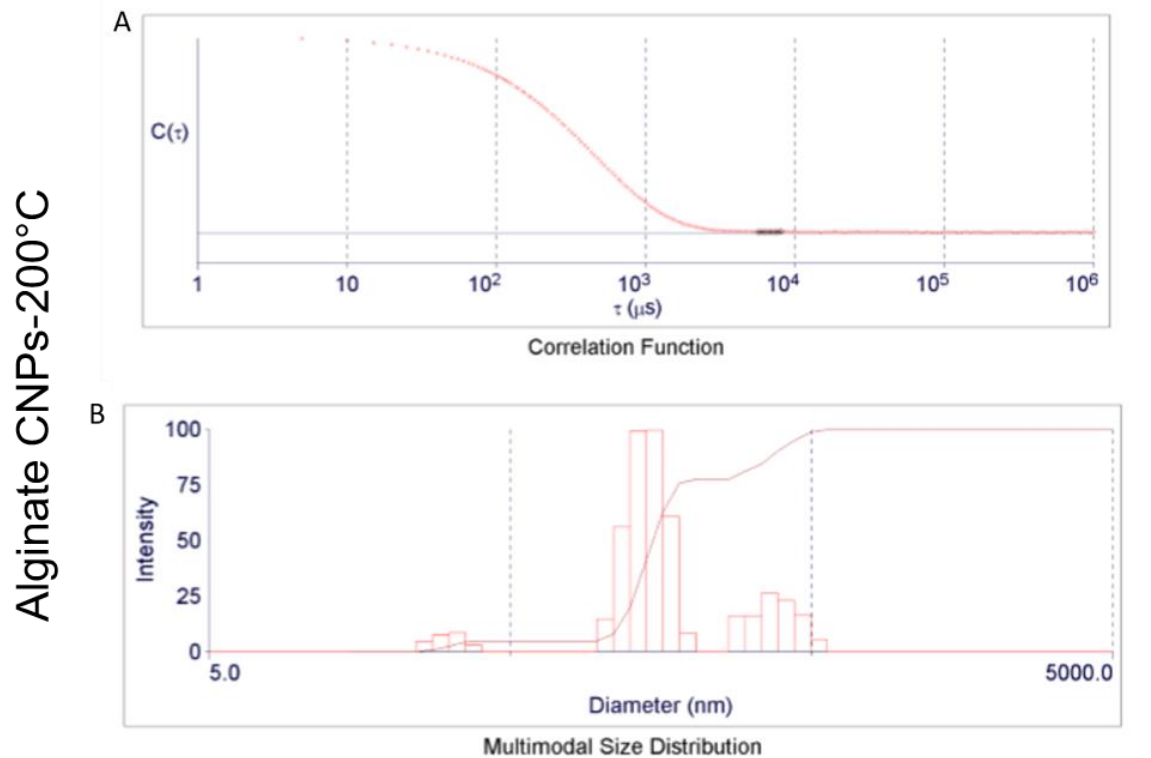


Figure 4.16. Dynamic light scattering (DLs) measurement of alginate CNPs heated for 5 minutes at 200°C (a) the correlation function and (b) the size distribution.

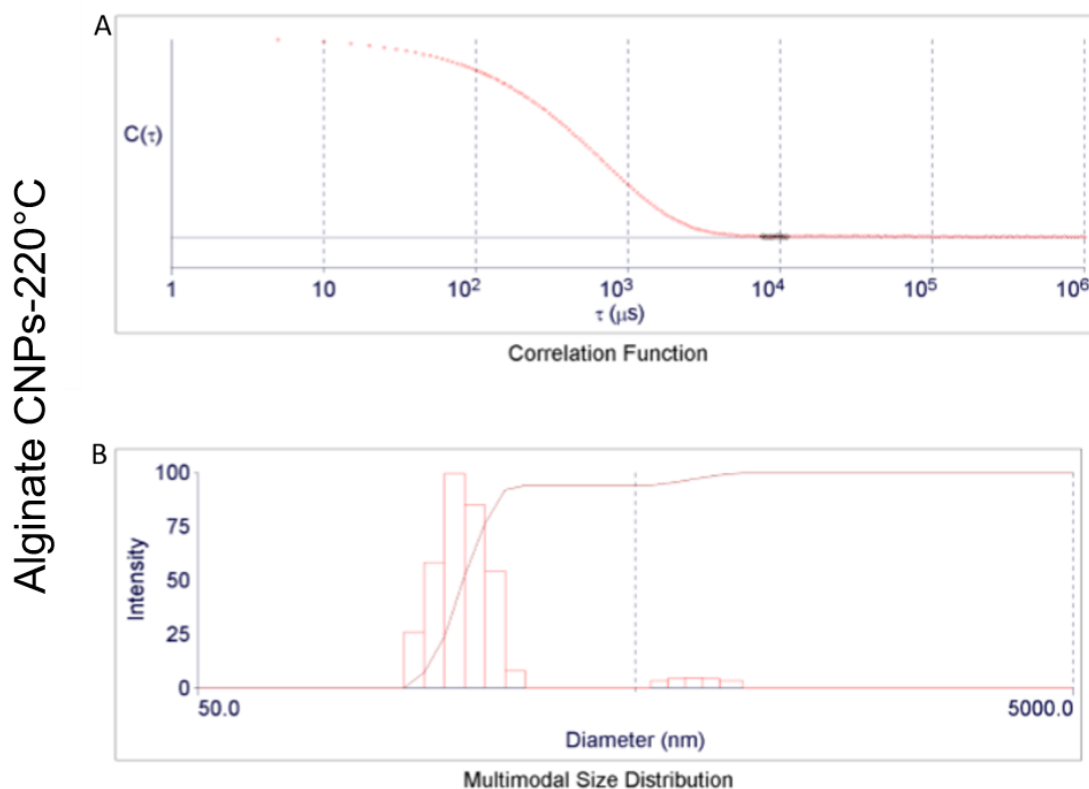


Figure 4.17. Dynamic light scattering (DLS) measurement of alginate CNPs heated for 5 minutes at 220°C. (a) correlation function and (b) the size distribution.

Comparison of the average size of nanoparticles synthesised at 200°C, reveals that the average diameter (247 nm) for the glucose samples is much larger than that of the alginate samples (145 nm). On the other hand, the polydispersity index (PDI) for nanoparticles prepared from glucose was low (0.19) relative to its alginate counterpart (0.21). In general, a narrow PDI is desired since this is indicative of a narrow size distribution, and thus more uniform nanoparticles. The data clearly implies that the choice of solvent had a profound impact on the size and distribution of the resulting nanoparticles. It is important to point out that the broad size distribution and larger particle size during the DLS measurements mask small carbon nanoparticles in the size distribution which is associated with inherent properties of the technique. An increase in the growth temperature to 220°C resulted in large particle sizes due to the Ostwald ripening process. The particle sizes were increased to 386 nm (PDI = 0.27) and 289 nm (PDI = 0.28) for glucose- and alginate-based samples, respectively.

4.3. Summary

In this chapter, highly fluorescent carbon nanoparticles were successfully synthesised in a single-step using microwave radiation, allowing control over the growth parameters due to uniform heating. For the synthesis, commonly found low-cost polysaccharide precursors, glucose and sodium alginate, were heated at growth temperatures of 200 and 220°C. For the glucose-based samples, a strong absorption peak was observed in the UV region and their wavelengths remained unchanged. Switching to a sodium alginate solvent, a broad peak shifted to higher wavelength once the sample was heated to 200°C, presumably due to the different chemical composition. Interestingly, increasing the processing temperature to 220°C did not yield any absorption peak. The fluorescence properties of carbon nanoparticles were found to be dependent on the excitation energies and their dominant peaks were located at different positions. Commonly, the peak positions red shifted with reduced intensity as the excitation energy value increased. For the Raman measurements, dominant peaks were found to be typical of D- and G-bands. The IR studies supported the presence of hydroxyl and carboxylate groups at the nanoparticle surfaces. The XPS findings revealed multiple species of oxygen and carbon. Moreover, the measurements also supported the formation of purer samples from glucose.

The TEM analysis showed the presence of non-spherical, highly aggregated particles, with decreased particle sizes at higher temperatures. The XRD measurements confirmed the amorphous nature of the as-prepared carbon nanoparticles. This was also confirmed by the absence of lattice planes in the HR-TEM image of nanoparticles. For a set temperature, the average particle size for glucose was much larger than for the alginate samples and demonstrated a narrower size distribution. These findings suggest potential for the development of a facile and cost-effective strategy for the preparation of highly fluorescent carbon nanoparticles and provide a useful avenue for sensing and biomedical applications.

Chapter Five: Assessment of toxicity

5. Chapter Five: Toxicity Assessment of Carbon Nanoparticles.

5.1. Introduction

Engineered nanoparticles' (NPs) unique optoelectronic properties have found applications in various fields including bio-imaging, sensing, solar cells, and light emitting diodes, driving worldwide interest. As the consumption of NPs increases, human exposure to various types of nanomaterials will inevitably increase as well. Nanomaterials may harm the environment and toxicologically effect animals including humans. Different types of NPs are expected to behave differently once inside a biological system; it is imperative to know what exactly is being tested under exposing cells. Therefore, NPs must be properly characterised in toxicological research. Moreover, it is vital to understand the interactions between NPs with biological entities such as DNA, proteins, membranes, tissues, and organs which will establish communications between NPs and biological systems.

To use the full spectrum of nanobiotechnology and nanomedicine, researchers must understand nanomaterial physicochemical properties in-depth, which will guide them to control nano–bio interfacial interactions (communication of nanomaterials with the biological world). Designing nanomaterials with distinctive properties will help overcome their potential hazards so that they can be used for safe therapeutic applications. The most commonly used semiconductor quantum dots with outstanding photoluminescent properties contain cadmium, lead, and tellurium, components which have raised concerns about in vivo toxicity and harmful environmental impact [112]. Photobleaching of organic dyes and cytotoxicity associated with semiconductor quantum dots have limited their use for cellular or sub-cellular labelling of cells. Researchers are cautious regarding biological and medical applications of quantum dots. It is worth noting that the quality of photoemission is dictated by the choice of solvent, any defect states and the presence of functional group at the surface of NPs [113].

The carbon NPs-based system serves as a good alternative to nuclear staining due to non-photobleaching, multi-photon emission, and good cellular distribution [114]. The synthesis of carbon NPs involves the use of low-cost precursors which do not contain toxic heavy metals. The surface of carbon NPs often contain carboxylic acid functionalities which help to increase their water solubility character and can be further substituted with other coordinating ligands having a variety of inorganic, organic, polymeric or biological moieties. Their well-defined morphology, nanoscale dimensions, ability for chemical functionalisation and a variety of inexpensive precursors and synthesis routes provide a favourable platform from

which carbon NPs can be tuned between ultraviolet and infrared regions. For example, by altering the amount of nitrogen during the solvothermal synthesis, carbon NPs exhibiting blue, green, and red colours can be produced. Additionally, by modifying reaction parameters during the synthesis, a continuous red shift due to quantum confinement has been noted [114]. Using water as a reaction medium, carbon NPs with full-colour emission are produced which demonstrates their potential for bio imaging, both in vitro and in vivo [115].

As mentioned earlier, the synthesis and processing of carbon NPs is straightforward and does not involve expensive precursors. Carbon NPs can be produced from polysaccharides such as sodium alginate, glucose or sucrose via a number of readily available synthetic processes. Indeed oxidation and reduction of glucose, sucrose and alginate affects the photoluminescence properties due to different structures of saccharides involved [116]. As expected, the shape, size and particle distribution depend on the growth parameters, solution concentration and growth temperature [116]. It is expected that the key to creating successfully fluorescent carbon NPs which can be translocated within cells depends on number of factors, including passivating ligand, diameter, and carbon source.

The chapter aims is to assess and determine the cell metabolic activity and toxicity effects (if any) of carbon NPs on human cells. The fate of carbon NPs generally depends on multiple factors such as local anatomy, physiology of the exposure route, surface and physical properties of NPs [117]. These factors may affect their potential toxicity both in vitro and in vivo. It is expected that the NPs, by virtue of their attachment to a variety of molecules, are capable of exerting (cyto)toxic effects. This makes the surface chemistry of NPs of immense importance in determining the toxicity. Several surface-related factors including crystallinity, surface charge, surface adsorption of other molecules like protein have been linked to the toxicity of NPs [118].

From the physical properties of NPs, two parameters are critical in assessing their behaviour [119]. 1) Due to their small size, the NP can get access to parts of the cells inaccessible to larger particles; 2) The ratio of the length and width of the nanomaterial (aspect ratio) has been found to be important in determining cytotoxicity. High aspect ratio nanomaterials like carbon nanotubes, can induce cytotoxic effects and induce inflammatory responses, as has been reported in the literature, in a similar way to silicosis, in human lungs [120]. NPs also form stable colloidal suspensions in liquids and biological cell culture mediums which are related to their surface characteristics. Depending on variations in their local environment such as concentration, dispersion medium, sonication, or presence of protein, NPs can either

exist in a monodispersed or agglomerated form [121]. Interestingly, the agglomeration phase of the NP had been found to influence cellular interactions and toxicity [120, 121].

5.2. Statistical analysis

The data is expressed as the means \pm SD. Significant differences among multiple groups were determined using a two-way analysis of variance (ANOVA) followed by Tukey's post-hoc tests. Probabilities of $P < 0.05$ were considered statistically significant. All these tests were conducted using GraphPad Prism 4 (GraphPad Software, USA). In the cell scratch, the data mean standard error of the mean values were used to study the significance between the control and human dermal fibroblasts (HDF) and C8161 incubated with carbon nanoparticles followed by Tukey's multiple comparisons test ' $P < 0.05$ were also considered.

5.3. Results and Discussion.

5.3.1. Toxicity study of Alginate CNPs in Human Dermal Fibroblast cells.

The study examined the toxicity of CNPs from both alginate and glucose CNPs at 200°C and 220°C in Human Dermal Fibroblast cells.

Figure 5.1 shows the effect of using alginate CNPs heated at 200 and 220°C in the live cells. Absorbance values were measured as function of added CNP concentration after 24, 48 and 72hrs of incubation. The data used to deduce the relative cell viability as a function of CNP concentration and over a period of three days.

For CNPs at 200°C, the absorbance values stay approximately constant regardless the added CNP concentration for the samples incubated for 24 hrs and 72 hrs. The samples incubated for 48hrs show higher absorbance values compared to other two sets of samples and decreasing absorbance when increasing the CNP concentration. Considering the relatively cell viability, only samples with 10 $\mu\text{g/ml}$ added CNPs seems to have slightly lower values.

For CNPs at 220°C, the samples incubated for 24 hrs, show absorbance of 0.5 while samples incubated for 48hrs and 72hrs, start at absorbance of 1 and decrease with increasing concentration of added CNPs. The relative cell viability decreases with increasing the added CNP concentration. After 72hrs incubation, the samples with 200 and 250 $\mu\text{g/ml}$ concentration of CNPs show lowest relative cell viability at 45% and 53%, respectively.

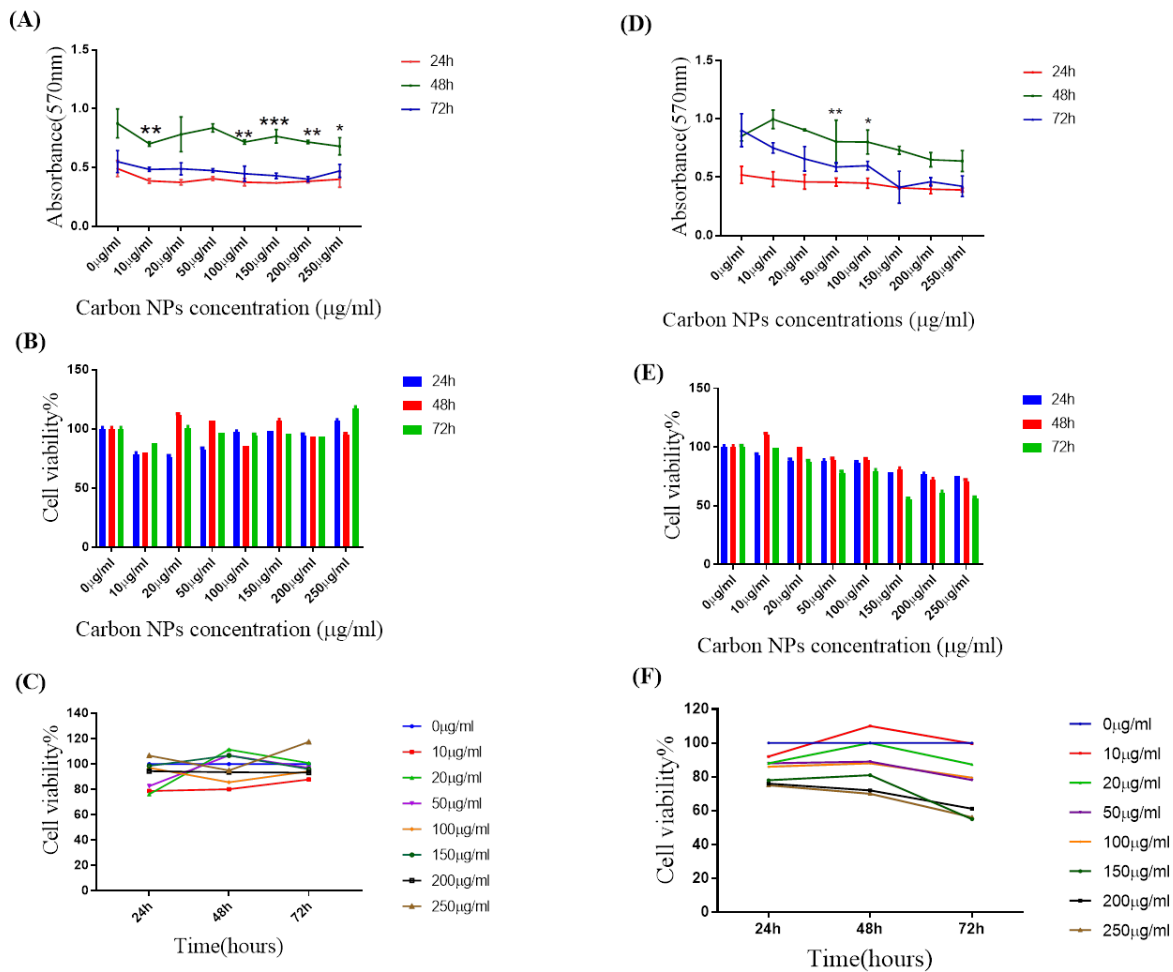


Figure 5.1. Cytotoxicity studies of alginate CNPs Human Dermal Fibroblast cells. (A,D) absorbance value against the concentration of CNPs (B,E) relative cell viability against the concentration of CNP and (C,F) Relative Cell viability against time. (A,B and C) alginate CNPs at 200°C. (D,E and F) alginate CNPs at 220 °C.

In order to verify the significance of the above discussed results, statistical analysis was carried out on the data and the results are presented in Table 5.1. Results are analysed by using a two-way ANOVA mean \pm SD of at least three independent experiments. Statistically significant difference determined by (* $p < 0.05$, ** $p < 0.01$, and *** $p < 0.001$) between each concentration and Control (cells and medium without carbon nanoparticle).

Reduction in the cell viability after 72 hrs relative to the control is proved to be significant with the p -value < 0.001 .

Table 5.1: Cell viability evaluation (resazurin assays) after 24, 48, and 72h of incubation with fibroblasts and increasing concentrations of alginate CNPs.

Sample	Incub. time	10µg/ml	20µg/ml	50µg/ml	100µg/ml	150µg/ml	200µg/ml	250µg/ml
CNPs at 200°C	24h	Ns	ns	ns	ns	ns	ns	ns
	48h	Ns	**	**	ns	*	ns	ns
	72h	****	****	****	****	****	****	****
CNPs at 220°C	24h	Ns	ns	ns	ns	ns	ns	ns
	48h	*	ns	ns	ns	ns	ns	ns
	72h	Ns	*	***	**	****	****	****

5.3.2. Toxicity study of glucose CNPs in Human Dermal Fibroblast cells.

Figure 5.2 shows the effect of using glucose CNPs heated at 200 and 220°C in the live cells. Like in the case of alginate CNPs, absorbance values were measured as function of added CNP concentration after 24, 48 and 72hrs of incubation. The data used to deduce the cell viability as a function of CNP concentration and over a period of three days.

For CNPs at 200°C, the absorbance values stay approximately constant regardless the added CNP concentration for all the samples. However, the samples incubated for 48hrs show higher absorbance values compared to other two sets of samples. Unlike for the alginate samples, the relatively cell viability, decreases for all the samples incubated 24hrs. Surprisingly, for samples incubated 48 hrs and 72hrs, cell viability increases.

Glucose CNPs at 220°C indicate similar absorbance behaviour to low temperature samples. However, the relative cell viability is much improved for the higher temperature samples compared to those heated at 200°C. The reduction shown in relative cell viability for the samples incubated 24hrs, seems to recover after 48hrs except for the two highest added CNP concentrations where the values are in the range of 80 to 90%.

The cell viability in carbon nanoparticles from glucose demonstrated less toxicity compared with the cell viability for the alginate samples.

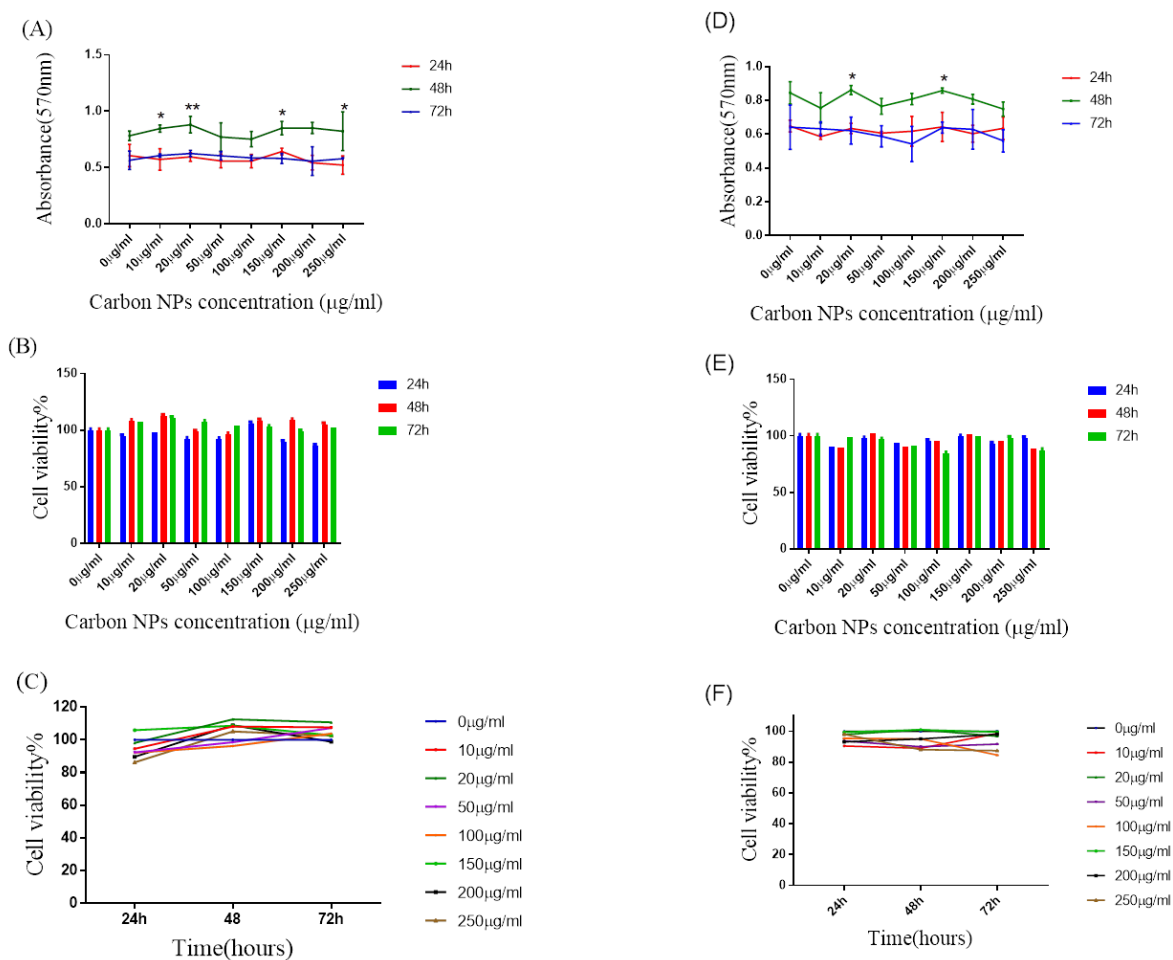


Figure 5.2. Cytotoxicity studies of glucose CNPs Human Dermal Fibroblast cells. (A,D) absorbance value against the concentration of CNPs (B,E) relative cell viability against the concentration of CNP and (C,F) Relative Cell viability against time. (A,B and C) glucose CNPs at 200°C. (D,E and F) glucose CNPs at 220 °C.

Like with results of the alginate CNP samples, statistical validation was carried out on the data and the results are presented in Table 5.2. Results were analysed by using a two-way ANOVA mean \pm SD of at least three independent experiments. Statistically significant difference determined by (* $p < 0.05$, ** $p < 0.01$, and *** $p < 0.001$) between each concentration and the positive control (cells and medium without carbon nanoparticle). Statistical analysis shows no significance in the data at different concentration or at different incubation time.

Overall data indicates that the relative cell viability in carbon nanoparticles from glucose demonstrated less toxicity compared with the cell viability for the alginate samples.

Table 5.2: Cell viability evaluation (resazurin assays) after 24, 48, and 72h of incubation with fibroblasts and increasing concentrations of glucose CNPs.

Sample	Incub. time	10µg/ml	20µg/ml	50µg/ml	100µg/ml	150µg/ml	200µg/ml	250µg/ml
CNPs at 200°C	24h	ns	ns	ns	ns	ns	ns	ns
	48h	**	***	ns	ns	**	**	*
	72h	***	****	****	****	****	****	****
CNPs at 220°C	24h	ns	ns	ns	ns	ns	ns	ns
	48h	ns	ns	ns	ns	*	ns	ns
	72h	ns	ns	ns	**	ns	ns	*

5.3.3. Toxicity studies of alginate CNPs on melanoma C8161 cells

Toxicity studies of alginate CNPs on melanoma C8161 cells carried out and results are shown in Figure 5.2. Absorbance values were measured as function of added CNP concentration after 24, 48 and 72hrs of incubation. The data used to deduce the cell viability as a function of CNP concentration and over a period of three days.

For CNPs at 200°C, the absorbance values stay approximately constant regardless the added CNP concentration only for the samples incubated for 24hrs. The other two samples behave differently; the samples incubated for 48hrs, absorbance starts at around 0.6 for the control sample, but increases up to 1 when concentration of CNP increases. The samples incubated for 72hrs behave opposite manner, starting at about 0.9 absorbance to decrease to about 0.6 while the added CNP concentration increases. The relative cell viability data shows 100% relative cell viability for the samples incubated for 24hrs, then an increase in value for the samples incubated for 48 hrs. Finally, the relative cell viability decreases below 80% for all the samples incubated for 72 hrs. At added CNP concentrations of 200 and 250 µg/ml, the relative cell viability values are the lowest at approximately 60%.

For CNPs at 220°C, the samples incubated for 24 hrs and 48hrs, show absorbance of 0.8 to 0.9 which stays constant regardless the added concentration of CNP while for samples incubated for 72hrs, the absorbance starts at around 1.2, and sharply decreases with added CNP concentration until the concentration reaches 100 µg/ml and then plateaus off.

The relative cell viability stays constant for all the samples incubated for 24hrs and 48hrs regardless the added CNP concentration. After 72hrs incubation, however, the relative cell viability decreases gradually with increasing concentration of CNPs. For the sample with 10 $\mu\text{g/ml}$ CNPs, the relative cell viability value decreases to 85% and reaching below 70% for the samples with 150 and 250 $\mu\text{g/ml}$ of CNPs.

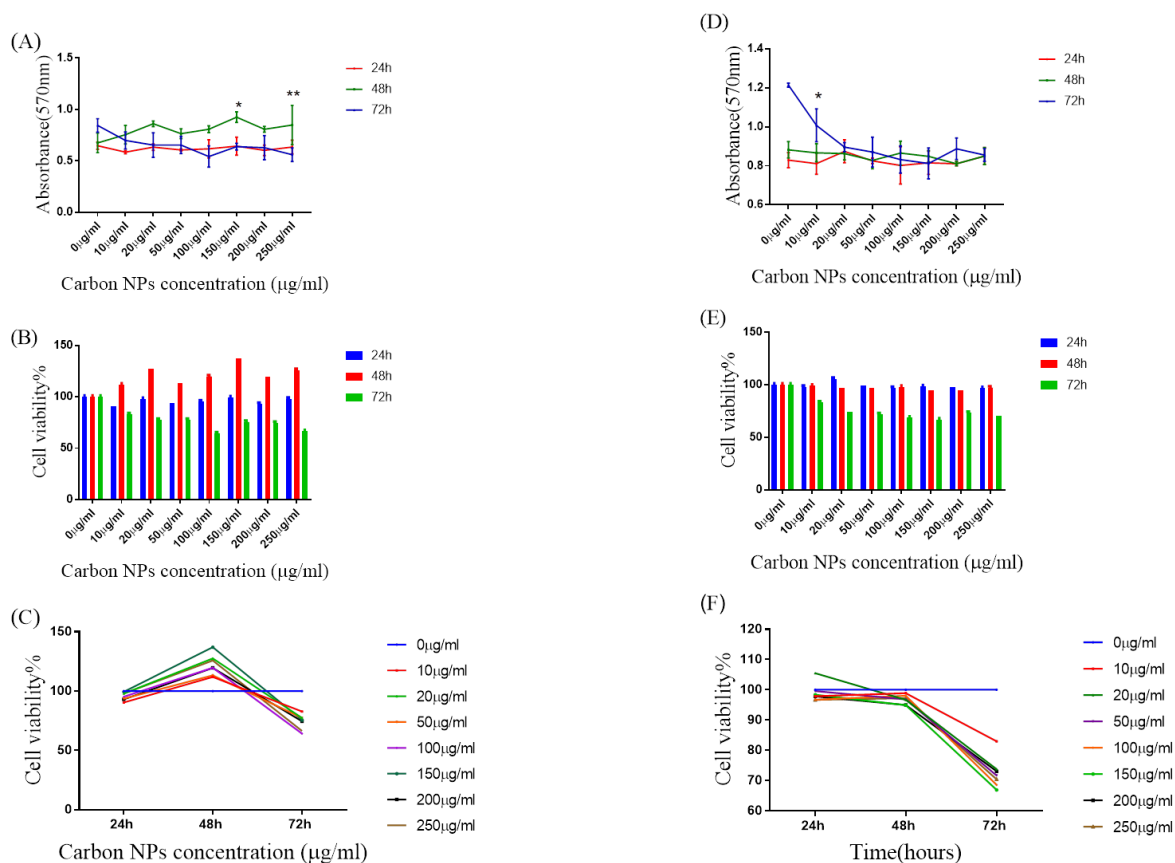


Figure 5.3. Cytotoxicity studies of alginate CNPs on Melanoma Cancer (C8161) cells. (A,D) absorbance value against the concentration of CNPs (B,E) relative cell viability against the concentration of CNP and (C,F) Relative Cell viability against time. (A,B and C) alginate CNPs at 200°C. (D,E and F) alginate CNPs at 220 °C.

As previously, the significance of the data was analysed by using a two-way ANOVA mean \pm SD of at least three independent experiments. The results are presented in Table 5.3.

For the samples with added CNP produced at 200°C, the statistical analysis shows no significance in the data at different concentration or at different incubation time. On the other hand, for the samples with added CNPs at 220°C and incubated for 72hrs, the reduction in the cell viability vs CNP concentration relative to the control is proved to be significant with the p-value < 0.001.

Table 5.3: Cell viability evaluation (resazurin assays) after 24, 48, and 72h of incubation with Melanoma Cancer (C8161) cells and increasing concentrations of alginate CNPs.

Sample	Incub. time	10µg/ml	20µg/ml	50µg/ml	100µg/ml	150µg/ml	200µg/ml	250µg/ml
CNPs at 200°C	24h	ns	ns	ns	ns	ns	ns	ns
	48h	ns	ns	ns	ns	ns	ns	ns
	72h	ns	ns	ns	**	ns	ns	ns
CNPs at 220°C	24h	ns	ns	ns	ns	ns	ns	ns
	48h	ns	ns	ns	ns	*	*	***
	72h	**	****	****	****	****	****	****

5.3.4. Toxicity studies of glucose CNPs on melanoma C8161 cells.

Figure 5.4 show the results of toxicity studies of glucose CNPs on melanoma C8161 cells. Absorbance values were measured as function of added CNP concentration after 24, 48 and 72hrs of incubation. The data used to deduce the cell viability as a function of CNP concentration and over a period of three days.

For CNPs at 200°C, the absorbance values were slightly decreasing with increasing the added CNP concentration only for all the samples. The relative cell viability data for 24hrs incubated samples stays above 100%, but for the samples incubated 48hrs and 72hrs, slight decrease in values vs concentration of added CNPs.

For CNPs at 220°C, the absorbance behaviour found to be like the samples with CNPs at 200°C. This is also true for the relative cell viability results, however, reduction in cell liability is much higher for CNPs at 220°C compared to the CNPs at 200°C. In summary, the CNPs synthesised from glucose at 200 and 220°C showed less toxicity, even at a higher concentration (250 µg/ml).

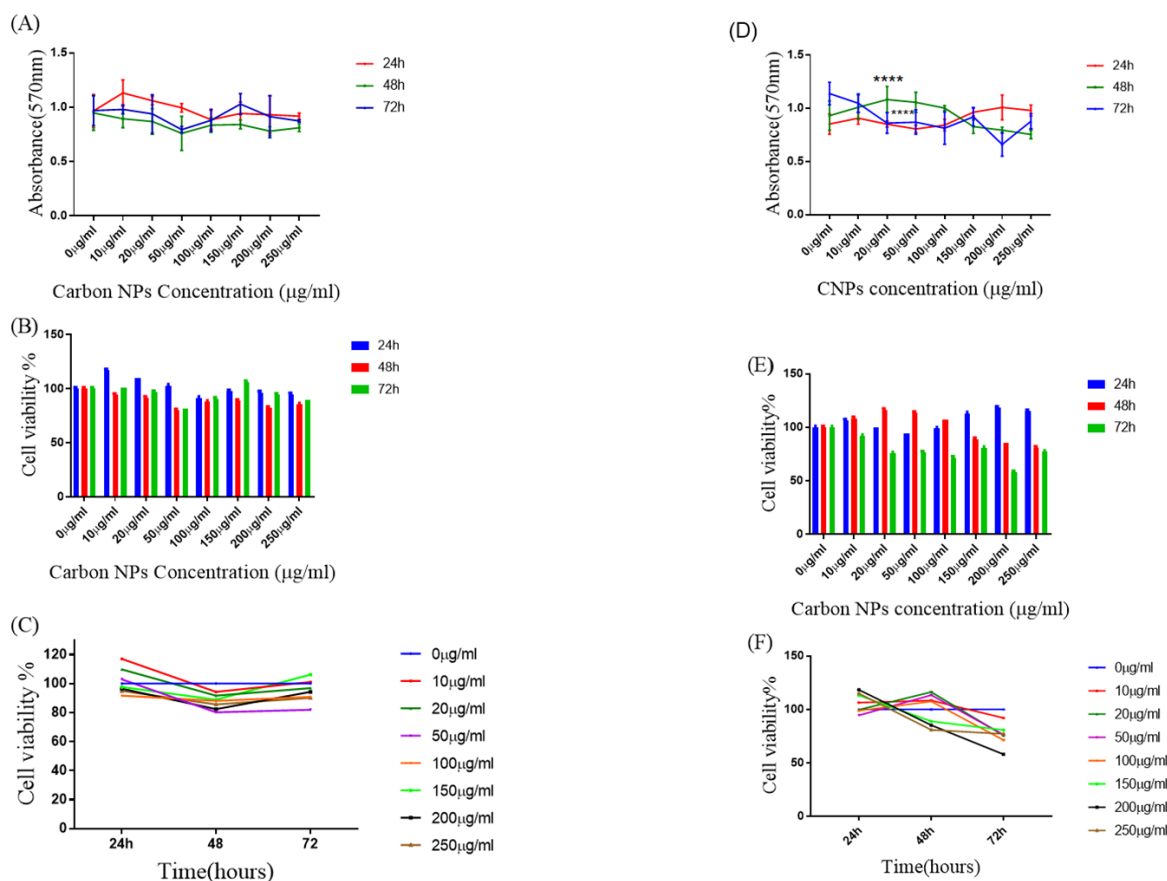


Figure 5.4. Cytotoxicity studies of glucose CNPs on Melanoma Cancer (C8161) cells. (A,D) absorbance value against the concentration of CNPs (B,E) relative cell viability against the concentration of CNP and (C,F) Relative Cell viability against time. (A,B and C) glucose CNPs at 200°C. (D,E and F) glucose CNPs at 220 °C.

The statistical analysis of the results is presented in Table 5.4. For all the samples studied, statistical analysis shows no significance in the data at different concentration or at different incubation time.

Table 5.4: Cell viability evaluation (resazurin assays) after 24, 48, and 72h of incubation with Melanoma Cancer (C8161) cells and increasing concentrations of glucose CNPs.

Sample	Incub. time	10µg/ml	20µg/ml	50µg/ml	100µg/ml	150µg/ml	200µg/ml	250µg/ml
CNPs at 200°C	24h	ns	ns	ns	ns	ns	ns	ns
	48h	ns	ns	ns	ns	ns	ns	ns
	72h	ns	ns	ns	ns	ns	ns	ns
CNPs at 220°C	24h	ns	ns	ns	ns	ns	ns	ns
	48h	ns	ns	ns	ns	*	ns	ns

220 ⁰ C	72h	ns	ns	ns	**	ns	ns	*
--------------------	-----	----	----	----	----	----	----	---

5.4. Wound healing study

Another method used to assess the biocompatibility of CNPs when interacting with cells is a cell scratch assay. The method is modelled upon the fact that a ‘scratch’, which is a new artificial gap, is formed on a confluent cell monolayer. A scratch, or gap, develops when the area’s cells are removed or physical exclusion occurs in a monolayer due to various methods, such as chemical, mechanical, or thermal damage. After this, images are captured at the beginning and at regular intervals to monitor cell migration in the gap’s direction. These images are then compared to calculate the cell migration rate. As this assay is versatile and convenient, it can be used for several purposes and achieve better results on a high throughput screen platform. Wound-healing assay data was acquired after calculation in ImageJ. The WH_NJ macro was validated by evaluating its precision in the detection and calculation of areas related to wounds made in the cell monolayer.

5.4.1. Image capture and data analysis

Images at time zero (t = 0 h) were captured to record the initial area of the wounds, and the recovery of the wounded monolayers due to cell migration toward the denuded area was evaluated different time points. The images were captured using an optical microscope (10× objective) equipped with a Motic digital camera. The area of wound was quantified by Image J software (NIH, USA) using the polygon selection mode. The migration of cells toward the wounds was expressed as percentage of wound closure.

5.4.2. Wound healing Scratch assay in Melanoma C8161

Figures 5.10-5.13 show the phase contrast between optical micrographs of the cultured melanoma (C8161) incubated with CNPs from glucose and alginate produced at different temperatures. The scratch assay was used and observed at 0, 1, 2, and 24h. At zero hours, the distance between two regions became evident where melanoma cells at 90% confluence were separated by pipette tips. The figures show that there was no significant difference between the control with the medium and CNPs incubated with glucose and alginate. The cells, the control, and cells with particles experienced a rapid movement in the first hour. The smaller distance was observed after 2h when the cells were incubated with the CNPs; the distance is much wider in the control group. After 24h, the scratch region was completely closed from both sides. It was previously reported that melanoma C8161 has a 20h doubling time. When the melanoma was incubated with glucose at 200°C, the cells treated with the particles migrated faster than the control. This result is in line with a previous study where onion carbon dots lead the cells to migrate faster than the control [94].

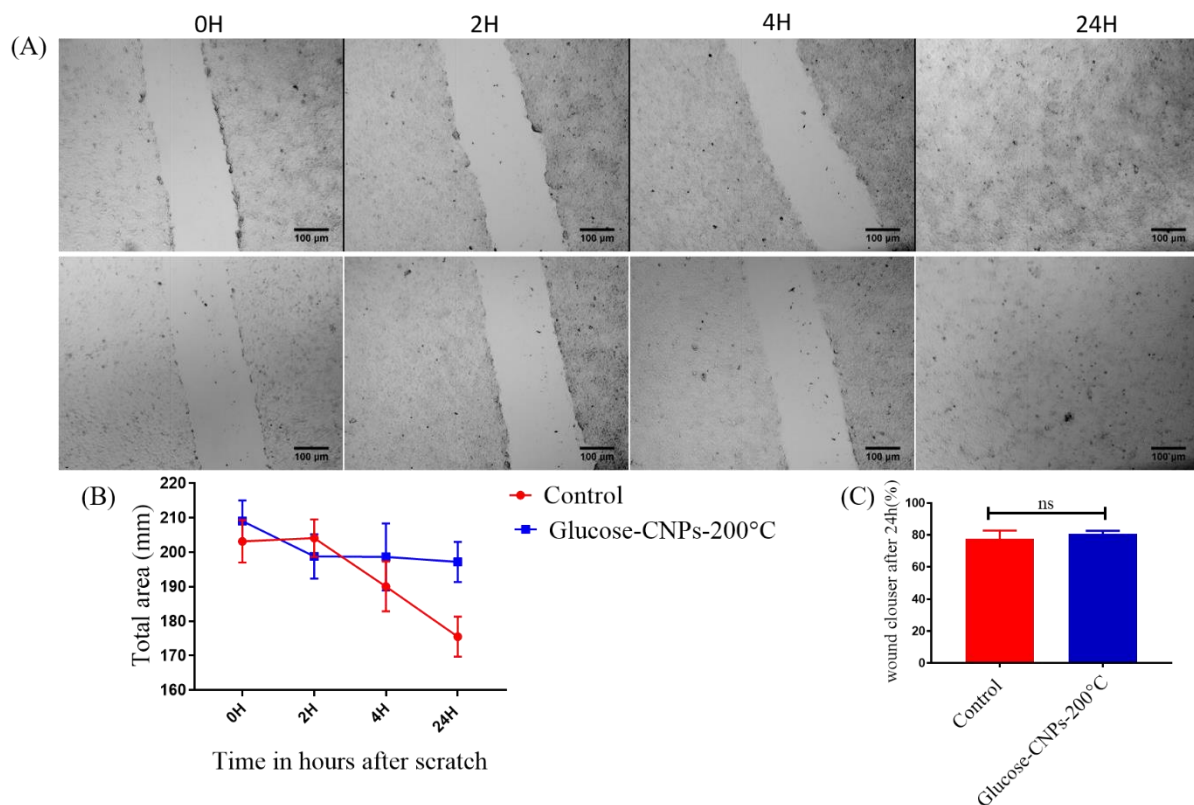


Figure 5.2. A) Wound healing assay in melanoma cancer cells forming a confluent monolayer. 100 mg/ml CNPs from glucose at 200°C was added to the cells and incubated for different durations; the images were taken at each time point (B) Quantification of total area analysis and (C) Statistical analysis expressed as percentage of wound closure.

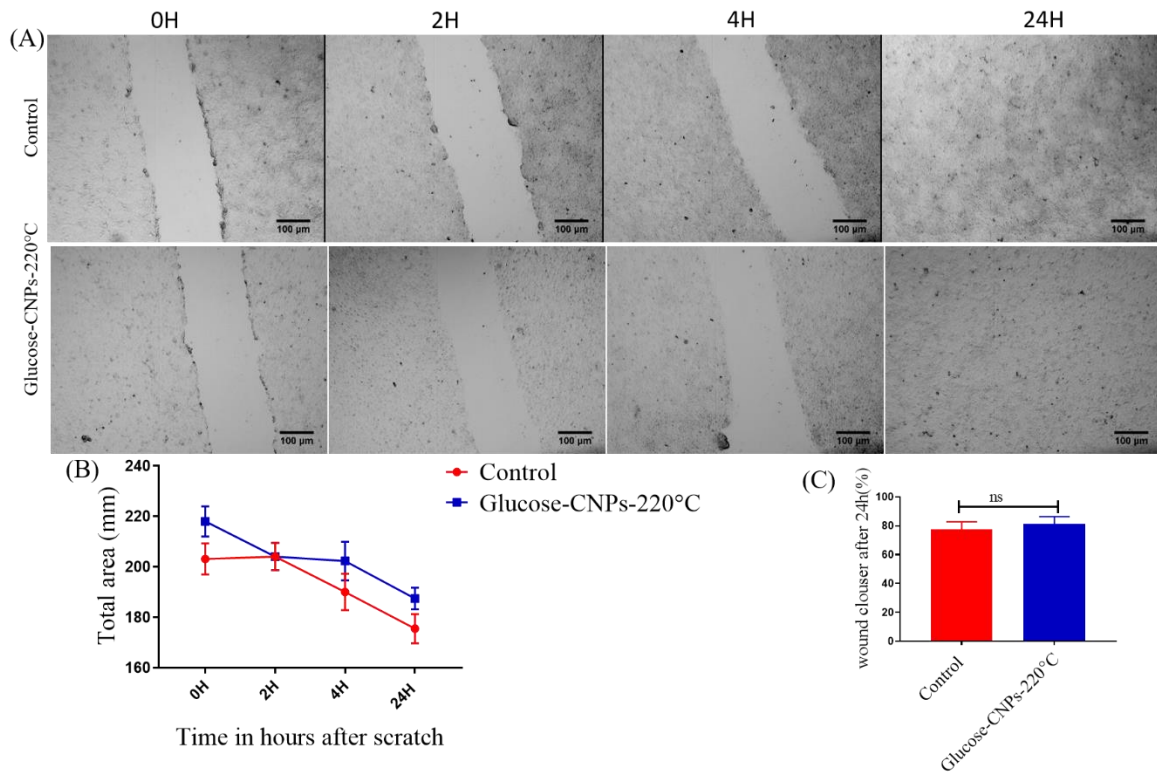


Figure 5.3. (A) Wound healing assay in melanoma cancer cells forming a confluent monolayer. 100 mg/ml CNPs from glucose at 220°C was added to the cells and incubated for different durations; the images were taken at each time points. (B) Quantification of total area analysis and (C) Statistical analysis expressed as percentage of wound closure

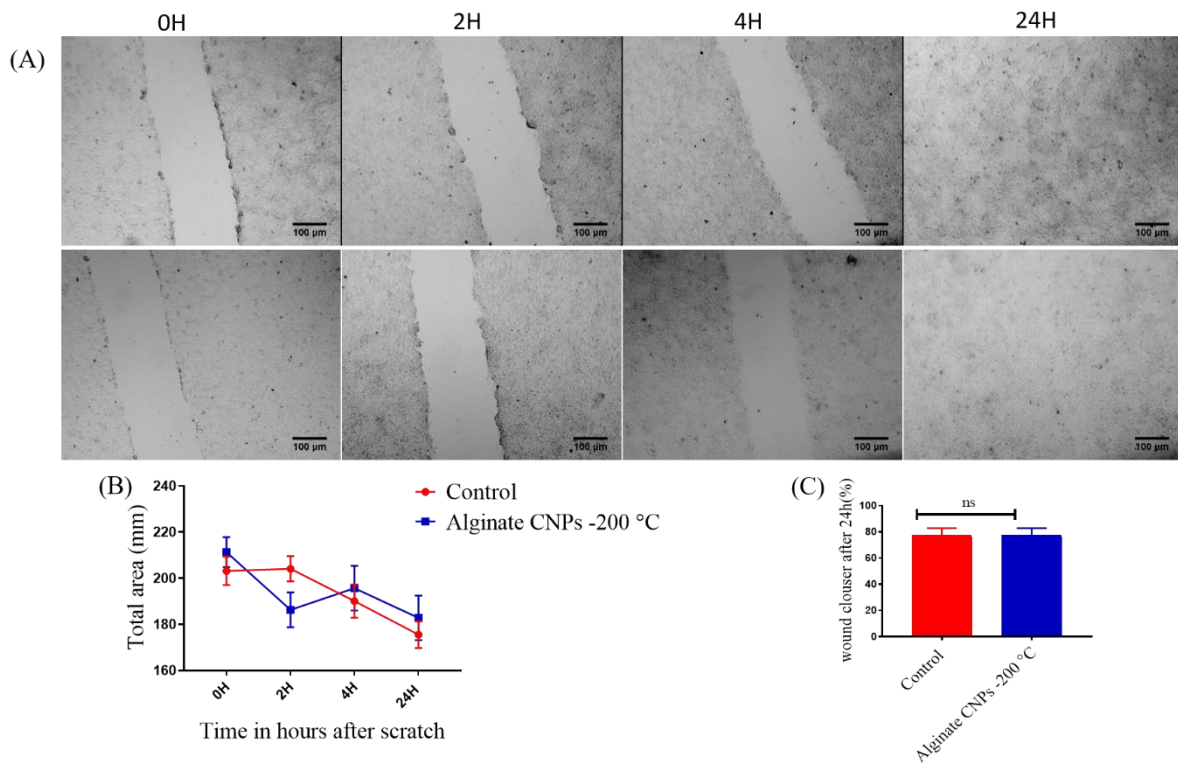


Figure 5.4. Wound healing assay in melanoma cancer cells forming a confluent monolayer. 100 mg/ml CNPs from alginate at 200°C was added to the cells and incubated for different durations; the images were taken at each time points, (B) Quantification of total area analysis and (C) Statistical analysis expressed as percentage of wound closure.

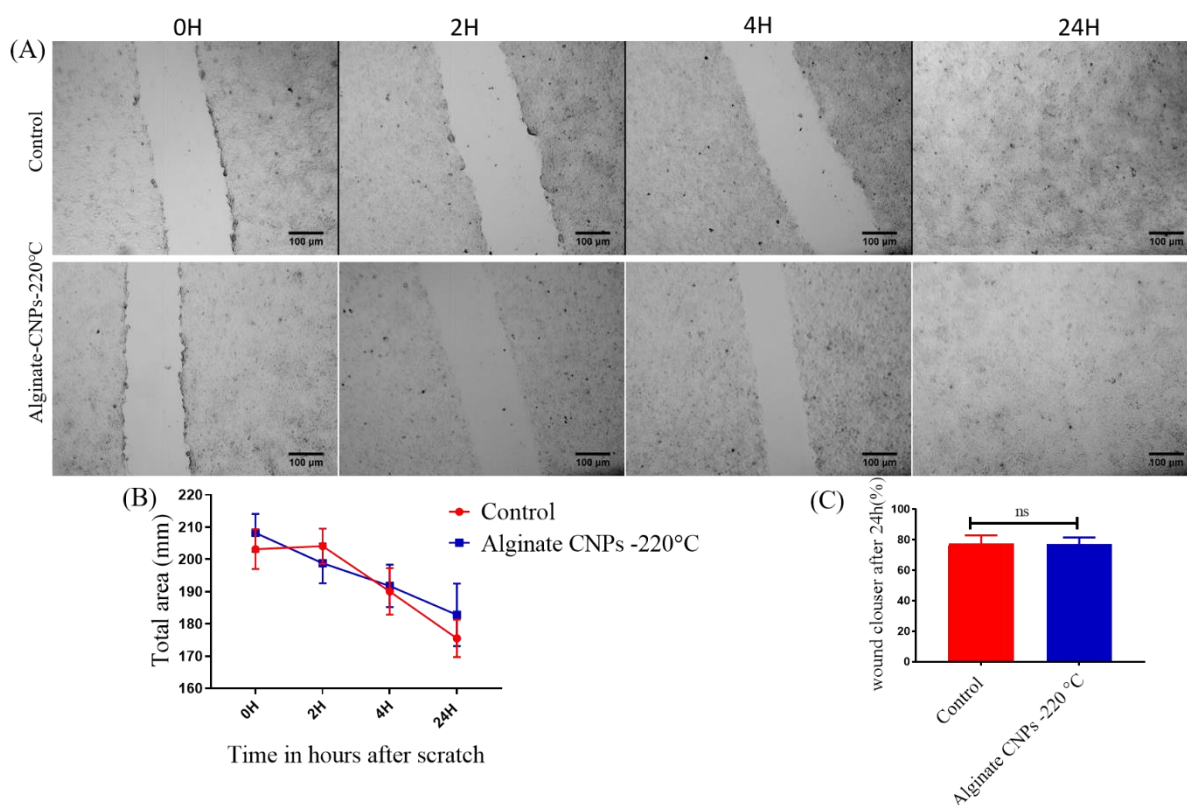


Figure 5.5. A) Wound healing assay in melanoma cancer cells forming a confluent monolayer. 100 mg/ml CNPs from alginate at 220°C was added to the cells and incubated for different durations; the images were taken at each time points (B) Quantification of total area analysis and (C) Statistical analysis expressed as percentage of wound closure.

5.4.3. Wound healing Scratch assay in fibroblast cells.

The HDF cells were used to evaluate the cell migration after incubation with CNPs. Figures 5.14 -5.17 A represent phase contrast optical micrographs of the cultured HDF with CNPs produced from alginate at 200 and 220°C and glucose 220°C. Figures 5.15 – 5.17 B show the effect of CNPs on the migration of C8161 melanoma cells over 24h following a scratch, while the corresponding figure (C) demonstrates the effect of CNPs on HDF migration at 48h after a scratch.

In the above scratch wound healing assay, the random migration of HDF cells was studied using simple wound healing assays to visualise cell movement after being treated with CNPs. The figures indicate that the fibroblast moved as single cells migrated from the edge to another area of the scratch. In alginate CNPs, the scratch was completely closed after 53h. Conversely, the figures indicate that the cells treated with glucose CNPs healed faster than the control. After comparison with the control, the cells treated with CNPs migrated slightly

faster than the cells treated with the medium only. Overall, there was no difference in migration rates between the control and the cells treated with CNPs.

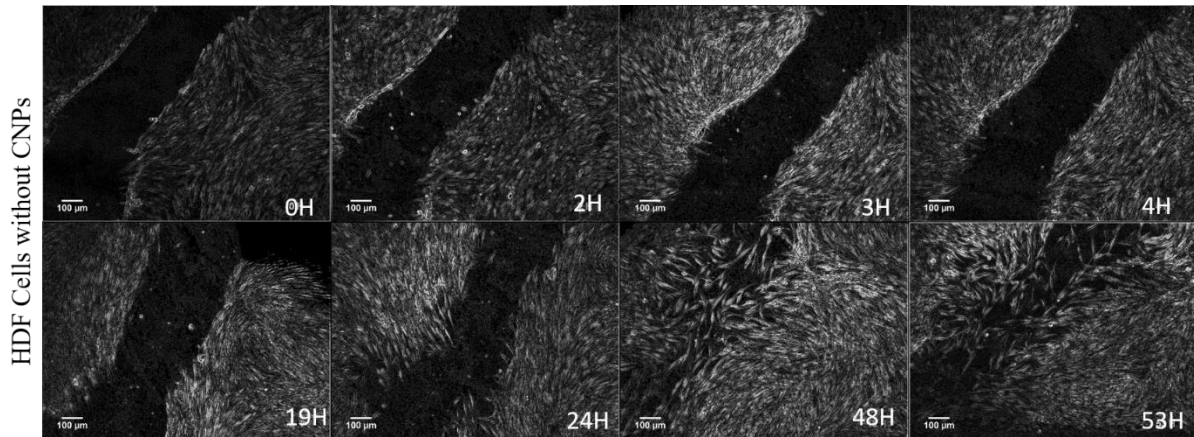


Figure 5.6. Wound healing assay in HDF cells forming a confluent monolayer. Important to notice that the cells were not treated with the CNPs. Scale bar 100µm.

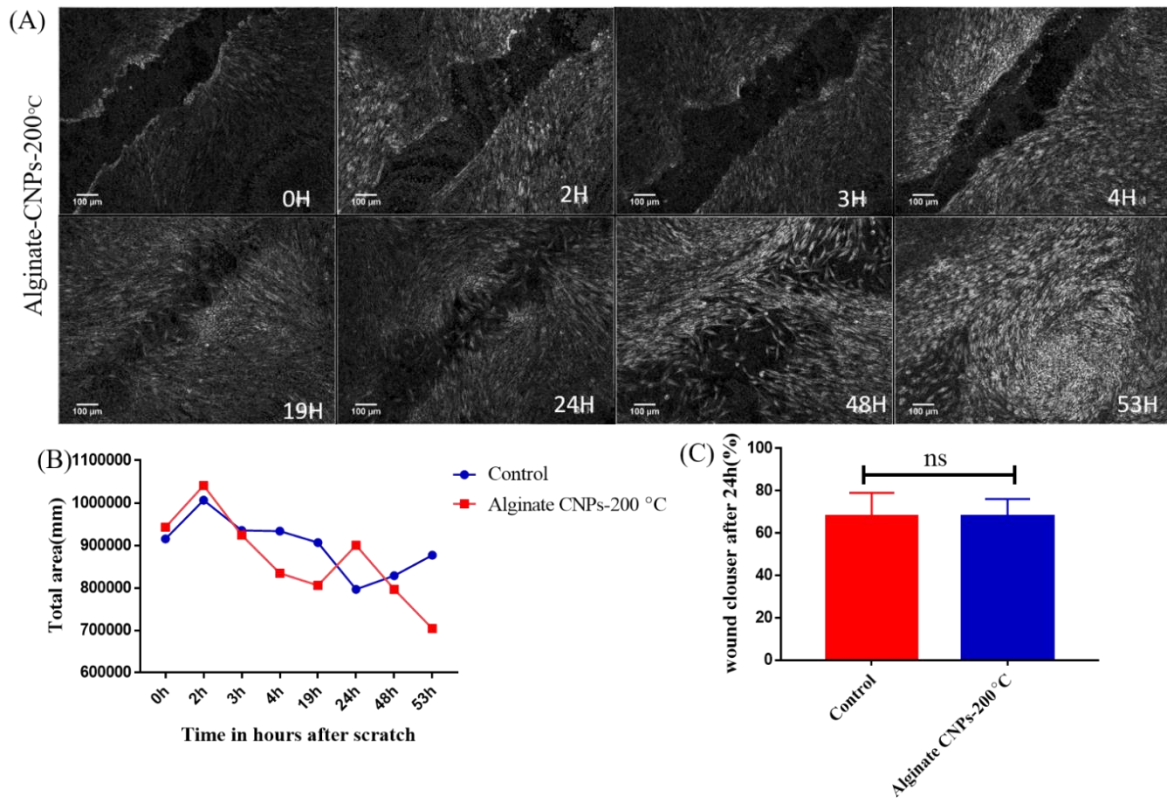


Figure 5.7. (A) Wound healing assay in melanoma cells forming a confluent monolayer. 100 mg/ml CNPs from alginate at 200°C added to the cells and incubated for different durations; the images were taken at each time interval; (B) Quantification analysis shows the reduction distance after scratch;(C) Statistical analysis, Scale bare 100µm

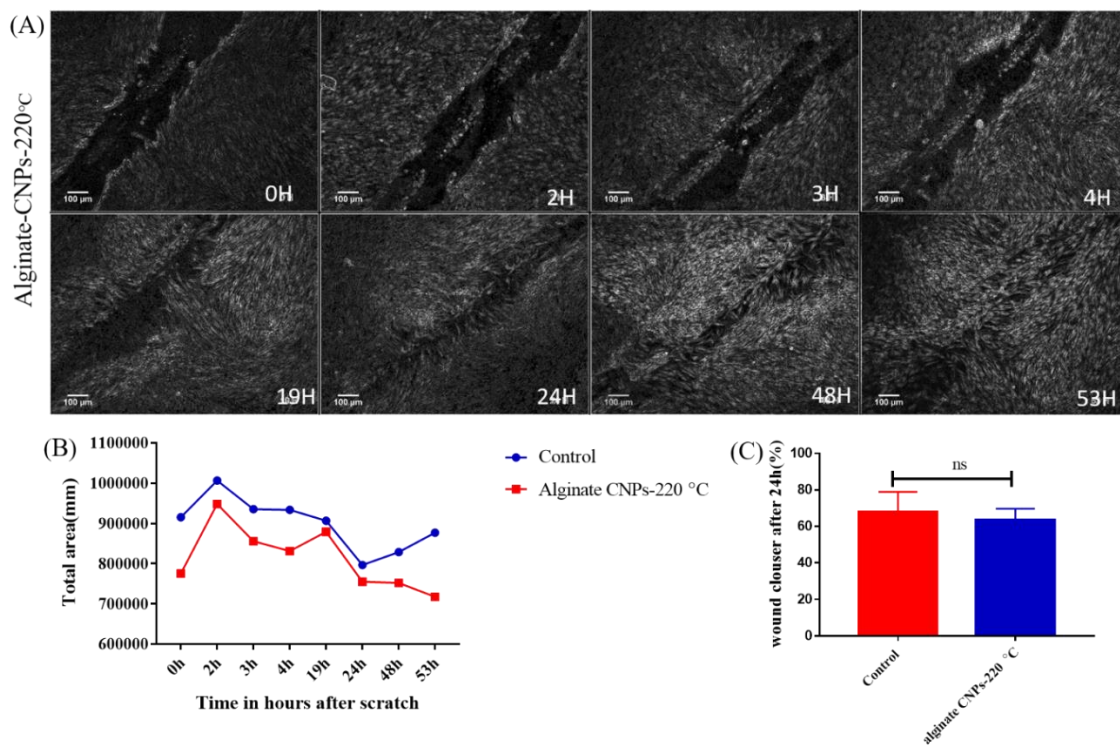


Figure 5.8. (A) Wound healing assay in melanoma cells forming a confluent monolayer. 100 mg/ml CNPs from alginate at 220°C added to the cells and incubated for different durations; the images were taken at each time interval; (B) Quantification analysis shows the reduction distance after scratch; (C) Statistical analysis. Scale bar 100µm.

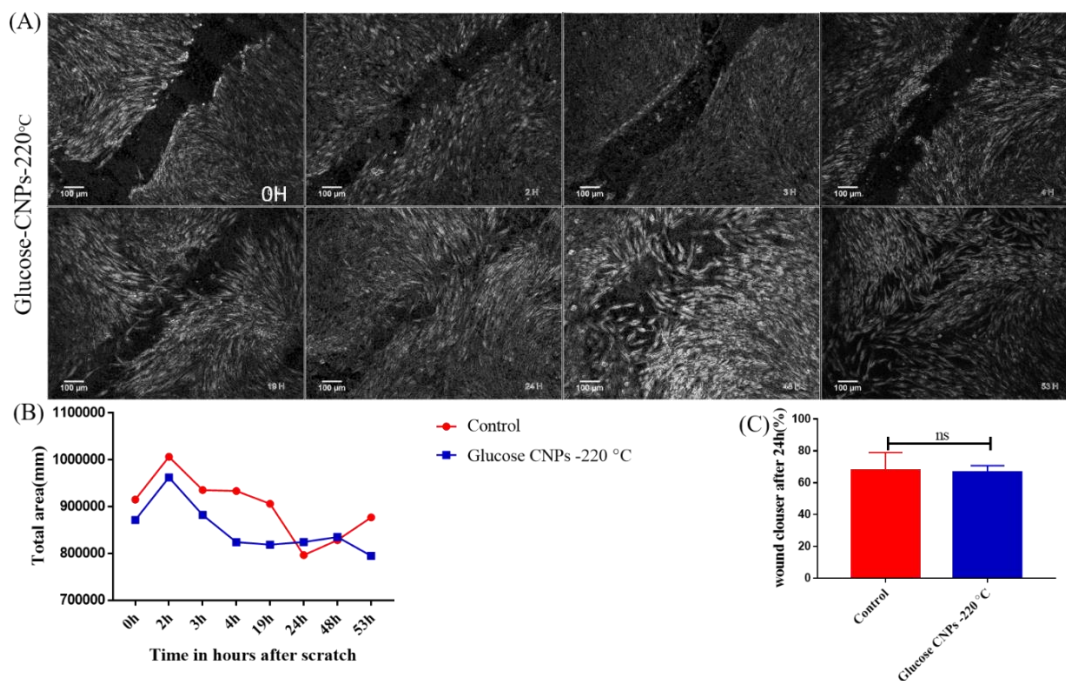


Figure 5.9. A) Wound healing assay in melanoma cells forming a confluent monolayer. A 200-µl sterile tip made the wound across an HDF monolayer. 100 mg/ml CNPs from glucose at 220°C added to the cells and incubated for different durations; the images were taken at each time interval; (B) Quantification analysis shows the reduction distance after scratch; (C) Statistical analysis.

In Summary, two types of cells, HDF and C8161, were used in this study. The HDF cells are located all through the human body and are responsible for the protection of soft tissue integrity via their primary characteristic, collagen expression. While human melanoma cancer (C8161 line) is one of the most aggressive and lethal skin cancers, it can be easily detected before metastasizing [122]. The cell migration study showed a different effect on the two cells. In fibroblasts, the cells with media only migrated faster than the cells incubated with particles; however, there was no significant effect on cell migration overall. The gaps were completely closed. The effect of onion carbon nanodots on the migration of HDFs has been studied before, with the results showing a significant increase in the migration of HDF compared with control media only [94]. The CNPs from glucose and alginate showed no significant effect when HDF and melanoma were incubated with the particles. The study suggested that the higher concentration of onion carbon nanodots might delay the cell migration.

However, the cell migration study on melanoma cancer cells was performed and the particles derived from glucose and alginate showed no significant effect compared with the control. Interestingly, the melanoma cancer cells migrated and healed faster than fibroblasts, which reportedly have a 20h doubling time [123]. Incubating the cells with CNPs had no effect on cell migration, similarly to cells incubated with melanoma. We found that in the first 24 hours, the cells migrated very fast and the gaps were closed completely. Re-incubation for another 24h demonstrated no significant difference in the cell migration.

***Chapter Six: Cellular Uptake of Carbon Nanoparticles as Determined by
Experimental Conditions and Cell Type***

6. Chapter Six: Cellular Uptake of Carbon Nanoparticles as Determined by Experimental Conditions and Cell Type

6.1. Introduction

A tremendous worldwide interest in the last two decades has resulted in novel functional nanomaterials for drug discovery to clinical, bio-imaging and diagnostic applications [2]. However, our understanding of engineered nanoparticles' adverse effects on humans and the environment is still far from complete [124]. Several studies have shown the localization of nanomaterials within the cells but their toxicological effects were carried out without determining the exact uptake mechanism of the elements involved [125].

We must fully understand the nanomaterials' properties as they ultimately determine the delivery and uptake through the cellular membranes and enhance our understanding of their toxicity. This could potentially aid the design of customised nanoparticles for a given application. Toxic effects often originate from the presence of toxic inner cells [65]. In addition, toxicity is dependent on the entrance path and the final intracellular localization. The physicochemical properties of nanomaterials, in conjunction with cell characteristics and extracellular media (e.g. protein or lipid adsorption patterns) govern the localization process within the cells. As mentioned above, several reports have also found that the uptake mechanism is associated with the experimental conditions and resulting characteristics of nanomaterials.

This study reviews uptake mechanisms of nanomaterials in various cell types, discovering that the experimental conditions and properties of nanomaterials determine the delivery within the cellular membranes along with their uptake. Identifying the role of elements that determine nanoparticle uptake by way of cells is the first step to elucidating how the materials will accumulate and exert toxic effects without any challenging experiments. Such protocol is routinely employed to determine the hazards associated with conventional chemicals. Carbon nanoparticles (CNPs) are an excellent example of fluorescent nanomaterials that exhibit excellent biocompatibility and good cell permeation. The CNPs only consist of carbon, hydrogen, and oxygen, and their quasi-spherical form makes them attractive for various bio-applications such as bio-sensing and optical probing technologies. Other attractive features include low toxicity, solubility, and biocompatibility which makes CNPs attractive for bio-imaging. Significantly, the synthesis of CNPs does not involve any toxic elements such as cadmium, lead, selenium, and tellurium and the material is easily taken up at the cellular

levels [126]. Their fluorescent properties makes it choice of material for cellular imaging under fluorescence confocal microscope and their use for internalising the cells through *caveolae*-mediated endocytosis [127].

In this chapter will study the relationship between CNP concentration and cellular uptake behaviour, and to understand the uptake mechanism of carbon NPs in three different type of cells: Melanoma cancer cells C8161, Human derma fibroblast HDF, and NIH 3T3. The three cell lines were used because they extend across a range of phenotypes. Human dermal fibroblasts are normal cell line, which can be cultured easily, up to passage 10, Melanoma (C8161) is cancer cells, which can be cultured, and passage indefinitely, and (3T3) is mice fibroblast. This chapter will also study the localisation of these particles by using a mitochondrial deep red tracker. Mitotracker dyes are useful in multiple labelling experiments where you want to follow different organelles, membranes, or physiological changes at the same time. Mitotracker deep red was used to avoid the spectral overlap between CNPs and the dye. The mitochondria are the organelles within a cell, which are responsible for cellular respiration to produce adenosine triphosphate (ATP). Mitochondria is one of the principal sources for producing reactive oxygen species (ROS).

6.2. Statistical analysis

All confocal images were analysed using ImageJ software. The images were analysed to indicate any significant difference in intensity between samples and types of cells. Five cells in each image were measured by the area. The integrated density and mean grey value were obtained from an area with no fluorescent activity and later averaged. Then the corrected total fluorescence was measured using the formula:

$$CTCF \text{ (Corrected Total Cell Fluorescence)} = \text{Integrated Density} - (\text{Area of selected cell} \times \text{Mean fluorescence of background readings})$$

After that the data was copied to GraphPad Prism and one-way ANOVA was used to indicate the significance. Co-localisation analysis was performed by using a JACoP plugin of the mage to calculate the Pearson's Coefficient.

6.3. Results and discussion

In this studies, three different cell types were used; human dermal fibroblast (HDF), melanoma cancer cells (C8161) and NIH 3T3 fibroblast. Confocal microscopy was used to observe the particles interlined within the target cells. The cellular uptake of CNPs was studied using five different concentrations incubated for 5, 10, 20, 30 and 60 min. More

details were given in chapter 3. To study the effect of CNPs concentration on cellular uptake, the CNPs were incubated with the cells at different concentrations (10 µg/ml, 20 µg/ml, 50 µg/ml, 100 µg/ml, 150 µg/ml and 200 µg/ml) in DMEM media supplemented with (10 % (v/v) FCS) and 1% (v/v) A/A between 5 – 60 minutes.

6.3.1. Cellular Uptake Studies of alginate CNPs at 200°C in HDF cells.

Figure 6.1A shows the results obtained from the cellular uptake studies on alginate at 200°C in HDF Cells. Visual appearance in these images do not provide clear indication of effect of concentration of CNPs added or the time of incubation on the cell uptake. A quantitative analysis was carried out by integrating the intensity of green fluorescent channel of the micrograph for each concentration of CNP at times points from 5 min to 60 min. These results are illustrated in Figure 6.1B and C.

It was clear from these data that the concentration plays an important role in the cellular uptake; increasing the concentration lead to a corresponding increase in the fluorescent intensity. 200 µg/ml showed a two-fold increase in the fluorescent intensity as compared to 10 µg/ml. Although the increase in fluorescence scaled with increased concentration of particles, there was only a two-fold increase in intensity for a 20 times higher nanoparticle concentration. As expected, the fluorescent intensity increased compared to the control as no CNPs were added to the cells. Incubating cells for a long time also led to an increase in the fluorescence intensity. Overall, that there was an increase in fluorescence but no significant difference in response with concentration. Overall fluorescence intensity is shown for all the samples is shown as a function of time of incubation.

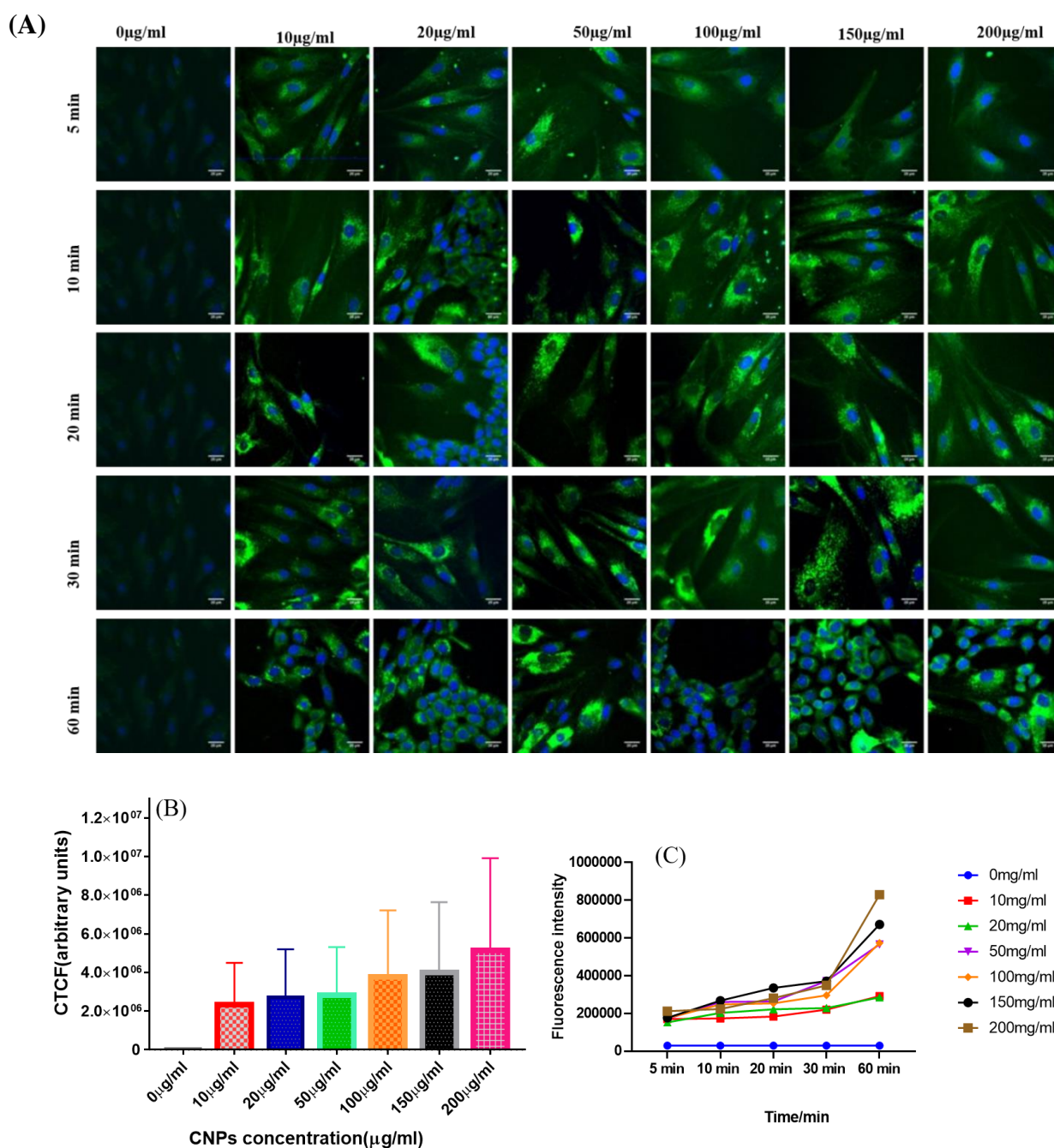


Figure 6.1. (A) Cellular Uptake of CNPs derived from alginate at 200°C onto HDF cells at different concentrations and incubation times (B) Integrated intensity of green fluorescent channel of the micrograph vs. the concentration at times points from 5min to 60 min (C) Time points and concentration-dependent uptake of Alginate CNPs in HDF cells. Scale bare 25µm.

6.3.2. Cellular uptake studies of alginate CNPs at 200°C in C8161 cells

The concentration and incubation time effect of alginate CNPs at 200°C on cellular uptake of melanoma C8161 cells are shown in Figure 6.2. On the contrary, with C8161 melanoma

cancer cells, there was a slight increase in the fluorescence intensity when the cells were incubated with 200 $\mu\text{g/ml}$ relative to 10 $\mu\text{g/ml}$. A three-fold increase in the fluorescence intensity was observed compared with the control. The confocal microscopy images revealed that the CNPs uptake very fast, a five-minute process in all the cells.

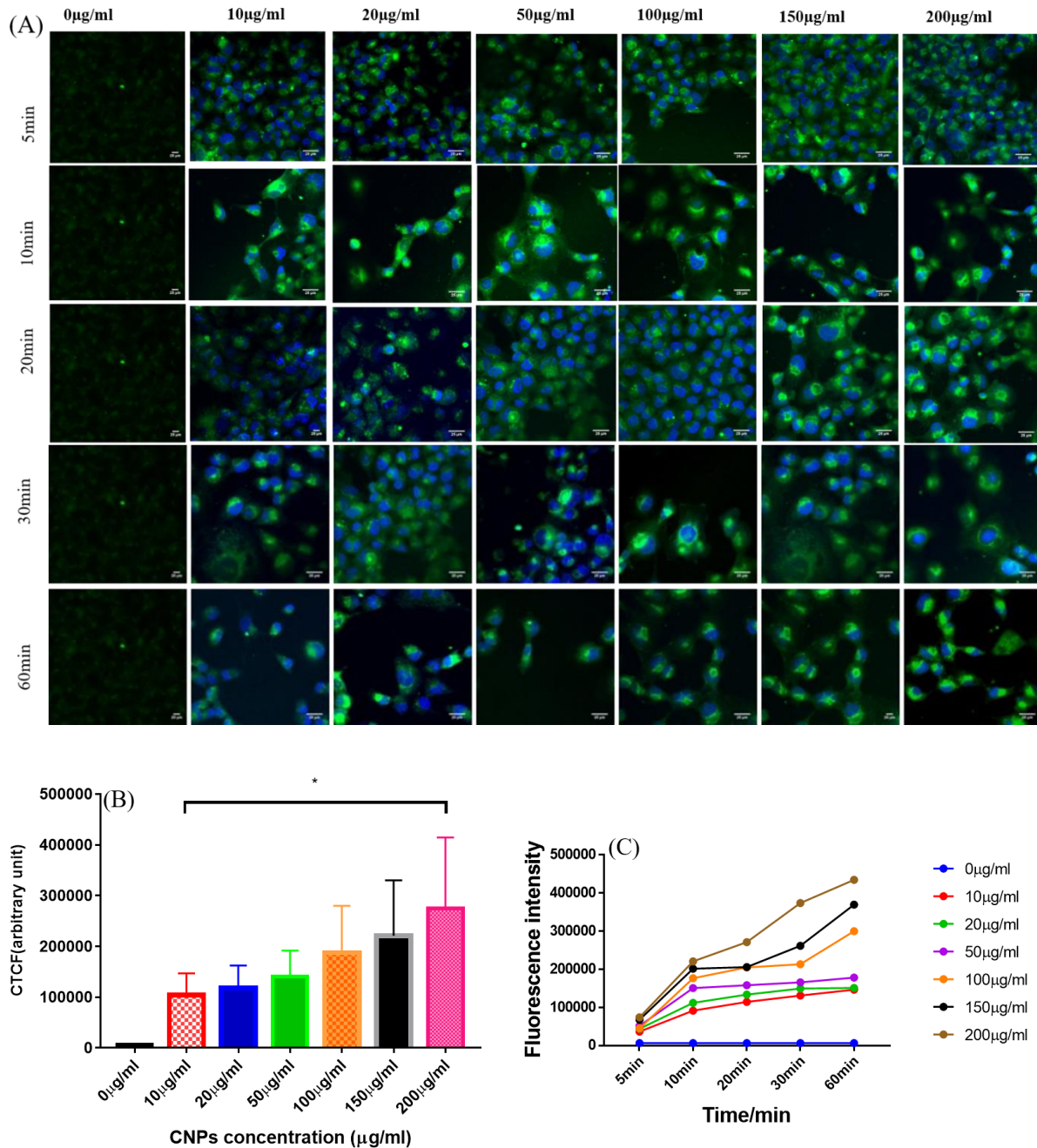


Figure 6.2. (A) Cellular Uptake of CNPs derived from alginate at 200°C onto Melanoma (C8161) cells, at different concentrations and incubation times. (B) Integrated intensity of green fluorescent channel of the micrograph against the concentration at times points from 5min to 60 min. (C) Time points and concentration-dependent uptake of Alginate CNPs in C8161 cells.

6.3.3. Cellular uptake studies of alginate CNPs at 200°C in NIH 3T3 cells

For NIH 3T3 the cellular uptake study results are shown in Figure 6.3. The concentration and incubation time effect of alginate CNPs at 200°C on cellular uptake of NIH3T3 cells clearly is prominent from the results shown in Figure 6.3. As the cells incubated with 150 µg/ml demonstrated three-fold increase in the florescent intensity when compared to 10 µg/ml and four-fold increase when incubated with 200 µg/ml in all types of cells. In terms of morphologies, no change was observed based on a visual of the cells.

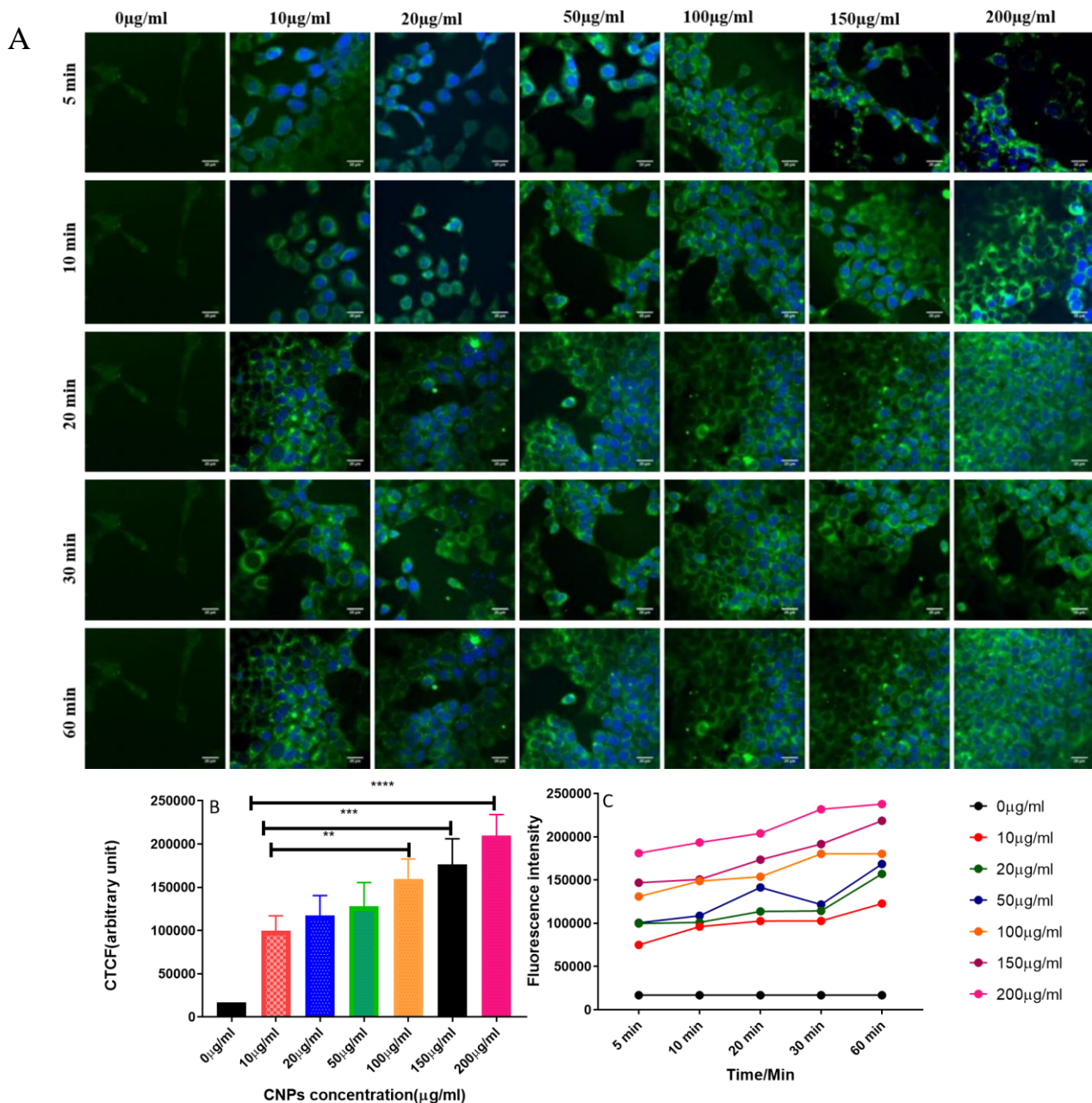


Figure 6.3. A) Cellular Uptake of CNPs derived from alginate at 200° C cells into NIH 3T3 cells at different concentrations and incubation times. (B) Integrated intensity of green fluorescent channel of the micrograph vs the concentration at times points from 5min to 60 min. (C) Time points and concentration-dependent uptake of Alginate CNPs in NIH 3T3cells.

In summary, all the above fluorescence images indicate that the CNPs exhibit strong fluorescence when incubated with all type of cells at five minutes. These particles were readily taken up by the cells, thus increasing their potential for bio-imaging. Using different incubation times provided an indication of the cell uptake of these particles. It was obvious from the results that the fluorescent intensity increased significantly with longer incubation times.

6.3.4. Cellular uptake studies of glucose CNPs at 200°C in HDF cells

Figures 6.4 shows the confocal microscopy images of HDF, after being treated with glucose CNPs at 200°C with concentration ranging between 0 – 200 µg/ml and incubation time between 5 – 60 min.

The statistical data for HDF indicates that the fluorescent intensity increased alongside increasing concentration. For low concentrations, the increase in fluorescence does not vary with the incubation time. However, for higher CNP concentrations (>100 µg/ml) the fluorescence increases proportional to the added concentration of CNPs. There was a significant increase in the fluorescence intensity after incubating with 200 µg/ml as compared to 10 µg/ml.

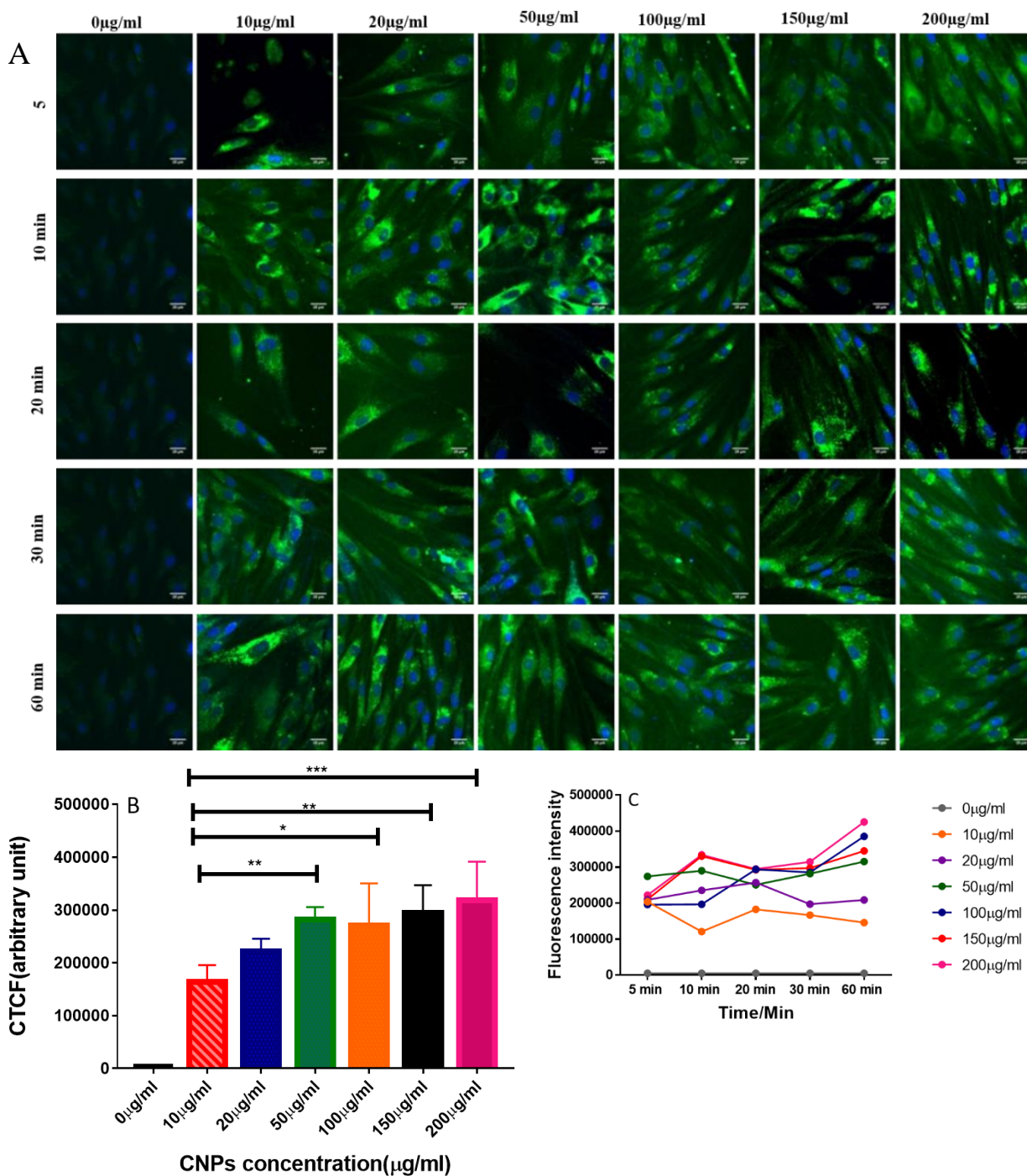


Figure 6.4. Cellular uptake of CNPs derived from glucose at 200°C onto HDF cells, at different concentrations and incubation times. (B) Integrated intensity of green fluorescent channel of the micrograph vs the concentration at times points from 5min to 60 min. (C) Time points and concentration-dependent uptake of Glucose CNPs in HDF cells.

6.3.5. Cellular uptake studies of glucose CNPs at 200°C in C8161 cells

Confocal microscopic images collected from the cellular uptake studies of glucose CNPs in C8161 cell are shown in Figure 6.5. The fluorescent intensities measured was less than that for the samples with HDF. Quantitative analysis of fluorescence shows that there was an

increase in the fluorescence after the particles were incubated with the cells for longer than 30 min and with increased concentration of CNPs above 150 $\mu\text{g/ml}$.

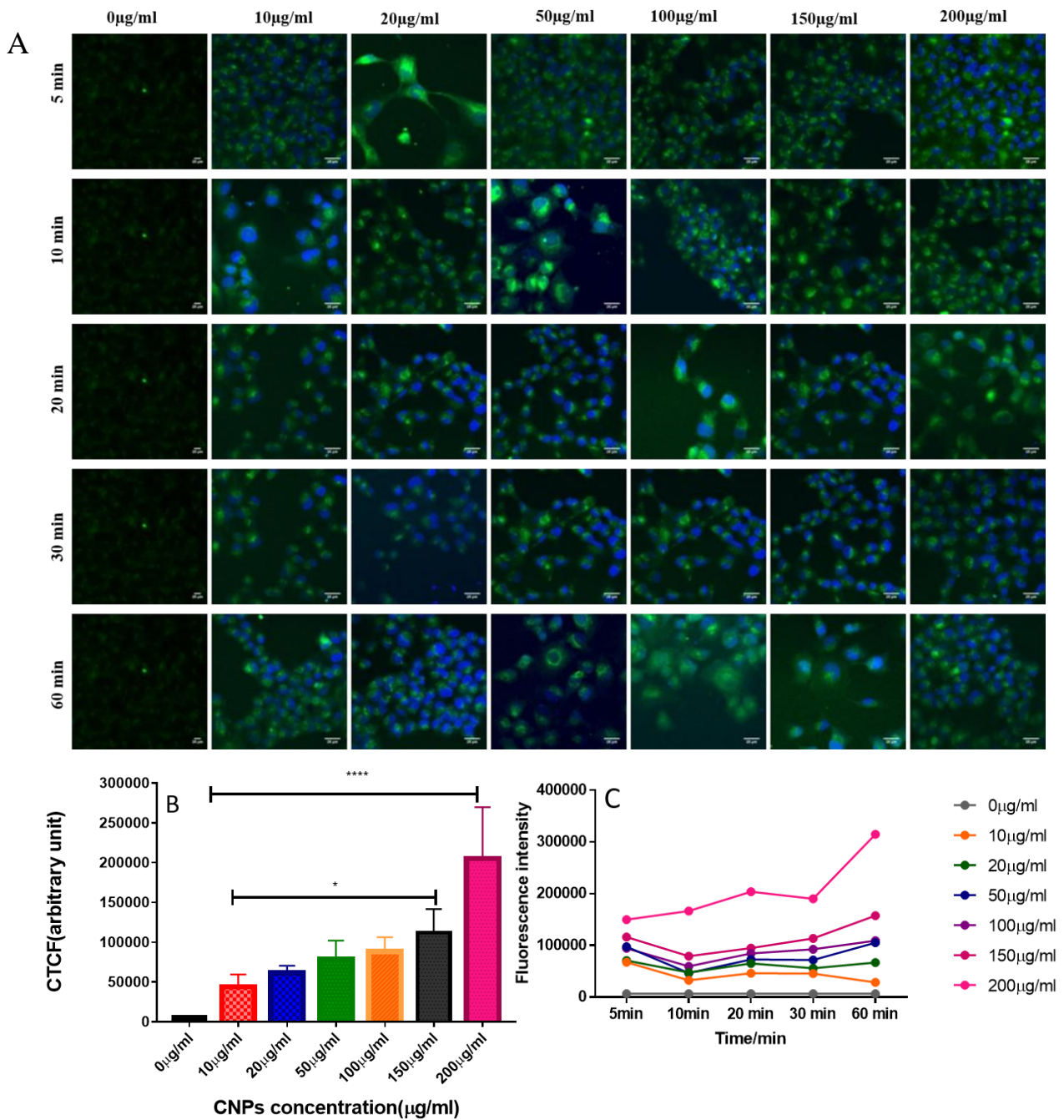


Figure 6.5. Cellular uptake of CNPs derived from glucose 200 $^{\circ}\text{C}$ onto Melanoma (C8161) cells at different concentrations and incubation times. (B) Integrated intensity of green fluorescent channel of the micrograph vs the concentration at times points from 5min to 60 min. (C) Time points and concentration-dependent uptake of Glucose CNPs in C8161 cells.

6.3.6. Cellular uptake studies of glucose CNPs at 200 $^{\circ}\text{C}$ in NIH 3T3 cells

The confocal microscopy images for NIH 3T3 fibroblast with added glucose CNPs at 200°C are shown in Figure 6.6. The cellular uptake of these particles increases gradually with increasing CNPs concentration, however, do not show any particular dependency of incubation times.

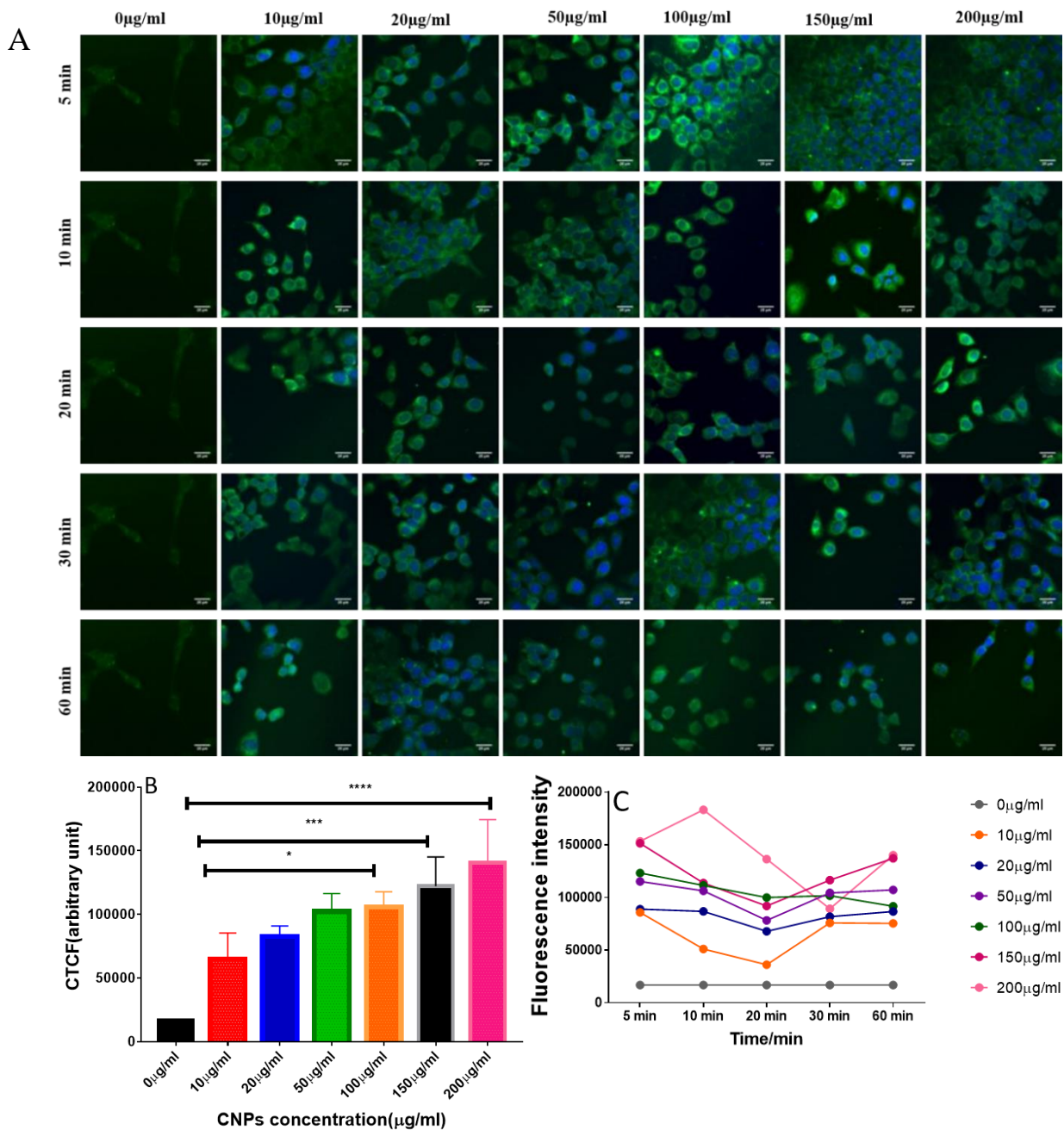


Figure 6.6. Cellular uptake of CNPs derived from glucose at 200°C into NIH3T3 cells at different concentrations and incubation times. (B) Integrated intensity of green fluorescent channel of the micrograph vs the concentration at times points from 5 to 60 min. (C) Time points and concentration-dependent uptake of glucose CNPs in NIH 3T3 cells.

6.3.7. Comparison of fluorescence emissions of alginate CNPs at 200°C, after 1 hr incubation

In order to understand the cellular uptake of alginate CNPs by different cell types, and the effect of incubation time, the confocal images of the samples over an hr of incubation time was put in the same pellet along with the plot of fluorescence counts as a function of incubation time for all cell types (Figure 6.7 & 6.8).

Comparison of the fluorescent intensity showed the highest contrast can be seen for the cell type HDF, with sudden increase in intensity at 1hr incubation time compared to the samples incubated up to 30min. This is also the highest intensity achieved for all the samples studied. For the other two cell types, NIH3T3 and C8161, a fluctuation in the fluorescence intensity with increase in the incubation time, was evident as well as the slight increase in the intensity at longer incubation time

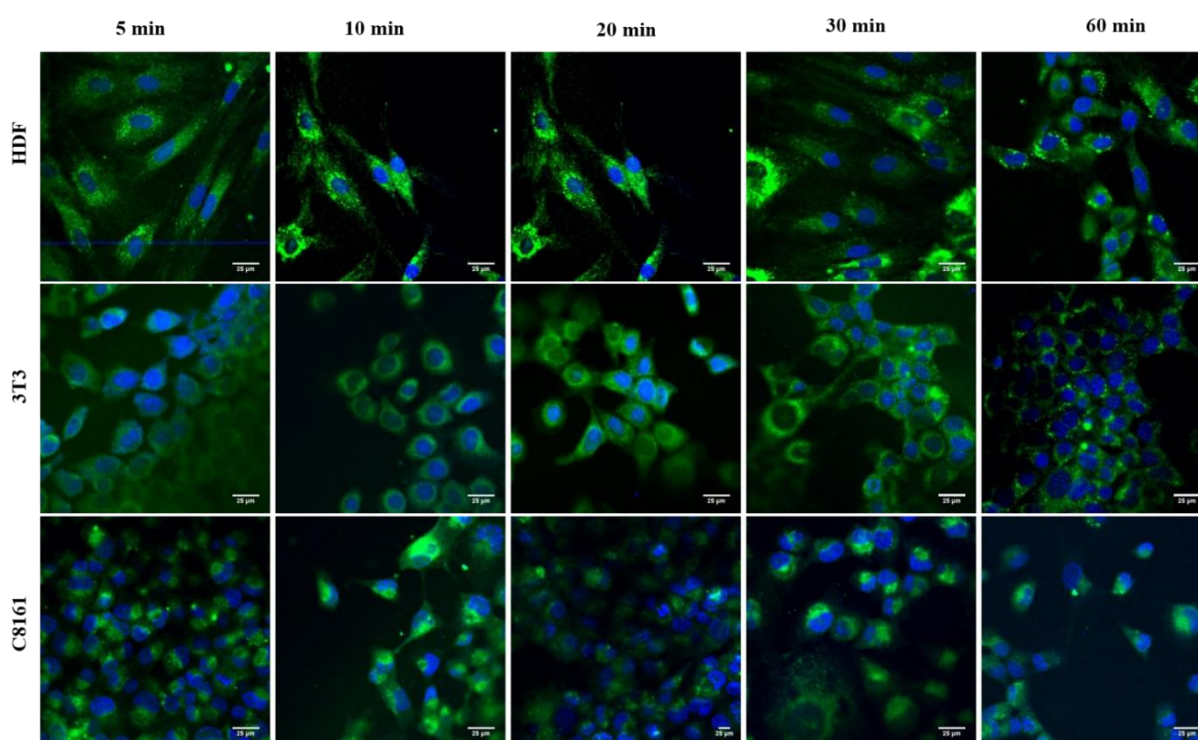


Figure 6.7. Time-course confocal microscopy images of cellular uptake of Alginate CNPs by HDF, NIH 3T3 and C8161 cells in DMEM supplemented with 1% (v/v) at different times. Green colour represents cell membrane. Nuclei stained with DAPI ($\lambda_{ex}=488$ nm $\lambda_{em}=780$ nm) Scale bars = 25 μ m.

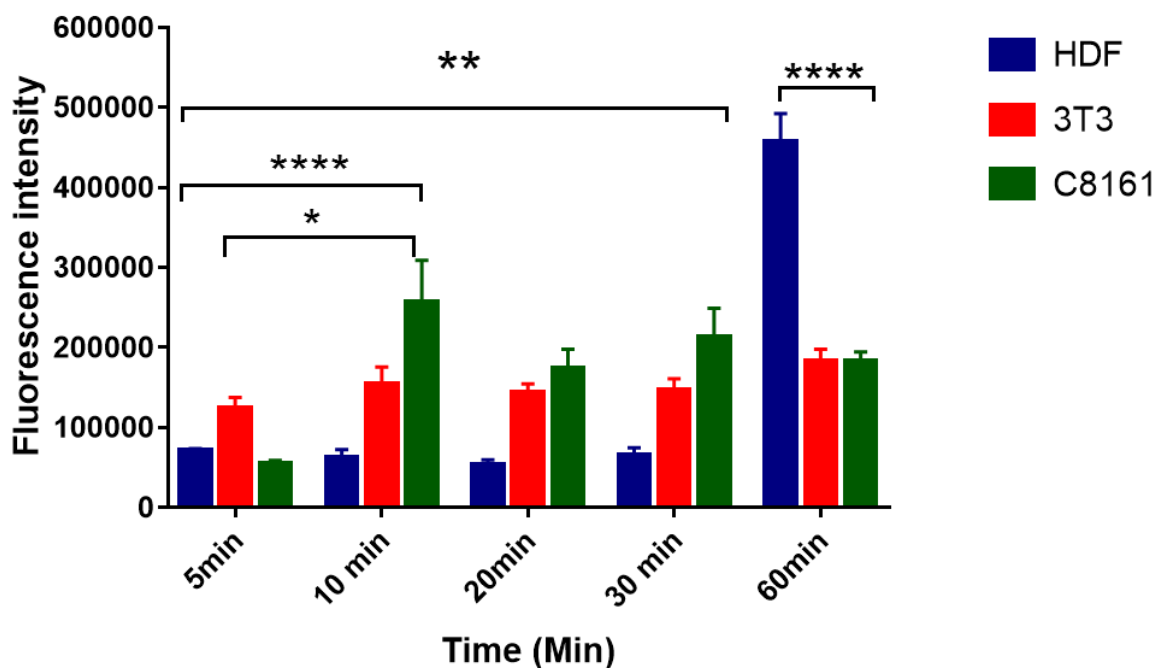


Figure 6.8. Fluorescence data from Confocal microscopy of cellular uptake of alginate 200°C CNPs by HDF, NIH 3T3 and C8161 cells in DMEM supplemented with 1% (v/v) FCS at different times points. Two ANOVA Comparing the means of each column with the mean of every other column'. Significance was denoted by a * symbol (* $p < 0.05$, ** $p < 0.01$, *** $p < 0.001$).

Similar comparison has also been done for uptake CNPs derived from glucose by HDF, NIH3T3 and C8161 at different time points (Figure 6.9 and 6.10). All three types of cells show a incubation time independent fluorescence intensity. However, HDF shows the highest fluorescence intensity over time compared to C8161 and NIH3T3.

6.3.8. Comparison of fluorescence emissions of glucose CNPs at 200°C, after 1 hr incubation

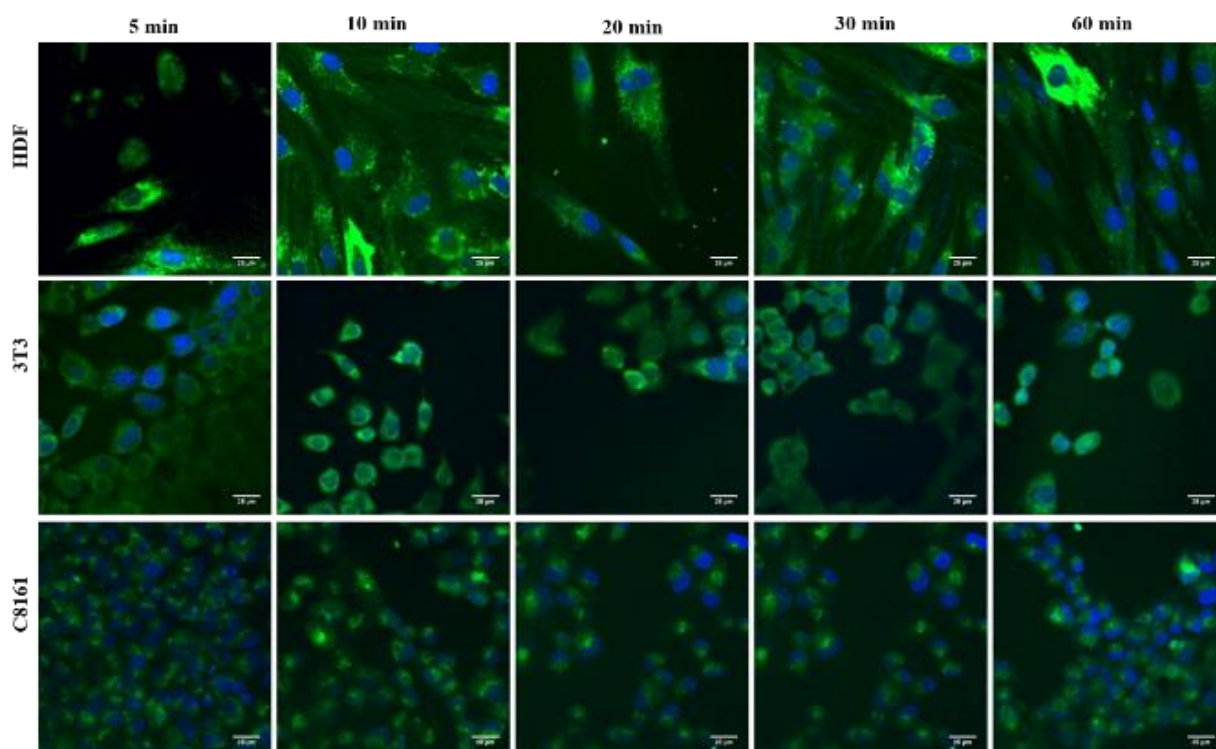


Figure 6.9. Time-course confocal microscopy images of cellular uptake of glucose CNPs by HDF, NIH3T3 and C8161 cells in DMEM supplemented with 1% (v/v) FCS at different times. Green colour represents cell membrane. Nuclei stained with $\lambda_{ex}=488\text{nm}$ DAPI $\lambda_{em}=780\text{ nm}$. Scale bars = 25 μm .

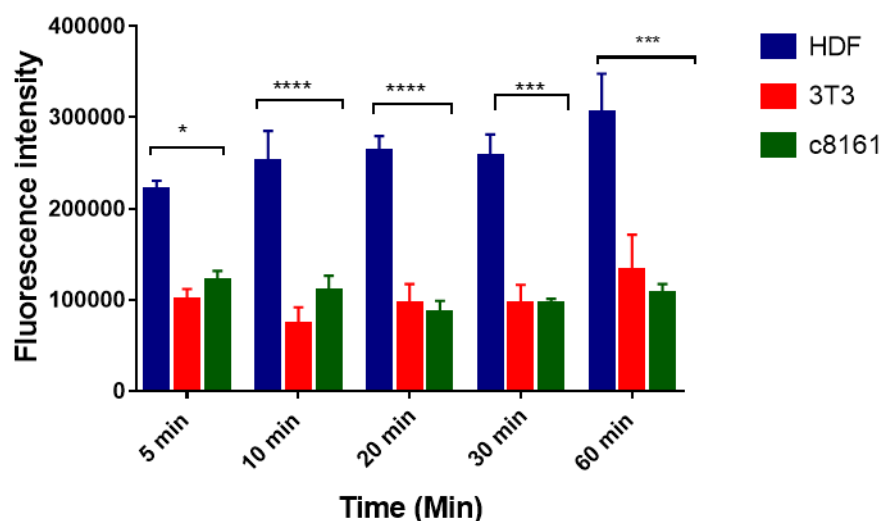


Figure 6.10. Confocal microscopy data of cellular uptake of glucose CNPs by HDF, NIH3T3 and C8161 cells in DMEM supplemented with 1% (v/v) FCS at one hour of incubation. Two ANOVA Comparing the means of each column with the mean of every other column'. Significance was denoted by a * symbol (* $p < 0.05$, ** $p < 0.01$, *** $p < 0.001$).

6.4. Localisation studies by fluorescence microscopy

To understand the cellular uptake in detail, localisation experiments were carried out. Mitochondrial deep tracker red was added in different concentrations to HDF and C8161 with 30 or 150 $\mu\text{g/ml}$ concentrations of CNPs (alginate 200°C, alginate 220°C, glucose 200°C and glucose 220°C). The cells were incubated with CNPs for an hour.

Figure 6.11 shows the confocal microscopy images of human fibroblast incubated with alginate at 200 and 220°C. The CNPs in the image concentrated around the nucleus and mainly in the cytoplasm. Merging the images from CNP fluorescence and Mitotracker deep red, gives details of co-localisation. Based on the quantitative analysis of the co-localisation image J produces scatter plot as shown in (d). The scatter plot demonstrates the population of the two dyes, green and red fluorescence, respectively. The Pearson's correlation coefficients are calculated from these scatter plots and for alginate at 200°C and alginate at 220°C was found to be 0.815 and 0.786 respectively. This exercise was carried out on six images. The Pearson's correlation coefficient <1 suggests that the particle did not target the mitochondria.

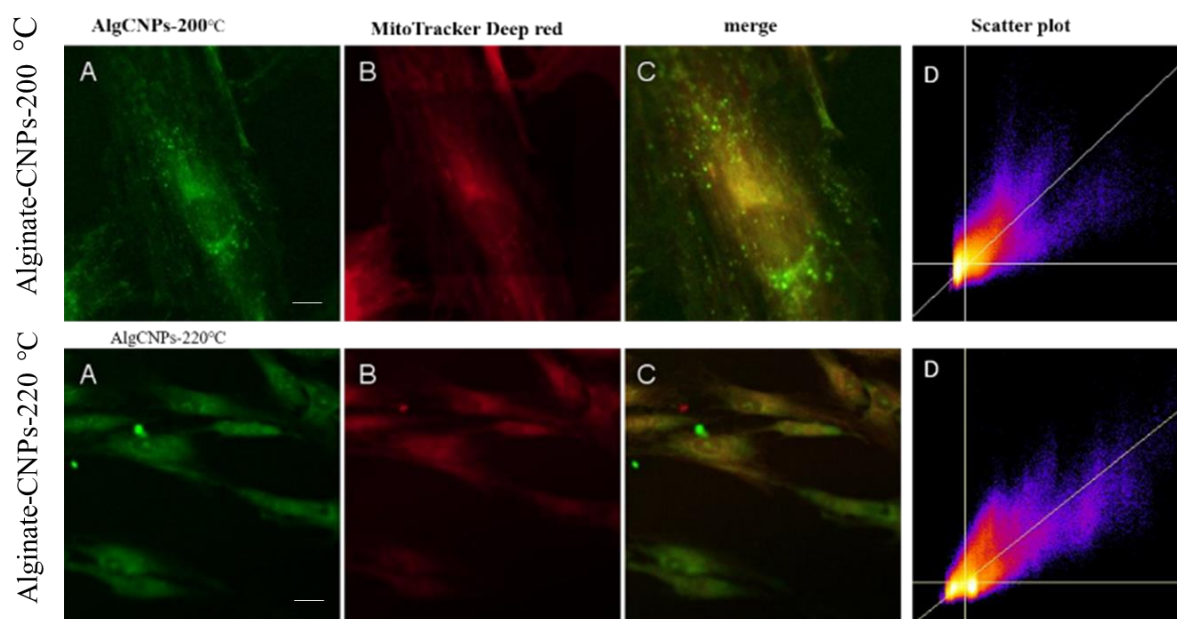


Figure 6.11. Localisation of photo luminescent alginate CNPs in Human dermal fibroblast. (A) Confocal microscopy images of HDF incubated with (30 $\mu\text{g/ml}$) alginate CNPs at 200°C and 220°C Green channel (488nm). (B) Cells were labelled with mitochondrial deep red tracker 25nM. mitochondrial deep red tracker channel 633 nm. (C) Merged images of both channels. (D) Scatter plot of red and green pixel intensities of the image shown in C. Scale bar 25 μm

Results of localisation studies of glucose CNPs at 200 and 220°C in HDF show in Figure 6.12. Similar features to the previous case can be seen. The Pearson's correlation coefficient

in glucose at 200°C and 220°C was found to be 0.854 and 0.851 respectively, which was also an indication that CNPs were not accumulated in the mitochondria.

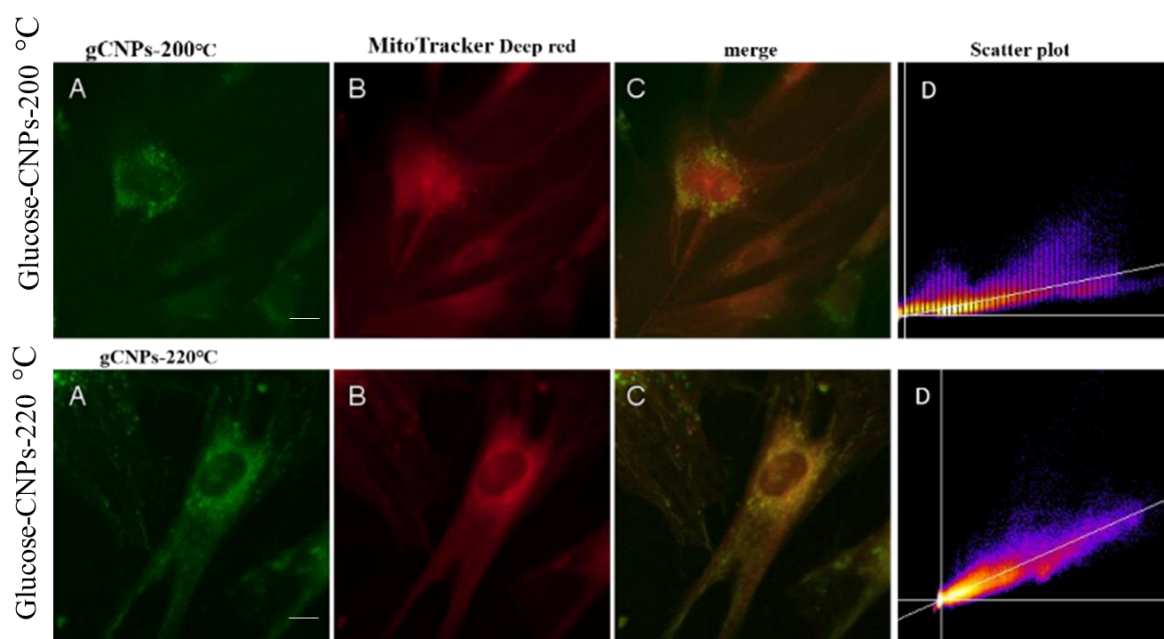


Figure 6.12. Localisation of photo luminescent CNPs in human dermal fibroblast. (A) Confocal microscopy images of HDF incubated with (30 µg/ml) glucose CNPs from heated at 200°C and 220°C Green channel (488) nm. (B) Cells were labelled with mitochondrial deep red tracker 25nM. mitochondrial deep red tracker channel 633 nm. (C) Merged images of both channels. (D) Scatterplot of red and green pixel intensities of the image shown in C. Scale bar 25µm

Figures 6.13 shows the results of localisation study for alginate CNPs in C8161 melanoma cancer cells. The merged image revealed that the CNPs from glucose and alginate were not located in the mitochondrial based on the quantitative analysis. Based on the quantitative analysis, Pearson correlation coefficient was determined to be 0.828 and 0.531 for alginate CNP samples at 200 and 220°C, respectively.

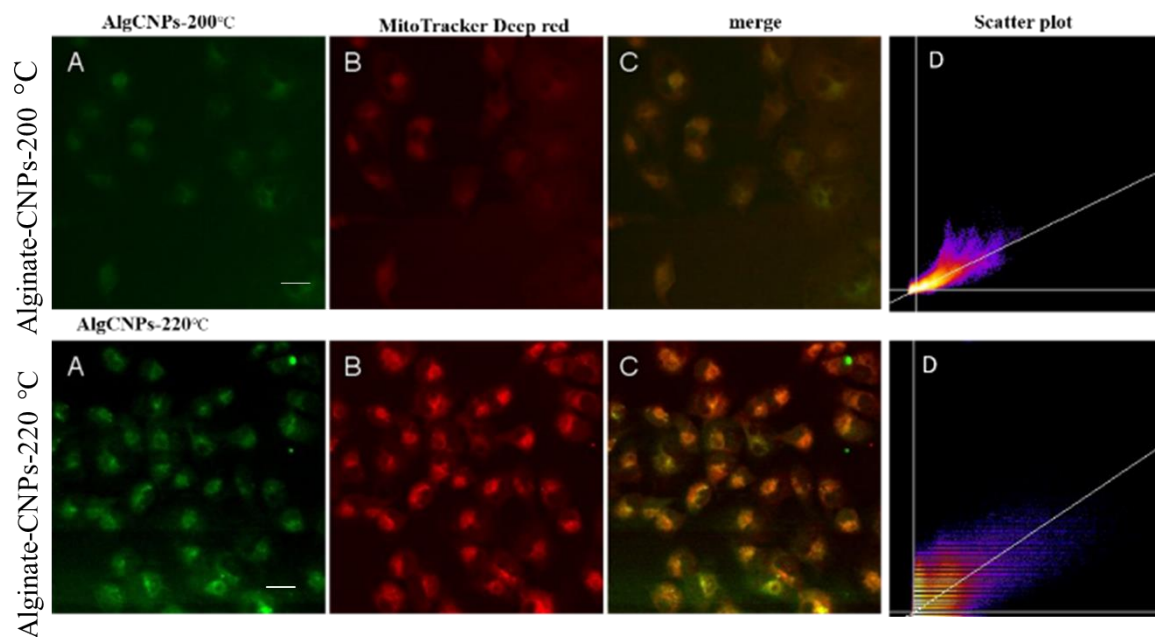


Figure 6.13. Localisation of photoluminescent CNPs C8161 melanoma cancer cells. (A) Confocal microscopy images of HDF incubated with (30 $\mu\text{g}/\text{ml}$) alginate CNPs from heated at 200°C and 220 °C. Green channel (488) nm. (B) Cells were labelled with mitochondrial deep red tracker 25nM. Mitochondrial deep red tracker channel 633 nm. (C) Merged images of both channels. (D) Scatterplot of red and green pixel intensities of the image shown in C. Scale bar 25 μm .

The same observation was noticed in Figure 6.14. The Pearson correlation coefficients were found to be 0.854 and 0.786 for glucose at 200°C and at 220°C respectively. Both cell lines, HDF and C8161 show a high uptake of the CNPs by the cells and are mainly located in the cell membrane and cytoplasm, without the observation of dots in the cell nucleus.

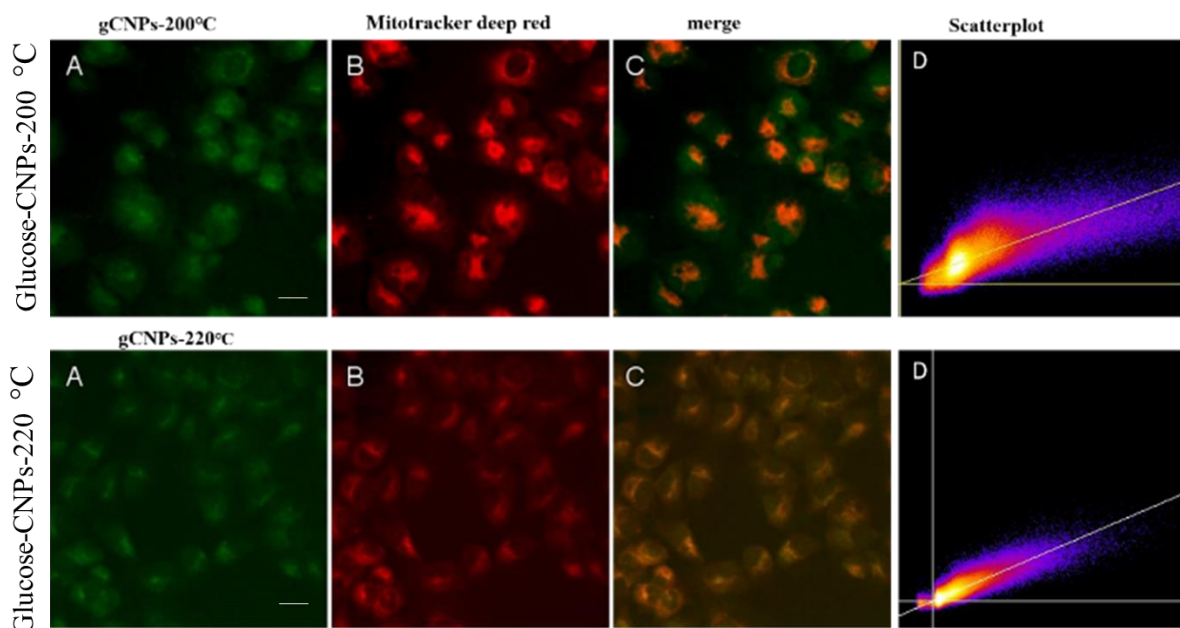


Figure 6.14. Localisation of photoluminescent CNPs in C8161. (A) Confocal microscopy images of HDF incubated with (30 $\mu\text{g}/\text{ml}$) glucose CNPs heated at 200 and 220 $^{\circ}\text{C}$ Green channel (488) nm. (B) Cells were labelled with mitochondrial deep red tracker 25nM. Mitochondrial deep red tracker channel 633 nm. (C) Merged images of both channels. (D) Scatterplot of red and green pixel intensities of the image shown in C. Scale bar 25 μm

Another study was carried out to further confirm the localisation of CNPs. In figures 6.15 and 6.16), 150 $\mu\text{g}/\text{ml}$ of CNPs from alginate and glucose were incubated with human dermal fibroblast for an hour and labelled with 50 nM mitotracker deep red. By increasing the concentration of CNPs, fluorescent intensity increased. The Pearson's coefficient in alginate at 200 $^{\circ}\text{C}$ was determined to be 0.825 and 0.785 at 220 $^{\circ}\text{C}$. For glucose samples at 200 and 220 $^{\circ}\text{C}$, the values were found to be 0.3 for both sets. Thus, increasing the concentration of nanoparticles did not affect the mitochondria.

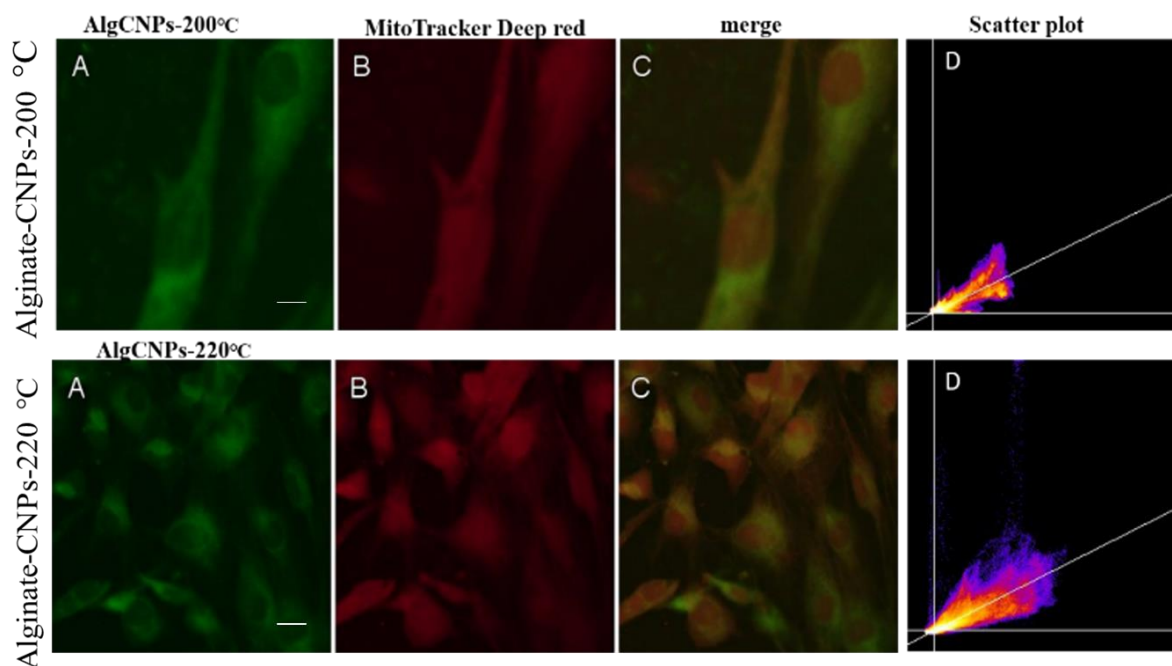


Figure 6.15. Localisation of photoluminescent CNPs in human dermal (A) Confocal microscopy images of HDF incubated with (150 $\mu\text{g}/\text{ml}$) alginate CNPs from heated at 200 and 220°C. Green channel (488) nm. (B) Cells were labelled with mitochondrial deep red tracker 50 nM. Mitochondrial deep red tracker channel 633 nm. (C) Merged images of both channels. (D) Scatterplot of red and green pixel intensities of the image shown in C. Scale bar 25 μm

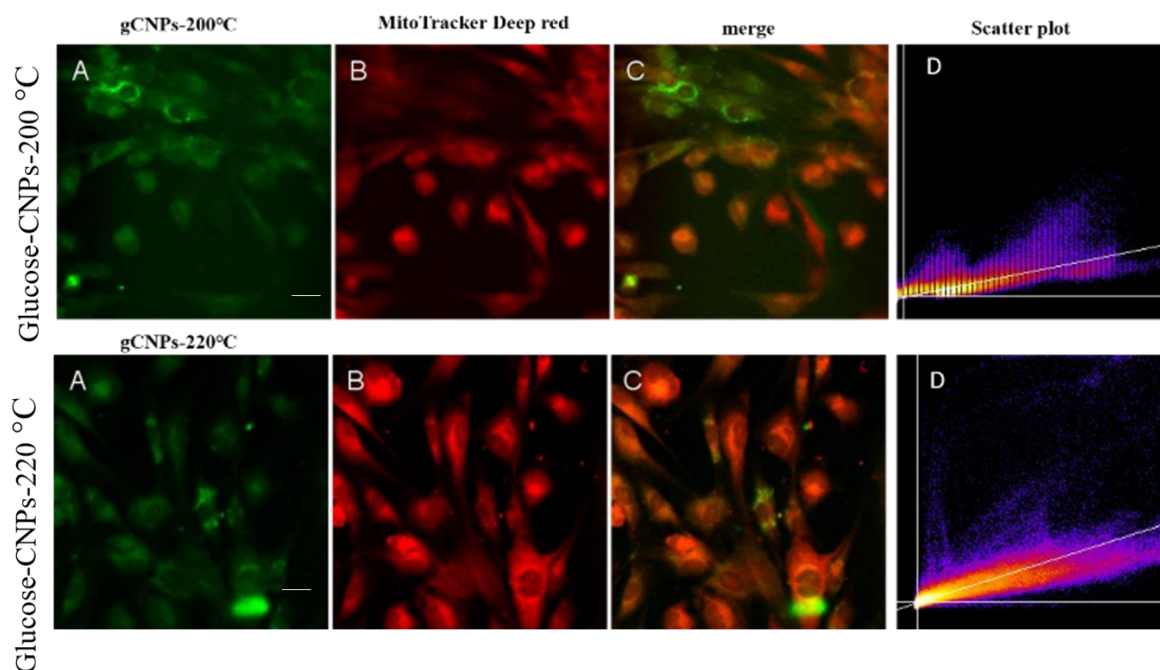


Figure 6.16. Localisation of photoluminescent CNPs in Human dermal fibroblast. (A) Confocal microscopy images of HDF incubated with (150 $\mu\text{g}/\text{ml}$) glucose CNPs heated at 200 and 220°C. Green channel (488) nm. (B) Cells were labelled with mitochondrial deep red tracker 50 nM. Mitochondrial deep red tracker channel 633 nm. (C) Merged images of both channels. (D) Scatterplot of red and green pixel intensities of the image shown in C. Scale bar 25 μm

The same studies were performed for melanoma cancer cells C8161 and results are shown in Figure 6.17 and Figure 6.18. The results show that the green fluorescence improved with increased concentration. The merged images were noticed to be yellow which was due to overlap of two green and red images. The quantities analysis of the co-localisation images resulted in the values of 0.781 and 0.052 for alginate samples at 200 and 220°C, respectively. For glucose samples, the value was calculated to be 0.31 at 200 and 220°C.

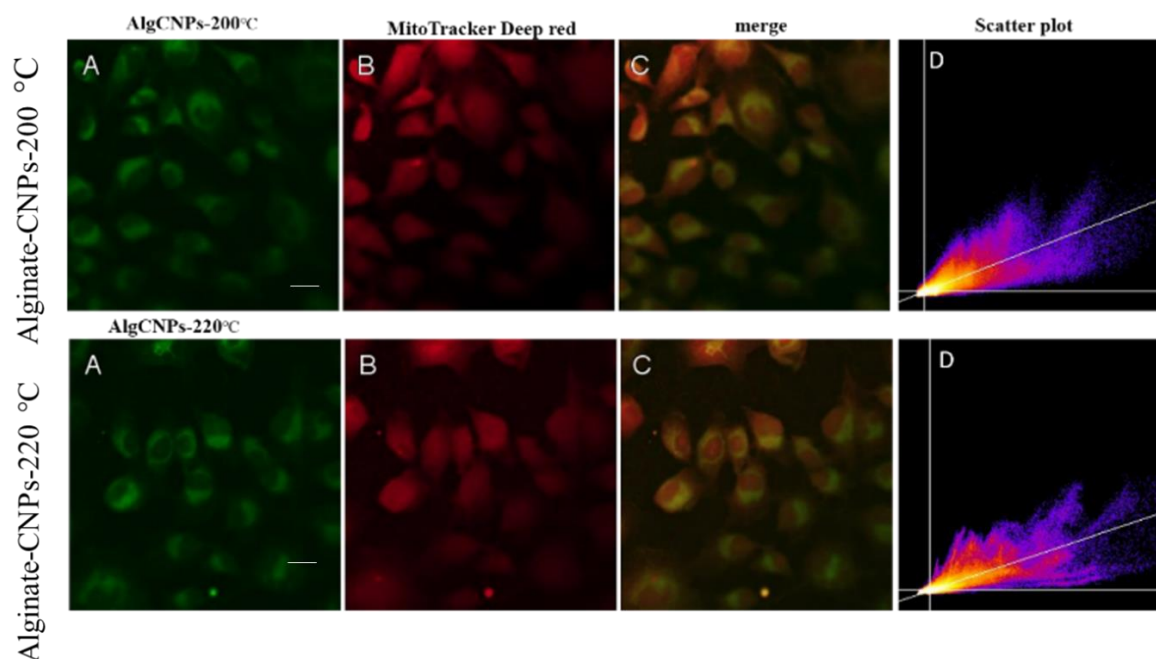


Figure 6.17. Localisation of photoluminescent CNPs in c8161. (A) Confocal microscopy images of HDF incubated with (150 $\mu\text{g}/\text{ml}$) alginate CNPs heated at 200 and 220°C. (B) Cells were labelled with mitochondrial deep red tracker 50 nM. Green channel (488) nm. (B) Mitochondrial deep red tracker channel 633 nm. (C) Merged images of both channels. (D) Scatterplot of red and green pixel intensities of the image shown in C. Scale bar 25 μm

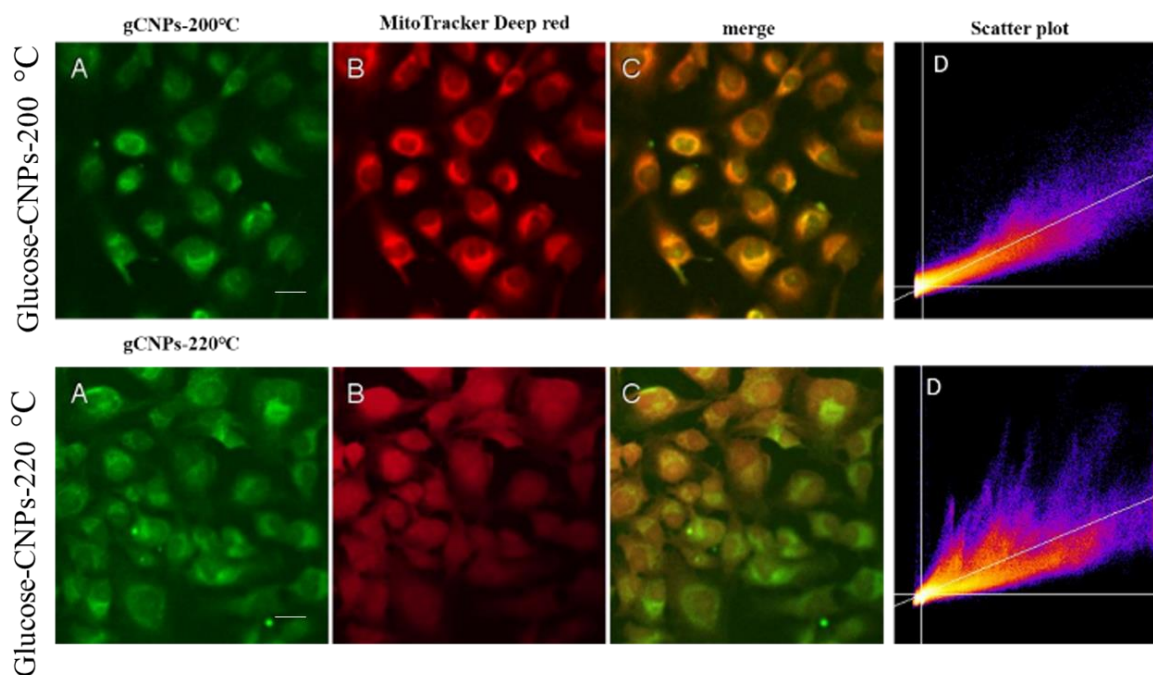


Figure 6.18. Localisation of photoluminescent CNPs in c8161. (A) Confocal microscopy images of HDF incubated with (150 $\mu\text{g}/\text{ml}$) glucose CNPs heated at 200 and 220 $^{\circ}\text{C}$. (B) Cells were labelled with mitochondrial deep red tracker 50 nM. Green channel (488) nm. (B) Mitochondrial deep red tracker channel 633 nm. (C) Merged images of both channels. (D) Scatterplot of red and green pixel intensities of the image shown in C. Scale bare 25 μm

6.5. Co-culture experiments.

Co-culture is largely used to recreate microenvironment for in vivo studied. Also, it is important to study the cellular uptake of carbon nanoparticles in co-culture to assess their targeting specificity. Co-culture experiments were carried out to investigate the fluorescence intensity of the cellular uptake by C8161 and HDF. Evolution of the culture plates over 48 hrs was observed and two optical images of 24hr and 48hrs culture evolution are shown in Figure 6.19.

Confocal microscopy images of co-cultured C8161 melanoma cancer cell and HDF cells with added alginate CNPS at 200 $^{\circ}\text{C}$ are shown in Figure 6.20 A, green fluorescence is for CNPs and red fluorescence is for deep red tracker of the two different cell lines. Figure 6.20B shows the T-test results for the data. P value of 0.8116 indicates no significant difference in the data for the two different cell types. Time course analysis of the fluorescence data show a fluctuation in the data against the incubation time for both cell type, but also an increase in the fluorescence counts with increasing incubation time.

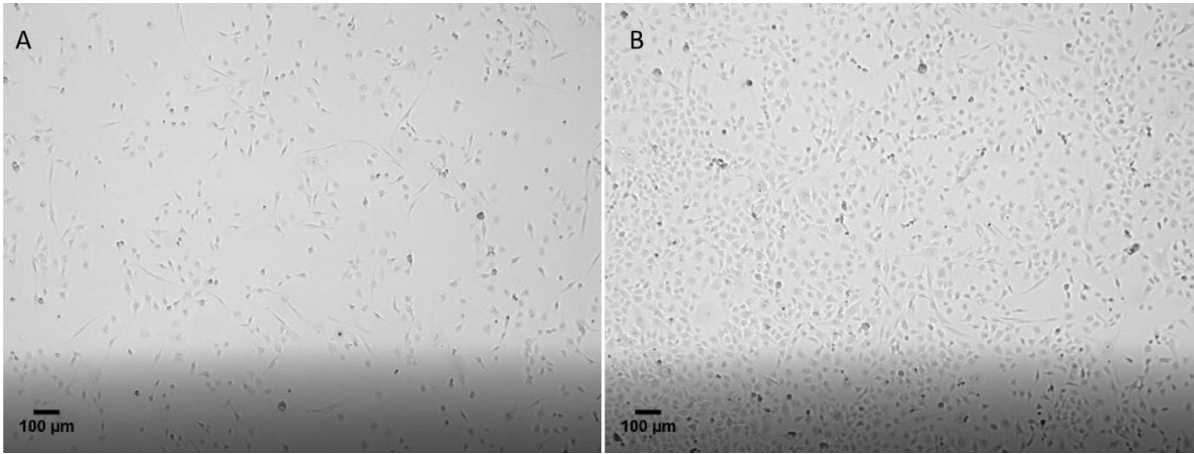


Figure 6.19. Optical images of C8161 and HDF co-cultures of ratios 1:1 during (A) 24h and (B) 48h of culture. Original magnification 10×

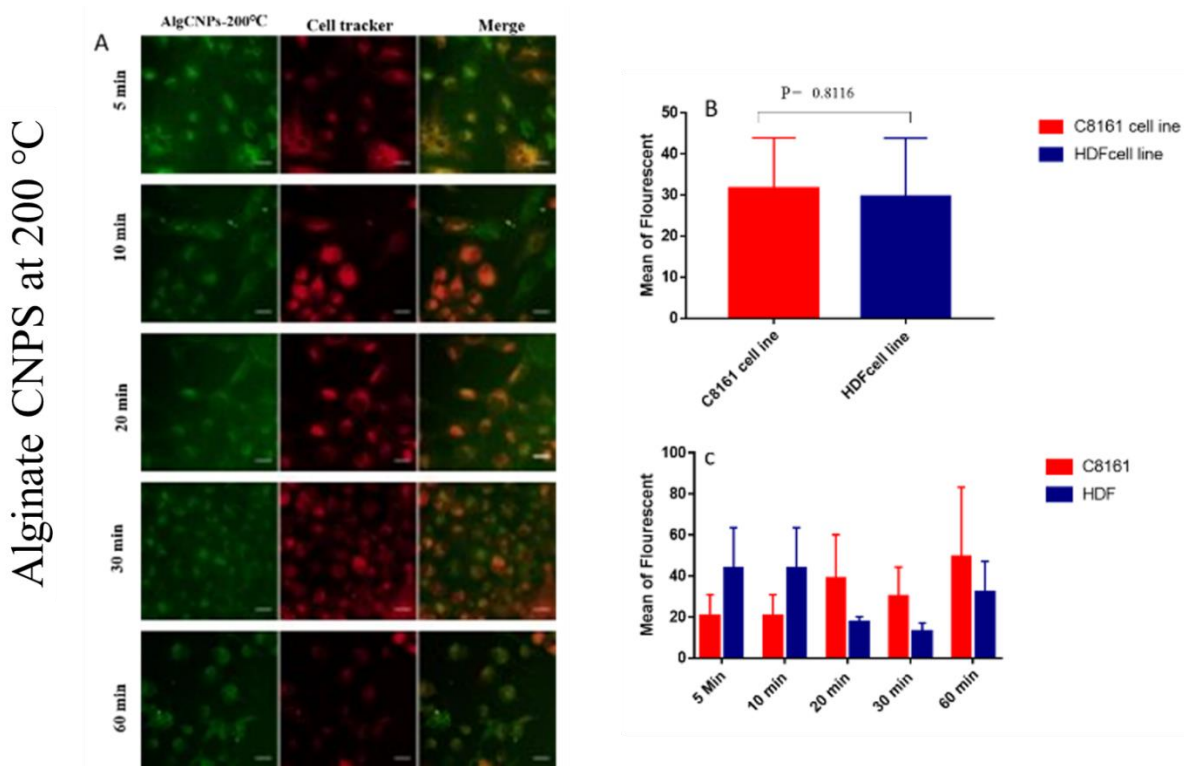


Figure 6.20. A) Co-culture of C8161 melanoma cancer cell and HDF cells incubated between 5-60 min with 150 µg alginate samples at 200°C green: (CNPs) red: deep cell tracker red, magnification: 40× scale bar 25 µm. (B) Quantitative analysis by using T-Test shows the significant differences between two cells. (C) Time course analysis for cellular uptake of alginate CNPs (200°C). Scale bar 25µm

Confocal microscopy images of co-cultured C8161 melanoma cancer cell and HDF cells with added alginate CNPs at 220°C are shown in Figure 6.21A. Quantitative analysis of the data using t-test results is presented in Figure 6.21B. In this case the P value is lower at 0.1147. There is an indication of a significant difference in the data for the two different cell types. Time course analysis of the fluorescence data show a fluctuation in the data against the

incubation time for both cell types, but more prominent for HDF. However, no significant difference in the incubation dependency for HDF cells while clear increase in fluorescence counts when the incubation reaches 60 min for C8161.

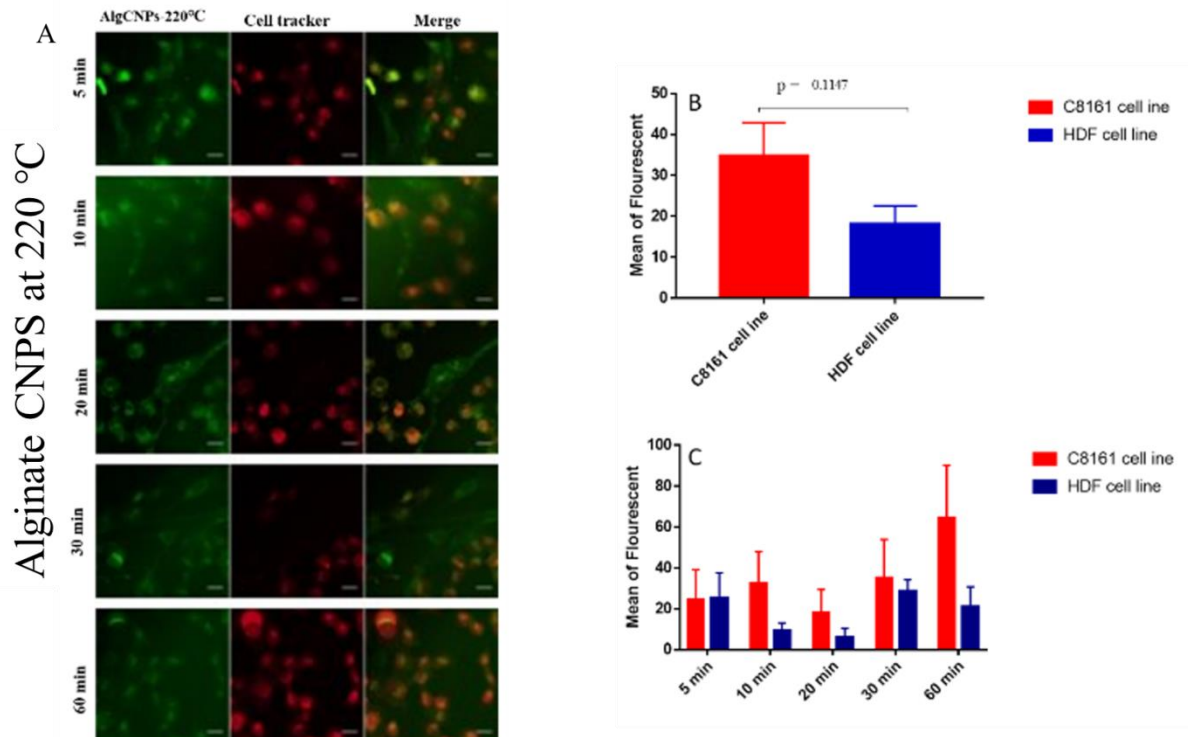


Figure 6.21. (A) Co-culture of C8161 melanoma cancer cells and HDF cells incubated for 5-60 min with 150 μg alginate sample at 220°C green: (CNPs) red: deep cell tracker red, magnification: 40 \times scale bar 25 μm . (B) Quantitative analysis by using T-Test shows the significant differences between two cells. (C) Time course analysis for cellular uptake of alginate CNPs. (220°C).

Co culture studies of glucose CNPs at 200°C added to co-cultured C8161 melanoma cancer cell and HDF cells are shown in Figure 6.22. Quantitative analysis of the data using t-test results is presented in Figure 6.21B. It is not possible to clearly say that if the difference in the data is a significant for two type cells. Time course analysis of the fluorescence data show a fluctuation in the data against the incubation time for both cell types, but a clear increase in the fluorescence increase for the samples with incubation time 60 min for both cell types.

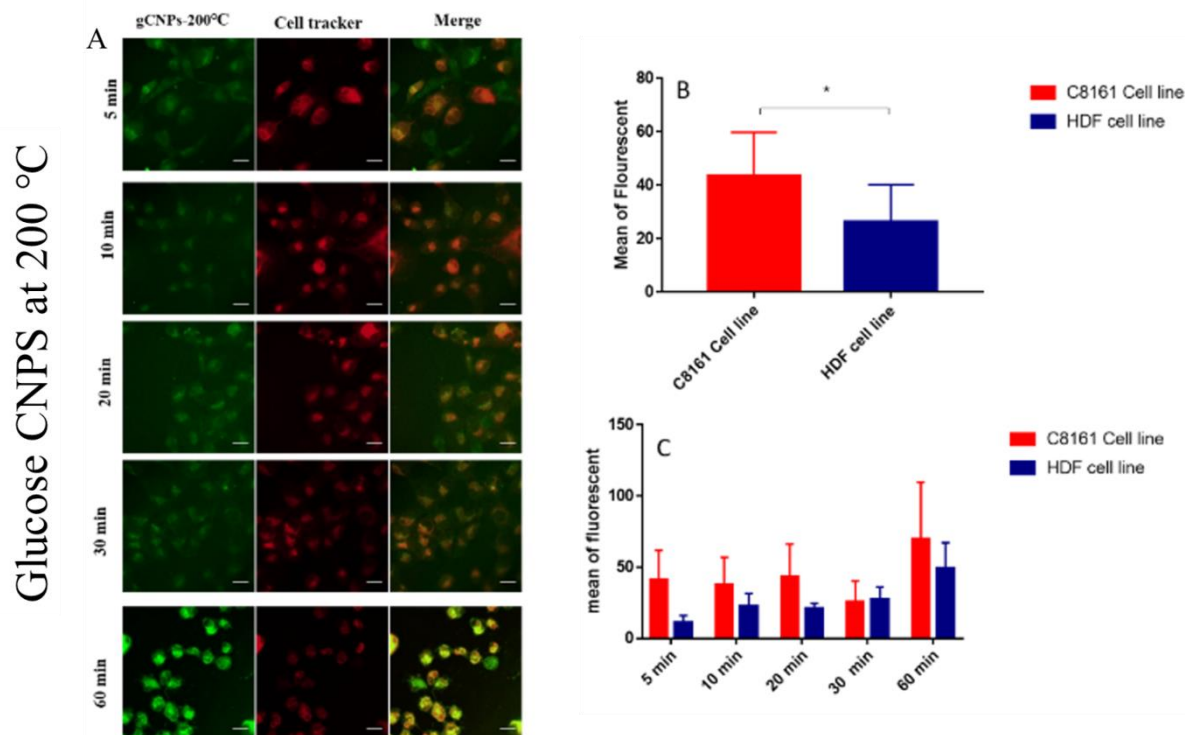


Figure 6.22. (A) Co-culture of C8161 melanoma cancer cells and HDF cells incubated for 5-60 min with 150 µg glucose 200°C green: (CNPs) red: deep cell tracker red, magnification: 40X scale bar 25µm. (B) Quantitative analysis by using T-Test shows the significant differences between two cells. (C) Time course analysis for cellular uptake of glucose CNPs (200°C).

Confocal microscopy images of co-cultured C8161 melanoma cancer cell and HDF cells with added glucose CNPS at 220°C are shown in Figure 6.23A. Quantitative analysis of the data using T-test results is presented in Figure 6.23B, which indicates a significant difference in the data for the two different cell types. Time course analysis of the fluorescence data show a gradual increase in fluorescence counts for the samples in both cell types against the incubation time.

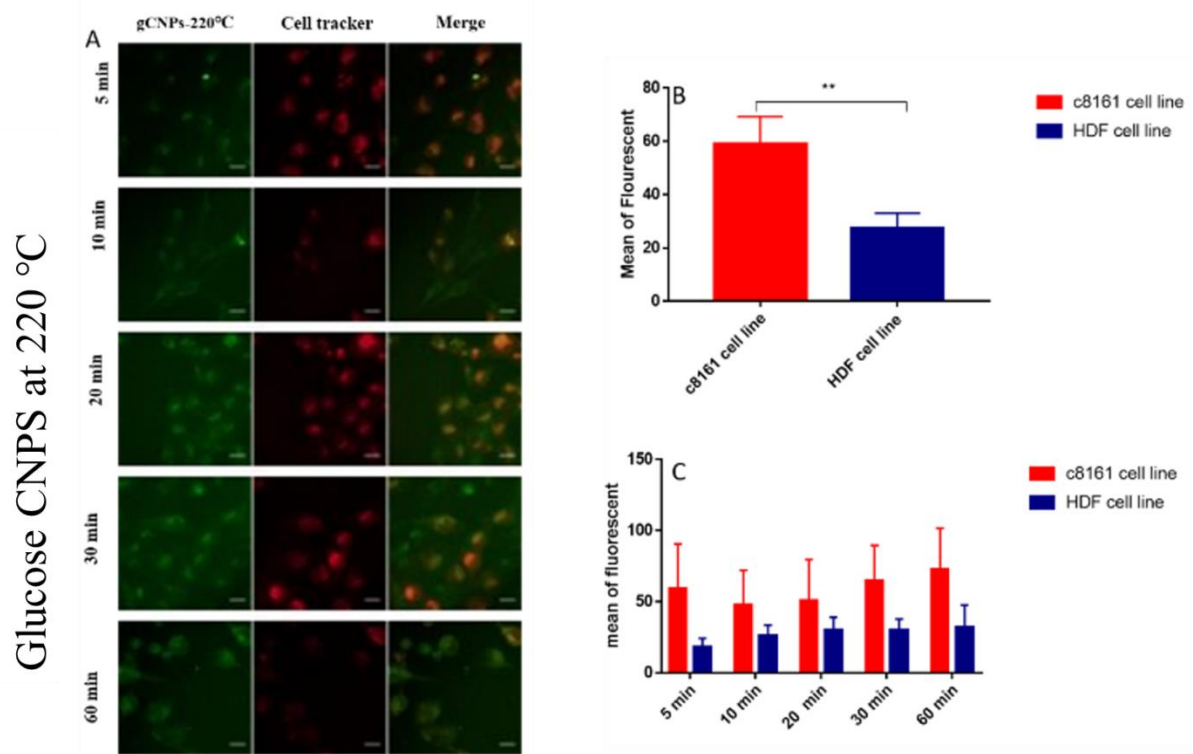


Figure 6.23. (A) Co-culture of C8161 melanoma cancer cells and HDF cells incubated for 5-60 min with 150 μg glucose 220°C green: (CNPs) red: deep cell tracker red, magnification:40X scale bar 25 μm . (B) Quantitative analysis by using T-Test shows the significant differences between two cells. (C)Time course analysis for cellular uptake of glucose CNPs (220°C).

6.6. Discussion

In general, when the particle sizes are large, cell membranes have a tendency to be impermeable. If the particle sizes are about 10-30 nm, the particles can easily cross the membrane [6]. The cells membrane act as a barrier isolating the external surroundings from the internal of the cell, permitting elements to be concentrated in cells or excluded from cells. One factor to overcome this obstacle is the endocytosis [128]. Endocytosis and diffusion have been considered as mechanisms for the cellular uptake of nanoparticles [128].

Uptake study mechanism in this project was applied using alginate and glucose as carbon sources through a bottom-up processing method. The cell internalisation of alginate and glucose CNPs was studied using melanoma cancer cells C8161, fibroblast and NIH-3T3 with particles at different concentration from 0 to 250 μg and different incubation times. Confocal microscopy was used to observe the internalisation of these particles into cells. From the images, it became evident that all cells types incubated with CNPs from glucose and alginate were visible in all the images. These particles indicate the ability of CNPs to penetrate the cells and their successful application as a staining probe for cell imaging.

The fluorescence properties of CNPs are dominated by important properties, such as low toxicity, photostability, long fluorescence lifetime, high photo stability, strong fluorescence, broad excitation spectra, narrow and tuneable emission spectra [129-132]. These superior properties of CNPs makes them desirable for bio-applications than other nanoparticles reported before. For example, gold nanoparticles are limited in applications relative to CNPs for cell imaging because of the high scattering background [26]. Also, quantum dots have limited applications due to the high toxicity of cadmium and lead. In contrast, fluorescence CNPs from glucose and alginate are non-toxic, easily synthesised and have highly fluorescent.

In the present work, confocal microscopy images were recorded at different time points of 5 min intervals. In all cell types we used, the cell started internalised within 5 minutes as indicate in the figures above. The intensity after 5 min was low compared with 60 min, meaning the fluorescent was increased by increasing the incubation time.

The intensity of the fluorescent was also dependent on the concentrations. The quantitative studies based on the confocal microscopy images were used to compare between different cell types and concentrations at different points. Fibroblast showed a higher uptake as compared to melanoma and NIH 3T3. Previous studies showed that the microscope images of

NIH 3T3 cells labelled with CDs-PEG (neutral surface charge) did not demonstrate any changes in the morphology even at higher concentrations of ($400 \mu\text{g mL}^{-1}$) [133]. Similarly, Beer and Pedersen (2006) reported that NIH-3T3 cells can uptake amphitropic murine leukaemia virus by a caveola-dependent pathway [134, 135]. This is similar to the endocytic pathway for quantum dots [124, 135]. Interestingly, the CNPs from glucose and alginate had similar behaviour and took up by NIH 3T3 but the size differences with the leukaemia virus was 110 nm, and thus, is different from our CNPs[124].

Yang and co-workers have previously used sodium alginate as a carbon source for cell imaging. However, the method for the synthesis and processing of CNPs was different from ours. The authors used an autoclave which was heated to 220°C for 12 h [77]. The result CNPs from alginate were able to label the cells but could not enter the nucleus and is similar to what we have also observed. However, using a microwave speeds up the synthesis of CNPs within five minutes at 220°C , which is much faster than autoclave technique and shown fast uptake in both carbon nanoparticles [13].

Preliminary experimental work focused on the imaging of human breast cancer MCF-7 cells using CNPs capped with poly(propionyl-ethylenimine-co-ethylenimine) [136]. After incubation cells with the CNPs in the media followed by washing, it was discovered the cell membrane and cytoplasm displayed vivid green fluorescence. It was confirmed that the particles were taken up by the cells through endocytosis. At low temperature (4°C), uptake of the nanoparticles did not appear. Cellular imaging of NPs (2–6 nm) has also been achieved in Ehrlich ascites carcinoma cells [137]. For the imaging, there was no need for any surface passivation. Similarly, imaging experiments have also been performed for *E. Coli* bacteria and murine progenitor cells. In the studies, fluorescence was photostable and was not affected by photobleaching [138]. In another study, CNPs could be passed through the nuclear membrane of cells through their attachment to proteins or peptides, allowing the CNPs on the nuclei to be effectively researched [2].

For a biological label to be suitable for in vivo studies, it needs to be non-toxic, biocompatible, photostable and sufficiently bright for easy detection. Despite the cytotoxicity issues associated with other carbon-based nanomaterials such as carbon nanotubes, research in CNPs suggest few if any safety concerns. Several studies have shown that the CNPs pose minimal toxicity risks at concentrations permissible for bio-imaging purposes [139]. For example, Sun et al. have tested the in vivo effects of CNPs in a murine model [140].

Following CNPs intravenous exposure, no adverse signs were observed after 4 weeks. The organs showed no abnormalities which in itself brings successful *in vivo* bioimaging trials of CNPs. The ease with which NPs migrated during *in vivo* studies was an indicative of numerous translocation processes and permitted infiltration of cells and tissues. Murine models had been produced to test *in vivo* efficacy of CNPs capped with polyethylene glycol (PEG) [141]. Within the studies, CNPs migrated to the auxiliary lymph nodes following intradermal delivery. Interestingly after the intravenous application, CNPs travelled around the body *via* the bloodstream. Photoluminescence emission was observed from the urine after 3 hours of injection. After harvesting the organs, CNPs were found to be accumulated in the kidneys. Contrary to a previous study, CNPs were found in liver rather than kidney which was attributed to the presence of PEG at the surface [140]]. This decreased protein affinity of the NPs, causing them to pass quickly to the kidney for excretion.

It is becoming ever more important to evaluate the cellular uptake of CNPs in a co-culture to determine their targeting ability. Each cell lines had different characteristic and environment when interacting with particles. Herein, CNPs from glucose and alginate were cultured with fibroblast and melanoma cancer cells in a 1:1 ratio. The analysis showed that the particles were taken up by both melanoma and fibroblast. However, in a co-culture study, it was noticed from the quantitative analysis that the fluorescent intensity was higher in melanoma compared with fibroblast. A previous study has been reported the co-culture between MCF-7 breast cancer cells and human dermal fibroblast (hFIB) using different ratios. The cells were incubated with chitosan–histidine arginine (CH-H-R) nanoparticles [142]. There was a good interaction between the two cell lines. The cellular uptake was significantly higher for MCF-7 breast cancer than (hFIB) irrespective of the ratios. These findings are in in-line with the current results obtained for glucose and alginate based CNPs. The statistical analyses based on confocal microscopy indicated a higher percentage of melanoma cancer cells than human dermal fibroblast. Gaspar and co-workers have suggested that many other factors may also affect the cellular uptake in a co-culture module, for example the number of seeding in both cells lines which were absent in the present work. As the number of fibroblast increased, it was found that fewer cancerous cells internalised nanoparticles [142].

After the observation that CNPs were taken up by the cells, it became obvious to study the localisation of these particles in the cells. Co-localisation experiments were studied using confocal microscopy images. After the cells were labelled with deep red Mitotracker, our results revealed that the nanoparticles were not accumulated in the mitochondria based on the

acquired quantitative information. On the contrary, the CNPs derived from folic acid had been shown to target mitochondrial once incubated with KB cells (oral cancer cells) [20]. Their results revealed that F-FNP treated KB cells enhanced the merged fluorescence (LysoTracker with Mitotracker) after increasing the incubation time. Strong overlap of FCNPs with the lysotracker indicated the accumulation [143].

6.1 Summary

Cellular uptake mechanism of CNPs exhibiting exceptional properties have been of tremendous interest worldwide. The mechanism of the cellular uptake by CNPs is still not clear due to the effect of many properties such as size, shapes, surface charge, emission and excitation, absorbance etc.

This chapter was focuses on the mechanism uptake of CNPs based on different cell lines (melanoma cancer cells C8161, human dermal fibroblast and NIH-3T3 fibroblast). Also, the effects of different incubation times along with different concentrations have been studied. We studied the internalisation of different CNPs into cells using confocal microscopy. Analysing the fluorescence intensity of each image to understand the differences between different type of particles and different cell line was successfully applied. Our work shows that CNPs from glucose and alginate were able to label the cells and can be used for bio-imaging applications. Our study found that CNPs can easily and readily enter the cells giving green fluorescence under the confocal microscopy. Also, localization studies provide evidence that the particles are not targeting the mitochondria and it is interring directly with the cytoplasm. The cancer cells uptake was faster by CNPs than fibroblast. It is important to mention that co- culture experiments are relatively straight forward and inexpensive and can be easily applied to determine the biological activity of nanoparticles in vitro.

7. Chapter Seven: General Discussion, Conclusion and Future Work

7.1. Discussion

The fate of nanoparticles for biomedical applications depends on the local anatomy and physiology of the exposure route, along with the surface and physical properties of the nanoparticles[144]. Alternative to heavy-metal free quantum dots, CNPs have emerged in last few years as a viable non-toxic and highly fluorescent probe for bio-applications because of high water solubility, excellent biocompatibility, high photostability, flexibility in surface modification with various chemicals and good cell permeability[2, 145]. Considering the CNPs are made up of only carbon with inherent fluorescence properties, so their toxicity should be minimal. Comparing with noble metal nanoparticles such as gold and silver, CNPs are generally brighter and are not prone to surface oxidation. Their potential for use as replacements of toxic metal-based quantum dots is significant [146]. Before CNPs can be truly considered for bio-applications, low-cost and facile methodologies resulting in their synthesis and characterisation need to be investigated.

Herein, we have conclusively shown that after heating inexpensive precursors (glucose and sodium alginate) at 220°C in a microwave, good-quality CNPs were readily obtained only after 5 minutes. This bottom-up approach allowed high product yield and high effective product rate for the large amounts of CNPs within a short time. Due to amphiphilic nature of the polysaccharides used, both precursors can assemble into ordered aggregates within aqueous environment and have molecular chains which can be chemically modified and adapted. The current method is a significant improvement from previous reported methods where thermal oxidation of citrate salts in the presence of long chain amines was carried out to produce fluorescent CNPs. [147]. However, this multi-step process was slow and expensive and had little control the particle sizes. Through the use of uniform heating in the microwave herein, the reaction was accelerated to yield surface rich CNPs to ensure their availability for conjugation with the biomolecules of interest.

The toxicity and bio-applications of CNPs need understanding in the framework of the material characterisation. If the materials from a physical and chemical perspective are not understood, it becomes challenging to interpret exposure or toxicity measurements [148]. One of the important characteristics of resulting CNPs was their strong fluorescence which was a result of emissive traps at the nanoparticle surfaces. It is worth emphasising that due to relatively large size of CNPs, it is highly unlikely quantum confinement process will dominate the excitation-dependent fluorescent properties. In the absorption spectra, glucose

based samples exhibited $n-\pi^*$ and $\pi-\pi^*$ transitions associated with an aromatic π system which is consistent with carbon nanoparticles synthesized by carbonization of chitosan and glucose [149, 150]. This band has already been recognized as being related to a typical absorption peak π aromatic system, similar to those derived from polycyclic aromatic hydrocarbons [151]. Increasing the growth temperature from 200 to 220 °C resulted improved absorption characteristics of glucose based CNPs. For alginate samples, a much reduced absorption peak was observed which vanished after increasing the growth temperature to 220°C, possibly due to the absence of a conjugated structure within the alginate system . In addition, the absence of the absorption on the alginate could be the reaction time is not enough to form these particles [111].

For the Raman spectroscopy, showed two different Raman, which corresponds to sp^2 carbon (G band) with D-band defects on Carbon NPs [152]. The range D is related to the oscillations of the carbon atoms within disordered graphite. The band G is set to the graphite mode E_{2g} , which is related to the vibration of the carbon atoms sp^2 in a hexagonal two-dimensional grid. Several papers reported Raman spectra of carbohydrates affected by product concentrations and wavelength of the excitation laser [153, 154].

The X-ray powder diffraction studies confirmed the formation of amorphous CNPs which was further corroborated by the absence of lattice planes in high-resolution transmission electron microscope images. As a result of Ostwald ripening process, increasing growth temperature resulted in much larger particle sizes (133.4 ± 22.8 vs. 174 ± 30.8 nm) for glucose based CNPs. Interestingly, size estimated during dynamic light scattering for the glucose were also similar (within standard deviation), i.e. 247 (at 200°C) and 386 nm (at 220°C). For alginate samples, CNPs size determined were 145 nm at 200°C and 289 nm at 220°C. Apart from the sizes, polydispersity index values for glucose samples were narrower than alginate samples, reflecting narrow size distributions along with the uniformity of CNPs.

As the NPs enter the body, they are expected to cause a wide range of biological responses, such as the formation of reactive oxygen species, change of the cell cycle, and abnormality in cell behaviour, cell adhesion and migration [155]. For targeted bio-applications of CNPs, an understanding of their toxicity behaviour is essential, including issues on potential defunctionalisation of the CNPs in biological systems that might result in the exposure of the carbon core. Many studied have been conclude that CNPs pose minimal toxicity risks at concentrations permissible for bio imaging applications [2].

Following preparation and characterisation of CNPs, biocompatibility and cytotoxicity of resulting materials on melanoma cancer cells and human dermal fibroblasts were investigated. Irrespective of the samples, biocompatibility experiments with human dermal fibroblasts showed an increase in the cell viability during 48 hours after which the viability was decreased (after 72 hours). This reduction in cell viability was attributed to the cell death. Similarly, CNPs derived from bagasse which is that the fibre left over when the juice has been squeezed out of sugarcane stalk, also showed similar visible patterns, suggesting good biocompatibility and uptake by the living cancer cells [156]. With melanoma cancer cells, the cell visibility was also reduced after long incubation time at high concentrations. No real visibility differences between glucose and alginate CNPs were noted. In parallel, tests on melanoma cells were also carried out to determine the toxicity of CNPs. The CNPs derived from the glucose samples at 200°C were found to be less toxic even at high concentrations. On the contrary, alginate based CNPs showed virtually no effect under various concentrations. Only found 48 hours, a minor change was observed. Surprisingly, for alginate sample at 220°C, the cell viability was improved relative the one prepared at 200°C. No effect of different growth temperatures was observed for CNPs.

For wound healing assays, cultures of melanoma and CNPs derived from glucose and alginate were tested at various periods using a scratch technique. From the Image J analysis, no difference was visible between the control and CNPs. After 24 hours, the scratch area was completed sealed. During the cell movements, it was identified that the single human dermal fibroblasts cells moved from the edges to area around the scratch and filled the scratch. The rate at which the closing of scratches is carried out further determines the potential of CNPs for wound healing applications. In general, increasing the cell migration in the wound area generally leads to enhance desirable wound healing effects. From the results, it became obvious that the scratching filling was considerably faster for glucose based CNPs and their movement was slightly faster in medium. Similar cell migration study have been done with onion carbon Dots (OCND), it was observed that OCND was migrate faster than the control and complete closure of the wound in 24 hours compared to the control.[94].

Cellular uptake and trafficking mechanisms of CNPs is *critical* in designing molecular mechanisms to elucidate the molecular interactions promoting CNPs uptake. Through understanding of the processes, it is possible to engineer the CNPs that do not penetrate cells

and are selectively taken up by the specific cells. Microscopy especially fluorescence and confocal is an established technique of observing the microstructures and molecules within cells and quantum dots are increasingly being used as fluorescent labels for cellular and molecular imaging. They can facilitate in the visualisation of cellular structures and receptors in both fixed and live cells. In the present work, human dermal fibroblasts, melanoma and NIH 3T3 were readily up-taken by the CNPs and migrated to the cytoplasm through the endocytosis. The process was complete within 5 minutes. In general, it was found that the concentration strongly affects the quality of green emission. We noticed that for melanoma, its fluorescence spectra were decreased which was possibly due to different number of cells. Incubation time also affected the fluorescence signals which could be improved by increasing the incubation time. The localisation of CNPs was estimated using Pearson's correlation coefficient which was calculated to be 0.815 and 0.786 for alginate based CNPs at 200 and 220°C, respectively. For glucose based CNPs, the values are marginally higher, i.e. 0.854 at 200°C and 0.851 at 220°C and indicate that significant amount of CNPs did not accumulated in the mitochondria. This was further consolidated in colonisation experiments involving melanoma cells which according to Pearson's correlation coefficient confirmed the CNPs were not located in the mitochondria. It was established that high uptake of CNPs occurs through the cell membranes and cytoplasm. Moreover, increasing the concentration of CNPs does not have any bearing on the exact location of CNPs.

The fluorescence intensity after the uptake by human dermal fibroblasts and C8161 melanoma cells was probed in co-cultured experiments. This powerful concept was successfully used to establish correlations between the cell cultures and in vivo systems. After 48 hours, the cells were restricted to *adherent cell co-culture* alone. At large, it was found that the growth of C8161 melanoma was much faster than human dermal fibroblasts. The fluorescence emission within the experiments was found to be dependent on the incubation time as well as the type of cells. To illustrate the point, increasing the incubation time from 5 to 60 minutes increased the fluorescence intensity and a slight increase in fluorescence emission for C8161 melanoma than fibroblasts was observed.

7.2. Conclusions

This thesis demonstrates that CNPs is an important class of carbon-based nanomaterials which possess a number of properties that render them useful in a vast range of applications. The CNPs offer in particular unprecedented opportunities for monitoring and manipulating

biological systems. To realize the full potential of technology, understanding how CNPs precisely interact with biological systems is of paramount importance. The work herein initially demonstrated how low-cost and readily available starting materials of glucose and sodium alginate could be effectively used in a bottom-up process to yield CNPs. The CNP sizes depended on the starting precursors where samples from glucose were found to be larger with narrow size distribution than alginate ones. Emission spectra were dependent on the excitation energies used. The UV-Vis spectra for CNPs derived from glucose were consistent of an aromatic π system and their resulting light absorption properties improved with increased growth temperature. Due to absence of a conjugated structure in alginate, resulting CNPs exhibited much reduced absorption properties which vanished after increasing growth temperature. All the CNPs samples were found to be amorphous based on the X-ray power diffraction and high-resolution transmission electron microscope observations.

Investigation of how the NPs interact with cells and the subsequent intracellular stability is the first step towards understanding the true nature of the NP-mediated biological effects. Biocompatibility tests on various cell types showed an increased cell visibility. The CNPs showed no toxic effects on melanoma, even at high concentrations. Using scratch tests, cultures of melanoma containing various CNPs were tested for wound heal analysis which after 24 hours showed the filling of the gap. It was identified during cell movements that human dermal fibroblasts cells moved from the edges to scratch area and filled the gap between the scratch. The rate at which the gaps were filled, the glucose based CNPs covered much quickly than alginate based CNPs. The work proves to be an important development for biocompatible and traceable imaging probes.

The studies further showed that human dermal fibroblasts, melanoma and NIH 3T3 were readily up-taken by the CNPs within five minutes, which migrated to the cytoplasm through the endocytosis. Through the analysis, it was determined that the quality of emitted fluorescence strongly depended on the CNP concentration which was further improved through the increasing the incubation time. The Pearson's correlation coefficient values indicated that CNPs did not accumulate in the mitochondria and were corroborated by the colonisation experiments. The work also demonstrated that the uptake of CNPs happens through the cell membranes and cytoplasm.

In summary, the straightforward synthesis and bio-applications demonstrated in this thesis shows the effectiveness and the versatility of CNPs. It illustrates that non-toxic CNPs can be

synthesised and modified to attain properties desirable for target biological applications. In future, it is expected the technology will provide a general pathway for developing non-toxic biomedicines and improved surfaces as traceable imaging probes inside living cells.

7.3. **Future Work**

As stated previously, different types of nanoparticles will enter cells by different pathways; however, the mechanism of this uptake remains unclear. Studying the cellular uptake of different nanoparticles on different types of cells will improve our understanding of the cellular uptake mechanism. This can be done by investigating the many parameters of nanoparticles that are involved in cell targeting.

Although several aspects of cellular uptake have been explored in this thesis, further investigation is needed to link carbon nanoparticles parameters' effect on it. For example, in this study, the transmission electron microscopy (TEM) images of carbon nanoparticles from alginate were not successfully obtained due to the aggregation of nanoparticles. Therefore, further study is required to accurately determine the size of alginate carbon nanoparticles. In addition, TEM could be used to determine the intracellular localisation of the nanoparticles through high-resolution images of the subcellular structures. Numerous studies have used surface passivation to produce stronger fluorescence emission following excitation. [157-159] However, that technique was not considered in this thesis due to the high fluorescence that was recorded on the fluorimeter and confocal microscopy when the CNPs were incubated with different types of cells, even though investigation of the effect of PEGylating would be interesting. It would also be interesting to investigate the changing pH of the solutions to see the effect on the fluorescence emission and excitation of the nanoparticles.

In chapter five, the main aim was to study both the toxicity and the biocompatibility of nanoparticles. Further cytotoxicity studies are needed to determine the effect of the high concentration of CNPs on the internalisation of the cells. It might be valuable to increase the concentration of carbon NPs to investigate when this particle would become harmful to the cells as well as to study the effect of nanoparticles' charges on cellular uptake. Several studies have reported the effect of physiochemical properties of nanoparticles, such as surface charge, surface functionalisation, shapes and size, on the cellular uptake of nanoparticles because they play an important role in understanding direct interaction with the cells. [160]

Chapter six focused on the cellular uptake of nanoparticles on different types of cells, such as melanoma C8161, human dermal fibroblast and the NIH 3T3 cell line. It is important to investigate the mechanism of cellular uptake in much greater detail. Some studies have found that there is a different pathway for internalising the cells, depending on many properties such as shapes, size and surface charge [160]. To understand the endocytosis pathway of carbon nanoparticles, inhibitors are needed to identify the effect on the cellular uptake. Although a localisation study has been done on melanoma and human dermal fibroblast, it would be beneficial to conduct a study on NIH 3T3 to include all the different types used in this thesis. Another nanoparticle localisation study could use transferrin (clathrin) or dextran (micropinocytosis) to localise both the endosomes and the lysosomes.

There are a wide range of advanced imaging techniques available for visualising the internalisation of nanoparticles into cells. Confocal microscopy was successfully used in this thesis; it produced clear and detailed images of the nanoparticles' uptake. Nevertheless, it would be interesting to utilise a technique that could obtain even more detail, such as atomic force microscopy (AFM) and scanning ion-conductance microscopy (SICM). Scanning ion-conductance microscopy (SICM) technique provides information on nanoscale images of nanoparticles' cellular uptake with very small regions of cell membrane; its advanced system can create images in real time on live cells. It has also been reported that combined fluorescence and scanning probe techniques can offer an overview of the interactions on both the nano- and micro-scales [161, 162].

Another future improvement could also be the use of a better quantitative analysis method, such as flow cytometry combined with confocal microscopy, to measure nanoparticles' cellular uptake and generate reliable data.

Finally, the biological applications of these particles, as bio-imaging has proven in this thesis, include low cytotoxicity, biocompatibility and photo stability, which make it ideal for labelling. To go a step further, it would be interesting to take advantage of these particles by investigating them in *in vivo* studies for both diagnostic and therapeutic purposes.

References

1. Ibarra-Ruiz, A.M., D.C. Rodríguez Burbano, and J.A. Capobianco, Photoluminescent nanoplatforms in biomedical applications. *Advances in Physics: X*, 2016. **1**(2): p. 194-225.
2. Baker, S.N. and G.A. Baker, Luminescent carbon nanodots: emergent nanolights. *Angew Chem Int Ed Engl*, 2010. **49**(38): p. 6726-44.
3. Riggs, J.E., et al., Strong Luminescence of Solubilized Carbon Nanotubes. *Journal of the American Chemical Society*, 2000. **122**(24): p. 5879-5880.
4. Liu, J.H., et al., Fluorescent carbon dots and nanodiamonds for biological imaging: preparation, application, pharmacokinetics and toxicity. *Curr Drug Metab*, 2012. **13**(8): p. 1046-56.
5. Li, L., et al., Focusing on luminescent graphene quantum dots: current status and future perspectives. *Nanoscale*, 2013. **5**(10): p. 4015-4039.
6. Zuo, P., et al., A review on syntheses, properties, characterization and bioanalytical applications of fluorescent carbon dots. *Microchimica Acta*, 2016. **183**(2): p. 519-542.
7. Esteves da Silva, J.C.G. and H.M.R. Gonçalves, Analytical and bioanalytical applications of carbon dots. *TrAC Trends in Analytical Chemistry*, 2011. **30**(8): p. 1327-1336.
8. Li, H., et al., Carbon nanodots: synthesis, properties and applications. *Journal of Materials Chemistry*, 2012. **22**(46): p. 24230-24253.
9. Jiyang, F. and C.P. K., Group IV Nanoparticles: Synthesis, Properties, and Biological Applications. *Small*, 2010. **6**(19): p. 2080-2098.
10. Zänker, H. and A. Schierz, Engineered Nanoparticles and Their Identification Among Natural Nanoparticles. *Annual Review of Analytical Chemistry*, 2012. **5**(1): p. 107-132.
11. Singh, A.K., 'Structure, synthesis and application of nanoparticles.' In: *Engineered Nanoparticles: Structure, Properties and Mechanisms of Toxicity*. 2016.
12. E, Y., et al., Electrochemically generated fluorescent fullerene[60] nanoparticles as a new and viable bioimaging platform. *Journal of Materials Chemistry*, 2011. **21**(3): p. 819-823.
13. Eatemadi, A., et al., Carbon nanotubes: properties, synthesis, purification, and medical applications. *Nanoscale Research Letters*, 2014. **9**(1): p. 393.

14. Yu, L., et al., Catalytic synthesis of carbon nanofibers and nanotubes by the pyrolysis of acetylene with iron nanoparticles prepared using a hydrogen-arc plasma method. *Materials Letters*, 2009. **63**(20): p. 1677-1679.
15. Lim, S.Y., W. Shen, and Z. Gao, Carbon quantum dots and their applications. *Chemical Society Reviews*, 2015. **44**(1): p. 362-381.
16. Yin, P.T., et al., Design, Synthesis, and Characterization of Graphene–Nanoparticle Hybrid Materials for Bioapplications. *Chemical Reviews*, 2015. **115**(7): p. 2483-2531.
17. Giles, J. Scientists create fifth form of carbon. 23 March 2004; Available from: <http://www.nature.com/news/1998/040322/full/news040322-5.html>.
18. Lai, P., et al., Overview of the preparation of organic polymeric nanoparticles for drug delivery based on gelatine, chitosan, poly(d,l-lactide-co-glycolic acid) and polyalkylcyanoacrylate. *Colloids and Surfaces B: Biointerfaces*, 2014. **118**: p. 154-163.
19. Alina, A.K., et al., Luminescent carbon nanoparticles: synthesis, methods of investigation, applications. *Russian Chemical Reviews*, 2017. **86**(11): p. 1157.
20. Sun, X., et al., Microwave-assisted ultrafast and facile synthesis of fluorescent carbon nanoparticles from a single precursor: preparation, characterization and their application for the highly selective detection of explosive picric acid. *Journal of Materials Chemistry A*, 2016. **4**(11): p. 4161-4171.
21. Yih, T.C. and M. Al-Fandi, Engineered nanoparticles as precise drug delivery systems. *Journal of Cellular Biochemistry*, 2006. **97**(6): p. 1184-1190.
22. Sun, T., et al., Engineered Nanoparticles for Drug Delivery in Cancer Therapy. *Angewandte Chemie International Edition*, 2014. **53**(46): p. 12320-12364.
23. Shang, L., K. Nienhaus, and G.U. Nienhaus, Engineered nanoparticles interacting with cells: size matters. *Journal of Nanobiotechnology*, 2014. **12**(1): p. 5.
24. Mu, Q., et al., Chemical Basis of Interactions Between Engineered Nanoparticles and Biological Systems. *Chemical Reviews*, 2014. **114**(15): p. 7740-7781.
25. T, T., Commercial scale production of inorganic nanoparticles *Int. J. Nanotechno*, April 2009: p. 567–78.
26. Bhunia, S.K., et al., Carbon Nanoparticle-based Fluorescent Bioimaging Probes. *Scientific Reports*, 2013. **3**: p. 1473.
27. (Ed.), D.P.N., *Recent Advances in Graphene Research*. Soumyajyoti Haldar and Biplab Sanyal. 2016: Intech

28. Feng, L. and Z. Liu, Biomedical Applications of Carbon Nanomaterials, in Biomedical Applications and Toxicology of Carbon Nanomaterials. 2016, Wiley-VCH Verlag GmbH & Co. KGaA. p. 131-162.
29. Dresselhaus, M.S., G. Dresselhaus, and P.C. Eklund, Chapter 7 - Crystalline Structure of Fullerene Solids, in Science of Fullerenes and Carbon Nanotubes. 1996, Academic Press: San Diego. p. 171-223.
30. Kroto, H.W., et al., C₆₀: Buckminsterfullerene. Nature, 1985. **318**(6042): p. 162-163.
31. Zhang, F., Y. Fang, and X. Zhang, Fluorescence emission properties of C₆₀ nanoparticles. Spectrochimica Acta Part A: Molecular and Biomolecular Spectroscopy, 2013. **106**: p. 242-246.
32. Jeong, J., et al., Color-Tunable Photoluminescent Fullerene Nanoparticles. Advanced Materials, 2012. **24**(15): p. 1999-2003.
33. Wei, P., et al., C₆₀(Nd) nanoparticles enhance chemotherapeutic susceptibility of cancer cells by modulation of autophag. Vol. 21. 2010. 495101.
34. Shi, J., et al., Fullerene (C₆₀)-based tumor-targeting nanoparticles with “off-on” state for enhanced treatment of cancer. Journal of Controlled Release, 2016. **235**: p. 245-258.
35. Lee, A.J., et al., Bright Fluorescence from Individual Single-Walled Carbon Nanotubes. Nano Letters, 2011. **11**(4): p. 1636-1640.
36. Zhou, J., et al., Highly efficient fluorescent multi-walled carbon nanotubes functionalized with diamines and amides. Journal of Materials Chemistry, 2012. **22**(24): p. 11912-11914.
37. Popov, V.N., Carbon nanotubes: properties and application. Materials Science and Engineering: R: Reports, 2004. **43**.
38. Liu, X., et al., Design of Covalently Functionalized Carbon Nanotubes Filled with Metal Oxide Nanoparticles for Imaging, Therapy, and Magnetic Manipulation. ACS Nano, 2014. **8**(11): p. 11290-11304.
39. Chen, J., et al., Functionalized Single-Walled Carbon Nanotubes as Rationally Designed Vehicles for Tumor-Targeted Drug Delivery. Journal of the American Chemical Society, 2008. **130**(49): p. 16778-16785.
40. Baker, S.N. and G.A. Baker, Luminescent Carbon Nanodots: Emergent Nanolights. Angewandte Chemie International Edition, 2010. **49**(38): p. 6726-6744.

41. Mao, X.-J., et al., Study on the fluorescence characteristics of carbon dots. *Spectrochimica Acta Part A: Molecular and Biomolecular Spectroscopy*, 2010. **75**(2): p. 553-557.
42. Zeng, Y.-W., et al., N, S co-doped carbon dots with orange luminescence synthesized through polymerization and carbonization reaction of amino acids. *Applied Surface Science*, 2015. **342**: p. 136-143.
43. Qu, D., et al., Tailoring color emissions from N-doped graphene quantum dots for bioimaging applications. *Light-Science & Applications*, 2015. **4**.
44. Ding, H., et al., DNA–Carbon Dots Function as Fluorescent Vehicles for Drug Delivery. *ACS Applied Materials & Interfaces*, 2015. **7**(12): p. 6889-6897.
45. Feng, T., et al., Charge-Convertible Carbon Dots for Imaging-Guided Drug Delivery with Enhanced in Vivo Cancer Therapeutic Efficiency. *ACS Nano*, 2016. **10**(4): p. 4410-4420.
46. Roy, P., et al., Photoluminescent carbon nanodots: synthesis, physicochemical properties and analytical applications. *Materials Today*, 2015. **18**(8): p. 447-458.
47. Guo, Y., et al., Thermal treatment of hair for the synthesis of sustainable carbon quantum dots and the applications for sensing Hg²⁺. *Scientific Reports*, 2016. **6**: p. 35795.
48. Chen, W., et al., Rapid Synthesis of Carbon Dots by Hydrothermal Treatment of Lignin. *Materials*, 2016. **9**(3): p. 184.
49. Wang, Q., et al., Microwave-assisted synthesis of carbon nanodots through an eggshell membrane and their fluorescent application. Vol. 137. 2012. 5392-7.
50. He, G., et al., Rapid solid-phase microwave synthesis of highly photoluminescent nitrogen-doped carbon dots for Fe(3+) detection and cellular bioimaging. *Nanotechnology*, 2016. **27**(39): p. 395706.
51. Zhang, X., et al., Rapid microwave synthesis of N-doped carbon nanodots with high fluorescence brightness for cell imaging and sensitive detection of iron (III). *Optical Materials*, 2017. **64**: p. 1-8.
52. Zhai, X., et al., Highly luminescent carbon nanodots by microwave-assisted pyrolysis. *Chemical Communications*, 2012. **48**(64): p. 7955-7957.
53. Reyes, D., et al., Laser Ablated Carbon Nanodots for Light Emission. *Nanoscale Research Letters*, 2016. **11**(1): p. 424.

54. Nguyen, V., et al., Femtosecond laser-assisted synthesis of highly photoluminescent carbon nanodots for Fe³⁺ detection with high sensitivity and selectivity. *Optical Materials Express*, 2016. **6**(2): p. 312-320.
55. Wang, C.-I., et al., Electrochemical synthesis of photoluminescent carbon nanodots from glycine for highly sensitive detection of hemoglobin. *Green Chemistry*, 2014. **16**(5): p. 2509-2514.
56. Niu, F., et al., Bottom-up electrochemical preparation of solid-state carbon nanodots directly from nitriles/ionic liquids using carbon-free electrodes and the applications in specific ferric ion detection and cell imaging. *Nanoscale*, 2016. **8**(10): p. 5470-5477.
57. Liu, H., et al., Microwave-Assisted Synthesis of Wavelength-Tunable Photoluminescent Carbon Nanodots and Their Potential Applications. *ACS Applied Materials & Interfaces*, 2015. **7**(8): p. 4913-4920.
58. Markus Sauer, J.H., Jörg Enderlein, *Handbook of Fluorescence Spectroscopy and Imaging: From Ensemble to Single Molecules*. Mar 2011: Wiley-VCH. 290.
59. ThermoFisher Scientific *Fluorescence Fundamentals, The Molecular Probes Handbook*. 1st May 2017).
60. Baker, S.N. and G.A. Baker, Luminescent carbon nanodots: Emergent nanolights. *Angewandte Chemie - International Edition*, 2010. **49**(38): p. 6726-6744 %!
Luminescent carbon nanodots: Emergent nanolights.
61. Li, J.-Y., et al., One-Pot Hydrothermal Synthesis of Carbon Dots with Efficient Up- and Down-Converted Photoluminescence for the Sensitive Detection of Morin in a Dual-Readout Assay. *Langmuir*, 2017. **33**(4): p. 1043-1050.
62. Li, H.T., et al., One-step ultrasonic synthesis of water-soluble carbon nanoparticles with excellent photoluminescent properties. *Carbon*, 2011. **49**(2): p. 605-609 One-step ultrasonic synthesis of water-soluble carbon nanoparticles with excellent photoluminescent properties 0008-6223.
63. Wang, X.H., et al., Microwave assisted one-step green synthesis of cell-permeable multicolor photoluminescent carbon dots without surface passivation reagents. *Journal of Materials Chemistry*, 2011. **21**(8): p. 2445-2450 %9 Article %!
Microwave assisted one-step green synthesis of cell-permeable multicolor photoluminescent carbon dots without surface passivation reagents %@ 0959-9428.
64. Zheng, M., et al., Self-Targeting Fluorescent Carbon Dots for Diagnosis of Brain Cancer Cells. *ACS Nano*, 2015. **9**(11): p. 11455-11461.

65. Kettler, K., et al., Cellular uptake of nanoparticles as determined by particle properties, experimental conditions, and cell type. *Environ Toxicol Chem*, 2014. **33**(3): p. 481-92.
66. Weissleder, R., M. Nahrendorf, and M.J. Pittet, Imaging macrophages with nanoparticles. *Nature Materials*, 2014. **13**: p. 125.
67. Shang, L., K. Nienhaus, and G.U. Nienhaus, Engineered nanoparticles interacting with cells: size matters. *Journal of Nanobiotechnology*, 2014. **12**: p. 5-5.
68. Park, S.Y., et al., Photoluminescent Green Carbon Nanodots from Food-Waste-Derived Sources: Large-Scale Synthesis, Properties, and Biomedical Applications. *ACS Applied Materials & Interfaces*, 2014. **6**(5): p. 3365-3370.
69. Zhang, J.-H., et al., In vivo characterization of hair and skin derived carbon quantum dots with high quantum yield as long-term bioprobes in zebrafish. *Scientific Reports*, 2016. **6**: p. 37860.
70. Huang, X., et al., Effect of Injection Routes on the Biodistribution, Clearance, and Tumor Uptake of Carbon Dots. *ACS Nano*, 2013. **7**(7): p. 5684-5693.
71. CEM Corporation.(2006). August 2014; Available from: <http://cem.com/discover-sp>.
72. Falco, C., N. Baccile, and M.-M. Titirici, Morphological and structural differences between glucose, cellulose and lignocellulosic biomass derived hydrothermal carbons. *Green Chemistry*, 2011. **13**(11): p. 3273-3281.
73. Liang, M., et al., One-step synthesis of nitrogen, boron co-doped fluorescent carbon nanoparticles for glucose detection. 2017. **32**(6): p. 1031-1038.
74. Zhu, H., et al., Microwave synthesis of fluorescent carbon nanoparticles with electrochemiluminescence properties. *Chemical Communications*, 2009(34): p. 5118-5120.
75. Anderson, D.M.W., et al., Dietary effects of sodium alginate in humans. *Food Additives & Contaminants*, 1991. **8**(3): p. 237-248.
76. Fong, J.F.Y., S.F. Chin, and S.M. Ng, Facile synthesis of carbon nanoparticles from sodium alginate via ultrasonic-assisted nano-precipitation and thermal acid dehydration for ferric ion sensing. *Sensors and Actuators B: Chemical*, 2015. **209**: p. 997-1004.
77. Zhou, J., et al., Cationic carbon quantum dots derived from alginate for gene delivery: One-step synthesis and cellular uptake. *Acta Biomaterialia*, 2016. **42**: p. 209-219.
78. Zhang, C., J.W. Chung, and R.D. Priestley, Dialysis nanoprecipitation of polystyrene nanoparticles. *Macromol Rapid Commun*, 2012. **33**(20): p. 1798-803.

79. Robertson, J.D., et al., Purification of Nanoparticles by Size and Shape. *Scientific Reports*, 2016. **6**: p. 27494.
80. Abdelwahed, W., et al., Freeze-drying of nanoparticles: formulation, process and storage considerations. *Adv Drug Deliv Rev*, 2006. **58**(15): p. 1688-713.
81. McCauley, J.W., Materials Characterization: Definition, Philosophy and Overview of Conference, in *Materials Characterization for Systems Performance and Reliability*, J.W. McCauley and V. Weiss, Editors. 1986, Springer US: Boston, MA. p. 1-11.
82. Bhatia, S., Chapter 2 Nanoparticles Types, Classification, Characterization, Fabrication Methods and Drug Delivery Applications

in *Natural Polymer Drug Delivery Systems 2016*, Springer International Publishing: Natural Polymer Drug Delivery Systems

83. Pennycook, S.J., et al. *Transmission electron microscopy: Overview and challenges*. 2003. Austin, Tx: Amer Inst Physics.
84. Nobbmann, U., et al., Dynamic light scattering as a relative tool for assessing the molecular integrity and stability of monoclonal antibodies. *Biotechnology and Genetic Engineering Reviews*, 2007. **24**(1): p. 117-128.
85. Hoo, C., et al., A comparison of atomic force microscopy (AFM) and dynamic light scattering (DLS) methods to characterize nanoparticle size distributions. *J Nanopart Res*, 2008. **10**.
86. M Joshia, A.B.S.W.A., Characterization techniques for nanotechnology applications in textiles. *Indian Journal of Fibre & Textile Research*, September 2008. **33**: p. 304-317.
87. Bumbrah, G.S. and R.M. Sharma, Raman spectroscopy – Basic principle, instrumentation and selected applications for the characterization of drugs of abuse. *Egyptian Journal of Forensic Sciences*, 2016. **6**(3): p. 209-215.
88. Movasaghi, Z., S. Rehman, and I.U. Rehman, Raman Spectroscopy of Biological Tissues. *Applied Spectroscopy Reviews*, 2007. **42**(5): p. 493-541.
89. McArthur, S.L., Applications of XPS in bioengineering. *Surface and Interface Analysis*, 2006. **38**(11): p. 1380-1385.
90. M. Z. Krolow, C.A.H., G. C. Link, C. W. Raubach, J. S. F. Pereira, R. S. Picoloto, M. R. F. Gonçalves, N. L. V. Carreño and M. F. Mesko, Synthesis and Characterisation of Carbon Nanocomposites, in *Carbon Nanostructures*, C. Avellaneda, Editor. NanoCarbon 2011, Springer-Verlag Berlin Heidelberg 2013.

91. Fluorometers.
92. Robert, H.W., Confocal optical microscopy. Reports on Progress in Physics, 1996. **59**(3): p. 427.
93. Crosera, M., et al., Nanoparticle dermal absorption and toxicity: a review of the literature. Int Arch Occup Environ Health, 2009. **82**(9): p. 1043-55.
94. Bankoti, K., et al., Onion derived carbon nanodots for live cell imaging and accelerated skin wound healing. Journal of Materials Chemistry B, 2017. **5**(32): p. 6579-6592.
95. Janus, L., et al., Chitosan-Based Carbon Quantum Dots for Biomedical Applications: Synthesis and Characterization. Nanomaterials (Basel), 2019. **9**(2).
96. Lamb, R. and C.A. Ambler, Keratinocytes propagated in serum-free, feeder-free culture conditions fail to form stratified epidermis in a reconstituted skin model. PLoS One, 2013. **8**(1): p. e52494.
97. Ryoo, S.-R., et al., Behaviors of NIH-3T3 Fibroblasts on Graphene/Carbon Nanotubes: Proliferation, Focal Adhesion, and Gene Transfection Studies. ACS Nano, 2010. **4**(11): p. 6587-6598.
98. Fletcher, D.A. and R.D. Mullins, Cell mechanics and the cytoskeleton. Nature, 2010. **463**: p. 485.
99. Mundra, V., W. Li, and R.I. Mahato, Nanoparticle-mediated drug delivery for treating melanoma. Nanomedicine (London, England), 2015. **10**(16): p. 2613-2633.
100. Orthaber, K., et al., Skin Cancer and Its Treatment: Novel Treatment Approaches with Emphasis on Nanotechnology %J Journal of Nanomaterials. 2017. **2017**: p. 20.
101. Eves, P.C., Human melanoma invasion and the antiinvasive and immunomodulatory role of α -melanocyte stimulating hormone (α -MSH). 2011, University of Sheffield.
102. O'Brien, J., et al., Investigation of the Alamar Blue (resazurin) fluorescent dye for the assessment of mammalian cell cytotoxicity. Eur J Biochem, 2000. **267**(17): p. 5421-6.
103. Zhou, W., et al., CellTrace™ Far Red & CellTracker™ Deep Red—long term live cell tracking for flow cytometry and fluorescence microscopy. 2016, 2016.
104. MitoTracker® Mitochondrion-Selective Probes
The Molecular Probes Handbook, The Molecular Probes Handbook.
105. Liang, C.C., A.Y. Park, and J.L. Guan, In vitro scratch assay: a convenient and inexpensive method for analysis of cell migration in vitro. Nat Protoc, 2007. **2**(2): p. 329-33.

106. Sahu, S., et al., Simple one-step synthesis of highly luminescent carbon dots from orange juice: application as excellent bio-imaging agents. *Chemical Communications*, 2012. **48**(70): p. 8835-8837.
107. Porres, L., et al., Absolute measurements of photoluminescence quantum yields of solutions using an integrating sphere. *J Fluoresc*, 2006. **16**(2): p. 267-72.
108. Hu, S.-L., et al., One-step synthesis of fluorescent carbon nanoparticles by laser irradiation. *Journal of Materials Chemistry*, 2009. **19**(4): p. 484-488.
109. Liu, H., T. Ye, and C. Mao, Fluorescent carbon nanoparticles derived from candle soot. *Angew Chem Int Ed Engl*, 2007. **46**(34): p. 6473-5.
110. Peng, H. and J. Travas-Sejdic, Simple Aqueous Solution Route to Luminescent Carbogenic Dots from Carbohydrates. *Chemistry of Materials*, 2009. **21**(23): p. 5563-5565.
111. Valdez, J., #xf3, and I. mez, One-Step Green Synthesis of Metallic Nanoparticles Using Sodium Alginate. *Journal of Nanomaterials*, 2016. **2016**: p. 7.
112. Nagy, A., et al., Comprehensive Analysis of the Effects of CdSe Quantum Dot Size, Surface Charge, and Functionalization on Primary Human Lung Cells. *ACS Nano*, 2012. **6**(6): p. 4748-4762.
113. Beigmoradi, R., A. Samimi, and D. Mohebbi-Kalhari, Engineering of oriented carbon nanotubes in composite materials. *Beilstein Journal of Nanotechnology*, 2018. **9**: p. 415-435.
114. Wang, Y. and A. Hu, Carbon quantum dots: synthesis, properties and applications. *Journal of Materials Chemistry C*, 2014. **2**(34): p. 6921-6939.
115. Nie, H., et al., Carbon Dots with Continuously Tunable Full-Color Emission and Their Application in Ratiometric pH Sensing. *Chemistry of Materials*, 2014. **26**(10): p. 3104-3112.
116. Hill, S. and M.C. Galan, Fluorescent carbon dots from mono- and polysaccharides: synthesis, properties and applications. *Beilstein Journal of Organic Chemistry*, 2017. **13**: p. 675-693.
117. Liong, M., et al., Multifunctional inorganic nanoparticles for imaging, targeting, and drug delivery. *ACS Nano*, 2008. **2**(5): p. 889-96.
118. Xia, T., et al., Comparison of the abilities of ambient and manufactured nanoparticles to induce cellular toxicity according to an oxidative stress paradigm. *Nano Lett*, 2006. **6**(8): p. 1794-807.

119. Lewinski, N., V. Colvin, and R. Drezek, Cytotoxicity of nanoparticles. *Small*, 2008. **4**(1): p. 26-49.
120. Bexiga, M.G., et al., Cationic nanoparticles induce caspase 3-, 7- and 9-mediated cytotoxicity in a human astrocytoma cell line. *Nanotoxicology*, 2011. **5**(4): p. 557-567.
121. Wani, M.Y., et al., Nanotoxicity: Dimensional and Morphological Concerns. *Advances in Physical Chemistry*, 2011. **2011**: p. 15.
122. Beack, S., et al., Photodynamic therapy of melanoma skin cancer using carbon dot – chlorin e6 – hyaluronate conjugate. *Acta Biomaterialia*, 2015. **26**: p. 295-305.
123. Zhu, N., et al., Melanoma cell migration is upregulated by tumour necrosis factor-alpha and suppressed by alpha-melanocyte-stimulating hormone. *Br J Cancer*, 2004. **90**(7): p. 1457-63.
124. Zhang, L.W. and N.A. Monteiro-Riviere, Mechanisms of quantum dot nanoparticle cellular uptake. *Toxicol Sci*, 2009. **110**(1): p. 138-55.
125. Zhao, C.-M. and W.-X. Wang, Size-Dependent Uptake of Silver Nanoparticles in *Daphnia magna*. *Environmental Science & Technology*, 2012. **46**(20): p. 11345-11351.
126. Thoo, L., et al., Interaction and cellular uptake of surface-modified carbon dot nanoparticles by J774.1 macrophages. *Central-European Journal of Immunology*, 2017. **42**(3): p. 324-330.
127. Song, Y., S. Zhu, and B. Yang, Bioimaging based on fluorescent carbon dots. *RSC Advances*, 2014. **4**(52): p. 27184-27200.
128. Katja, K., et al., Cellular uptake of nanoparticles as determined by particle properties, experimental conditions, and cell type. *Environmental Toxicology and Chemistry*, 2014. **33**(3): p. 481-492.
129. Li, H., Y. Zhang, and X. Wang, l-Carnitine capped quantum dots as luminescent probes for cadmium ions. *Sensors and Actuators B: Chemical*, 2007. **127**(2): p. 593-597.
130. Xie, H.-Y., et al., Luminescent CdSe-ZnS quantum dots as selective Cu²⁺ probe. *Spectrochimica Acta Part A: Molecular and Biomolecular Spectroscopy*, 2004. **60**(11): p. 2527-2530.
131. Chen, L.-D., et al., The biocompatibility of quantum dot probes used for the targeted imaging of hepatocellular carcinoma metastasis. *Biomaterials*, 2008. **29**(31): p. 4170-4176.

132. Zhang, S., et al., Study on the fluorescence carbon nanoparticles. *Materials Letters*, 2011. **65**(15): p. 2371-2373.
133. Havrdova, M., et al., Toxicity of carbon dots – Effect of surface functionalization on the cell viability, reactive oxygen species generation and cell cycle. *Carbon*, 2016. **99**: p. 238-248.
134. Beer, C., et al., Caveola-Dependent Endocytic Entry of Amphotropic Murine Leukemia Virus. *Journal of Virology*, 2005. **79**(16): p. 10776-10787.
135. Beer, C. and L. Pedersen, Amphotropic murine leukemia virus is preferentially attached to cholesterol-rich microdomains after binding to mouse fibroblasts. *Virology Journal*, 2006. **3**: p. 21-21.
136. Liu, J.-H., et al., Carbon “Quantum” Dots for Fluorescence Labeling of Cells. *ACS Applied Materials & Interfaces*, 2015. **7**(34): p. 19439-19445.
137. Ray, S.C., et al., Fluorescent Carbon Nanoparticles: Synthesis, Characterization, and Bioimaging Application. *The Journal of Physical Chemistry C*, 2009. **113**(43): p. 18546-18551.
138. Luo, P.G., et al., Carbon “quantum” dots for optical bioimaging. *Journal of Materials Chemistry B*, 2013. **1**(16): p. 2116-2127.
139. Kurantowicz, N., et al., Toxicity studies of six types of carbon nanoparticles in a chicken-embryo model. *Int J Nanomedicine*, 2017. **12**: p. 2887-2898.
140. Yang, S.T., et al., Carbon Dots as Nontoxic and High-Performance Fluorescence Imaging Agents. *J Phys Chem C Nanomater Interfaces*, 2009. **113**(42): p. 18110-18114.
141. Liu, R., et al., An aqueous route to multicolor photoluminescent carbon dots using silica spheres as carriers. *Angew Chem Int Ed Engl*, 2009. **48**(25): p. 4598-601.
142. Costa, E.C., et al., Evaluation of nanoparticle uptake in co-culture cancer models. *PLoS One*, 2013. **8**(7): p. e70072.
143. Kang, E.B., et al., Mitochondria-targeted fluorescent carbon nano-platform for NIR-triggered hyperthermia and mitochondrial inhibition. *Journal of Industrial and Engineering Chemistry*, 2017. **55**: p. 224-233.
144. Yildirimer, L., et al., Toxicology and clinical potential of nanoparticles. *Nano Today*, 2011. **6**(6): p. 585-607.
145. Bhunia, S.K., et al., Carbon nanoparticle-based fluorescent bioimaging probes. *Scientific reports*, 2013. **3**: p. 1473-1473.

146. Sharma, S., et al., Photoluminescent C-dots: An overview on the recent development in the synthesis, physiochemical properties and potential applications. *Journal of Alloys and Compounds*, 2018. **748**: p. 818-853.
147. Krysmann, M.J., et al., Formation mechanism of carbogenic nanoparticles with dual photoluminescence emission. *J Am Chem Soc*, 2012. **134**(2): p. 747-50.
148. Mattsson, M.-O. and M. Simkó, The changing face of nanomaterials: Risk assessment challenges along the value chain. *Regulatory Toxicology and Pharmacology*, 2017. **84**: p. 105-115.
149. Shen, P. and Y. Xia, Synthesis-Modification Integration: One-Step Fabrication of Boronic Acid Functionalized Carbon Dots for Fluorescent Blood Sugar Sensing. *Analytical Chemistry*, 2014. **86**(11): p. 5323-5329.
150. Yang, Y., et al., One-step synthesis of amino-functionalized fluorescent carbon nanoparticles by hydrothermal carbonization of chitosan. *Chem Commun (Camb)*, 2012. **48**(3): p. 380-2.
151. Li, H., et al., Fluorescent carbon nanoparticles: electrochemical synthesis and their pH sensitive photoluminescence properties. *New Journal of Chemistry*, 2011. **35**(11): p. 2666-2670.
152. Wu, W., et al., Photocatalytic H₂ evolution from NADH with carbon quantum dots/Pt and 2-phenyl-4-(1-naphthyl)quinolinium ion. *Journal of Photochemistry and Photobiology B: Biology*, 2015. **152**: p. 63-70.
153. Wang, Y. and J. Irudayaraj, Surface-enhanced Raman spectroscopy at single-molecule scale and its implications in biology. *Philosophical transactions of the Royal Society of London. Series B, Biological sciences*. **368**(1611): p. 20120026-20120026.
154. Söderholm, S., et al., Raman spectra of fructose and glucose in the amorphous and crystalline states. *journal of raman spectroscopy*, 22 November 1999.
155. Deng, J. and C. Gao, Recent advances in interactions of designed nanoparticles and cells with respect to cellular uptake, intracellular fate, degradation and cytotoxicity. *Nanotechnology*, 2016. **27**(41): p. 412002.
156. Du, F., et al., Economical and green synthesis of bagasse-derived fluorescent carbon dots for biomedical applications. *Nanotechnology*, 2014. **25**(31): p. 315702.
157. Sun, Y.-P., et al., Doped Carbon Nanoparticles as a New Platform for Highly Photoluminescent Dots. *The Journal of Physical Chemistry C*, 2008. **112**(47): p. 18295-18298.

158. Yang, S.-T., et al., Carbon Dots as Nontoxic and High-Performance Fluorescence Imaging Agents. *The Journal of Physical Chemistry C*, 2009. **113**(42): p. 18110-18114.
159. Sun, Y.P., et al., Quantum-sized carbon dots for bright and colorful photoluminescence. *J Am Chem Soc*, 2006. **128**(24): p. 7756-7.
160. Behzadi, S., et al., Cellular uptake of nanoparticles: journey inside the cell. *Chemical Society Reviews*, 2017. **46**(14): p. 4218-4244.
161. Müller, D.J. and Y.F. Dufrêne, Atomic force microscopy: a nanoscopic window on the cell surface. *Trends in Cell Biology*, 2011. **21**(8): p. 461-469.
162. Invited Review Article: Combining scanning probe microscopy with optical spectroscopy for applications in biology and materials science. *Review of Scientific Instruments*, 2012. **83**(6): p. 061101.

8. Appendix

8.1. Microwave synthesis of Carbon nanoparticles

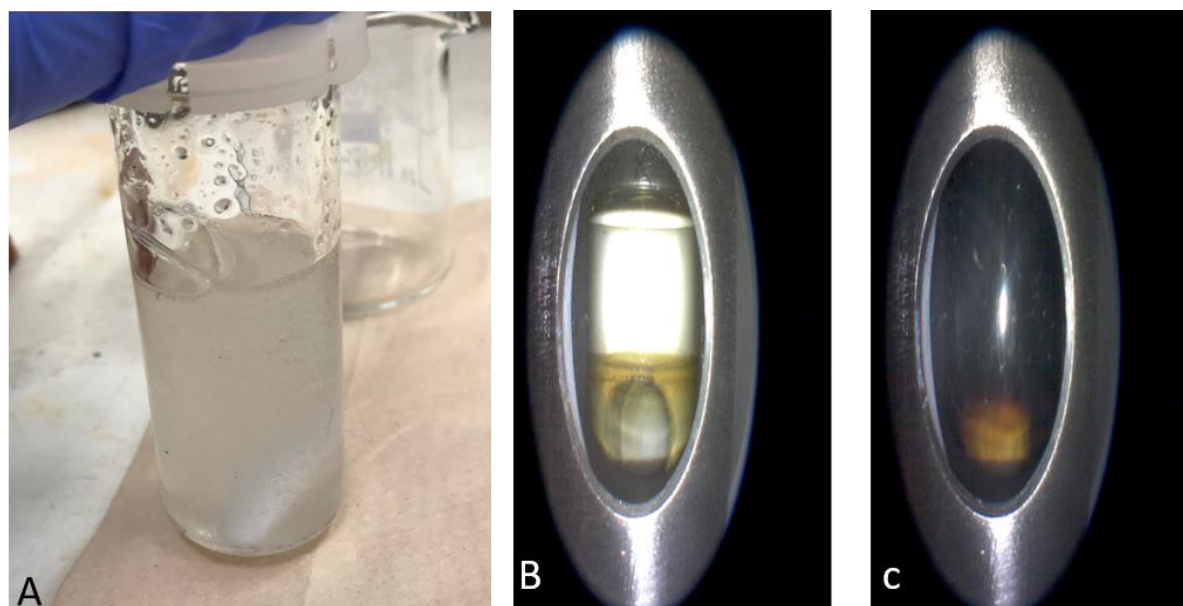
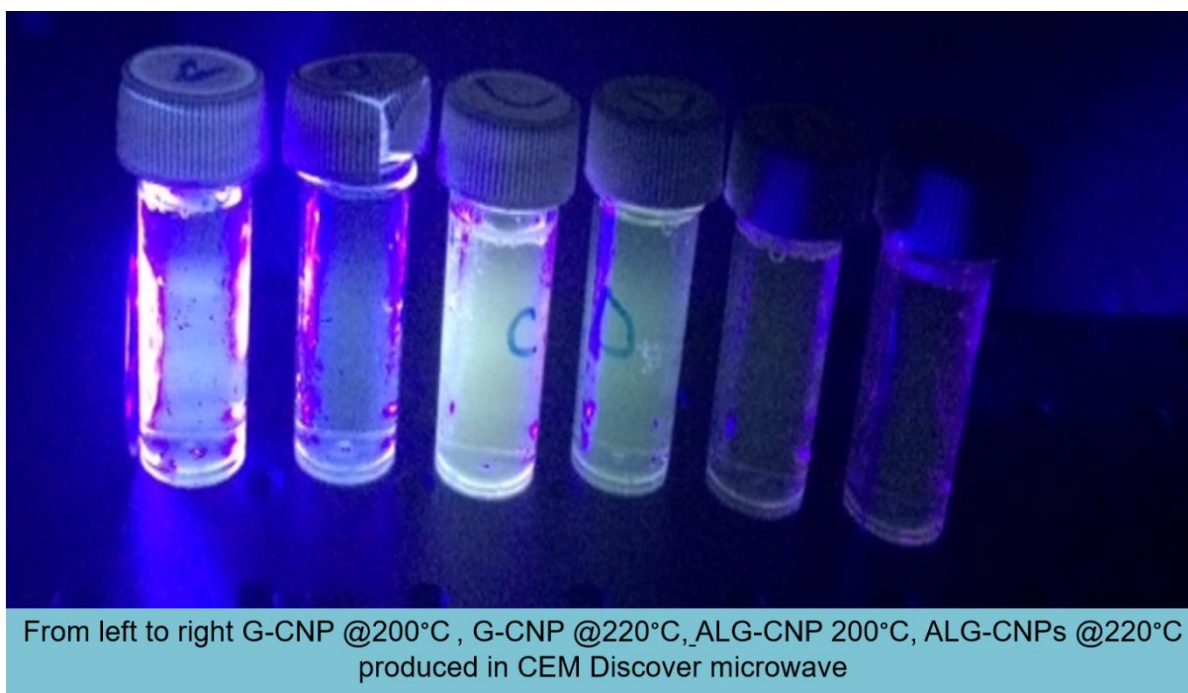


Figure 8.1. A glucose solution before the microwave reaction (B) reaction of glucose at 1 minute and (c) Carbonisation images of glucose inside the microwave at 5 minutes

8.2. Carbon nanoparticles Under UV light



From left to right G-CNP @200°C , G-CNP @220°C, ALG-CNP 200°C, ALG-CNPs @220°C produced in CEM Discover microwave

8.3. Two photon imaging for glucose and alginate CNPs at different excitation wavelengths

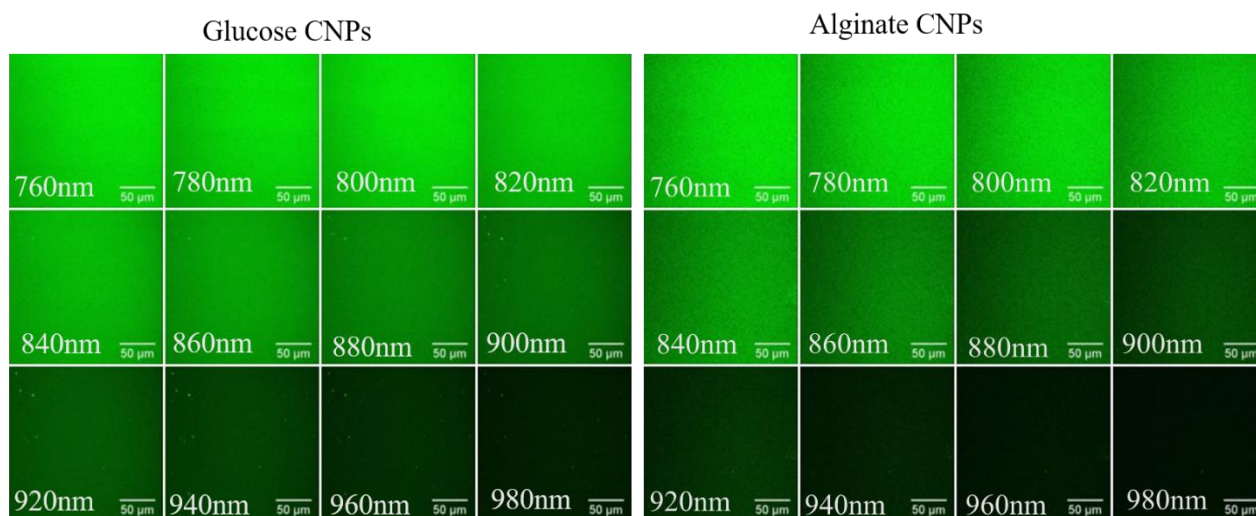


Figure 8.2. Confocal microscopy images for alginate carbon nanoparticles and glucose CNPs at different excitation wavelength (A) 760 nm , (B) 780 nm ,(C) 800 nm ,(D) 820 nm , (E) 840 nm , (F) 860 nm , (G) 880 nm, (H) 900 nm , (I) 920 nm, (J) 940 nm (K) 960 nm and (L) 980 nm. . A drop liquid of nanoparticles was placed into cover glass and images under two photon excitation.

8.4. Ultraviolet-Visible absorbance spectroscopy (λ_{ab})

UV spectroscopy is designed to measure the ability of the solution to absorb ultraviolet / visible radiation light depends on the wavelength of absorbed radiation. Analyze NPCs by this Method, different concentration of CNP was required in aqueous solution. (Figure 8.3). Absorption was seen in the 200–800 nm region. These peaks have been recognised before as relating to a typical absorption peak for an aromatic π system, similar to those derived from polycyclic aromatic hydrocarbons. While in alginate, the Peaks slightly increased with increasing the concentration.

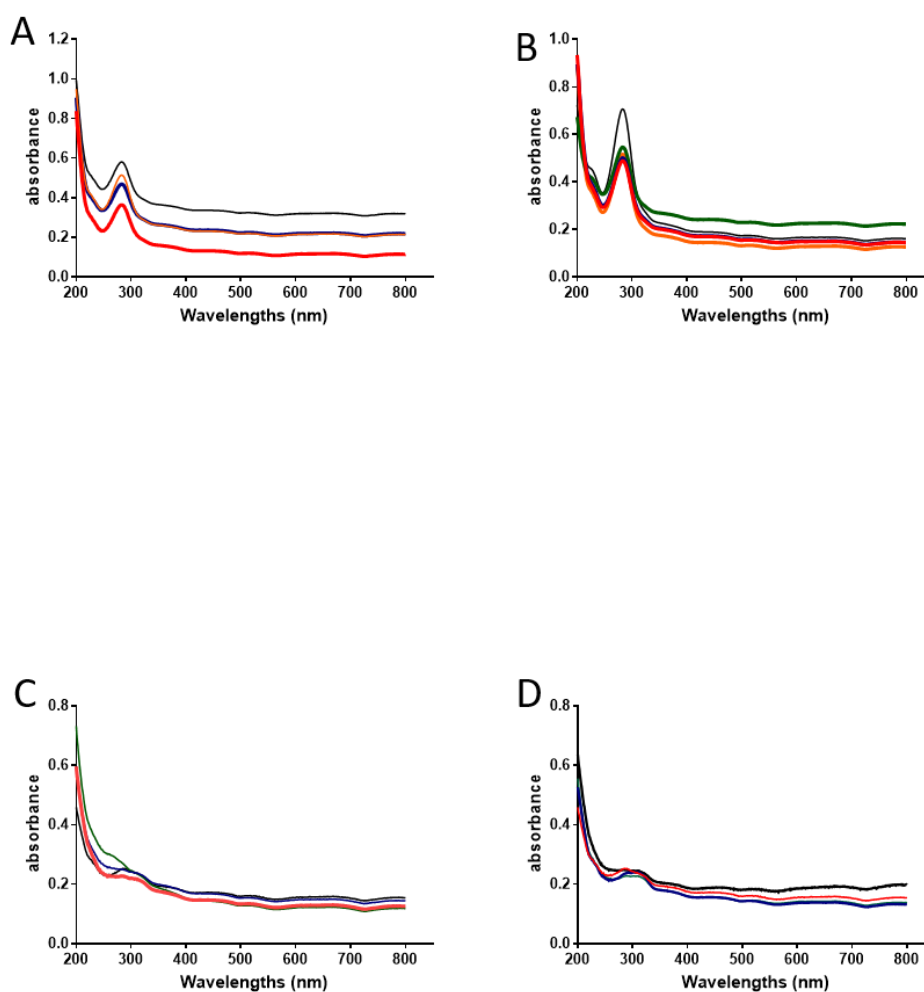


Figure 8.3. UV-Vis spectra for CNPs from (A) glucose at 200 °C (B) glucose 220 °C, (C) alginate 200 °C and (D) alginate 220 °C

8.5. Cellular uptake studies for alginate CNPs entering NIH-3T3 fibroblasts, human fibroblast and C8161 melanoma cells

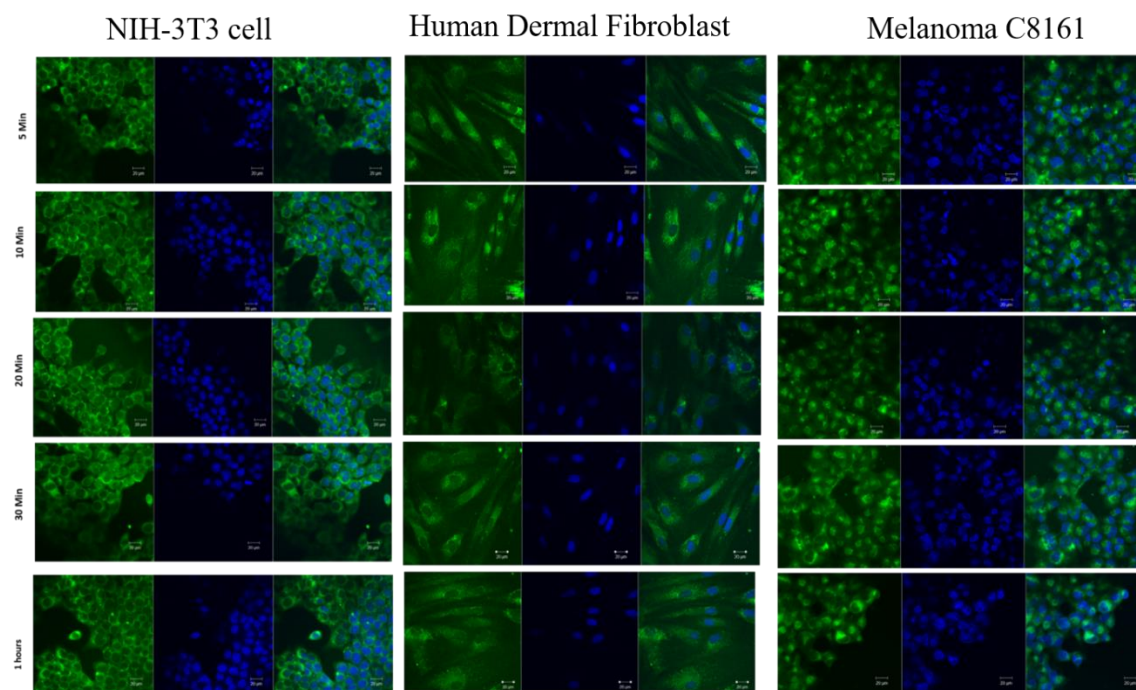


Figure 8.4 Confocal microscopy images showing the process of alginate CNPs entering NIH-3T3 fibroblasts, human fibroblast and C8161 melanoma cells. All the cells cultures were incubated with fluorescent Alginate CNPs (10 $\mu\text{g}/\text{ml}$, 5, 10, 20, 30 min and 1 h) . Excitation wavelength of 488 nm and 780 nm for green and blue fluorescence, respectively (Scale bar 20 μm).

8.6. Co-culture of C8161 melanoma cancer cells and HDF cells incubated for 60 min with 150 μg glucose and alginate at 200 and 220 $^{\circ}\text{C}$

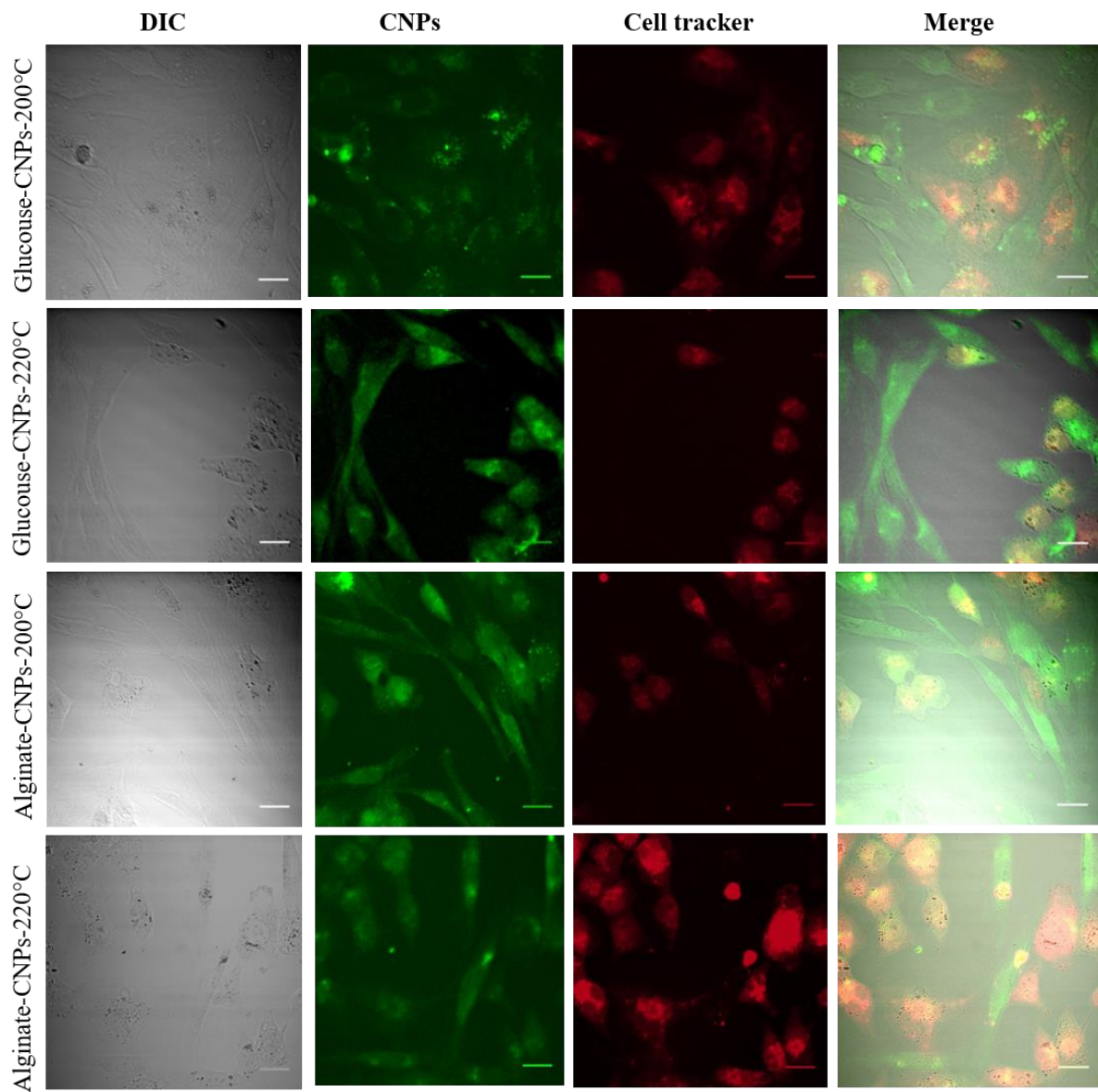


Figure 8.5: Co-culture of C8161 melanoma cancer cells and HDF cells incubated for 60 min with 150 μg glucose and alginate at 200 and 220 $^{\circ}\text{C}$ green: (CNPs) red: deep cell tracker red, magnification: 40X scale bar 25 μm .

8.7. Transmission electron microscopy (TEM) for alginate Carbon nanoparticles

The TEM micrographs for Alginate Carbon nanoparticles. Alginate Carbon NPs (Figure 8.6) show a spherical morphology and these nanoparticles had a size less than 100 nm. In addition, these analyses demonstrate higher sizes attributed to agglomerates in the sample and need further analysis and repletion in the future.

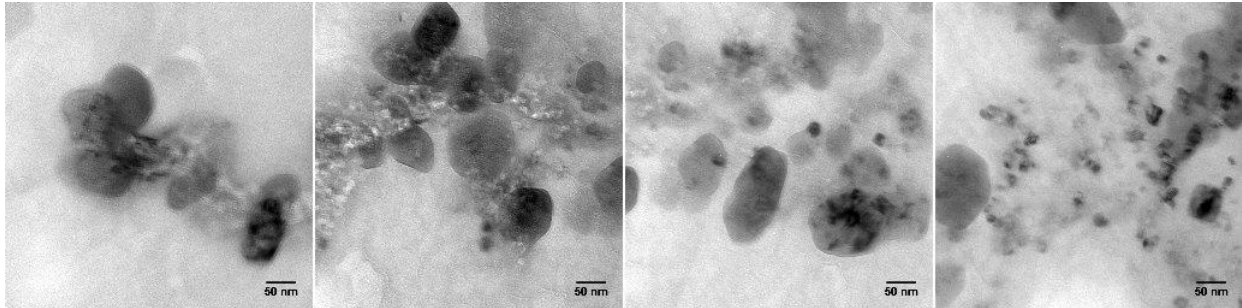


Figure 8.6: Transmission electron microscopy images of carbon nanoparticles obtained from alginate

8.8. Statistic analysis

Statistical Analysis of cell viability of alginate and glucose CNPs at 200 and 220°C. Statistical analyses was carried out using two-way ANOVA followed by Tukey's post-hoc comparison of means. The results of the pairwise comparisons are given in Tables

Table 8. 1: Cell viability evaluation (resazurin assays) after 24, 48 and 72h of incubation with fibroblast , increasing concentrations of alginate CNPs at 200 °C. Results are tested by using a two-way ANOVA means±SD of at least three independent experiments. *p < 0.05, **p <0.01, ***p < 0.001 for statistical significance of each concentration used for CNPs.

Tukey's multiple comparisons test	Mean Diff.	95.00% CI of diff.	Significant?	Summary	Adjusted P Value
24h :0mg/ml vs. 24h :10mg/ml	0.1043	-0.08438 to 0.293	No	Ns	0.8824
24h :0mg/ml vs. 24h :20mg/ml	0.1167	-0.07204 to 0.3054	No	Ns	0.7476
24h :0mg/ml vs. 24h :50mg/ml	0.08533	-0.1034 to 0.274	No	Ns	0.9821
24h :0mg/ml vs. 24h :100mg/ml	0.1153	-0.07338 to 0.304	No	Ns	0.7645
24h :0mg/ml vs. 24h :150mg/ml	0.1217	-0.06704 to 0.3104	No	Ns	0.6807
24h :0mg/ml vs. 24h :200mg/ml	0.1077	-0.08104 to 0.2964	No	Ns	0.8512
24h :0mg/ml vs. 24h :250mg/ml	0.09033	-0.09838 to 0.279	No	Ns	0.9675
24h :0mg/ml vs. 48h:0mg/ml	-0.06	-0.2487 to 0.1287	No	Ns	0.9998
24h :0mg/ml vs. 48h:10mg/ml	-0.2107	-0.3994 to -0.02196	Yes	*	0.0144
24h :0mg/ml vs. 48h:20mg/ml	-0.2913	-0.48 to -0.1026	Yes	****	<0.0001
24h :0mg/ml vs. 48h:50mg/ml	-0.3123	-0.501 to -0.1236	Yes	****	<0.0001
24h :0mg/ml vs. 48h:100mg/ml	-0.226	-0.4147 to -0.03729	Yes	**	0.0056
24h :0mg/ml vs. 48h:150mg/ml	-0.2747	-0.4634 to -0.08596	Yes	***	0.0002
24h :0mg/ml vs. 48h:200mg/ml	-0.101	-0.2897 to 0.08771	No	Ns	0.9094
24h :0mg/ml vs. 48h:250mg/ml	-0.19	-0.3787 to -0.001292	Yes	*	0.0466
24h :0mg/ml vs. 72h:0mg/ml	-0.3837	-0.5724 to -0.195	Yes	****	<0.0001
24h :0mg/ml vs. 72h:10mg/ml	0.00633 3	-0.1824 to 0.195	No	Ns	>0.9999

24h :0mg/ml vs. 72h:20mg/ml	0.002	-0.1867 to 0.1907	No	Ns	>0.9999
24h :0mg/ml vs. 72h:50mg/ml	0.01633	-0.1724 to 0.205	No	Ns	>0.9999
24h :0mg/ml vs. 72h:100mg/ml	0.04333	-0.1454 to 0.232	No	Ns	>0.9999
24h :0mg/ml vs. 72h:150mg/ml	0.061	-0.1277 to 0.2497	No	Ns	0.9998
24h :0mg/ml vs. 72h:200mg/ml	0.08967	-0.09904 to 0.2784	No	Ns	0.9698

Table 8. 2: Cell viability evaluation (resazurin assays) after 24, 48 and 72h of incubation with fibroblast , increasing concentrations of alginate CNPs at 220 °C. Results are tested by using a two-way ANOVA means±SD of at least three independent experiments. *p < 0.05, **p <0.01, ***p < 0.001 for statistical significance of each concentration used for CNPs.

Tukey's multiple comparisons test	Mean Diff.	95.00% CI of diff.	Significant?	Summary	Adjusted P Value
24h:0mg/ml vs. 24h:10mg	-0.09067	-0.3233 to 0.142	No	Ns	0.997
24h:0mg/ml vs. 24h:20mg	-0.006	-0.2387 to 0.2267	No	Ns	>0.9999
24h:0mg/ml vs. 24h:50mg	0.109	-0.1237 to 0.3417	No	Ns	0.9739
24h:0mg/ml vs. 24h:100mg	0.01767	-0.215 to 0.2503	No	Ns	>0.9999
24h:0mg/ml vs. 24h:150	0.157	-0.07566 to 0.3897	No	Ns	0.6003
24h:0mg/ml vs. 24h:200	0.169	-0.06366 to 0.4017	No	Ns	0.4616
24h:0mg/ml vs. 24h:250	0.1757	-0.05699 to 0.4083	No	Ns	0.3891
24h:0mg/ml vs. 48h:0mg/ml	-0.1863	-0.419 to 0.04632	No	Ns	0.286
24h:0mg/ml vs. 48h:10mg	-0.4303	-0.663 to -0.1977	Yes	****	<0.0001
24h:0mg/ml vs. 48h:20mg	-0.3383	-0.571 to -0.1057	Yes	***	0.0002
24h:0mg/ml vs. 48h:50mg	-0.237	-0.4697 to -0.004343	Yes	*	0.0413
24h:0mg/ml vs. 48h:100mg	-0.2347	-0.4673 to -0.00201	Yes	*	0.0458
24h:0mg/ml vs. 48h:150	-0.1643	-0.397 to 0.06832	No	Ns	0.5148
24h:0mg/ml vs. 48h:200	-0.083	-0.3157 to 0.1497	No	Ns	0.9991
24h:0mg/ml vs. 48h:250	-0.072	-0.3047 to	No	Ns	0.9999

		0.1607			
24h:0mg/ml vs. 72h:0mg/ml	-0.3357	-0.5683 to -0.103	Yes	***	0.0003
24h:0mg/ml vs. 72h:10mg	-0.184	-0.4167 to 0.04866	No	Ns	0.307
24h:0mg/ml vs. 72h:20mg	-0.09067	-0.3233 to 0.142	No	Ns	0.997
24h:0mg/ml vs. 72h:50mg	-0.02133	-0.254 to 0.2113	No	Ns	>0.9999
24h:0mg/ml vs. 72h:100mg	-0.032	-0.2647 to 0.2007	No	Ns	>0.9999
24h:0mg/ml vs. 72h:150	0.064	-0.1687 to 0.2967	No	Ns	>0.9999
24h:0mg/ml vs. 72h:200	0.1057	-0.127 to 0.3383	No	Ns	0.9813

Table 8. 3:Cell viability evaluation (resazurin assays) after 24, 48 and 72h of incubation with fibroblast , increasing concentrations of glucose CNPs at 200 °C. Results are tested by using a two-way ANOVA means±SD of at least three independent experiments. *p < 0.05, **p <0.01, ***p < 0.001 and ****p < 0.0001 for statistical significance of each concentration used for CNPs.

Tukey's multiple comparisons test	Mean Diff.	95.00% CI of diff.	Significant?	Summary	Adjusted P Value
24h					
0mg/ml vs. 10mg	-0.03233	-0.217 to 0.1524	No	ns	0.9992
0mg/ml vs. 20mg	-0.05433	-0.239 to 0.1304	No	ns	0.9813
0mg/ml vs. 50mg	-0.01867	-0.2034 to 0.166	No	ns	>0.9999
0mg/ml vs. 100mg	-0.01767	-0.2024 to 0.167	No	ns	>0.9999
0mg/ml vs. 150mg	-0.1017	-0.2864 to 0.08304	No	ns	0.6594
0mg/ml vs. 200mg	-0.00233	-0.187 to 0.1824	No	ns	>0.9999
0mg/ml vs. 250mg	0.01833	-0.1664 to 0.203	No	ns	>0.9999
48h					
0mg/ml vs. 10mg	-0.2773	-0.462 to -0.09262	Yes	***	0.0005
0mg/ml vs. 20mg	-0.312	-0.4967 to -0.1273	Yes	****	<0.0001
0mg/ml vs. 50mg	-0.2023	-0.387 to -0.01762	Yes	*	0.0227

0mg/ml vs. 100mg	-0.1843	-0.369 to 0.0003781	No	ns	0.0508
0mg/ml vs. 150mg	-0.281	-0.4657 to -0.09629	Yes	***	0.0004
0mg/ml vs. 200mg	-0.2833	-0.468 to -0.09862	Yes	***	0.0003
0mg/ml vs. 250mg	-0.2543	-0.439 to -0.06962	Yes	**	0.0016
0mg/ml vs. 10mg	0.1747	-0.01004 to 0.3594	No	ns	0.0761
0mg/ml vs. 20mg	0.157	-0.02771 to 0.3417	No	ns	0.1498
0mg/ml vs. 50mg	0.1767	-0.008045 to 0.3614	No	ns	0.0701
0mg/ml vs. 100mg	0.196	0.01129 to 0.3807	Yes	*	0.0304
0mg/ml vs. 150mg	0.2013	0.01662 to 0.386	Yes	*	0.0238
0mg/ml vs. 200mg	0.2243	0.03962 to 0.409	Yes	**	0.0078
0mg/ml vs. 250mg	0.2027	0.01796 to 0.3874	Yes	*	0.0223

Table 8. 4: Cell viability evaluation (resazurin assays) after 24, 48 and 72h of incubation with fibroblast, increasing concentrations of glucose CNPs at 220 °C. Results are tested by using a two-way ANOVA means±SD of at least three independent experiments. *p < 0.05, **p < 0.01, ***p < 0.001 for statistical significance of each concentration used for CNPs.

Tukey's multiple comparisons test	Mean Diff.	95.00% CI of diff.	Significant?	Summary	Adjusted P Value
24h					
0µg/ml vs. 10µg	0.062	-0.1414 to 0.2654	No	ns	0.9771
0µg/ml vs. 20 µg	0.01367	-0.1897 to 0.217	No	ns	>0.9999
0µg/ml vs. 50 µg	0.041	-0.1624 to 0.2444	No	ns	0.9981
0µg/ml vs. 100µg	0.03	-0.1734 to 0.2334	No	ns	0.9998
0µg/ml vs. 150µg	0.004	-0.1994 to 0.2074	No	ns	>0.9999
0µg/ml vs. 200µg	0.04467	-0.1587 to 0.248	No	ns	0.9967
0µg/ml vs. 250µg	0.013	-0.1904 to 0.2164	No	ns	>0.9999
0µg/ml vs. 10µg	-0.08033	-0.2837 to 0.123	No	ns	0.9117

0µg/ml vs. 20µg	-0.1863	-0.3897 to 0.01704	No	ns	0.0945
0µg/ml vs. 50µg	-0.09	-0.2934 to 0.1134	No	ns	0.8519
0µg/ml vs. 100µg	-0.1333	-0.3367 to 0.07004	No	ns	0.4437
0µg/ml vs. 150µg	-0.2503	-0.4537 to -0.04696	Yes	**	0.0067
0µg/ml vs. 200µg	-0.1323	-0.3357 to 0.07104	No	ns	0.4535
0µg/ml vs. 250µg	-0.1743	-0.3777 to 0.02904	No	ns	0.1427
0µg/ml vs. 10µg	0.1453	-0.05804 to 0.3487	No	ns	0.3341
0µg/ml vs. 20µg	0.1903	-0.01304 to 0.3937	No	ns	0.0818
0µg/ml vs. 50µg	0.1903	-0.01304 to 0.3937	No	ns	0.0818
0µg/ml vs. 100µg	0.3023	0.09896 to 0.5057	Yes	***	0.0005
0µg/ml vs. 150µg	0.206	0.002622 to 0.4094	Yes	*	0.0451
0µg/ml vs. 200µg	0.2153	0.01196 to 0.4187	Yes	*	0.031
0µg/ml vs. 250µg	0.284	0.08062 to 0.4874	Yes	**	0.0013

Table 8. 5: Cell viability evaluation (resazurin assays) after 24, 48 and 72h of incubation with melanoma C8161, increasing concentrations of alginate CNPs at 200°C. Results are tested by using a two-way ANOVA means±SD of at least three independent experiments. *p < 0.05, **p < 0.01, ***p < 0.001 for statistical significance of each concentration used for CNPs.

Tukey's multiple comparisons test	Mean Diff.	95.00% CI of diff.	Significant?	Summary	Adjusted P Value
24h :0mg/ml vs. 24h :10mg/ml	0.062	-0.1854 to 0.3094	No	ns	>0.9999
24h :0mg/ml vs. 24h :20 mg/ml	0.01367	-0.2338 to 0.2611	No	ns	>0.9999
24h :0mg/ml vs. 24h :50 mg/ml	0.041	-0.2064 to 0.2884	No	ns	>0.9999
24h :0mg/ml vs. 24h :100 mg/ml	0.03	-0.2174 to 0.2774	No	ns	>0.9999
24h :0mg/ml vs. 24h :150 mg/ml	0.004	-0.2434 to 0.2514	No	ns	>0.9999
24h :0mg/ml vs. 24h :200mg/ml	0.04467	-0.2028 to 0.2921	No	ns	>0.9999
24h :0mg/ml vs. 24h :250mg/ml	0.013	-0.2344 to 0.2604	No	ns	>0.9999
24h :0mg/ml vs. 48h :0mg/ml	-0.02733	-0.2748 to 0.2201	No	ns	>0.9999
24h :0mg/ml vs. 48h :10mg/ml	-0.1077	-0.3551 to 0.1398	No	ns	0.9884
24h :0mg/ml vs. 48h :20 mg/ml	-0.2137	-0.4611 to 0.03376	No	ns	0.1764
24h :0mg/ml vs. 48h :50 mg/ml	-0.1173	-0.3648 to 0.1301	No	ns	0.9704
24h :0mg/ml vs. 48h :100 mg/ml	-0.1607	-0.4081 to 0.08676	No	ns	0.6685
24h :0mg/ml vs. 48h :150 mg/ml	-0.2777	-0.5251 to -0.03024	Yes	*	0.0135
24h :0mg/ml vs. 48h :200mg/ml	-0.1597	-0.4071 to 0.08776	No	ns	0.6792
24h :0mg/ml vs. 48h :250mg/ml	-0.2017	-0.4491 to 0.04576	No	ns	0.258
24h :0mg/ml vs. 72h :0mg/ml	-0.197	-0.4444 to 0.05042	No	ns	0.2957
24h :0mg/ml vs.	-	-0.2991 to	No	ns	>0.9999

72h :10mg/ml	0.05167	0.1958			
24h :0mg/ml vs. 72h :20 mg/ml	- 0.00667	-0.2541 to 0.2408	No	ns	>0.9999
24h :0mg/ml vs. 72h :50 mg/ml	- 0.00667	-0.2541 to 0.2408	No	ns	>0.9999
24h :0mg/ml vs. 72h :100 mg/ml	0.1053	-0.1421 to 0.3528	No	ns	0.991
24h :0mg/ml vs. 72h :150 mg/ml	0.009	-0.2384 to 0.2564	No	ns	>0.9999
24h :0mg/ml vs. 72h :200mg/ml	0.01833	-0.2291 to 0.2658	No	ns	>0.9999
24h :0mg/ml vs. 72h :250mg/ml	0.087	-0.1604 to 0.3344	No	ns	0.9993

Table 8. 6: Cell viability evaluation (resazurin assays) after 24, 48 and 72h of incubation with melanoma C8161, increasing concentrations of alginate CNPs at 220 °C. Results are tested by using a two-way ANOVA means±SD of at least three independent experiments. *p < 0.05, **p < 0.01, ***p < 0.001 for statistical significance of each concentration used for CNPs.

Tukey's multiple comparisons test	Mean Diff.	95.00% CI of diff.	Significant?	Summary	Adjusted P Value
24h					
0µg/ml vs. 10µg/ml	- 0.01567	-0.1538 to 0.1225	No	ns	>0.9999
0µg/ml vs. 20µg/ml	- 0.04533	-0.1835 to 0.09285	No	ns	0.9657
0µg/ml vs. 50µg/ml	- 0.06333	-0.2015 to 0.07485	No	ns	0.828
0µg/ml vs. 100µg/ml	-0.073	-0.2112 to 0.06518	No	ns	0.7035
0µg/ml vs. 150µg/ml	-0.02	-0.1582 to 0.1182	No	ns	0.9998
0µg/ml vs. 200µg/ml	0.018	-0.1202 to 0.1562	No	ns	0.9999
0µg/ml vs. 250µg/ml	- 0.02133	-0.1595 to 0.1168	No	ns	0.9997

48h					
0µg/ml vs. 10µg/ml	-0.015	-0.1532 to 0.1232	No	ns	>0.9999
0µg/ml vs. 20µg/ml	0.004333	-0.1338 to 0.1425	No	ns	>0.9999
0µg/ml vs. 50µg/ml	0.039	-0.09918 to 0.1772	No	ns	0.9852
0µg/ml vs. 100µg/ml	0.001667	-0.1365 to 0.1398	No	ns	>0.9999
0µg/ml vs. 150µg/ml	-0.171	-0.3092 to -0.03282	Yes	**	0.0063
0µg/ml vs. 200µg/ml	-0.1693	-0.3075 to -0.03115	Yes	**	0.0071
0µg/ml vs. 250µg/ml	-0.2397	-0.3778 to -0.1015	Yes	****	<0.0001
72h					
0µg/ml vs. 10µg/ml	0.2063	0.06815 to 0.3445	Yes	***	0.0005
0µg/ml vs. 20µg/ml	0.318	0.1798 to 0.4562	Yes	****	<0.0001
0µg/ml vs. 50µg/ml	0.3437	0.2055 to 0.4818	Yes	****	<0.0001
0µg/ml vs. 100µg/ml	0.3817	0.2435 to 0.5198	Yes	****	<0.0001
0µg/ml vs. 150µg/ml	0.4017	0.2635 to 0.5398	Yes	****	<0.0001
0µg/ml vs. 200µg/ml	0.3267	0.1885 to 0.4648	Yes	****	<0.0001
0µg/ml vs. 250µg/ml	0.3587	0.2205 to 0.4968	Yes	****	<0.0001

Table 8. 7: Cell viability evaluation (resazurin assays) after 24, 48 and 72h of incubation with melanoma C8161, increasing concentrations of glucose CNPs at 200 °C. Results are tested by using a two-way ANOVA means±SD of at least three independent experiments. *p < 0.05, **p < 0.01, ***p < 0.001 for statistical significance of each concentraion used for CNPs.

Tukey's multiple	Mean	95.00% CI of	Significa	Summ	Adjusted P
------------------	------	--------------	-----------	------	------------

comparisons test	Diff.	diff.	nt?	ary	Value
24h:0 µg /ml vs 24h:10 µg /ml	-0.165	-0.5034 to 0.1734	No	ns	0.9609
24h: 0 µg /ml vs 24h:20 µg /ml	- 0.09467	-0.433 to 0.2437	No	ns	>0.9999
24h:0µg/ml vs. 24h:50µg/ml	-0.029	-0.3674 to 0.3094	No	ns	>0.9999
24h:0µg/ml vs. 24h:100µg/ml	0.08067	-0.2577 to 0.419	No	ns	>0.9999
24h:0µg/ml vs. 24h:150µg/ml	0.02267	-0.3157 to 0.361	No	ns	>0.9999
24h:0µg/ml vs. 24h:200µg/ml	0.034	-0.3044 to 0.3724	No	ns	>0.9999
24h:0µg/ml vs. 24h:250µg/ml	0.04833	-0.29 to 0.3867	No	ns	>0.9999
24h:0g/ml vs. 48h:0µg/ml	0.01833	-0.32 to 0.3567	No	ns	>0.9999
24h:0µg/ml vs. 48h:10µg/ml	0.07233	-0.266 to 0.4107	No	ns	>0.9999
24h:0µg/ml vs. 48h:20µg/ml	0.097	-0.2414 to 0.4354	No	ns	>0.9999
24h:0µg/ml vs. 48h:50µg/ml	0.2063	-0.132 to 0.5447	No	ns	0.7678
24h:0µg/ml vs. 48h:100µg/ml	0.1307	-0.2077 to 0.469	No	ns	0.9974
24h:0µg/ml vs. 48h:150µg/ml	0.124	-0.2144 to 0.4624	No	ns	0.9987
24h:0µg/ml vs. 48h:200µg/ml	0.1857	-0.1527 to 0.524	No	ns	0.8892
24h:0µg/ml vs. 48h:250µg/ml	0.1543	-0.184 to 0.4927	No	ns	0.9804
24h:0µg/ml vs. 72h:0µg/ml	- 0.00333	-0.3417 to 0.335	No	ns	>0.9999
24h: 0µg/ml vs. 72h:10µg/ml	- 0.01467	-0.353 to 0.3237	No	ns	>0.9999
24h: 0µg/ml vs. 72h:20 µg /ml	0.027	-0.3114 to 0.3654	No	ns	>0.9999
24h:0 µg/ml vs. 72h:50 µg/ml	0.1717	-0.1667 to 0.51	No	ns	0.9431
24h:0 µg/ml vs. 72h:100 µg/ml	0.08533	-0.253 to 0.4237	No	vσ	>0.9999
24h:0 µg/ml vs. 72h:150 µg/ml	- 0.06333	-0.4017 to 0.275	No	vσ	>0.9999
24h:0 µg/ml vs. 72h:200 µg/ml	0.05167	-0.2867 to 0.39	No	ns	>0.9999

Table 8. 8: Cell viability evaluation (resazurin assays) after 24, 48 and 72h of incubation with melanoma C8161, increasing concentrations of glucose CNPs at 220 °C. Results are tested by using a two-way ANOVA means±SD of at least three independent experiments. *p < 0.05, **p < 0.01, ***p < 0.001 for statistical significance of each concentraion used for CNPs.

Tukey's multiple comparisons test	Mean Diff.	95.00% CI of diff.	Significant?	Summary	Adjusted P Value
24h					
0µg/ml vs. 10µg/ml	-0.055	-0.2836 to 0.1736	No	ns	0.9943
0µg/ml vs. 20µg/ml	0.00133 3	-0.2272 to 0.2299	No	ns	>0.9999
0µg/ml vs. 50µg/ml	0.04633	-0.1822 to 0.2749	No	ns	0.998
0µg/ml vs. 100µg/ml	0.00933 3	-0.2192 to 0.2379	No	ns	>0.9999
0µg/ml vs. 150µg/ml	-0.112	-0.3406 to 0.1166	No	ns	0.7752
0µg/ml vs. 200µg/ml	-0.156	-0.3846 to 0.07258	No	ns	0.392
0µg/ml vs. 250µg/ml	-0.1273	-0.3559 to 0.1012	No	ns	0.6458
48h					
0µg/ml vs. 10µg/ml	- 0.07867	-0.3072 to 0.1499	No	ns	0.9558
0µg/ml vs. 20µg/ml	-0.1513	-0.3799 to 0.07724	No	ns	0.431
0µg/ml vs. 50µg/ml	-0.125	-0.3536 to 0.1036	No	ns	0.6665
0µg/ml vs. 100µg/ml	- 0.07033	-0.2989 to 0.1582	No	ns	0.9759
0µg/ml vs. 150µg/ml	0.103	-0.1256 to 0.3316	No	ns	0.8399
0µg/ml vs. 200µg/ml	0.137	-0.09158 to 0.3656	No	ns	0.5583
72h					
0µg/ml vs. 250µg/ml	0.177	-0.05158 to 0.4056	No	ns	0.2403
0µg/ml vs. 10µg/ml	0.091	-0.1376 to 0.3196	No	ns	0.9083
0µg/ml vs. 20µg/ml	0.2773	0.04876 to 0.5059	Yes	**	0.0079
0µg/ml vs. 50µg/ml	0.2687	0.04009 to 0.4972	Yes	*	0.0112
0µg/ml vs. 100µg/ml	0.3247	0.09609 to 0.5532	Yes	**	0.0011
0µg/ml vs. 150µg/ml	0.219	-0.009577 to 0.4476	No	ns	0.0692
0µg/ml vs. 200µg/ml	0.4773	0.2488 to	Yes	****	<0.0001

		0.7059			
0µg/ml vs. 250µg/ml	0.2603	0.03176 to 0.4889	Yes	*	0.0155